# The University of Sheffield

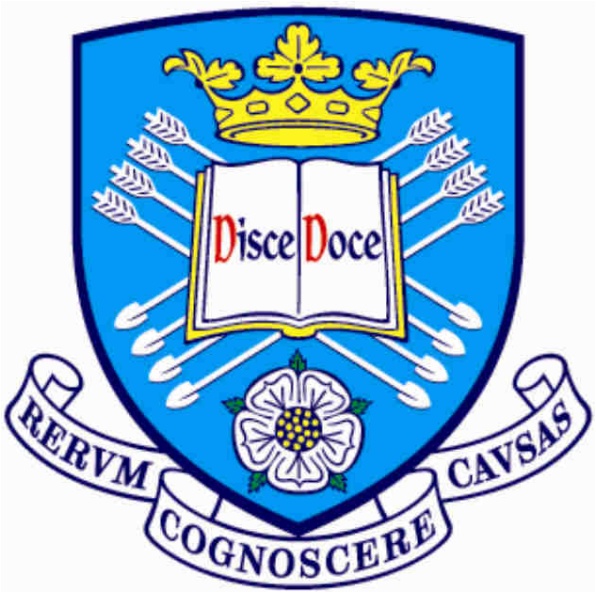


# Sensorless Control of Switched-Flux Permanent Magnet Machines

**Tzu-Chi LIN**

A thesis submitted for the degree of Doctor of Philosophy

Department of Electronic and Electrical Engineering

The University of Sheffield

Mappin Street, Sheffield, S1 3JD, UK

**20 April 2015**

# PUBLICATIONS

**Best Paper Award**

1. The following paper was awarded the **Best Paper Price** by ***the 2014 Ninth International Conference on Ecological Vehicles and Renewable Energies (EVER)*:**

   **T.C. Lin** and Z.Q. Zhu, "Sensorless operation capability of surface-mounted permanent magnet machine based on high-frequency signal injection methods," ***2014 Ninth Int. Conf. Ecological Vehicles and Renewable Energies (EVER),*** pp.1-7, 25-27 March 2014, Monaco.

   Its enhanced version was recommended and accepted for publication in **IEEE Trans. on Industry Applications**.

**Journal Papers**

1. **T.C. Lin**, L.M. Gong, J.M. Liu, and Z.Q. Zhu, "Investigation of saliency in switched-flux permanent magnet machine using high-frequency signal injection," ***IEEE Trans. Ind. Electron.***, vol. 61, no. 9, pp. 5094-5104, September. 2014.
2. **T.C. Lin** and Z.Q. Zhu, "Sensorless operation capability of surface-mounted permanent magnet machine based on high-frequency signal injection methods, Accepted for ***IEEE Trans. Ind. Appl.***, December, 2014, in press.
3. **T.C. Lin**, J.M. Liu and Z.Q. Zhu, "Sixth-harmonic back-EMF based sensorless control for switched-flux permanent magnet machine" Submitted to ***IEEE Trans. Ind. Electron*.**
4. **T.C. Lin**, Z.Q. Zhu and J.M. Liu, "Improved rotor position estimation in sensorless controlled permanent magnet synchronous machine having asymmetric-EMF with harmonic compensation," Accepted for ***IEEE Trans. Ind. Electron.***, April, 2015, in press.
5. **T.C. Lin**, Z.Q. Zhu, and K. Liu "Improved sensorless control of switched-flux permanent magnet machine based on different winding configurations," Submitted to ***IEEE Trans. Ind. Electron*.** Under review.

**Conference Papers**

1. **T.C. Lin**, L.M. Gong, and Z.Q. Zhu, "Saliency investigation of switched-flux PM brushless AC machine for saliency-tracking-based sensorless control," in ***XXth Int. Conf. Electric. Mach. (ICEM)***, 2-5 Sept. 2012, pp.2238-2244, France.
2. **T.C. Lin**, and Z.Q. Zhu, "Sensorless operation capability of surface-mounted permanent magnet machine based on high-frequency signal injection methods," ***2014 Ninth Int. Conf***. on ***Ecological Vehicles and Renewable Energies (EVER),*** pp.1-7, 25-27 March 2014, Monaco.
3. **T.C. Lin**, Z.Q. Zhu, and K. Liu, "Improved high-frequency carrier voltage measurement for position estimation of switched-flux permanent magnet machines," Submitted to ***2015 IEEE 6th International Symposium on Sensorless Control for Electrical Drives (SLED 2015)***, 7-8 June 2015, Sydney, Australia.

# ABSTRACT

This thesis investigates the sensorless control strategies of permanent magnet synchronous machines (PMSMs), with particular reference to switched-flux permanent magnet (SFPM) machines, based on high-frequency signal injection methods for low speed and standstill and the back-EMF based methods for medium and high speeds.

For the low speed and standstill operations, the carrier signal injection techniques are usually employed, which require the saliency property resulting from machine magnetic-saturation or geometric rotor. In order to evaluate the saliency level, a systematic experimental method is presented, in which the saliency can be experimentally measured under various load conditions, including the secondary saliency. According to the measured machine saliency information, the potential sensorless operation capability considering the cross-saturation effect in PMSM is systematically investigated based on signal injections.

Furthermore, based on different winding configurations, i.e. all poles wound (double layer winding) and alternate poles wound (single layer winding) topologies, as well as the different winding coil connections, the SFPM machines exhibit different saliency characteristics. In comparison, the all poles wound topology is expected to exhibit lower saliency level due to saliency cancellation effect. However, although the saliency level based on the alternate poles wound machine is significantly higher, the accuracy of rotor position estimation is still deteriorated by the influence of multiple saliencies. Hence, the orthogonal signal based observer, rather than existing position observers, is proposed to improve the accuracy of rotor position estimation, by minimizing or cancelling the effect of multiple saliencies. Also, a simple position error compensation method is proposed for improving the sensorless operation based on different winding coil connections.

For the medium or high speed operations, the back-EMF based sensorless control methods can successfully estimate the rotor position. Similarly, the back-EMF can be measured based on the different winding configurations. The alternate poles wound SFPM machine is found to exhibit asymmetric back-EMF which may deteriorate the rotor position estimation. In order to minimize the influence of asymmetric back-EMF, a control strategy, which has some advantages, such as easy implementation and less sensitive to the machine parameters, is proposed for the enhancement of rotor position estimation with the aid of elimination of back-EMF harmonics.

Moreover, another sensorless control method is to utilize the harmonic back-EMF for the sensorless rotor position estimation. Since the sixth-harmonic component is much bigger than the third-harmonic back-EMF in SFPM machines. Hence, several new sensorless control strategies based on the sixth-harmonic back-EMF are proposed for rotor position estimation based on integration, zero-crossing detection, and continuous sinusoidal signal. By eliminating the influence of third-harmonic back-EMF effect and with the aid of synchronous reference frame filter, the high accurate sensorless rotor position can be derived comparing to those of the methods based on the fundamental and the third-harmonic back-EMF methods.

# ACKNOWLEDGEMENT

Many thanks to my supervisor, Prof. Zi-Qiang ZHU, for his professional technical guidance, thoughtful comments and continued encouragement throughout the whole Ph.D. study, which has been constructive help and invaluable in the completion of this thesis.

The author is very grateful to Dr. Li-Ming GONG and Prof. Jia-Bing HU for their teaching that helped him starting the research study. Many thanks go to Dr. Nick LEONG, Dr. Jia-Ming LIU and Dr. Xu LIU for their technical assistances in many ways. Great suggestions from the discussions with Dr. Kai WANG, Dr. Kan LIU, and Mr. Pei-Lin XU were also very useful and helpful.

The author also wishes to acknowledge all staff members of the Electrical Machines and Drives Group, at the University of Sheffield, for their assistance on the experimental equipment and the professional advices.

Finally, grateful thanks to the author's family for their love, understanding, support and endless care.

# CONTENTS

# LIST OF SYMBOLS

| | |
|---|---|
| $A_{ap}$ | Amplitude of sixth-harmonic flux-linkage |
| $A_p$ | Amplitude of compensated 6th-harmonic flux-linkage |
| $d^v$-$q^v$ | Virtual synchronous *d*- and *q*-axis reference frame |
| $e_a$, $e_b$, and $e_c$ | Three-phase back-EMFs |
| $E_{mg}$ | Magnitude of phase back-EMF |
| $e_{mg1}$ and $e_{mg3}$ | Magnitudes of back-EMF harmonics |
| $f(\Delta\theta)$ | Position error signal |
| $f_c$ | Frequency of injected signal |
| $hm$ | Harmonic component and order of primary or secondary saliency |
| $h_n$ | Harmonic component in phase back-EMF |
| $i_{dh}^v$ , $i_{qh}^v$ | Virtual high frequency *d*- and *q*-axis currents |
| $\lvert i_{dh}^v \rvert$, $\lvert i_{qh}^v \rvert$ | Estimated *d*- and *q*-axis currents from primary saliency estimation |
| $\lvert i_{dh}^e \rvert$, $\lvert i_{qh}^e \rvert$ | Estimated *d*- and *q*-axis currents from secondary saliency estimation |
| $i_a$, $i_b$, and $i_c$ | Three-phase currents |
| $i_{abc}$ | Three phase current |
| $i_{dh}$ , $i_{qh}$ | Actual high frequency *d*- and *q*-axis currents |
| $I_n$ | Critical current parameter for determining the radius of saliency circle |
| $I_{n\_hm}$ | Disturbance current depending on rotor position due to secondary saliency |
| $I_p$ | Critical current parameter for determining the center point of saliency |
| $I_s$ | Stator current vector |
| $k$ | Adaption value |
| $K_{ap}$ | Amplitude of 6th-harmonic back-EMF |

| | |
|---|---|
| $L$ | Inductances |
| $L_{dh}$, $L_{qh}$ | *d*- and *q*-axis incremental self- inductances |
| $L_{dqh}$, $L_{qdh}$ | Incremental mutual-inductances between *d*- and *q*-axes |
| $L_n$ | Machine saliency level |
| $L_p$ | Equivalent positive sequence inductance |
| $L_s$ | Stator winding inductance |
| $L_{sa}$ | Average of *d*- and *q*-axis incremental inductances |
| $L_{sd}$ | Difference of *q*- and *d*-axis incremental inductances |
| M | Mutual-inductance |
| $p$ | Differential operator, $p=d/dt$ |
| $R_s$ | Phase resistance |
| $T(\Delta\theta)$ | Rotation matrix from actual to estimated reference frame |
| $t_d$ | Time interval of two zero-crossings |
| $v^{v}_{dh}$, $v^{v}_{qh}$ | Virtual high frequency *d*- and *q*-axis voltages |
| $u^{*}_{s2n}$ | Compensated sixth-harmonic back-EMF |
| $u_{an}$, $u_{bn}$, and $u_{cn}$ | Three-phase voltages |
| $U_c$ | Amplitude of injected high-frequency voltage signal |
| $U_s$ | Stator voltage vector |
| $u_{s1n}$ | Third-harmonic back-EMF |
| $u_{s2n}$ | Sixth-harmonic back-EMF |
| $V_c$ | Amplitude of injected high frequency voltage signal |
| $\alpha^*$ | New updated phase angle |
| $\Delta R$ | Differential value of resistance |
| $\Delta t_s$ | Time difference between two sampling instants |
| $\Delta\theta$ | Phase angle difference |

| | |
|---|---|
| $\Delta\theta^r$ | Position error between estimated and actual reference frames |
| $\Delta\varphi$ | Initial phase difference between primary and secondary saliencies |
| $\theta_0$ | Initial rotor position estimated from harmonic back-EMF |
| $\theta^e_{rf}$ | Estimated rotor position calculated from compensating flux-linkage vector |
| $\theta_m$ | Cross-saturation angle |
| $\theta_r$, $\theta_r^v$ | Actual and virtual rotor positions |
| $\Sigma L$ | Average inductance |
| $\Sigma R$ | Average value of resistance |
| $\varphi$ | Initial phase angle of injected carrier voltage |
| $\varphi_{i1}$ and $\varphi_{i3}$ | Phase angles of back-EMF harmonic |
| $\Psi^*_{f\alpha}$ and $\Psi^*_{f\beta}$ | Compensating flux-linkage vector |
| $\Psi_f$ | Total resultant PM excitation flux-linkage vector |
| $\Psi_{f(0)}$ | Excitation flux-linkage produced by PMs |
| $\psi_{pm}$ | Permanent magnet flux linkage |
| $\Psi_s$ | Stator winding flux-linkage |
| $\Psi_s$ | Stator winding flux-linkage vector |
| $\psi_{sn}$ | Sixth-harmonic flux-linkage |
| $\Psi_{s(0)}$ | Total stator winding flux-linkage |
| $\Psi_\alpha$, $\Psi_\beta$ | $\alpha$- and $\beta$-axis flux-linkages |
| $\omega_c$ | Angular speed of injected signal |
| $\omega_{cor}$ | Rotor speed correction |
| $\omega_h$ | Frequency of harmonics |

# LIST OF ABBREVIATIONS

| | |
|---|---|
| A/D | Analog to digital |
| AC | Alternating current |
| ADC | Analog-to-digital conversion |
| BLAC | Brushless AC |
| BLDC | Brushless DC |
| DSP | Digital signal processor |
| DSPM | Doubly salient permanent magnet |
| DTC | Direct-torque control |
| DWO | Digital Waveform Output |
| EKF | Extended Kalman filter |
| EMF | Electromotive force |
| FE | Finite element |
| FFT | Fast Fourier Transform |
| HF | High-frequency |
| HPF | High-pass filter |
| IGBT | Insulated-gate bipolar transistor |
| INFORM | Indirect flux detection by online reactance measurement |
| IPM | Interior permanent magnet |
| LPF | Low-pass filter |
| MWC | Machine winding configuration |
| PI | Proportional integral |
| PLL | Phase-locked loop |
| PM | Permanent magnet |

| | |
|---|---|
| PMSM | Permanent magnet synchronous machine |
| PWM | Pulse width modulation |
| RTP | Real-time processor |
| SFPM | Switched-flux permanent magnet |
| SMO | Sliding mode observer |
| SNR | Signal to noise ratio |
| SPM | Surface-mounted permanent magnet |
| SRFF | Synchronous reference frame filter |
| SVPWM | Space vector pulse width modulation |
| TP-PLL | Two-phase-type phase-locked loop |

# CHAPTER 1

# GENERAL INTRODUCTION

## 1.1 Introduction

Permanent magnet synchronous machines (PMSM) are being extensively employed for many industrial applications due to their advantages, i.e. brushless construction and outstanding performances, high torque density, improved power density, high efficiency and fast torque/speed response. In addition, the development of control techniques, power electronics and high performance of micro-processor systems are facilitating the implementation of machine drives with higher reliability, low cost and better dynamic performance. Therefore, the permanent magnet (PM) brushless machine drives are an attractive research topic in both academic study and industry.

In order to achieve high control performance and minimize the current harmonics and torque ripple, a high resolution vector controlled method which requires accurate rotor position information has to be applied. The rotor position information is normally obtained from a position sensor, i.e. Hall-effect sensor, resolver and absolute/incremental encoder etc., which is usually located on the rotor shaft, as shown in Fig. 1.1 (a). However, in some particular situation, the position sensor cannot be used, such as the increase of system size and cost and the low system reliability. Therefore, many high performance sensorless control techniques have been considered to replace the need of position sensor, as shown in Fig. 1.1 (b), in which the rotor position information can be estimated either from terminal voltages or currents of PMSMs.

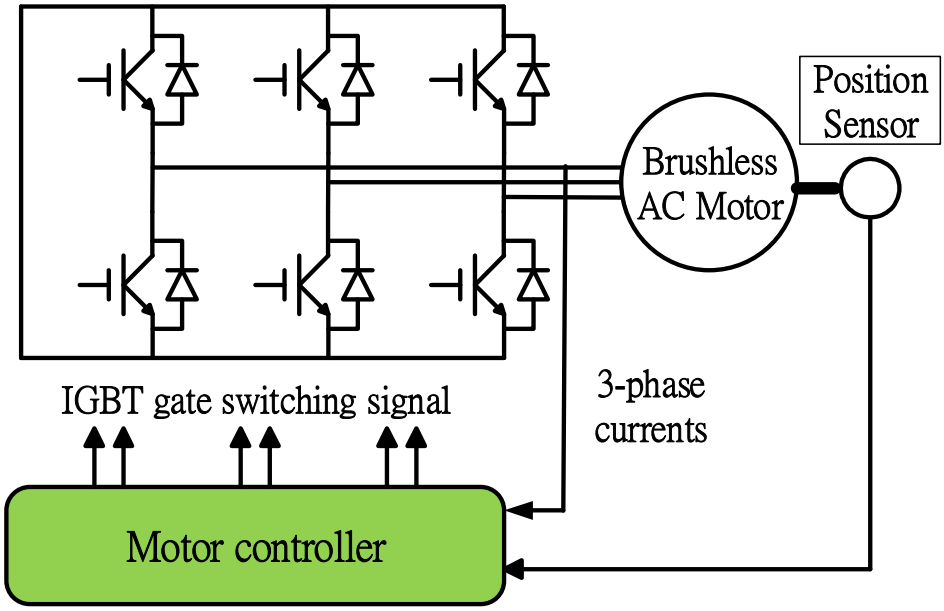


(a) Sensored operation for brushless PMSM

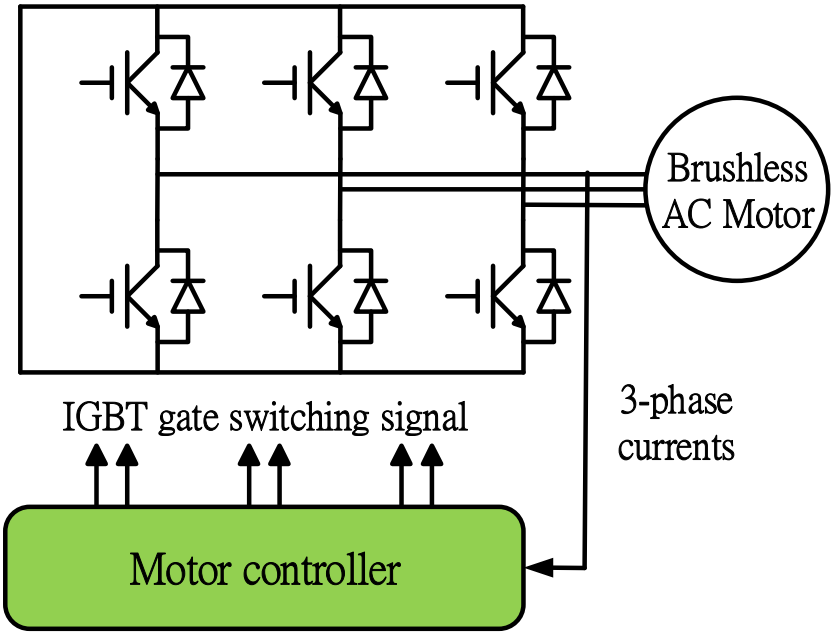


(b) Sensorless operation for brushless PMSM

Fig. 1.1. Control of brushless BLAC machine (a) Sensored model (b) Sensorless model.

The main focus of this chapter is to introduce various machine topologies for PMSM, as well as sensorless-based control techniques, i.e. back electromotive force (back-EMF) and machine saliency based methods. Additionally, the research outline and contributions will also be listed at the end of this chapter.

## 1.2 Permanent Magnet Synchronous Machines

### 1.2.1 Categories of Brushless Permanent Magnet Machines

The topologies of PM brushless machine can be classified into several forms, as discussed in and can be summarized in Fig 1.2.

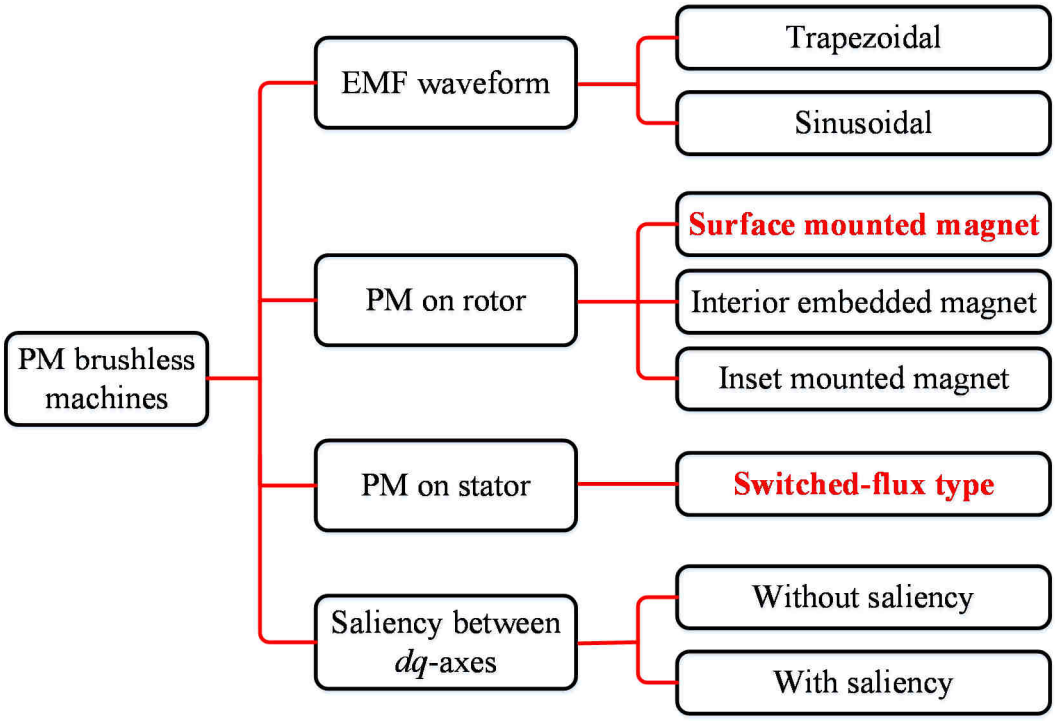


Fig. 1.2. Summary of PM brushless machine.

Brushless PM machine can be designed into two groups [ACA06] [PIL91]. The first category of PM machine is referred to as the machines with square-wave (or trapezoidal wave) back-EMF and square-wave currents, namely Brushless Direct Current (BLDC) machines. The second group, namely Brushless Alternating Current (BLAC) machines, has sinusoidal back-EMF and supplies sinusoidal currents by pulse width modulation (PWM) of the DC supply voltage [ACA06] [SAF95]. The phase back-EMF and current waveforms for BLDC and BLAC machine are shown in Fig. 1.3.

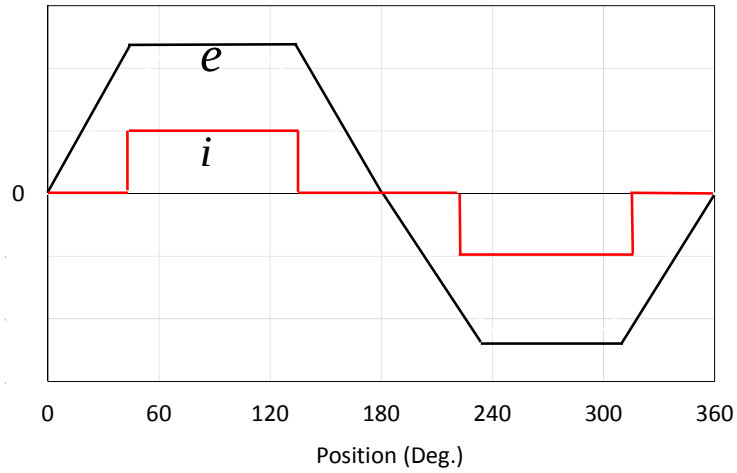


(a) BLDC operation mode

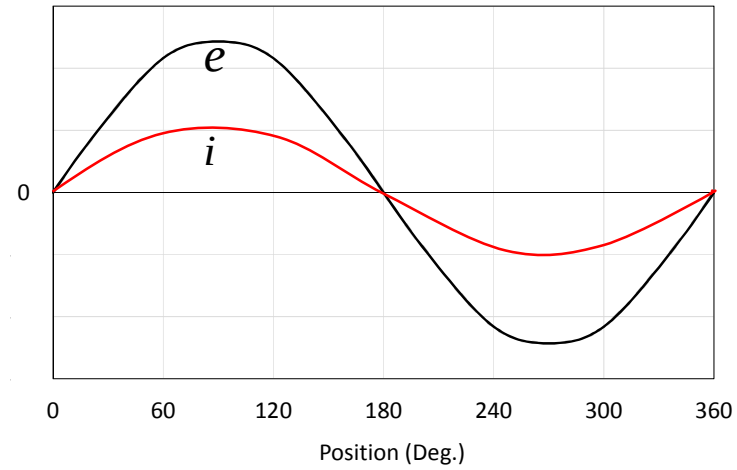


(b) BLAC operation mode

Fig. 1.3. Phase back-EMF and current waveforms for BLDC and BLAC machines

It is well known that the stator winding configurations can be referred to as either non-overlapping stator winding or overlapping stator winding, as shown in Fig. 1.4. In terms of non-overlapping stator winding topology, the machine winding factor is usually lower but the end winding is shorter and easy for manufacturing. Moreover, the cogging torque is relatively small because of fractional-slot. On the other hand, for the overlapping stator winding topology, the machine winding factor can be equal to 1 but its end winding is longer and the machine may produce large cogging torque [HEN94], which is opposite to the non-overlapping winding topology.

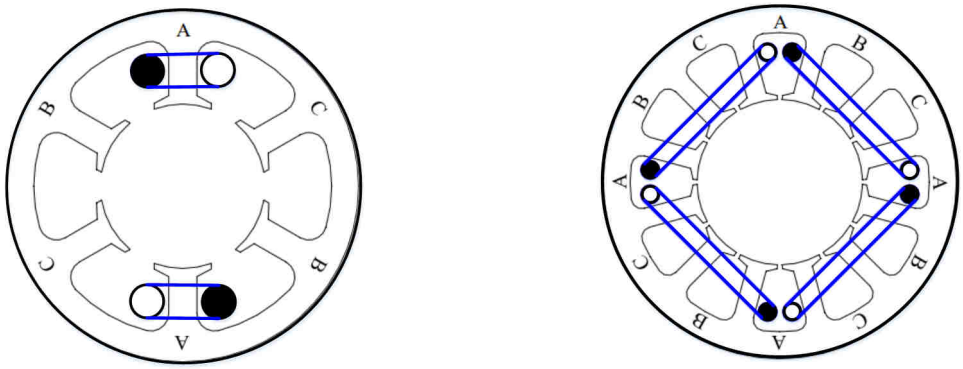


(a) Non-overlapping winding (b) Overlapping winding

Fig. 1.4. PM machine stator winding configurations [SHE02].

For the brushless PM machine, the inductance variation and the back-EMF are dependent on the magnetic structure. The machine is usually to have a field produced by the permanent magnet on the rotor and the armature winding on the stator. For the conventional radial-field PM machine, there are four major rotor structures, as depicted in Fig. 1.5 [CHE99] [LI09a]: (1) Surface mounted, (2) Inset, (3) Interior radial, and (4) Interior circumferential with potential of flux focusing. In the surface-mounted permanent magnet arrangement, Fig. 1.5 (a), the effective air-gap is equal to the physical air-gap between the rotor and the stator plus the magnet thickness [CHE99]. The armature field produced by current flowing conductors is relatively low. Hence, the inductance of the phase winding is small. Moreover, if the rotor surface is covered by a permanent magnet, the variation in winding inductance with rotor position can be ignored. The inset magnet rotor shown in Fig. 1.5 (b) is usually preferred for saliency torque production [CHE99]. The soft-magnetic material at the physical air-gap between the magnet poles can introduce a substantial variation in winding inductance with maximum inductance that will occur at a rotor position when the magnet pole arcs are misaligned with the axis of windings.

The other two topologies have magnets located in the rotor body as shown in Figs. 1.5 (c) and (d). For the interior magnet structure shown in Fig. 1.5 (c), the magnetization direction is radial. The final rotor structure is a flux focusing type, having magnets circumferentially

mounted, as shown in Fig. 1.5 (d). Both machines exhibit saliency due to the variation of winding inductance [CHE99].

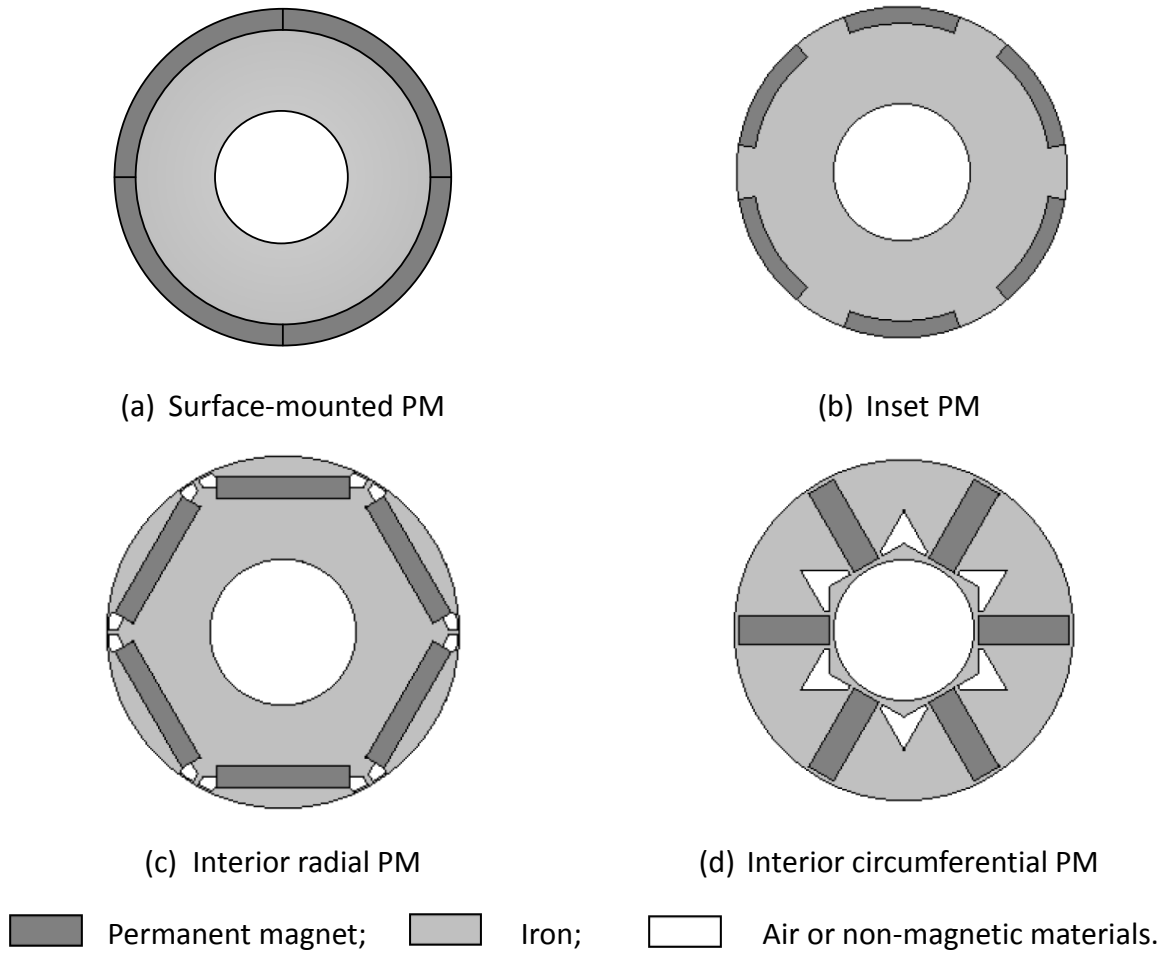


Fig. 1.5. Typical rotor designs of PM brushless machines [CHE99] [LI09a].

## 1.3 Sensorless Control of Permanent Magnet Brushless Machines

As mentioned in the previous section, the accurate rotor position information is an essential requirement for both BLDC and BLAC machines, which is usually obtained from the high-resolution position sensors. On the other hand, the use of these sensors will lead to some problems, such as additional cost and system physical size, lower system reliability and sensitivity to noise and vibration. To avoid these issues, the on-line rotor position estimation has been of increasingly attractive interest instead of measuring the position information from

the position sensor, namely sensorless or self-sensing control. In this thesis, the use of sensorless vector control technique is the only consideration for PM BLAC Machines.

Various sensorless control methods for PM BLAC machines can be categorized as machine signal injection based sensorless control methods and back-EMF based sensorless control methods, as shown in Fig. 1.6. However, since the frequency and magnitude of the back-EMF are both proportional to the rotor speed, the accuracy of rotor position is limited at zero and low speed, but shows good performance above a certain speed. Therefore, to overcome these limitations, the signal injection based techniques are usually employed at low speed. Since the machine saliency is not dependent on the rotor speed, the signal injection based methods can be effectively estimate the rotor position at low speed and standstill, but will deteriorate at high speed because of the signal to noise ratio (SNR) being too weak to extract the rotor position information.

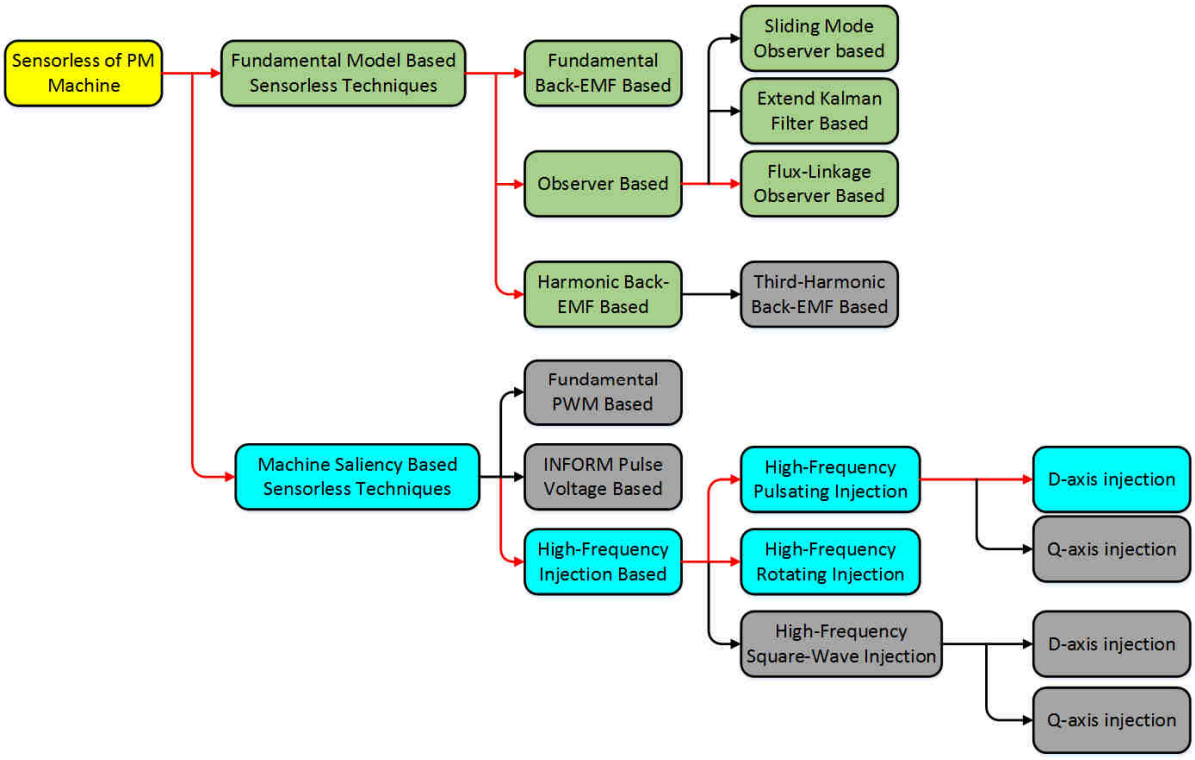


Fig. 1.6. Summary of sensorless control techniques.

### 1.3.1 Fundamental and Third-Harmonic Model Based Sensorless Techniques

Generally, the principle of fundamental model based sensorless control techniques is to extract the fundamental or harmonic back-EMF, or to observe the flux-linkage based on the machine fundamental model, in which the rotor position information can be obtained. Moreover, the other ways of the observer based method to gain the rotor position information, e.g. extended Kalman filter (EKF), sliding mode observer (SMO). These observers can directly estimate the rotor position without considering back-EMF or flux-linkage. There are several typical back-EMF based sensorless control techniques which are compared in Table 1.1.

TABLE 1.1

COMPARISON OF THREE BACK-EMF BASED SENSORLESS CONTROL METHODS

| | Fundamental Back-EMF Based | Flux-Linkage Observer Based | Third-Harmonic Back-EMF Based |
|---|---|---|---|
| Applicable Machine | BLAC | BLDC/BLAC | BLDC/BLAC |
| Terminal Voltage | Needed | None | Needed |
| Phase Current | Needed | Needed | None |
| Machine Neutral Point | None | None | Needed |
| Third-Harmonic in Back-EMF | None | None | Needed |

**A. Fundamental Back-EMF Based Method**

The back-EMF is induced when there is a motion between the armature windings and the air-gap magnetic field generated by the PMs, and proportional to the rotor speed. Since the

back-EMF is dependent on the rotor position, the rotor position information can be directly estimated from the back-EMF. However, for a salient PM machines, such as an interior PM machine, the fundamental back-EMF term would not completely contain the position information. Hence, the extended back-EMF method is considered to obtain the rotor position information for any types of salient machines [CHE00] [CHE03]. In addition, the improved method [LI07] based on the extended back-EMF has taken the cross-saturation effect into account. [WAN12] developed a new startup method based on the current regulation, which can solve the starting and low speed problems. Also, the switching procedure from startup to sensorless operation is smooth, even at different load conditions. A simple startup technique should be robust with any load condition.

In [FAT08], a first order compensator was employed to obtain the rotor position information by the back-EMF based method which heavily depends on the compensation parameters. Another method presented in [STI10] has a similar principle to the first order compensator and also very sensitive to the parameters of compensator to secure the good performance.

The back-EMF can also be estimated by a disturbance voltage observer based sensorless control [SEN95], and can also be implemented for the extended back-EMF estimation of interior PM machines [CHE03], as shown in Fig. 1.7. In [LEE11a], the disturbance observer based is also utilized to estimation the torque and produce the compensating signal to reduce the error in the rotor position estimation and improve the robustness to the load variation and sensorless operation.

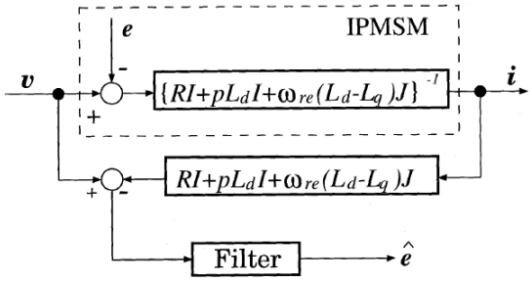


Fig. 1.7. Disturbance voltage observer for extend back-EMF estimation [CHE03].

**B. Flux-Linkage Based Observer**

The flux-linkage observation is an important feature in the direct-torque control (DTC), and also for the rotor position estimation in sensorless control. The rotor position is usually estimated by the PM excitation flux-linkage, since the rotor position information is contained in its phase angle, as demonstrated in Fig. 1.8 [WU91] [SHE02a].

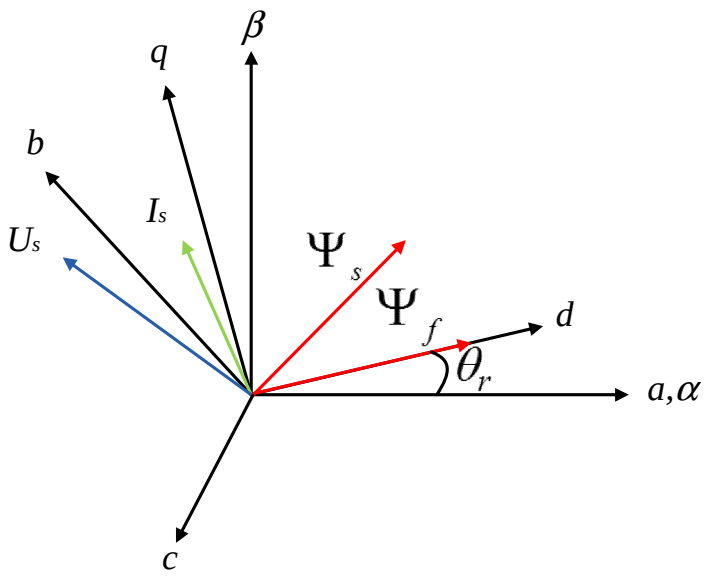


Fig. 1.8. Phasor diagram of different reference frame of PM machine.

The principle of flux-linkage observation is very simple, and the stator flux-linkage for PM machine can be obtained from the machine back-EMF and expressed in the stationary reference frame as

$$\Psi_s^* = \int \left( U^* - R_s I^* \right) dt \tag{1.1}$$

where $R_s$ is the stator resistance. The current vector $I^*$ and the voltage vector $U^*$ are derived from the phase current and terminal voltage, respectively. However, there are some problems for measuring the terminal voltage, such as isolation issues and additional cost for the voltage transducer. Hence, the applied voltage is calculated from the DC supply voltage and demands of SVPWM, but this may cause a certain error in the rotor position due to the dead-time

effect, which has been compensated in [HAR00].

Furthermore, the equation in (1.1) can be used to estimate the stator flux-linkage by an open-loop calculation, and some potential issues need to be taken into account, i.e. integration drift and stator resistance variations. The study in [WU91] used the integration of machine terminal voltage for the stator flux observation to detect the rotor position. However, it has some problems such as flux vector offset and drift due to the error occurs in the winding resistance. To avoid these issues, therefore, [WU91] proposed that the pure integrator can be replaced by a low-pass filter (LPF) then the accuracy of rotor position estimation can be improved. On the other hand, the use of a low-pass filter will cause a phase shift to the fundamental flux vector in a variable speed operation since its dynamic response is not fast enough.

In [LEE11b], discrete time stator current and flux-linkage observers were proposed for the stator flux-linkage observation. Moreover, other stator flux-linkage estimations based on either voltage or current methods have been discussed in [LUU03] [IDR02] [HIN03]. The stator flux-linkage observer that was proposed in [JEO05] can estimate the inductance online, but variations of the machine resistance and PM flux-linkage need to be taken into consideration. Moreover, the close-loop methods are also utilized to estimate the stator flux-linkage [HU98] [BOL09] [YOO09]. The current model and voltage model together, as shown in Fig. 1.9, is utilized for the stator flux-linkage observer in the rotor frame [YOO09] [XU14]. This type of observer can be applied over a wider speed region since the current model is dominant in the low frequency range, whereas the voltage model is dominant in the high frequency range.

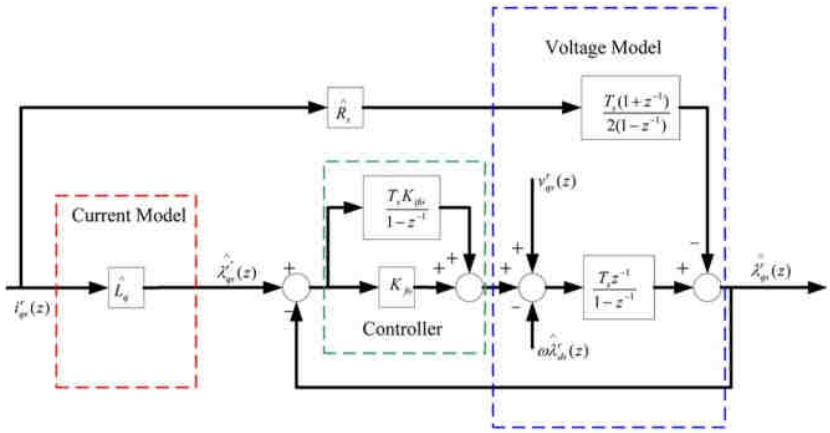


Fig. 1.9. Combined flux-linkage observer [XU14].

### C. Other Observer Based Methods

Based on the model of PM machines, there are still several types of observer that can be introduced, such as extended Kalman filter (EKF) [TER01] and sliding mode observer (SMO) [FOO10]. These observers have some benefits, i.e. robustness, quick convergence and response and insensitivity to machine parameter. Because of that, the observer based methods become more popular for rotor position estimation in sensorless control.

**(a) Extended Kalman filter (EKF)** is a continued application of the Kalman filter which can be used in a non-linear system including dynamic operation. The advantages of EKF, i.e. less influence by the noise (unknown harmonics in the input signal) and inaccurate machine parameters, in which the high accuracy of rotor position estimation can successfully achieve [BOL99] [TER01] [RIV13]. However, the reduced order EKF is proposed for enhancing the speed control due to free of noise [FUE11].

**(b) Sliding mode observer (SMO)** was first published in 1990s [FUR92] and used for the sensorless rotor and speed estimation. [LI05] [DER05] proposed to utilize the two sliding mode current observers to eliminate the influence of parameter variation and make more robust for the flux-linkage and speed estimations. [KIM11] presented a new SMO for a

robust sensorless control of PMSMs. It can solve the problem in the conventional SMO by using a sigmoid as a switching function instead of conventional sign function [ZHA06]. Combining the SMO with high-frequency injection method, a high steady-state and dynamic performances can be achieved over a wide speed range.

### D. Third-Harmonic Based Sensorless Control

Third-harmonic back-EMF is usually formed in the phase back-EMF and has only been utilized for the BLDC machines. However, [SHE04] utilized the zero-crossing points to detect the rotor position information for both BLDC and BLAC machines. Hence, the neutral point of the Y-connected windings, with a Y-connected resistance network, is essential for detecting the third harmonic back-EMF as shown in Fig. 1.10.

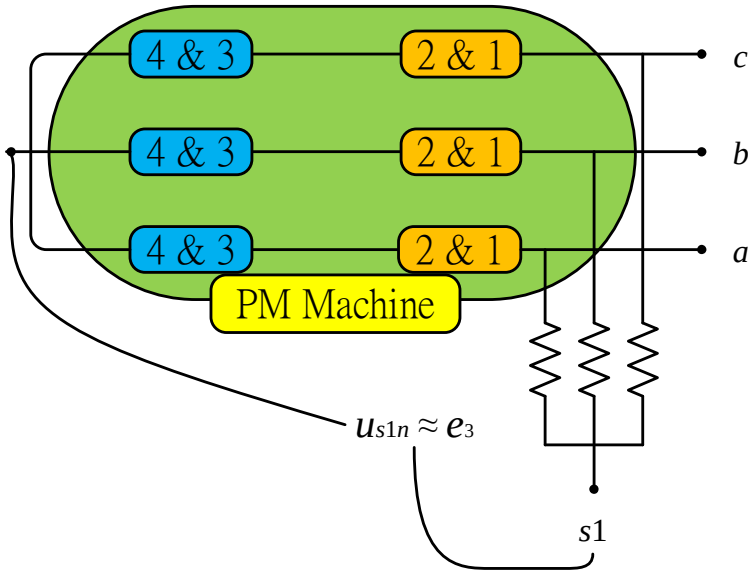


Fig. 1.10. Detection of harmonic back-EMFs.

Since the 3rd-harmonic back-EMF has three cycles in terms of frequency against the fundamental back-EMF, the zero-crossings in the 3rd-harmonic back-EMF are related to some particular positions [KER94], i.e. 0, π/3, 2π/3, π, 4π/3, 5π/3, 2π, as illustrated in Fig. 1.11.

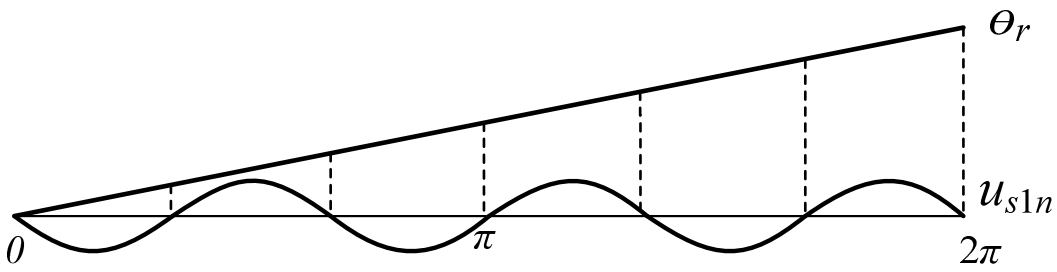


Fig. 1.11. Zero-crossings of the third-harmonic back-EMF.

According to [SHE06b][LIU14], the initial rotor position $\theta_0$ of each half-cycle between two zero-crossings could be known. Then, the estimated rotor position can be calculated by simple integration as

$$\theta_r^e = \theta_0 + \int_0^t \omega_r^e dt = \theta_0 + \int_0^t \frac{\pi/3}{t_d} dt \tag{1.2}$$

where $\omega_r^e$ in (1.2) is actually the average machine speed which can be calculated from the time cycle of zero-crossings, whilst $t_d$ is the time interval of position estimation. However, for the conventional 3rd-harmonic back-EMF based sensorless control, the estimated rotor position will only be accurate under steady-state and deteriorated during dynamic transient state.

When the machine is magnetically saturated, the air gap flux-linkage may include the harmonic components [MOR92]. These harmonic components are in synchronous rotation with the fundamental flux-linkage and related to the rotor position. Due to magnetic saturation or design features of a permanent magnet machine, the harmonic back-EMF is usually induced. The method proposed by Kim [KIM03] used a stationary reference frame state filter to detect the back-EMF and an enhanced Luenberger-type back-EMF tracking observer for the rotor position estimation.

In [SHE06a] [SHE06b] [SHE04] [KER94] [LIU14], some practical issues in implementing the 3rd-harmonic back-EMF based sensorless control were reported for the rotor position detection. In [GEN10], a novel sensorless control algorithm based on the back-EMF without the use of voltage probes was presented. A simple robust method that can easily allow a speed transition and smooth torque for the sensorless vector control strategy under different load conditions was developed in [WAN12]. In [FEA09], a new software scheme using a phase-locked loop (PLL) based on the 3rd-harmonic back-EMF detection was published and showed that the torque could be improved during the high speed operation. Moreover, the estimated flux-linkage harmonics resulting from the back-EMF can be utilized to compensate for the influence of harmonic currents by adding the harmonic currents to the fundamental currents in order to reduce the torque harmonics in [DEG98].

By comparison, the third-harmonic back-EMF based sensorless control method has several drawbacks (1) additional wire and resistances are required, (2) the machine must be Y-connected winding structure, (3) the machine neutral point is needed, (4) this method can only be applied for the machine containing the third harmonic in addition to its fundamental back-EMF.

### 1.3.2 Machine Saliency Based Sensorless Control Methods

Since the back-EMF is proportional to the machine rotor speed, the back-EMF based methods are not able to be used to estimate the rotor position at low speed and standstill. Hence, the saliency based techniques are developed to overcome these problems since the machine saliency is independent on the speed. The principle of saliency based sensorless control methods can be described that the winding inductance variation is an important feature for the rotor position estimation due to the machine magnetic saturation-induced saliency or geometric rotor saliency. In Fig. 1.12, the phase inductance variation is compared

with the rotor position for PM machines [KAN10]. It shows that the inductance is position-dependent, spatially salient and modulated as two cycles per signal cycle of electrical position.

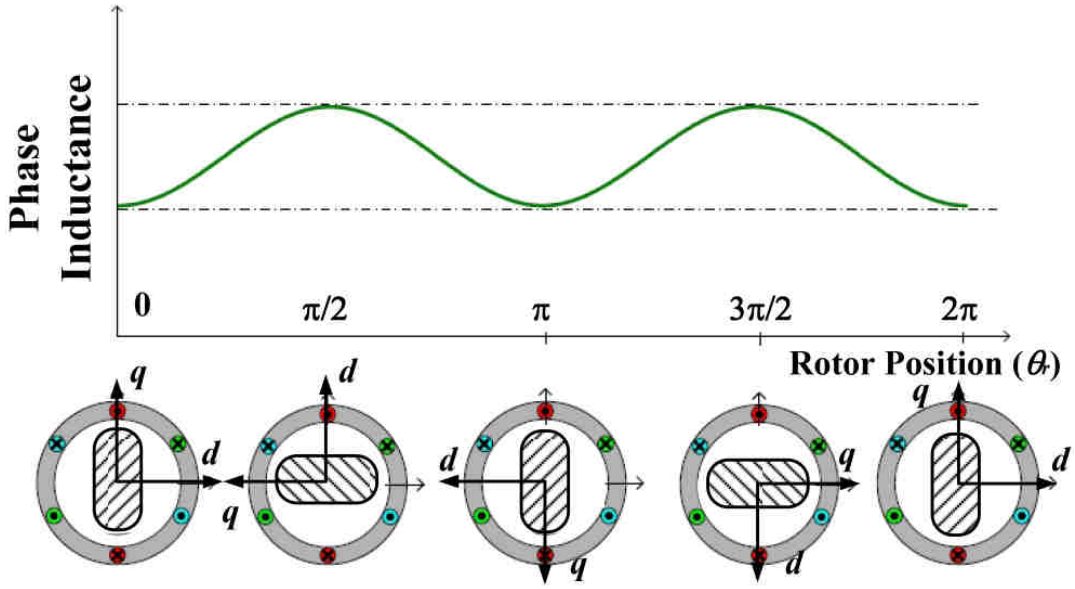


Fig. 1.12. Phase inductance variation dependent on the rotor position [KAN10].

To detect the rotor position information, machine saliency is necessary for high-frequency carrier signal injection to obtain the position-dependent current or voltage responses from the high frequency machine model. In terms of the injection signal, the signal injection based sensorless control techniques can be classified into several methods, i.e. pulse width modulation (PWM) based methods, INFORM pulse voltage based methods, high-frequency (HF) carrier signal based methods. Three types of signal injection based sensorless control techniques are summarized in Table 1.2.

TABLE 1.2

COMPARISON OF THREE TYPES OF SIGNAL INJECTION BASED SENSORLESS CONTROL METHODS

| | PWM Based | INFORM Pulse Voltage Based | High-Frequency Signal Injection Based |
|---|---|---|---|
| Injection Frequency Signal | High | Medium | Low |
| Dynamic Operation Response | Fast | Medium | Slow |
| Initial Rotor Position Detection | Not needed | Not needed | Needed |
| Current Sampling Accuracy | High | Low | Low |

**A. Pulse Width Modulation (PWM) Based Methods**

By injecting a sinusoidal signal into the machine, some potential problems may be introduced, such us acoustic noise and loss, current ripple. Therefore, the inherent Pulse Width Modulation (PWM) from the inverter output is considered as the injection signal [OGA98] [HUA07] [GAO07] [HUA10]. At higher modulation index, the current derivative to two specific voltage vectors within PWM period for positon estimation: active vectors and the null vectors, can be measured from the fundamental PWM switching cycles [HUA07], in which the rotor position information can be obtained [HOL05] [GAO07] [BOL11] [HUA11]. Also, the method for a higher modulation index is not applicable during the whole sensorless speed control range, and two improved estimation schemes are discussed in [HUA07]

[JUL05]. Furthermore, an extended modulation (EM) scheme was proposed in [HOL05], the modified PWM excitation used the current transient response to obtain the saliency information for the positon estimation.

Additionally, several different methods based on PWM excitation for position estimation are reported in [RAU10] [LEI11]. The second PWM harmonic was found that can be utilized as a pulsating voltage vector due to its large magnitude [RUA10]. Hence, the positon dependent impedance can be calculated by the second PWM voltage and current harmonic, and then the position dependent impedance can be used for the rotor position estimation. In [LE11], another effective method for the rotor position estimation was introduced to employ the zero sequence voltage measured from the standard PWM. This method can achieve the high signal to noise (SNR) ratio, however, the additional wire is required, and this will make the system more complex.

The PWM based method has some advantages such as faster dynamic response because of high frequency PWM and wide speed range operation, but the difficulty is the current derivative synchronous measurement in their practical application.

**B. INFORM Pulse Voltage Based Methods**

Indirect Flux detection by On-line Reactance Measurement (INFORM) method [SCH96] [ROB04] is designed to generate a pulse voltage during the zero vector for the PWM signal, which is similar to the method based on the PWM injection. INFORM method is to measure the current response produced by the voltage space phasor as shown in Fig. 1.13, and INFORM position estimation can be directly detected by interrupting the PWM pattern for a specific period of time [ROB04]. There is only one phase that can be evaluated during an INFORM measurement sequence in order to maintain the additional switching frequency at a low level. Therefore, the required current response from other phases can be evaluated from

the previous measurements [REB02]. The real-time inductance measurements are used for INFORM based sensorless rotor position [SCH96]. Moreover, in [SCH03], a more reliable transient performance from standstill using the INFORM method was introduced.

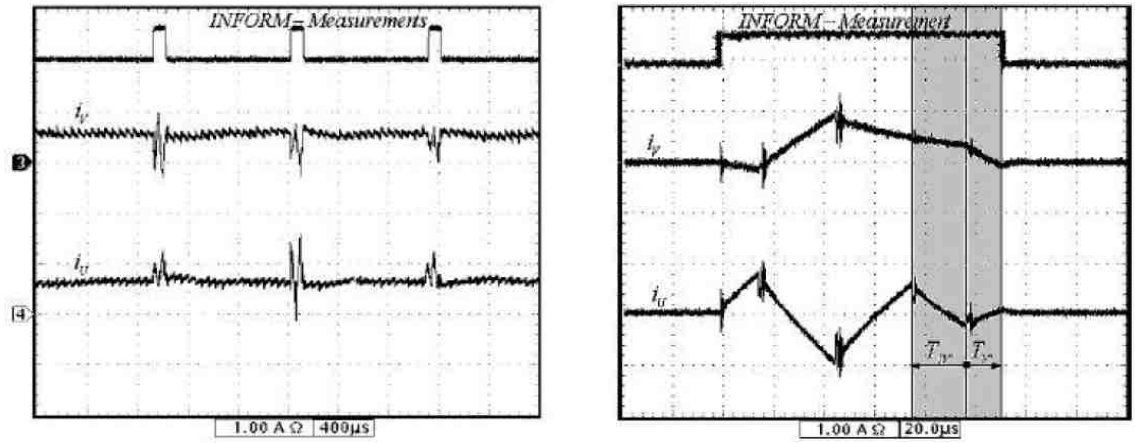


Fig. 1.13. Current waveforms of INFORM pulse injection method [ROB04].

By comparing with the PWM injection based techniques, the INFORM method has more advantages of injected current conditions. Hence, when the pulse signals are injected into the machine, the current will not produce as much noise and current losses as the sinusoidal carrier injection method. However, since the INFORM pulse voltage vector is not a continues signal, the estimated rotor position cannot be kept updating, hence, the dynamic response will be slow and not fast enough to reflect the dynamic transient state.

### C. High-Frequency Carrier Signal Injection Based Methods

High-frequency (HF) carrier signal injection-based sensorless control techniques are used to estimate the rotor position for PM machines, and have been widely employed due to their effectiveness at standstill and low speed operation range. The sensorless control operation based on the HF signal injection method is shown in Fig. 1. 14.

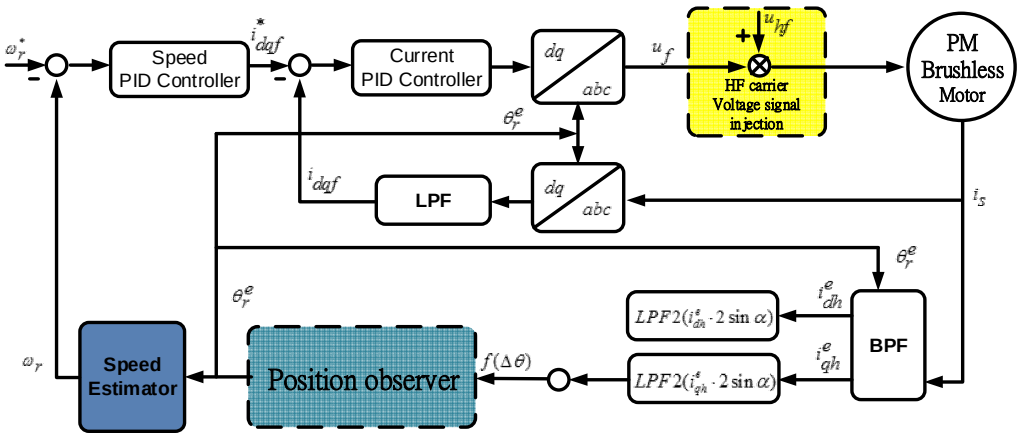


Fig. 1.14. HF signal injection based sensorless control.

The HF injection-based sensorless control injects an extra voltage or current signal into the machine windings and use the corresponding signals to detect the rotor position [LEI11], which can be categorised as rotating voltage [DEG18] [RAC10] [SIL06] [HOL98] [CAR06] [ZHU11], pulsating voltage [ZHU11] [COR98] [HAR00] [ACC12] [CUP11] and square-wave voltage signal injection [YOO11].

The rotating carrier signal injection based method is basically to inject a balanced high frequency three phase voltage in the stationary reference frame to form a rotating excitation vector [JAN95] [JOE05]. The carrier current response of rotating injection consists of two components: positive and negative sequence components, and usually the negative sequence component is used for the rotor position estimation since the position information is contained in its phase angle. Furthermore, with an aid of synchronous reference frame filter (SRFF) [DEG98] [GAR07] [RAC10], the negative sequence carrier current can be obtained, and the rotor position is derived from the position-modulated carrier current response. Additionally, the multiple saliencies effect [DEG98] [RAC08], inverter non-linearity [GUE05] [GON11], and cross-saturation effect [GUG06a] [ZHU07] [LI09] [GON11b] are taken into account since they will cause an error in the rotor position estimation.

For the pulsating injection method, a high frequency carrier signal is injected on the *d*- [CAR06] [FOO10] [HOL06] or *q*-axis [JAN04] [LIN03] in the estimated synchronous

reference frame, and the rotor position is estimated through minimization of the position error from the measured carrier current response signal. Normally, the *d*-axis injection is used, and the *q*-axis carrier current response is utilized for the rotor position estimation, since the current ripple on the *q*-axis is limited. On the other hand, using the *d*-axis carrier current response for the rotor position estimation when the *q*-axis injection is utilized, is also possible. However, the more current ripple and consequently torque ripple will occur, but this approach is less sensitive to the inverter non-linearity.

Although these two methods have been well developed, there is a dynamic bandwidth limitation for the control system due to the signal demodulation process cause by the low-pass filter (LPF) for both rotating and pulsating signal injections. In order to solve the bandwidth limitation, the square-wave voltage signal injection based method is utilized, which can operate without using a low-pass-filter for signal demodulation [YOO11]. Therefore, a higher bandwidth can be reached for the sensorless dynamic performance. In [YOO14], a square-wave voltage signal is injected on the *q*-axis, less harmonics are generated in the error signal compared with the conventional signal injection methods. Also, the robustness and torque controllability of sensorless control is significantly improved.

No matter which type of signal injection is applied, the HF carrier signal is superimposed on the fundamental excitation continuously, and the rotor position is normally tracked from the position-dependent carrier current response due to either the machine saturation-induced saliency or geometrical rotor saliency, which are considered in [JAN03] [AIH99]. Since all the HF signal injection-based sensorless control methods depend on the machine saliency level corresponding to the rotor position estimation, the machine saliency is a critical requirement for the practical implementation and valuable to be investigated in [KIM04] [KOC09]. In order to explain the machine saliency level of PM machines, saliency ratio [GUG06b] [YAN11] and feasible region [BIA07], have been reported. With the comparative study of the interior PM (IPM) machine and reluctance synchronous machine (RSM) in

[KOC09], the machine parameters or HF inductances $L_{dh}$ and $L_{qh}$ are dependent on the fundamental excitation current. Hence, the investigation of incremental inductances at different load conditions is required. However, as shown in [DEG98], there may exist the secondary saliency in a machine due to the non-sinusoidal distributed saliency and always resulted from the slotting and magnetic saturation. More recently, it has been published in [LIN12] which highlighted the influence on the accuracy of the machine saliency information estimation. However, the investigation in [LIN12] was restricted to the effectiveness of sensorless operation and performed the sensorless current control only; hence, the sensorless speed control needs to be taken into account.

In the case of a surface-mounted permanent magnet (SPM) machine, the main challenge is difficult to identify the rotor position due to its low ratio of spatial rotor saliency. In order to overcome this issue, some physical features, i.e. magnetic saturation-induced saliency [KOC09] [BIA08] and eddy-current loss [YAN12a] [YAN12b], have been successfully validated to be helpful for detecting the rotor position. In [YAN12a], the new sensorless rotor position estimation method based on resistance-based induced-saliency due to HF eddy-current loss was proposed for the SPM machine. The comparison between resistive saliency and inductive saliency was discussed in [YAN12b]. The magnetic-saturation induced-saliency is utilized to achieve the suitable saliency ratio for detecting the rotor position [BIA08], but not applicable to all SPM motors. Similarly, the SPM machine in [FAG13] has shown a magnetic saturation-induced saliency and has been compared with the IPM and inset PM machines. Moreover, the stator saturation induced saliency can also be employed for the rotor position estimation [JAN03] [HA08] [FRE05] In addition, the evaluation of closed-loop sensorless control was not demonstrated in [HA08]. On the other hand, the stator saturation induced-saliency and the closed-loop sensorless control performance were achieved in [JAN03], but the similar position estimation method with limited control performance was proposed for another SPM machine [FRE05]. Moreover,

[YAN11] proposed the systematical sensorless-oriented design method for SPM machines which has a reversal feature ($L_d > L_q$). It has the benefits of reducing degradation and enhancing performance for sensorless control at high load condition.

The comparison between three HF signal injection based sensorless control techniques is discussed in Table 1.3.

TABLE 1.3.

COMPARISON OF THREE HF CARRIER SIGNAL INJECTION BASED SENSORLESS CONTROL METHODS

| | HF Rotating Signal Injection | HF Pulsating Signal Injection | HF Square-Wave Signal Injection |
|---|---|---|---|
| Current Response | Slow | Medium | Fast |
| Torque Ripple | Large | Small | Medium |
| Cross-Saturation Effect | Equal | Equal | Equal |
| Stability | Good | Medium | Medium |
| Signal Processing | Complex | Simple | Simple |
| Dynamic Operation | Medium | Good | Good |

## 1.4 Scope of Research and Contributions

### 1.4.1 Scope of Research

The main research of the thesis is focused on the sensorless control of PMSM, with particular reference to switched flux PM machines. The research scope is illustrated in Fig.

1.15.

(a) The high-frequency signal injection for the investigation of machine saliency and validation of sensorless operation capability at standstill and zero speed.

(b) Back-EMF based methods, i.e. 6th-harmonic and asymmetric back-EMFs, for the development of rotor position estimation at medium or higher speed.

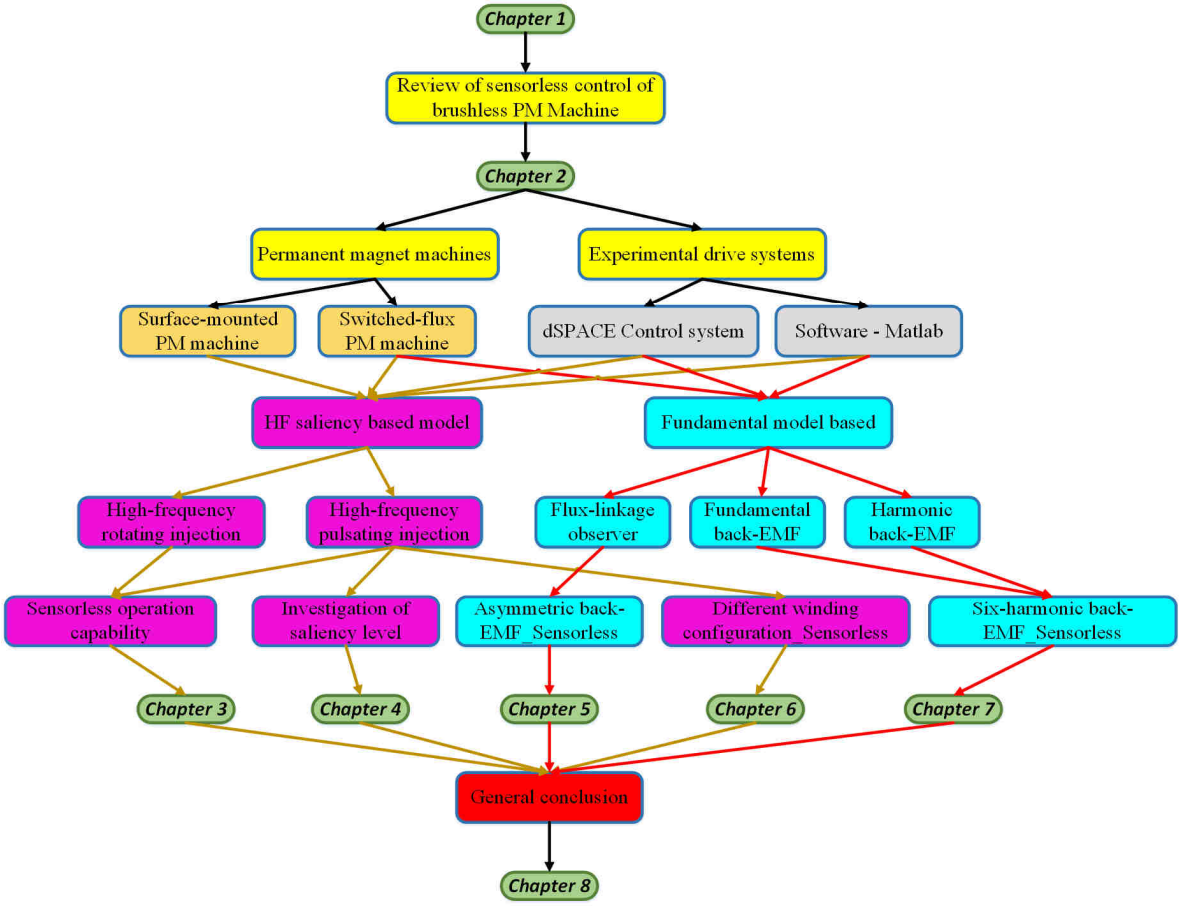


Fig. 1.15. Research scope.

The following chapters in the thesis are summarized as follows:

**Chapter 2:** General hardware and software environment based on the dSPACE control system and two test machines are introduced, in which various sensorless control methods can be implemented in the following chapters. Moreover, the sensored vector control is also given in details.

**Chapter 3:** The sensorless operation capability of an SPM machine, based on high-frequency (HF) voltage injection techniques is investigated and analyzed. Furthermore, the investigation has considered the resistance-based saliency due to HF eddy-current loss. In order to highlight the effectiveness of the sensorless operation capability, the tests are carried out under different operating conditions.

**Chapter 4:** In order to facilitate the selection of a machine as to whether it is suitable for high-frequency signal injection-based sensorless control or not, a complete experimental investigation method is proposed for a new type PM machine, and the influence of secondary saliency is also analyzed in detail. The conclusion is verified by the behavior of sensorless rotor position estimation.

**Chapter 5:** To minimize the influence of asymmetric back-EMF, a control strategy is proposed for the enhancement of rotor position estimation with the aid of elimination of back-EMF harmonics. It has the advantages i.e. easy implementation and less sensitive to the machine parameters. Furthermore, the experimental results confirm that the accurate rotor position estimation can be achieved at both steady and dynamic states as compared to those without compensation.

**Chapter 6:** The saliency level based on the different winding configurations are investigated and compared. The rotor positon error is increased for the alternative winding-based machines due to the multiple saliencies effect. Hence, the proposed rotor position estimation is used to compensate the error in the sensorless position estimation, and the sensorless control performance can be improved as well as the dual three-phase control application.

**Chapter 7:** The 6th-harmonic back-EMF is dominant, whilst the 3rd-harmonic back-EMF is much smaller in the switched-flux PM machine. Several new position estimation methods based on the 6th-harmonic back-EMF are applied in order to minimize the error in the rotor position estimation and improve the dynamic performance, which are compared with that of existing fundamental and 3rd-harmonic back-EMFs based methods.

**Chapter 8:** The general conclusion is summarized and some future works are discussed.

### 1.4.2 Contributions

(1) Based on HF carrier voltage signal based techniques, the sensorless operation capability of SPM machine is systematically investigated.

(2) A complete experimental investigation method for the analysis and validation of machine saliency level is proposed, including primary saliency and secondary saliency.

(3) The rotor position estimation is enhanced considering the multiple saliencies effect, which is based on the different winding topologies, and the sensorless control performance is significantly improved.

(4) A novel sensorless rotor position estimation based on the 6th-harmonic back-EMF is proposed. By applying the proposed compensation method, the continuous rotor position can be obtained, and the rotor positon estimation is improved at both steady and dynamic states.

(5) An improved observer is implemented with the synergies of the harmonic elimination technique and the proposed position error compensation scheme to achieve more accurate rotor position estimation in PMSMs having asymmetric back-EMFs.

## References


[ACA06] P.P. Acarnley and J.F. Watson, “Review of position-sensorless operation of brushless permanent-magnet machines,” *IEEE Trans. Ind. Appl*., vol. 53, no.2, pp. 352-362, 2006.

[ACC12] A. Accetta, M. Cirrincione, M. Pucci, and G. Vitale, “Sensorless control of PMSM fractional horsepower drives by signal injection and neural adaptive-band filtering,” *IEEE Trans. Ind. Electron.*, vol. 59, no. 3, pp. 1355–1366, Mar. 2012.

[AIH99] T. Aihara, A. Toba, T. Yanase, A. Mashimo, and K. Endo, “Sensorless torque control of salient-pole synchronous motor at zero-speed operation,” *IEEE Trans. Power Electron.*, vol. 14, no.1, pp. 202–208, Jan. 1999.

[BIA07] N. Bianchi, S. Bolognami, J.H. Jang, and S.K. Sul, “Comparison of PM motor structures and sensorless control techniques for zero-speed rotor position detection,” *IEEE Trans. Power Electron*., vol. 22, no. 6, pp. 2466–2475, Nov. 2007.

[BIA08] N. Bianchi, S. Bolognani, J.-H. Jang, and S.-K. Sul, “Advantages of inset PM machines for zero-speed sensorless position detection,” *IEEE Trans. Ind. Appl.*, vol. 44, no. 4, pp. 1190–1198, Jul./Aug. 2008.

[BOL09] I. Boldea, M. C. Paicu, G. D. Andreescu, and F. Blaabjerg, “Active flux DTFC-SVM sensorless control of IPMSM,” *IEEE Trans. Energy Conversion*, vol. 24, no. 2, pp. 314-322, 2009.

[BOL11] S. Bolognani, S. Calligaro, R. Petrella, and M. Sterpellone, “Sensorless control for IPMSM using PWM excitation: Analytical developments and implementation issues,” *Symposium on Sensorless Control for Electrical Drives*, 2011, pp. 64-73.

[CAR06] C. Caruana, G. M. Asher, and M. Sumner, “Performance of HF signal injection techniques for zero-low-frequency vector control of induction machines under sensorless conditions,” *IEEE Trans. Ind. Electron.*, vol. 53, no. 1, pp. 225–238, Feb. 2006.

[CHE00] Z. Chen, M. Tomita, S. Ichikawa, S. Doki, and S. Okuma, “Sensorless control of interior permanent magnet synchronous motor by estimation of an extended electromotive force,” *Industry Applications Conference*, vol.3, pp. 1814-1819, 2000.

[CHE03] Z. Chen, M. Tomita, S. Doki, and S. Okuma, “An extended electromotive force model for sensorless control of interior permanent-magnet synchronous motors,” *IEEE Trans. Ind. Electron*., vol. 50, no. 2, pp. 288-295, 2003.

[CHE99] Y. S. Chen, Motor topologies and control strategies for permanent magnet brushless AC drives, PhD Thesis, research Group of Electric Machines and Drives, University of Sheffield, 1999.

[COR98] M. J. Corley and R. D. Lorenz, “Rotor position and velocity estimation for a salient-pole permanent magnet synchronous machine at standstill and high speed,” *IEEE Trans. Ind. Appl.*, vol.34, no. 4, pp. 784–789, 1998.

[CUP11] F. Cupertino, P. Giangrande, G. Pellegrino and L. Salvatore, “End effects in linear tubular motors and compensated position sensorless control based on pulsating voltage injection,” *IEEE Trans. Ind. Electron.*, vol. 58, no.2, pp.494-502, Feb. 2011.

[DEG98] M.W. Degner, and R.D Lorenz, “Using multiple saliencies for the estimation of flux, position, and velocity in AC machines,” *IEEE Trans. Ind. Appl.*, vol. 34, no. 5, pp. 1097–1104, 1998.

[DER05] A. Derdiyok, “Speed-sensorless control of induction motor using a continuous control approach of sliding-mode and flux observer,” *IEEE Trans. Ind. Electron*., vol.52, no.4, pp.1170-1176, Aug. 2005.

[FAG13] A. Faggion, Fornasiero, E. Fornasiero, Bianchi, N. Bianchi and S. Bolognani, “Sensorless Capability of fractional-slot surface-mounted PM motors,” *IEEE Trans. Ind. Appl*., vol.49, no.3, pp.1325,1332, May-June 2013.

[FAT08] M. Fatu, R. Teodorescu, I. Boldea, and G. D. Andreescu, “I-F starting method with smooth transition to EMF based motion-sensorless vector control of PM synchronous motor/generator,” in *Conf. Rec. Power Electron. Spec. Conf.*, pp. 1481–1487, 2008.

[FEA09] M. Faeq and D. Ishak, “A new scheme sensorless control of BLDC motor using software PLL and third harmonic back-EMF,” *Industrial Electronics & Applications, 2009. ISIEA 2009. IEEE Symposium on*, vol. 2, pp. 861 – 865, 2009.

[FOO10] G. Foo, and M.F. Rahman, “Sensorless sliding-mode MTPA control of an IPM synchronous motor drive using a sliding-mode observer and HF signal injection,” *IEEE Trans. Ind. Electron*., vol. 57, no. 4, pp. 1270 – 1278, 2010.

[FRE05] T. Frenzke, “Impacts of cross-saturation on sensorless control of surface permanent magnet synchronous motors,” in *Proc. Eur. Conf. Power Electron. Appl.*, 2005, pp. 1–10.

[FUR92] T. Furuhashi, S. Sangwongwanich, and S. Okuma, “A position and velocity sensorless control for brushless DC motors using an adaptive sliding mode observer,” *IEEE Trans. Ind. Electron*., vol. 39, no. 2, pp. 89 – 95, 1992.

[GAO07] Q. Gao, G.M. Asher, M. Sumner, and P. Makys, “Position estimation of AC machines over a wide frequency range based on space vector PWM

excitation," *IEEE Trans. Ind. Appl*., vol.43, no.4 , pp. 1001 – 101, 2007.

[GAR07] P. Garcia, F. Briz, M.W. Degner, and D. Diaz-Reigosa, "Accuracy, bandwidth, and stability limits of carrier-signal-injection-based sensorless control methods," *IEEE Trans. Ind. Appl*., vol. 43, no. 4, pp. 990 – 1000, 2007.

[GEN10] F. Genduso, R. Miceli, C. Rando, and G.R.Galluzzo, "Back EMF Sensorless-Control Algorithm for High-Dynamic Performance PMSM," *IEEE Trans. Ind. Electron.*, vol.57, no.6, pp.2092-2100, June 2010.

[GON11a] L.M. Gong, and Z.Q. Zhu, "A novel method for compensating inverter nonlinearity effects in carrier signal injection-based sensorless control from positive-sequence carrier current distortion," *IEEE Trans. Ind. Appl*., vol. 47, no. 3, pp. 1283 – 1292, 2011.

[GON11b] L.M. Gong, and Z.Q. Zhu, "Improved rotating carrier signal injection method for sensorless control of PM brushless AC motors, accounting for cross-saturation effect," *Power Electronics and ECCE Asia* (ICPE & ECCE), 2011, pp. 1132 – 1139.

[GON12] L. Gong, "Carrier signal injection based sensorless control of permanent magnet brushless ac machines", PhD Thesis, Research Group of Electric Machines and Drives, Department of Electronic and Electrical Engineering, University of Sheffield, 2012.

[GUE05] J.M. Guerrero, M. Leetmaa, F. Briz, A. Zamarron, and R.D. Lorenz,"Inverter nonlinearity effects in high-frequency signal-injection-based sensorless control methods," *IEEE Trans. Ind. Appl*., vol. 41, no. 2, pp. 618 – 626, 2005.

[GUG06a] P. Guglielmi, M. Pastorelli, and A. Vagati, "Cross-saturation effects in IPM motors and related impact on sensorless control," *IEEE Trans. Ind. Appl*., vol. 42, no. 6, pp. 1516 – 1522, 2006.

[GUG06b] P. Guglielmi, M. Pastorelli, and A. Vagati, "Impact of cross-saturation in sensorless control of transverse laminated synchronous reluctance motors," *IEEE Trans. Ind. Electron*., vol. 53, no 2, pp. 429–439, Apr. 2006.

[HA08] J. I. Ha, "Analysis of inherent magnetic position sensors in symmetric AC machines for zero or low speed sensorless drives," *IEEE Trans. Magn.*, vol. 44, no. 12, pp. 4689–4696, Dec. 2008.

[HAR00] L. Harnefors, and H.P. Nee, "A general algorithm for speed and position estimation of AC motors," *IEEE Trans. Ind. Electron.*, vol. 47, no. 1, pp. 77-83, 2000.

[HEN94] J.R. Hendershot, and T.J.E. Miller, "Design of brushless permanent magnet motors," Magna Physics Publishing and Clarendon Press, Oxford, 1994.

[HIN03] M. Hinkkanen, and J. Luomi, "Modified integrator for voltage model flux estimation of induction motors," *IEEE Trans. Ind. Electron.*, vol. 50,no. 4,

Aug. 2003.

[HOL05] J. Holtz, and J. Juliet, “Sensorless acquisition of the rotor position angle of induction motors with arbitrary stator windings,” *IEEE Trans. Ind. Appl*., vol. 41, no. 6, pp. 1675-1682, 2005.

[HOL06] J. Holtz, “Sensorless control of induction machines—With or without signal injection,” *IEEE Trans. Ind. Electron.*, vol. 53, no. 1, pp. 7–30, Feb. 2006.

[HOL98] J. Holtz, “Sensorless position control of induction motors—An emerging technology,” *IEEE Trans. Ind. Electron.*, vol. 45, no.6, pp. 840–851, Dec. 1998.

[HU98] J. Hu, and B. Wu, “New integration algorithms for estimating motor flux over a wide speed range,” *IEEE Trans. Power Electron*., vol. 13, no. 5, pp. 969 – 977, 1998.

[HUA07] Y. Hua, G.M. Asher, M. Sumner, and Q. Gao, “Sensorless control of surface mounted permanent magnet machine using the standard space vector PWM,” *IEEE IAS Annual Meeting*, USA, 2007, pp. 661 – 667.

[HUA11] Y. Hua, M. Sumner, G. Asher, Q. Gao, and K. Saleh, “Improved sensorless control of a permanent magnet machine using fundamental pulse width modulation excitation,” *IET Electric Power Appl*., vol. 5, no. 4, pp. 359-370, 2011.

[IDR02] N. R. N. Idris, and A. H. M. Yatim, “An improved stator flux estimation in steady-state operation for direct torque control of induction machines,” *IEEE Trans. Ind. Appl.*, vol. 38, no. 1, pp. 110–116, Jan./Feb. 2002.

[JAN03] I.H. Jang, S.K. Sul, J.I. Ha, K. Ide and M. Sawamura, “Sensorless drive of surface-mounted permanent-magnet motor by high-frequency signal injection based on magnetic saliency,” *IEEE Trans. Ind. Appl*., vol.39, no. 4, pp. 1031-1039, July-Aug. 2003.

[JAN04] J.H. Jang, J.I. Ha, M. Ohto, K. Ide, and S.K. Sul, “Analysis of permanent-magnet machine for sensorless control based on high-frequency signal injection,” *IEEE Trans. Ind. Appl*., vol. 40, no. 6, pp. 1595-1604, Nov./Dec., 2004.

[JAN95] P.L. Jansen, and R.D. Lorenz, “Transducer-less position and velocity estimation in induction and salient AC machines,” *IEEE Trans., Ind. Appl*., vol. 31, no. 2, pp. 240 – 247, 1995.

[JEO05] Y. Jeong, and S. Sul, “Adaptive Flux Observer with On-line Inductance Estimation of an IPMSM Considering Magnetic Saturation,” *Proc. Of IEEE Power Electronics Specialists Conf.*, PESC, pp.2467-2473, 16-16 June 2005.

[JOE05] Y.S. Jeong, R.D. Lorenz, T.M. Jahns, and S.K. Sul, “Initial rotor position estimation of an interior permanent-magnet synchronous machine using

carrier-frequency injection methods," *IEEE Trans. Ind. Appl.*, vol. 41, no. 1, pp. 38–45, 2005.

[JUL05] J. Holtz, and J. Juliet, "Sensorless acquisition of the rotor position angle of induction motors with arbitrary stator windings," *IEEE Trans. Ind. Appl.*, vol.41, no.6, pp.1675-1682, Nov.-Dec. 2005.

[KAN10] J. Kang, "Sensorless control of permanent magnet motors," Control Engineering, vol. 57, no. 4, pp. 1-4, 2010.

[KER94] L. Kreindler, J.C. Moreira, A. Testa, and T. A. Lipo, "Direct Field Orientation Controller Using the Stator Phase Voltage Third Harmonic," *IEEE Trans. Ind. Appl.*, vol. 30, no. 2, pp. 441-447, 1994.

[KIM03] H. Kim, M. C. Harke, and R. D. Lorenz, "Sensorless control of interior permanent-magnet machine drives with zero-phase lag position estimation," *IEEE Trans. Ind. Appl.*, vol. 39, no. 6, pp. 1726–1733, Nov./Dec. 2003.

[KIM04] H. Kim and R.D. Lorenz, "Carrier signal injection based sensorless control methods for IPM synchronous machine drives," *IEEE Ind. Appl. Conf.* (IAS2004), vol. 2, 2004, pp. 977-984.

[KIM11] H. Kim, J. Son, and J. Lee, "A High-Speed Sliding-Mode Observer for the Sensorless Speed Control of a PMSM," *IEEE Trans. Ind. Electron.*, vol.58, no.9, pp.4069,4077, Sept. 2011.

[KOC09] W.H. De Kock, M.J. Kamper, R.M. Kennel, "Anisotropy comparison of reluctance and PM synchronous machines for position sensorless control using HF carrier injection," *IEEE Trans. Power Electron.*, vol. 24, no.8, pp.1905-1913, 2009.

[LEE11a] K. Lee, I. Choy, J. Back, and J. Choi, "Disturbance observer based sensorless speed controller for PMSM with improved robustness against load torque variation," *IEEE Power Electronics and ECCE Asia* (ICPE & ECCE), 2011, pp. 2537 – 2543.

[LEE11b] J.S. Lee, C.H. Choi, J.K. Seok, and R.D. Lorenz, "Deadbeat direct torque and flux control of interior permanent magnet machines with discrete time stator current and stator flux linkage observer," *IEEE Trans. Ind. Appl.*, vol. 47, no. 4, July/Aug. 2011.

[LEI11] R. Leidhold, "Position sensorless control of PM synchronous motors based on zero-sequence carrier injection," *IEEE Trans. Ind. Electron.*, vol. 58, no. 12, pp. 5371-5379, 2011.

[LI05] J. Li, L. Xu, and Z. Zhang, "An adaptive sliding-mode observer for induction motor sensorless speed control," *IEEE Trans. Ind. Appl.*, vol.41, no.4, pp.1039,1046, July-Aug. 2005.

[LI07] Y. Li, Z.Q. Zhu, D. Howe, and C. M. Bingham, "Modelling of cross-coupling

magnetic saturation in signal injection based sensorless control of permanent magnet brushless AC motors," *IEEE Trans. on Magnet.*, vol.43, no.6, pp.2552-2554, June 2007.

[LI09] Y. Li, Z.Q. Zhu, D. Howe, C.M. Bingham, and D. Stone, "Improved rotor position estimation by signal injection in brushless AC motors, accounting for cross-coupling magnetic saturation," *IEEE Trans. Ind. Appl.*, vol.45, no.5, pp.1843-1849, 2009.

[LI09a] Y. Li, "Sensorless control of permanent magnet brushless AC motors accounting for cross-coupling magnetic saturation", PhD Thesis, Department of Electronic and Electrical Engineering, University of Sheffield, 2009.

[LIN03] M. Linke, R. Kennel, and J. Holtz, "Sensorless speed and position control of synchronous machines using alternating carrier injection," *Electric Machines and Drives Conference*, vol.2, pp. 1211-1217, 2003.

[LIU14] J. Liu and Z. Zhu, "Improved Sensorless Control of Permanent Magnet Synchronous Machine Based on Third-Harmonic Back-EMF," *IEEE Trans. Ind. Appl.*, vol.50, no.3, pp.1861-1870, May-June 2014.

[LUU03] J. Luukko, M. Niemela, and J. Pyrhonen, "Estimation of the flux linkage in a direct-torque-controlled drive" *IEEE Trans. Ind. Electron.*, vol. 50, no. 2, pp. 283–287, Apr. 2003.

[MOR92] J. Moreira, and T.A. Lipo, "Modeling saturated AC machines including air gap flux harmonic components," *IEEE Trans. Ind. Appl.*, vol. 28, no.2, pp. 343-349, 1992.

[OGA98] S. Ogasawara, and H. Akagi, "Implementation and position control performance of a position-sensorless IPM motor drive system based on magnetic saliency," *IEEE Trans. Ind. Appl.*, vol. 34, no. 4, pp. 806–812, July/August 1998.

[PIL91] P. Pillay and R. Krishnan, "Application characteristics of permanent magnet synchronous and brushless DC motors for servo drives," *IEEE Trans. Ind. Appl.*, vol. 27, no. 5, pp. 986–996, Sep./Oct. 1991.

[RAC08] D. Raca, P. Garcia, D. Reigosa, F. Briz, and R. Lorenz, "A comparative analysis of pulsating vs. rotating vector carrier signal injection-based sensorless control," *Applied Power Electronics Conference and Exposition*. APEC08, 2008, pp. 879 – 885.

[RAC10] D. Raca, P. Garcia, D.D. Reigosa, F. Briz, R.D. Lorenz, "Carrier-signal selection for sensorless control of PM synchronous machines at zero and very low speeds," *IEEE Trans. Ind. Appl.*, vol. 46, no.1, pp.167-178, 2010.

[RAU10] R. Raute, C. Caruana, C. S. Staines, J. Cilia, M. Sumner, and G. M. Asher, Sensorless control of induction machines at low and zero speed by using

PWM harmonics for rotor-bar slotting detection," *IEEE Trans. Ind. Appl.*, vol. 46, no. 5, pp. 1989-1998, 2010.

[REB02] E. Robeischl, M. Schroedl, and K. Salutt, "Improved INFORM-measurement sequence and evaluation for sensorless permanent magnet synchronous motor drives," in the 10th Int. *Power Electronics and Motion Control Conf*., Cavtat and Dubrovnik, Croatia, Sept. 9–11, 2002.

[ROB04] E. Robeischl, and M. Schroedl, "Optimized INFORM measurement sequence for sensorless PM synchronous motor drives with respect to minimum current distortion," *IEEE Trans. Ind. Appl*., vol. 40, no. 2, pp. 591-598, 2004.

[SAF95] S. K. Safi, P. P. Acarnley, and A. G. Jack, "Analysis and simulation of the high-speed torque performance of brushless DC motor drives," *Proc. Inst. Elect. Eng.-Electr. Power Appl*., vol. 142, no. 3, pp. 191–200, Mar. 1995.

[SCH03] M. Schrodl, and M. Lambeck, "Statistic properties of the INFORM method for highly dynamic sensorless control of PM motor down to standstill," *Proc. IECON*.2003, vol. 2, pp. 1479–1486, 2003.

[SCH96] M. Schroedl, "Sensorless control of AC machines at low speed and Standstill based on the 'INFORM' method," *Conf. Rec. IEEE-IAS Annual Meeting*, 1996, pp. 270–277.

[SEN95] T. Senjyu, M. Tomita, S. Doki, and S. Okuma, "Sensorless vector control of brushless DC motors using disturbance observer," *IEEE Power Electronics Specialists Conference*, PESC '95, vol. 2, 1995, pp. 772 – 777.

[SHE02a] J.X. Shen, Z.Q. Zhu, and D, Howe, "Improved speed estimation in sensorless PM brushless AC drives " *IEEE Trans. Ind. Appl*., vol. 38, no. 4, pp. 1072-1080, 2002.

[SHE04] J.X. Shen, Z. Q. Zhu, and D. Howe, "Sensorless flux-weakening control of permanent-magnet brushless machines using third-harmonic back EMF," *IEEE Trans. Ind. Appl*., vol. 40, no. 6, pp. 1629-1636, 2004.

[SHE06a] J.X. Shen, and S. Iwasaki, "Sensorless control of ultrahigh-speed PM brushless motor using PLL and third harmonic back EMF," *IEEE Trans. Indus. Electron*., vol. 53 , no. 2, pp. 421 - 428, 2006.

[SHE06b] J.X. Shen, Z.Q. Zhu, and D. Howe, "Practical issues in sensorless control of PM brushless machines using third-harmonic back-EMF," *IEEE 5th International Power Electronics and Motion Control Conference*, IPEMC2006, pp.1-5, 2006.

[SIL06] C. Silva, G. M. Asher, and M. Sumner, "Hybrid rotor position observer for wide speed ranger sensorless PM motor drives including zero speed," *IEEE Trans. Ind. Electron.*, vol. 53, no. 2, pp. 373–378, Apr. 2006.

[STI10] A. Stirban, I. Boldea, G.-D. Andreescu, D. Iles, and F. Blaabjerg, "Motion

sensorless control of BLDC PM motor with offline FEM info assisted state observer," in *12th Int. Conf. OPTIM*, pp. 321–328, 2010.

[TER01] B. Terzic, and M. Jadric, "Design and implementation of the extended Kalman filter for the speed and rotor position estimation of brushless DC motor," *IEEE Trans. Indus. Electron*., vol. 48, no. 6, pp. 1065-1073, 2001.

[WAN12] Z. Wang, K. Lu, and F. Blaabjerg, "A Simple startup strategy based on current regulation for back-EMF-based sensorless control of PMSM," *IEEE Trans. Power Electron*., vol. 27, no. 8, pp. 3817 – 3825, 2012.

[WU91] R. Wu, and G.R. Slemon, "A permanent magnet motor drive without a shaft sensor," *IEEE Trans. Ind. Appl*., vol.27, no.5, pp. 1005–1011, 1991.

[XU14] W. Xu and R.D.Lorenz, "Reduced parameter sensitivity stator flux linkage observer in deadbeat-direct torque and flux control for IPMSMs," *IEEE Trans. Ind. Appl.*, vol.50, no.4, pp.2626,2636, July-Aug. 2014.

[YAN11] S.C. Yang, T. Suzuki, R.D. Lorenz, and T.M. Jahns,"Surface permanent magnet synchronous machine design for saliency tracking self-sensing position estimation at zero and low speeds," *IEEE Trans. Ind. Appl.*, vol. 47, no. 5, pp. 2103-2116, 2011.

[YAN12a] S.-C. Yang, and R. D. Lorenz, "Surface permanent magnet synchronous machine self-sensing position estimation at low speed using eddy current reflected asymmetric resistance," *IEEE Trans. Power Electron.*, vol. 27, no. 5, pp. 2595–2604, May 2012.

[YAN12b] S.-C. Yang and R. D. Lorenz, "Comparison of resistance-based and inductance-based self-sensing controls for surface permanent-magnet machines using high-frequency signal injection," *IEEE Trans. Ind. Appl.*, vol.48, no.3, pp.977-986, May-June 2012.

[YOO09] A. Yoo, and S.K. Sul, "Design of flux observer robust to interior permanent-magnet synchronous motor flux variation," *IEEE Trans. Ind. Appl*., vol. 45, no. 5, pp. 1670-1677, 2009.

[YOO11] Y.D. Yoon, S.K. Sul, S. Morimoto and K. Ide, "High bandwidth sensorless algorithm for AC machines based on square-wave type voltage injection," *IEEE Trans. Ind. Appl*., vol. 47, no. 3, pp. 1361–1370, 2011.

[YOO14] Y.d. Yoon, and S.K. Sul, "Sensorless control for induction machines based on square-wave voltage injection," *IEEE Trans. Power Electron.*, vol.29, no.7, pp.3637-3645, July 2014.

[ZAH06] Z. Zhang, H. Xu, L. Xu, and L.E. Heilman, "Sensorless direct field oriented control of three-phase induction motors based on "Sliding Mode" for washing-machine drive applications," *IEEE Trans. Ind. Appl.*, vol. 42, no. 3, pp, 694 – 701, 2006.

[ZHU07] Z.Q. Zhu, Y. Li, D. Howe, and C.M. Bingham, “Compensation for rotor position estimation error due to cross-coupling magnetic saturation in signal injection based sensorless control of PM brushless AC motors,” *IEEE Electric Machines & Drives Conference*, IEMDC '07. 2007, vol. 1, pp. 208 - 213

[ZHU11] Z.Q. Zhu and L.M. Gong, “Investigation of effectiveness of sensorless operation in carrier signal injection based sensorless control Methods,” *IEEE Trans. Ind. Electron.*, vol. 58, no. 8, pp. 3431-3439, 2011.

# CHAPTER 2

# EXPERIMENTAL DRIVE SYSTEMS AND PERMENENT MAGNET SYNCHRONOUS MACHINES

## 2.1 Introduction

This chapter introduces an overview and description of the experimental hardware platform and software environment based on a dSPACE control system and Matlab/Simulink, respectively, which are utilized to implement the developed control strategies for the prototype machines. In addition, the detailed information of dSPACE control system and the two test PM brushless machines will be described.

The experimental hardware platform includes: a three-phase IGBT inverter with gate drive circuits, a DC load machine, a BLAC PM machine with integrated encoder, a changeable resistance load and a dSPACE intelligent system-based motion controller. An oscilloscope is used to analysis and capture the data waveform. The overview of the motor control system is summarized in Fig. 2. 1.

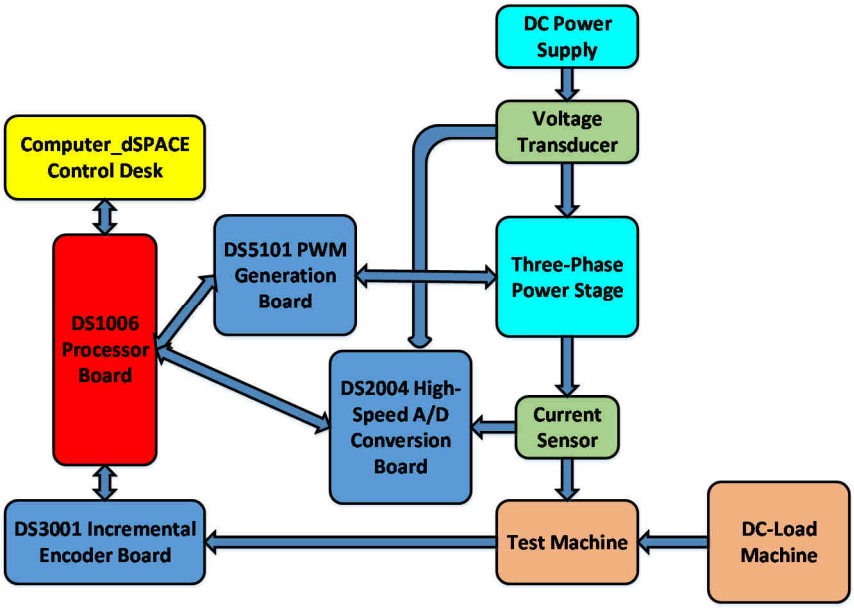

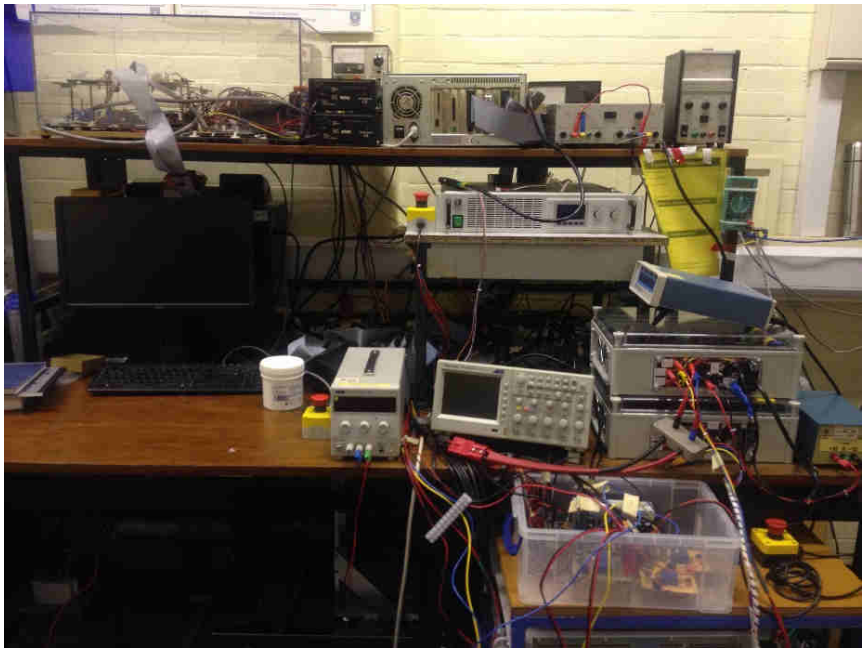

Fig. 2. 1 The overview of experimental system

In this thesis, all the experimental tests and measurements are based on this hardware and software platform.

## 2.2 dSPACE Control System and Software Environment

The detailed information of dSPACE motion control system and software which is Matlab/Simulink will be described in the following sections.

### 2.2.1 dSPACE Control System

#### A. DS5101 Three-Phase PWM Generation

The Digital Waveform Output (DWO) board, DS5101, is specifically designed for high speed signal generation at high resolution. The board can autonomously generate fast and complex signals, i.e. pulse-width modulation (PWM) waveforms. It has several features: (a) 25 ns high resolution, (b) Shortest pulse length, 250ns, (c) The time of delays which is from 250ns up to 26.8 seconds, (d) Delays can be interrupted for shorter delay values (e) All

channels can trigger each other, (f) Pulse patterns are up to 16 channels. An overview of the PWM generation board of DS5101 is shown in Fig. 2.2.

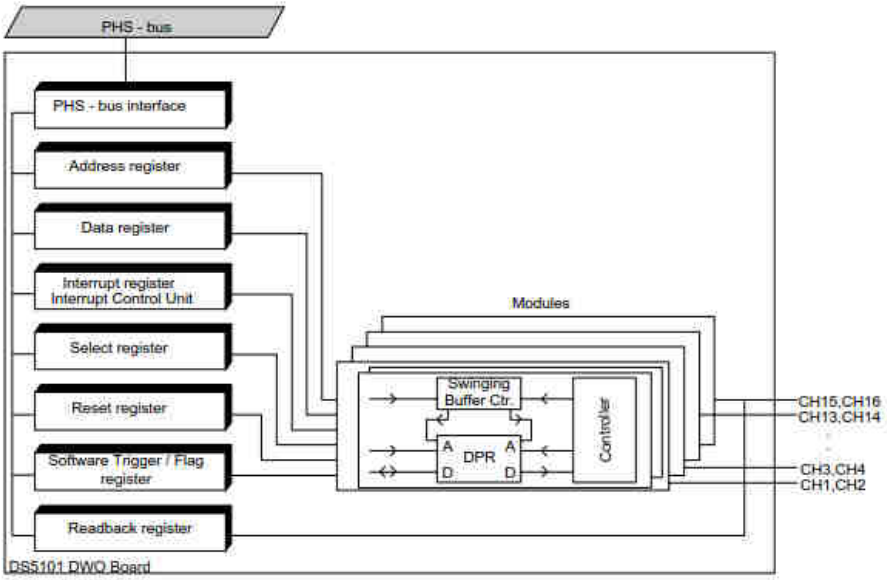


Fig. 2.2. An overview of the DS5101 PWM generation board [DSP10].

Since DS5101 has 16 channels, the signal generation board can be used to generate various pulse patterns, in which the motion control system can be applied to the multi-phase machines. Moreover, the DS5101 board provides three-phase/six-channel to the middle of high-level PWM pulses. In order to synchronize the 3 inverted output signals and 3 non-inverted output signals, a master clock signal is also utilized. Hence, the DS5101 board can work as a three-phase PWM application. In addition, DS5101 also provides the function of two sets of PWM output, which can be used to apply to two three-phase machines as a dual three-phase machine.

**B. DS3001 Incremental Encoder Interface Board**

The DS3001 incremental encoder board is a member of the dSPACE hardware family as it is designed for obtaining the rotor position information for the machine control application.

In addition, an incremental encoder with resolution of 2048PPR is equipped on the machine rotor shaft to provide the actual rotor position to the whole control system, in which the rotor position information measured from the encoder is utilized for the Park transformation. More importantly, the rotor position information obtained from the incremental encoder will be used to evaluate the rotor position estimation in sensorless control. The overview of DS3001 incremental encoder board is shown in Fig. 2.3.

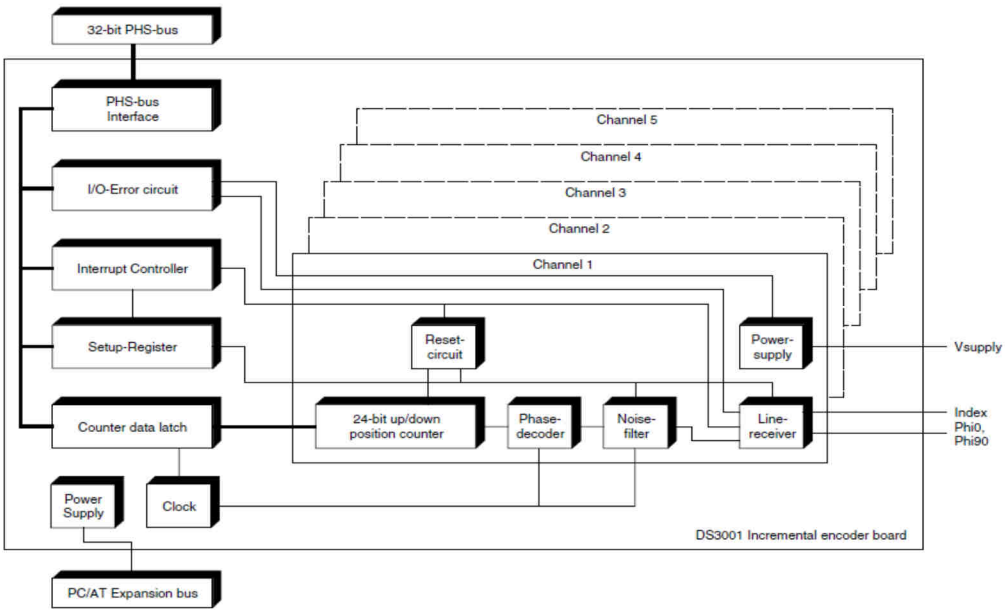


Fig. 2.3. Block diagram of the DS3001 [DSP10].

Furthermore, the use range of input encoder lines is from $-2^{21}$ to $+2^{21}$. Then, the radian position angle can be received from the scaled output signal by DS3001 Simulink model, which the calculation can be expressed as

$$\theta_r = 2^{21} \cdot \frac{2\pi}{encoder\_lines} \cdot scaled\_output \tag{2.1}$$

Then, the incremental encoder, 2048PPR, is employed in this thesis. The rotor position can be derived as

$$\theta_r = 2^{21} \cdot \frac{2\pi}{2048} \cdot scaled\_output \tag{2.2}$$

### C. DS2004 High-Speed A/D Board

The DS2004 high-speed A/D board is used in dSPACE modular systems based on processor boards DS1005 and DS1006 for digitizing analog input signals. The A/D converters of the DS2004 are equipped with differential inputs to particularly meet the requirements for digitizing analog input signals at high sampling rates, for example, for measuring internal cylinder pressures. The overview of the functional units of the DS2004 is drawn in Fig. 2.4.

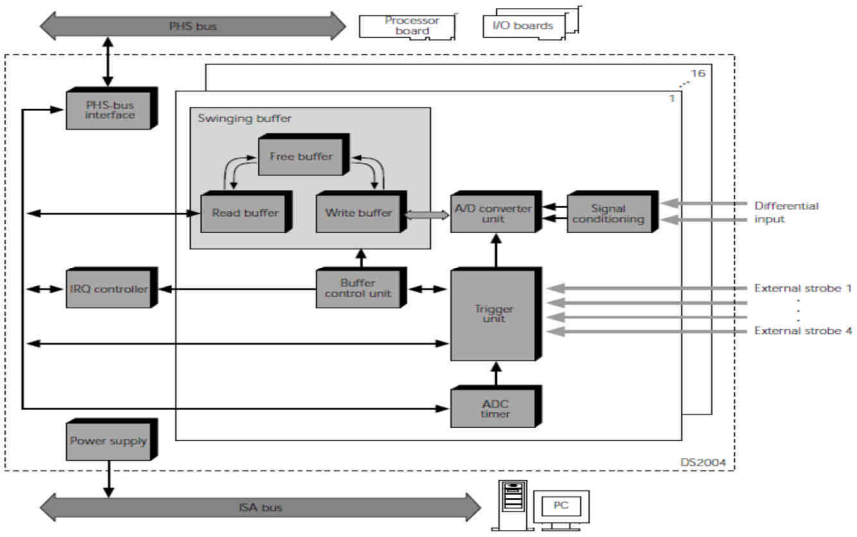


Fig. 2.4. Overview of the functional units of the DS2004 [DSP10].

Main components of a DS2004 conversion channel are summarized below:

- **Signal conditioning:** This unit adapts the input signals to the requirements of the A/D converter unit.
- **A/D converter unit:** This unit converts the received data for digitizing the analog input signal.
- **Trigger unit:** This unit evaluates the trigger configuration and controls the buffer control and A/D conversion units by reacting to conversion trigger signals.

- **Swinging buffer:** This unit comprises a write buffer, a read buffer, and a free buffer. The write buffer can be written and the read buffer can be read simultaneously.
- **Buffer control unit:** This unit controls the swinging buffer, and sets a flag indicating that new conversion results are ready to be read.
- **ADC timer:** This unit has a high-resolution timer that can be used as trigger source for the A/D conversions.

### D. DS1006 Processor Board

The DS1006 Processor Board is the major device in the dSPACE control system which is based on a single-core or a multicore Opteron TM processor. According to the dSPACE note, DS1006 is real-time processor (RTP) which is the main processing unit, and can access modular I/O boards via PHS bus. Also, the multiprocessing-cable is used to transmit the data via DS911 Giga-link Module. Due to the multi-processor, the real-time application can work on more processor cores. In Fig. 2.5, the overview of CPU DS1006 processor board in described. The operating frequency of DS1006 is 2.4GHz per core.

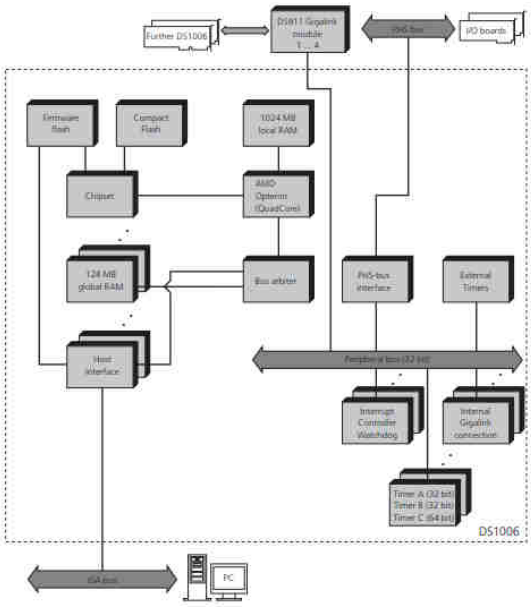


Fig. 2.5. Overview of DS1006 CPU processor board [DSP10].

### 2.2.2 Software Environment

In the investigation of sensor/sensorless operations of permanent magnet synchronous machines (PMSM), a good simulation environment is provided by Matlab/Simulink which provides an interactive environment for algorithm development, data visualization, data analysis and numeric computation. Also, the simulation model can be based on calculations to allow easy changes and evaluate its performance and efficiency in a simple manner. When Matlab/Simulink is used, technical computing problems can be solved faster than with any other programming languages such as C and C++. It also supports a wide range of applications, including control design, signal and image processing, test and measurement, communications, financial modeling and analysis.

Furthermore, the dSPACE control platform is operating with simulation model which is built by Matlab/Simulink, and can be simply applied to the experimental platform, such as test machines and developed control strategies. The use of a connection cable between dSPACE and computer is optical fibre cable which can provide the high speed (up to 100MB/s) signal transmission of real-time data to the computer, i.e. dSPACE control desk, from real-time operating platform. Due to dSPACE control desk, the real-time data and operating condition can be easily captured and monitored, which is different from the DSP based control system.

## 2.3 Permanent Magnet BLAC Machines under Investigation

Two prototype PM BLAC machines, namely Machine-I and Machine-II, are employed for the experimental investigation to develop sensorless control strategies, as summarized in Table 2.1. The detailed information of the two test machines are described in the following sections.

TABLE 2.1.

SUMMARY OF PM BLAC MACHINES UNDER INVESTIGATION FOR SENSORLESS CONTROL TECHNIQUES

| | | |
|---|---|---|
| Test Machine-I | Chapter 3 | Investigation of sensorless operation capability based on HF carrier signal injection techniques |
| Test Machine-II | Chapter 4 | Saliency evaluation using HF pulsating carrier signal injection and validation of sensorless control performances |
| | Chapter 5 | Investigation of asymmetric back-EMF effect in rotor flux-linkage based sensorless rotor position estimations |
| | Chapter 6 | Investigation of saliency effect on the sensorless rotor position estimation based on different on winding configurations for single and dual three-phase machines, and HF carrier voltage measurement for sensorless control by topped winding wire. |
| | Chapter 7 | Investigation of the 6th-harmonic back-EMF based sensorless rotor position estimations and the enhancement of sensorless control performances |

### 2.3.1 Details of Test Machine-I

Test Machine-I was designed by [ZHU97] and prototyped in the Electrical Machines and Drives Group at the University of Sheffield, and is a surface-mounted PM machine. Fig. 2.6 shows Test Machine-I before assembly, which has two diametrically-magnetized surface-mounted PMs on the rotor body. The stator has three teeth and each tooth for each phase which was designed as two concentrated coils (non-overlapping winding coils.) in series connection in the same phase. The two winding coils were originally connected in

parallel. In addition, the air-gap distribution is sine-wave, which has been experimentally proved [ZHU97]. Since the air-gap distribution is almost sinusoidal, the winding factor is 0, which means the third-harmonic may not contain in the fundamental back-EMF. The prototype machine equipped with the DC-load machine and the measured three-phase back-EMF waveforms are shown in Figs. 2.7 and 2.8, respectively.

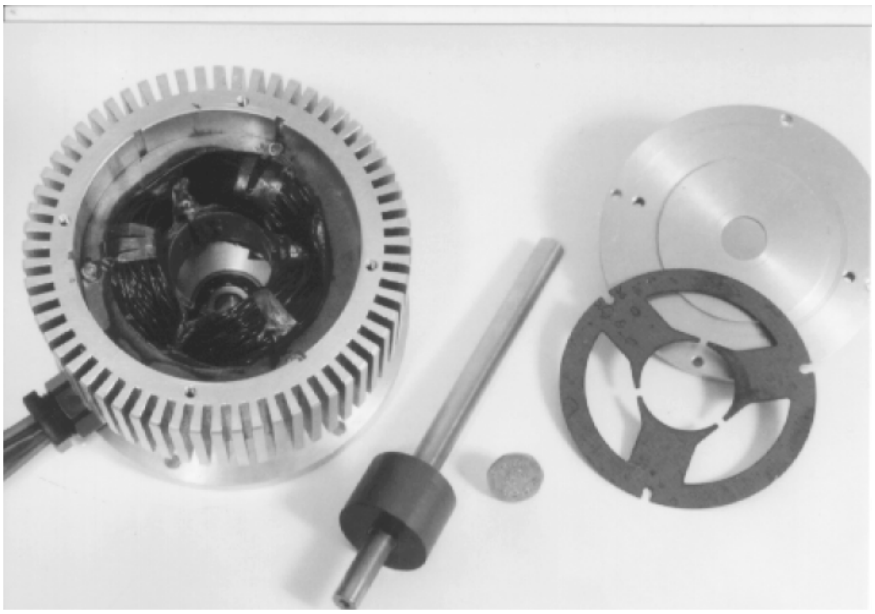

Fig. 2. 6. Prototype 2-pole brushless AC machine before assembly

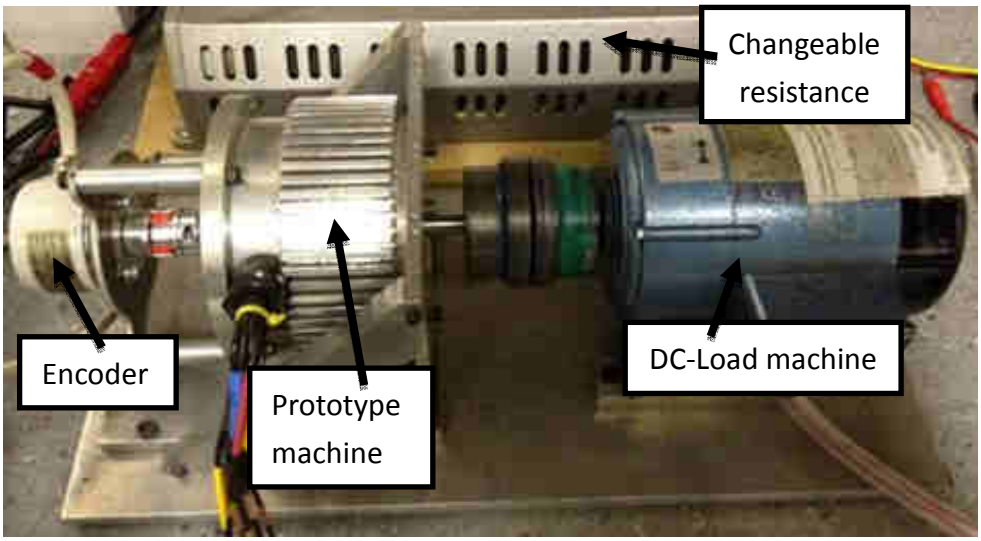


Fig. 2. 7. Prototype 2-pole brushless AC machine coupled to DC-load machine

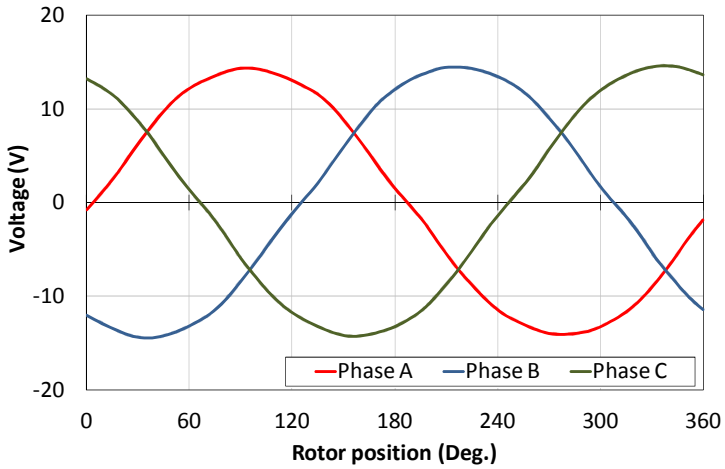


Fig. 2. 8. Measured three-phase back-EMF waveforms, 1500 r/min.

In fact, the original rated speed for Test Machine-I was 20,000 r/min, and the maximum speed of DC-load machine is 3000 r/min. In this case, the rated speed for the test machine-I has to be limited within the rated speed of DC-load machine, and the DC link voltage also needs to be reduced from 200V to 70V. The parameters of Test Machine-I are summarized in Table 2.2.

TABLE 2.2.

PARAMETERS OF MACHINE-I

| Quantity | Value | Unit |
|---|---|---|
| Rated current | 2.2 | A |
| Rated DC voltage | 70 | V |
| Rated torque | 0.3 | Nm |
| Rated speed | 3000 | r/min |
| Max. phase current | 6 | A |
| Stator pole number | 3 | |
| Rotor pole number | 2 | |
| Self *dq*-axis inductance | 3.19 | mH |
| Phase resistance | 0.466 | Ohm |

In Fig. 2.9, an intelligent power module (IPM) PS21255, which is made by Mitsubishi and located underneath the PCB circuit board, is employed to control the Test Machine-I. The maximum voltage and current of IPM PS21255 are 600V and 20A, respectively. In addition, the three-phase IGBT Inverter with gate drive and the protection function are also integrated with IPM PS21255. The dead-time is 2μs. The integration structure in the IPM has some advantages such as increased overall system reliability and reduced complexity of external circuit. For the isolation, the opto-coupler, HCPL-4506, is utilized to pass the signals from gate drive which is from the PWM generator, dSPACE DS5101 Digital PWM Waveform Output Board to the power stage. Additionally, the two transformers of isolated DC output voltage, +15V, are supplied to the gate drive system.

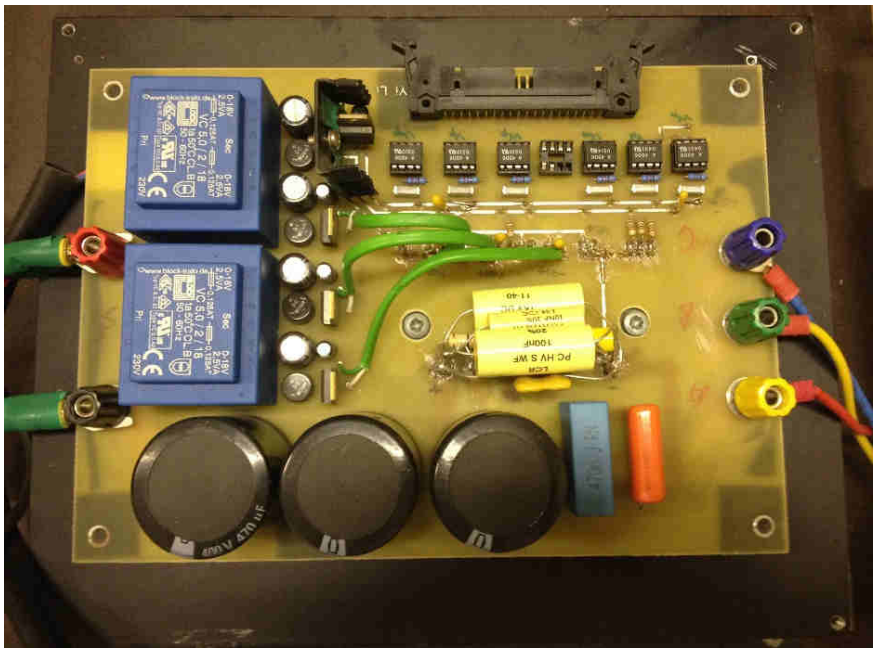

Fig. 2. 9. Single three-phase power stage.

It is well known that the machine saliency is quite small in the surface-mounted machine, in terms of sensorless rotor position estimation. Hence, Test Machine-I will be evaluated for its potential sensorless capability by the HF carrier signal injection based sensorless control methods, which will be discussed in Chapter 3.

### 2.3.2 Details of Test Machine-II

Test machine-II was designed by [CHE10] and prototyped in the Electrical Machines and Drives Group at the University of Sheffield, which is a switched-flux 12/10 stator/rotor poles brushless PM (SFPM) machine. Its specification and parameters are listed in Table 2.3. The cross-section and machine winding configuration of Test machine-II is shown in Fig. 2.10, and its prototype machine is shown in Fig. 2.11.

TABLE 2.3.

PARAMETERS OF MACHINE-II

| Quantity | Value | Unit |
|---|---|---|
| Rated current | 15 | A |
| Rated DC voltage | 36 | V |
| Rated torque | 2.7 | Nm |
| Rated speed | 400 | r/min |
| Max. phase current | 10 | A |
| Stator pole number | 12 | |
| Rotor pole number | 10 | |
| *d*-axis inductance, $L_d$ | 0.277 | mH |
| *q*-axis inductance, $L_q$ | 0.339 | mH |
| Stator resistance | 0.5 | ohm |

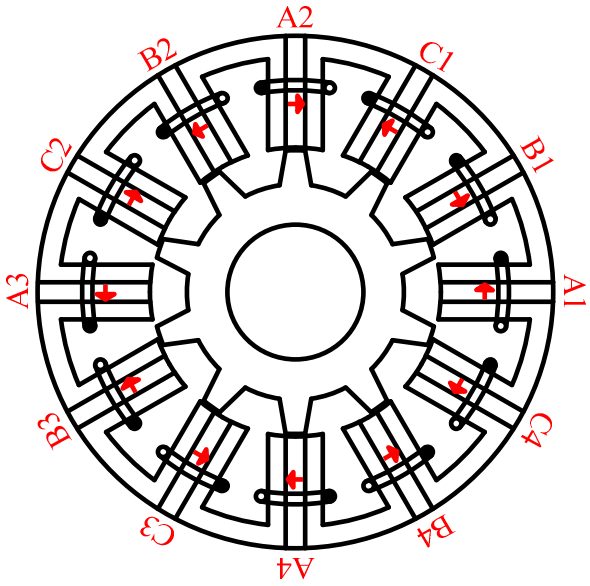


Fig. 2. 10. Topology of 12/10 stator/rotor poles machine.

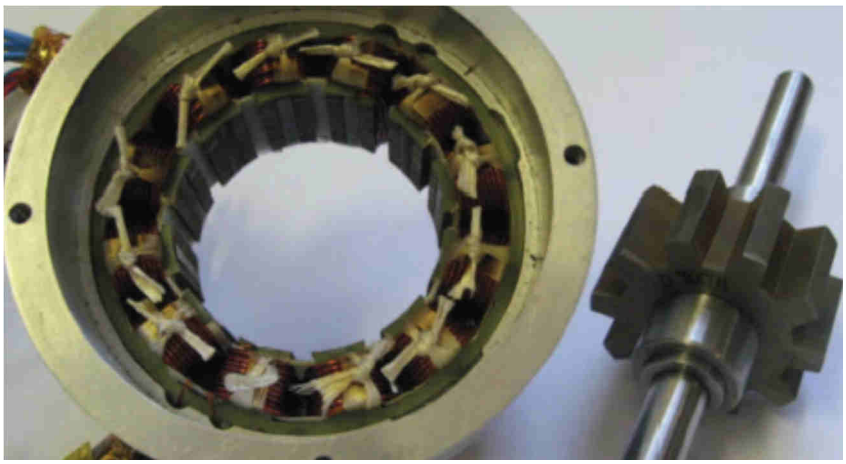

Fig. 2. 11. Prototype 12/10 stator/rotor poles brushless AC machine.

The SFPM machine topologies have very simple and robust rotor, and "U-shaped" laminated iron segments around magnetized PMs in the stator. The magnetization is kept in opposite polarities from one magnet to the adjacent one. A stator pole established by two iron legs from adjacent segments and a magnet is wounded by coils, which is a part of the stator winding. Furthermore, the original design of Test Machine-II is a single three-phase machine, and controlled by the power stage shown in Fig. 2.9, and the measured three-phase back-EMF waveforms are shown in Fig. 2.12. Moreover, it can also be applied as an alternative machine winding configuration, such as one single three-phase machine or two

three-phase machines (dual three-phase machine), and controlled by the dual-inverter shown in Fig. 2.13.

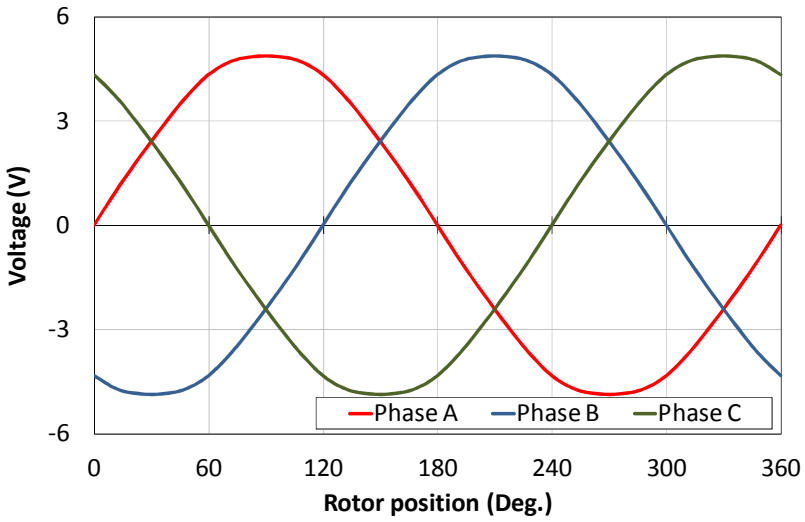


Fig. 2. 12. Three-phase Back-EMFs, 400 r/min.

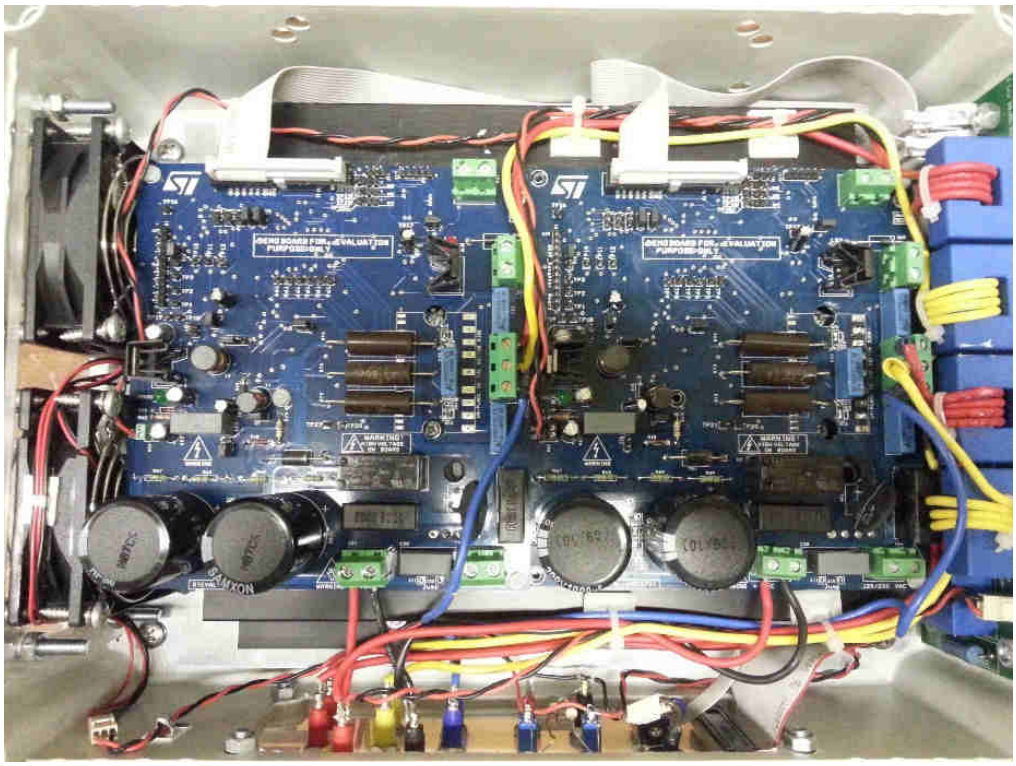

Fig. 2. 13. Dual three-phase power stage.

In Fig. 2.13, the dual three-phase power stage is based on STEVAL-IHM027V1 and the

power is 1kW for each inverter. The IGBT intelligent power module, STGIPS10K60A, in which the maximum voltage and current are 600V and 10A, respectively, is designed by STMicroelectronics Ltd. The operating frequency is 10 kHz and the dead-time is 2μs, but there is a voltage drop about 2.1 volts at the temperature of $25^0$C. It has a feature that the single three-phase AC voltage can be supplied within 90 to 220V, or DC supply voltage within 125 to 350V. Moreover, an interface board is employed to transfer the gate drive signal from the PWM generator, DS5101 Digital Waveform Output Board, to the power stage, and also has the function for measuring the DC-link voltage and phase current and feedback the measured DC voltage and phase current to DS2004 High-Speed A/D Board.

The Test Machine-II will be used to demonstrate the investigated control strategies such as saliency-based methods in Chapters 4 and 6, and fundamental-based methods in Chapter 5 and 7 for sensorless rotor position estimations and the sensorless operation improvements.

## 2.4 Conclusion

This chapter describes the detailed information about the experimental hardware platform and software environment based on a dSPACE control system and Matlab/Simulink, respectively. Two test machines which will be investigated in this research study are also introduced. Several control strategies will be applied to these two test machines since their structures and specifications are all different which will be discussed in depth in each of the related chapters.

## References


[CHE10] J.T. Chen, and Z.Q. Zhu, “Winding configurations and optimal stator and rotor pole combination of flux-switching PM brushless AC Machines,” *IEEE Trans. Energy Conver.*, vol.25, no.2, pp.293-302, June 2010.

[DSP10] dSPACE, “Hardware installation and configuration reference,” Release 6.6, May 2010.

[ZHU97] Z.Q. Zhu, K. Ng, and D. Howe, “Design and analysis of high-speed brushless permanent magnet motors,” *Electrical Machines and Drives, 1997 Eighth International Conference* on (Conf. Publ. No. 444), pp.381-385, 1-3 Sep 1997.

# CHAPTER 3

# SENSORLESS OPERATION CAPABILITY OF PERMANENT MAGNET SYNCHRONOUS MACHINES

## 3.1 Introduction

In terms of the effectiveness at standstill and low speed operating ranges, the machine saliency is an essential requirement for saliency tracking based techniques in sensorless control of PM BLAC machines, such as high-frequency (HF) signal injection-based methods. It normally injects an extra signal into the machine windings and uses the phase carrier current response signal for the rotor position estimation [LEI11], which can be categorized into two major methods: rotating [ZHU11] and pulsating carrier vector [ZHU11] [KOC09] signal injections. Furthermore, the high-frequency rotating and pulsating carrier signal injections were compared in several publications [OVR04] [KIM04] [RAC08]. The basic implementation of both injection methods were experimentally compared by considering the bandwidth limitations and parameter sensitivity [OVR04]. In [KIM04], the comparison focused on the estimated position error under various load conditions. In these two studies, the HF pulsating injection was found to be more accurate than the HF rotating injection, but [OVR04] explained that the HF rotating injection was more robust. In [RAC08], the extended research was made from [OVR04] [KIM04] which includes magnet polarity detection, analysis of resistance effect in the testing machine and the experimental implementation issues.

In this chapter, the potential sensorless operation capability of SPM machine (Test Machine-I) is systematically investigated based on HF carrier signal injection techniques. First of all, with the aid of actual rotor position from an encoder, the machine saliency is

experimentally measured by applying different load conditions. Meanwhile, the cross-saturation effect is also considered to examine its influence on the accuracy of rotor position estimation. Furthermore, before the drive into sensorless control operation, a simple experimental method is employed to detect the magnetic polarity, which utilizes the amplitude of estimated *d*-axis carrier current response. Additionally, the high-frequency eddy-current loss reflected resistance-based saliency is taken into account by finite element (FE) analysis. Finally, the effectiveness of rotor position and speed estimation with the compensation of cross-saturation effect are fully analyzed and implemented under several operating conditions in order to verify the conclusion on sensorless capability of the prototype Test Machine-I.

## 3.2 Models of High-Frequency Carrier Signal Injection Techniques

### 3.2.1 High-Frequency Rotating Carrier Voltage Signal Injection

The rotating carrier signal injection approach usually injects a balanced three-phase carrier voltage vector onto the fundamental excitation voltage in the stationary reference frame [ZHU11] [JAN03] [OVR04] [JAN04] as shown in Fig. 3. 1.

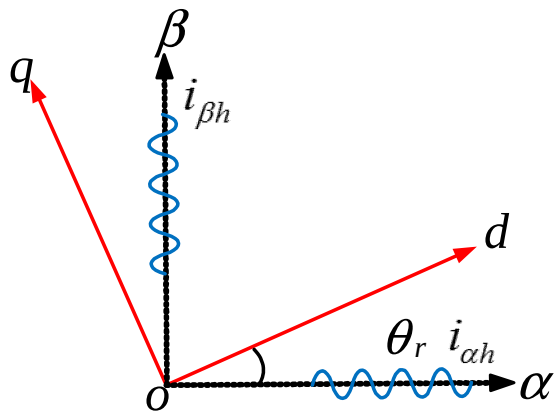


Fig. 3.1. Rotating voltage signal injection.

By injecting a balanced high-frequency rotating carrier voltage signal (3.1) into the

stationary reference frame,

$$\begin{bmatrix} v_{\alpha h} \\ v_{\beta h} \end{bmatrix} = U_c \begin{bmatrix} \cos\alpha \\ \sin\alpha \end{bmatrix}, \quad \alpha = \omega_c + \varphi \tag{3.1}$$

where $U_c$, $\omega_c$ and $\varphi$ are referred as the amplitude, angular speed and initial phase angle of the injected high-frequency rotating carrier voltage signal, respectively.

The differential carrier current response in the stationary reference frame can be presented as

$$p\begin{bmatrix} i_{\alpha h} \\ i_{\beta h} \end{bmatrix} = \begin{bmatrix} \frac{1}{L_p} + \frac{1}{L_n}\cos\left(2\theta_r + \theta_m\right) & \frac{1}{L_n}\sin\left(2\theta_r + \theta_m\right) \\ \frac{1}{L_n}\sin\left(2\theta_r + \theta_m\right) & \frac{1}{L_p} - \frac{1}{L_n}\cos\left(2\theta_r + \theta_m\right) \end{bmatrix} \cdot U_c \begin{bmatrix} \cos\alpha \\ \sin\alpha \end{bmatrix} \tag{3.2}$$

$$\theta_m = \tan^{-1}\left(\frac{-L_{dqh}}{L_{sd}}\right), \quad L_p = \frac{L_{dh}L_{qh} - L_{dqh}^2}{L_{s\alpha}}, \quad L_n = \frac{L_{dh}L_{qh} - L_{dqh}^2}{\sqrt{L_{sd}^2 + L_{dqh}^2}} \tag{3.3}$$

Then, the resultant position-dependent carrier current response in the stationary reference frame can be expressed as

$$\begin{aligned} \begin{bmatrix} i_{\alpha h} \\ i_{\beta h} \end{bmatrix} &= \frac{U_c}{\omega_c} \begin{bmatrix} \frac{1}{L_p} + \frac{1}{L_n}\cos\left(2\theta_r + \theta_m\right) & \frac{1}{L_n}\sin\left(2\theta_r + \theta_m\right) \\ \frac{1}{L_n}\sin\left(2\theta_r + \theta_m\right) & \frac{1}{L_p} - \frac{1}{L_n}\cos\left(2\theta_r + \theta_m\right) \end{bmatrix} \cdot U_c \begin{bmatrix} \sin\alpha \\ -\cos\alpha \end{bmatrix} \\ &= \begin{bmatrix} I_p \cos\left(\alpha - \frac{\pi}{2}\right) \\ I_p \sin\left(\alpha - \frac{\pi}{2}\right) \end{bmatrix} + \begin{bmatrix} I_n \cos\left(-\alpha + 2\theta_r + \theta_m + \frac{\pi}{2}\right) \\ I_n \sin\left(-\alpha + 2\theta_r + \theta_m + \frac{\pi}{2}\right) \end{bmatrix} \end{aligned} \tag{3.4}$$

where

$$I_p = \frac{U_c}{\omega_c L_p}, \quad I_n = \frac{U_c}{\omega_c L_n} \tag{3.5}$$

where $I_p$ and $I_n$ are the amplitude of positive and negative sequence carrier currents, $\theta_m$ is referred to as the cross-saturation angle which is defined in (3.3) that is introduced by the

cross-saturation effect. $L_p$ and $L_n$ are the equivalent positive and negative sequence inductances, respectively. $\theta_r$ is the actual rotor position. $L_{sa}$ and $L_{sd}$ are the average and difference of *d*- and *q*-axis incremental inductances, which are explained as

$$\begin{cases} L_{s\alpha} = \left( L_{qh} + L_{dh} \right) / 2 \\ L_{sd} = \left( L_{qh} - L_{dh} \right) / 2 \end{cases} \tag{3.6}$$

The HF rotating carrier signal voltage injection can be summarized according to the analysis in (3.3), as follows:

(a) The carrier current can be derived as two carrier components [RAC08] such as positive and negative sequence components, as defined in (3.3), respectively. The positive sequence component has the same angular speed and rotating direction as the injected carrier signal. The negative sequence component has the combination of magnetic saliency and cross-saturation introduced carrier current, in which the rotor position information is contained in the phase angle of negative sequence component. Consequently, the negative sequence carrier current is usually utilized for the sensorless rotor position estimation.

(b) Different from the HF pulsating carrier signal injection, the carrier current responses, i.e. positive and negative sequence components are asymmetric. Also, $I_p$ and $I_n$ are parameter-dependent.

(c) The phase angle of negative sequence current component is phase-modulated by the rotor position and cross-saturation angle. Therefore, the DC constant error will occur in the rotor position estimation due to the cross-saturation effect.

Since the negative sequence carrier current contains the rotor position information, the synchronous reference frame filter (SRFF) [DEG98] [RAC10] [REI13] can be employed.

Basically, SRFF uses the reference frame transformation synchronizing system. When applying the frame transformation with the aid of estimated rotor position, the two input signals are the spectral components of interest and will be centered at DC (0Hz). Then, with the aid of a LPF, the DC component can be obtained without phase leg. Meanwhile, by applying the reverse frame transformation, and subtracting from the original carrier current input signals, the spectral components of interest which are the fundamental and positive carrier current component can be filtered out, and then the negative sequence carrier current will be derived from the remaining component by SRFF. The signal modulation together with SRFF used to obtain the positive and negative sequence signals are shown in Fig. 3.2 [GON12].

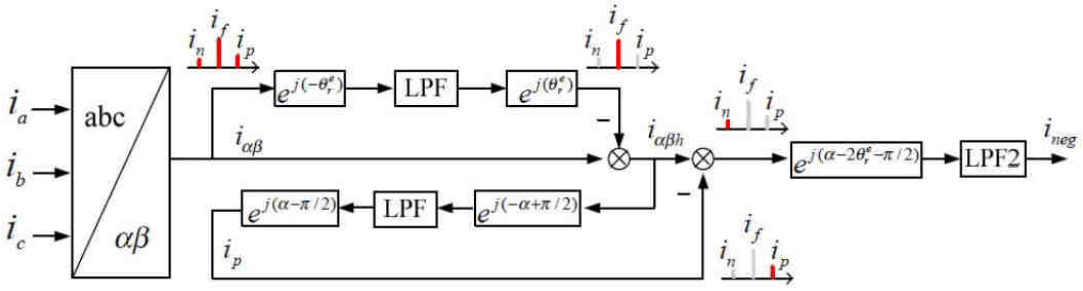


Fig. 3.2. Signal demodulation for HF rotating injection [GON12].

In the synchronous reference frame with the estimated carrier frequency, the negative-sequence carrier current response can be given by

$$\begin{bmatrix} i_{neg\_d} \\ i_{neg\_q} \end{bmatrix} = LPF \cdot \left\{ \begin{bmatrix} \cos\left(-\alpha+2\theta_r^e+\frac{\pi}{2}\right) & \sin\left(-\alpha+2\theta_r^e+\frac{\pi}{2}\right) \\ -\sin\left(-\alpha+2\theta_r^e+\frac{\pi}{2}\right) & \cos\left(-\alpha+2\theta_r^e+\frac{\pi}{2}\right) \end{bmatrix} \cdot \begin{bmatrix} I_n \cos\left(-\alpha+2\theta_r+\theta_m+\frac{\pi}{2}\right) \\ I_n \sin\left(-\alpha+2\theta_r+\theta_m+\frac{\pi}{2}\right) \end{bmatrix} \right\}$$
$$= \begin{bmatrix} I_n \cos\left(2\Delta\theta+\theta_m\right) \\ I_n \sin\left(2\Delta\theta+\theta_m\right) \end{bmatrix}$$
$$= \begin{bmatrix} I_n \cos\theta_{neg} \\ I_n \sin\theta_{neg} \end{bmatrix} \tag{3.7}$$

where $\Delta\theta$ is the position estimation error and θm presents the cross-saturation angle. The *q*-axis carrier current is usually used as the input signal $f(\Delta\theta)$ to the position tracking observer [JAN95] [DEG98], which can be written as

$$f\left(\Delta\theta\right)=i_{neg\_q}=I_n\sin\left(2\Delta\theta+\theta_m\right) \tag{3.8}$$

Considering the cross-saturation effect, the position estimation error ($-\theta_m/2$) for the HF rotating carrier signal injection would be generated. In order to compensate the cross-saturation angle, the phase angle of injection signal can be re-presented as

$$\alpha^*=\alpha+\theta_m \tag{3.9}$$

where $\alpha^*$ is new updated phase angle. Hence, the carrier response current by the complex vector can be express as

$$i_{neg\_dq}=I_{pos\_dq}\cdot e^{j(\alpha+\theta_m-\pi/2)}+I_{neg\_dq}\cdot e^{j(-\alpha+2\theta_r+\pi/2)} \tag{3.10}$$

Clearly, it can be found that only positive sequence component has the cross-saturation angle. Hence, the negative carrier sequence current according to (3.7) can be re-written as

$$\begin{bmatrix} i_{neg\_d} \\ i_{neg\_q} \end{bmatrix}=\begin{bmatrix} I_n\cos\left(2\Delta\theta\right) \\ I_n\sin\left(2\Delta\theta\right) \end{bmatrix} \tag{3.11}$$

Then, the input signal $f(\Delta\theta)$ to the position tracking observer can re-expressed as

$$f\left(\Delta\theta\right)=i_{neg\_q}=I_n\sin\left(2\Delta\theta\right) \tag{3.12}$$

### 3.2.2 High-Frequency Pulsating Carrier Voltage Signal Injection

Similarly, a high-frequency pulsating carrier voltage signal is injected into the *d*-axis estimated synchronous reference frame [ZHU11] [KOC09] [JAN03] [KIM04] [JAN04] as two superposition rotating carrier vectors with opposite direction as shown in Fig. 3.3, and different from the HF rotating carrier voltage signal injection. The rotor position could be obtained from the amplitude-modulated carrier current response.

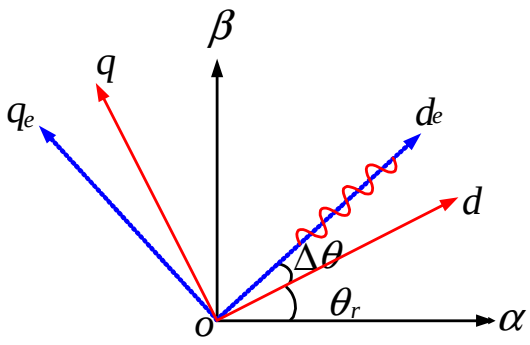


Fig. 3.3. HF *d*-axis pulsating voltage signal injection.

For high-frequency *d*-axis pulsating carrier voltage signal injection, the voltage is (3.13) injected on the *d*-axis estimated synchronous reference frame

$$\begin{bmatrix} v_{dh}^{e} \\ v_{qh}^{e} \end{bmatrix} = U_c \begin{bmatrix} \cos\alpha \\ 0 \end{bmatrix}, \quad \alpha = \omega_c + \varphi \tag{3.13}$$

where $V_c$, $\omega_c$ and $\varphi$ are the amplitude, angular speed and initial phase angle of the injected high-frequency pulsating carrier voltage signal, respectively.

The differential of HF carrier current in the estimated synchronous reference frame can be given as

$$p\begin{bmatrix} i_{dh}^{e} \\ i_{qh}^{e} \end{bmatrix} = \begin{bmatrix} \frac{1}{L_p} + \frac{1}{L_n}\cos\left(2\Delta\theta + \theta_m\right) & \frac{1}{L_n}\sin\left(2\Delta\theta + \theta_m\right) \\ \frac{1}{L_n}\sin\left(2\Delta\theta + \theta_m\right) & \frac{1}{L_p} - \frac{1}{L_n}\cos\left(2\Delta\theta + \theta_m\right) \end{bmatrix} \cdot U_c \begin{bmatrix} \cos\alpha \\ 0 \end{bmatrix} \tag{3.14}$$

Then, the resultant carrier response current in the estimated synchronous reference frame can be explained as

$$\begin{bmatrix} i_{dh}^{e} \\ i_{qh}^{e} \end{bmatrix} = \begin{bmatrix} \frac{U_c}{\omega_c L_p} + \frac{U_c}{\omega_c L_n}\cos\left(2\Delta\theta + \theta_m\right) \\ \frac{U_c}{\omega_c L_n}\sin\left(2\Delta\theta + \theta_m\right) \end{bmatrix} \cdot \sin\alpha = \begin{bmatrix} I_p + I_n\cos\left(2\Delta\theta + \theta_m\right) \\ I_n\sin\left(2\Delta\theta + \theta_m\right) \end{bmatrix} \cdot \sin\alpha \tag{3.15}$$

where

$$I_p = \frac{U_c}{\omega_c L_p}, \quad I_n = \frac{U_c}{\omega_c L_n} \tag{3.16}$$

Clearly, the carrier current response signal is basically amplitude modulated by the rotor position information (if cross-saturation angle $\theta_m$ is constant). In addition, when the position error $\Delta\theta$ is small, the high-frequency $q$-axis carrier current response will become very small. Hence, the $q$-axis carrier current is normally employed for the rotor position estimation due to less current and torque ripples.

From the discussions above, the features of HF pulsating carrier signal injection can be summarized as follows:

(a) The HF pulsating method also has two rotating carrier vectors, superposition on the fundamental excitation, i.e. rotational positive and negative rotating carrier vectors.

(b) Two carrier sequence current components in the estimated synchronous reference frame are similar to the HF rotating signal injection method, but in HF pulsating injection method, these two components are symmetrical.

(c) The magnitudes of positive and negative sequence components are amplitude-modulated by the position estimation error which can be used for the rotor position estimation.

To obtain the carrier current amplitude from the HF carrier current response, the synchronous detection method is employed [MAD95] [LI09a]. Two carrier current signals have to be multiplied by 2sin$\alpha$ and applied by the LPF afterward, the amplitudes of the $d$- and $q$-axis carrier current responses can be obtained as

$$\begin{bmatrix} \left|i_{dh}^{e}\right| \\ \left|i_{qh}^{e}\right| \end{bmatrix} = LPF\left(\begin{bmatrix} i_{dh}^{e} \\ i_{qh}^{e} \end{bmatrix} \cdot 2\sin\alpha\right) = \begin{bmatrix} I_p + I_n\cos\left(2\Delta\theta + \theta_m\right) \\ I_n\sin\left(2\Delta\theta + \theta_m\right) \end{bmatrix} \tag{3.17}$$

In the HF $d$-axis pulsating carrier signal injection, the amplitude of $q$-axis carrier current is usually used to be the input signal to the position tracking observer,

$$f\left(\Delta\theta\right) = \left|i_{n\_q}\right| = I_n\sin\left(2\Delta\theta + \theta_m\right) \tag{3.18}$$

The input carrier current is load-dependent estimated error (-$\theta_m$/2) and can be easily to be

compensated [ZHU11][LI09].

### 3.2.3 Carrier Current Response and Spectral Distribution

A high-frequency carrier voltage signal with a magnitude of 10V, and frequency of 330Hz are selected for this measurement. With the aid of position sensor, the Test Machine-II is operated in sensored mode ($\Delta\theta$=0) that the measured response current for the rotating carrier voltage signal injection is shown in Fig. 3.4. The carrier response current in the synchronous reference frame is elliptic form as shown in Fig. 3.4 (a). Obviously, since there is more current ripple on *q*-axis, the more torque ripple would occur for the HF rotating carrier signal injection.

By comparison, the measured current response for *d*-axis pulsating injection technique can be presented in stationary and synchronous frame, respectively, as shown in Fig. 3.5. According to Fig 3.5 (a), it can be seen that the *d*-axis pulsating carrier voltage signal injection produces the oscillating *d*-axis current, but there is a limitated current ripple in *q*-axis. In addition, if the rotor position estimation error is small and close to zero, the *d*-axis current ripple would be ($I_p$+$I_n$cos$\theta_m$) while the amplitude of *q*-axis current ripple is ($I_n$sin$\theta_m$).

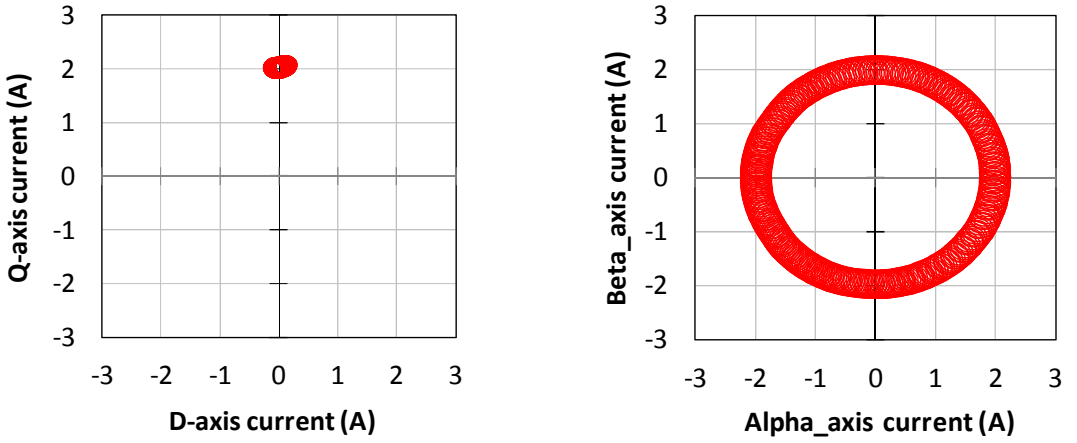


(a) Synchronous reference frame (b) Stationary reference frame

Fig. 3.4. Carrier current response for rotating voltage signal injection when $i_d$ = 0A, $i_q$ = 2A, and $f$ = 4Hz.

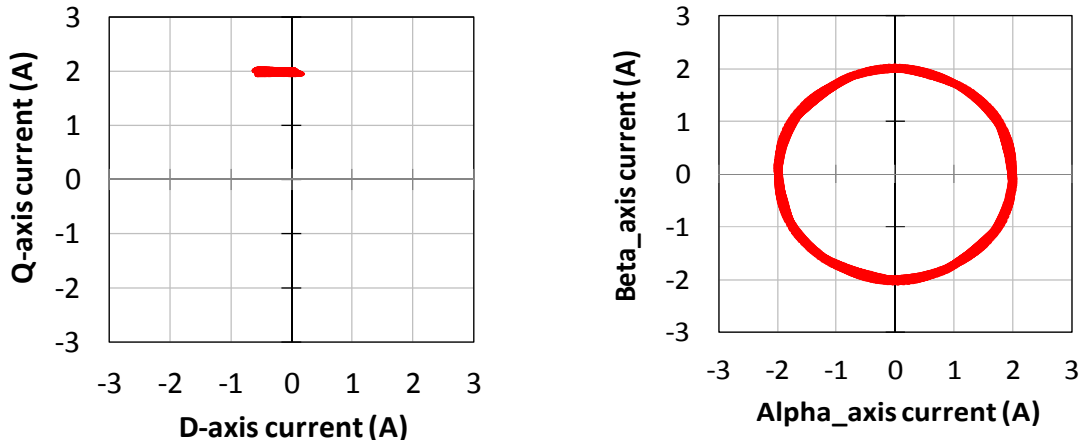


(a) Synchronous reference frame (b) Stationary reference stationary

Fig. 3.5. Carrier current response for pulsating voltage signal injection when $i_d$ = 0A, $i_q$ = 2A, and $f$=4Hz.

Moreover, for rotating carrier voltage signal injection, the frequency domain analysis shows the carrier current in the stationary reference frame have an asymmetric distribution, as described in Fig. 3.6. Similarly, a symmetric spectrum for the pulsating carrier voltage signal injection method in the synchronous reference frame can be observed in Fig. 3.7.

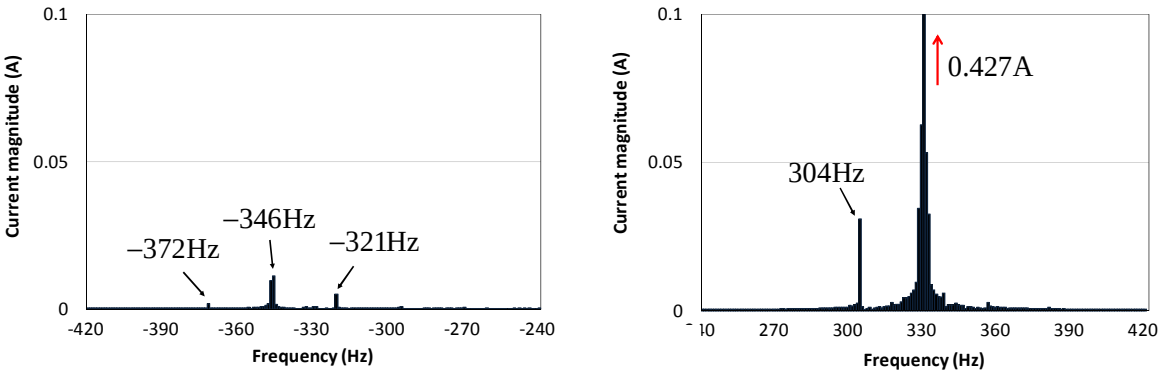


(a) Negative sequence components (b) Positive sequence components

Fig. 3.6. Carrier current frequency spectra for rotating voltage injection when $i_d$ = 0A, $i_q$ = 2A, and $f$=4Hz.

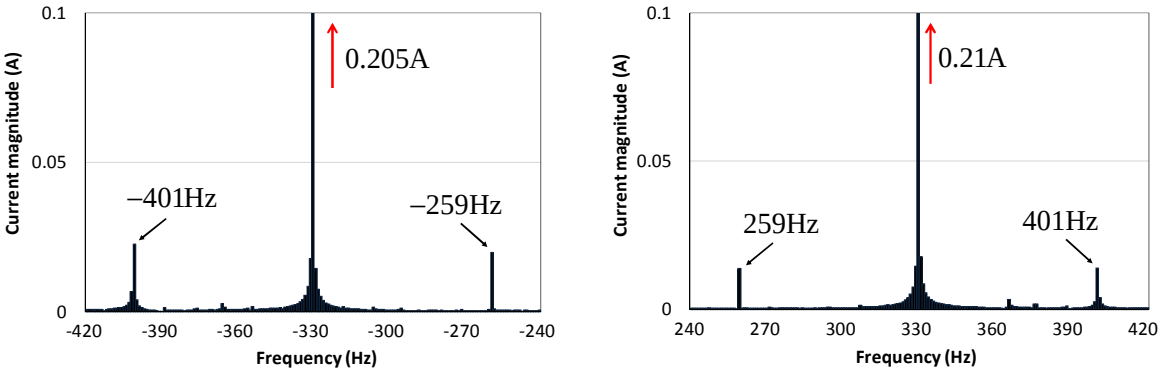


(a) Negative sequence components (b) Positive sequence components

Fig. 3.7. Carrier current frequency spectra for pulsating voltage injection when $i_d$ = 0A, $i_q$ = 2A, and $f$=4Hz.

Different types of injection will have different spectral distributions due to injection signal. Moreover, the rotating voltage signal injection method is essentially characterized by the asymmetric rotating vector signal in one direction. On the other hand, the pulsating voltage signal injection strategy is to use two symmetrical rotating vector components, which are the positive and negative sequence components and rotating in the opposite direction, respectively.

Additionally, some harmonics exist in the negative and positive sequence components for pulsating injection technique, but for rotating injection technique, the harmonics only occur in the negative sequence as shown in Fig. 3.8. These can be described as secondary saliency (multiple saliencies effect) [OVR04] [FRE05] [DEG98] due to the saturation-induced saliency or inverter nonlinearity effects [FRE05] [GON11].

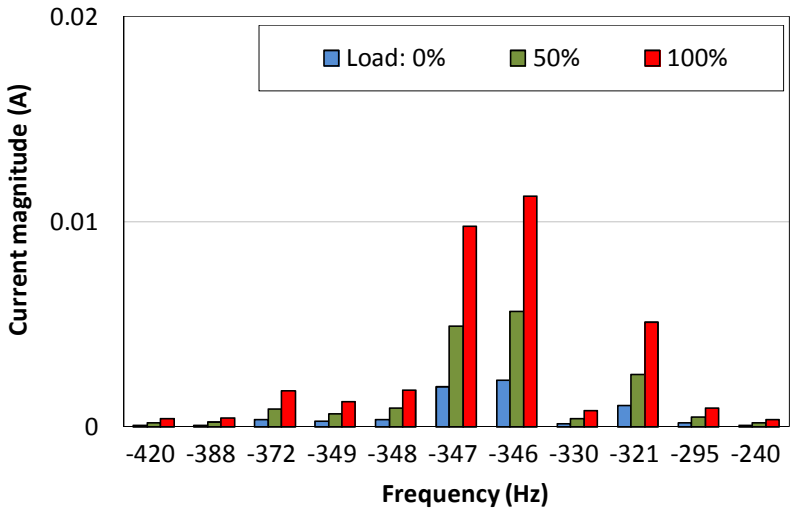


(a) Negative sequence components – Rotating

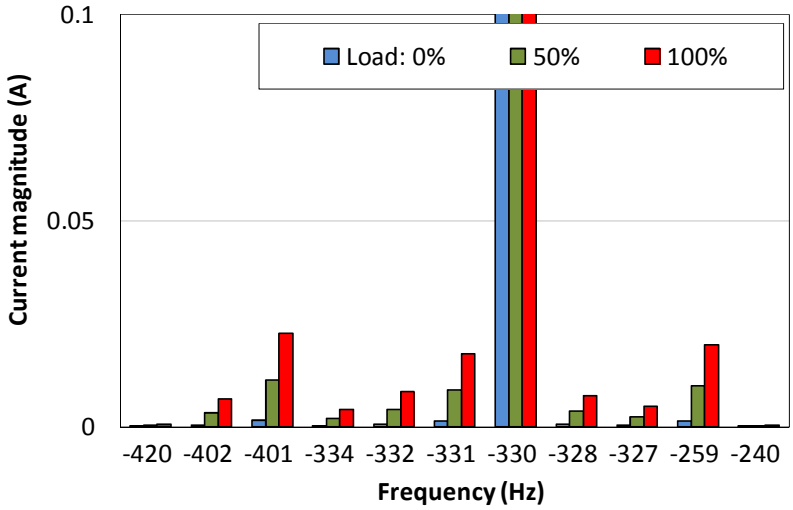


(b) Negative sequence components – Pulsating

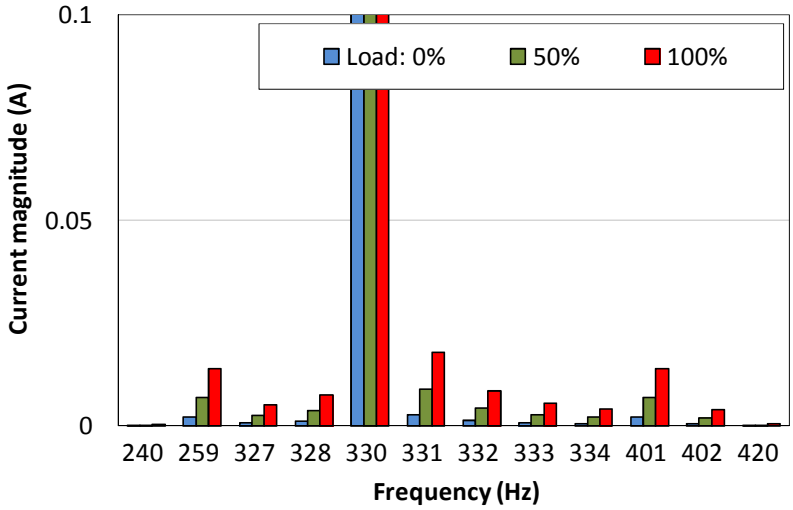


(c) Positive sequence components - Pulsating

Fig. 3.8. Frequency spectra under load conditions.

## 3.3 Evaluation of Saliency Accounting For Cross-Saturation Effect

Before applying the HF carrier voltage signal injection based techniques, the first procedure it to investigate the level of machine saliency since it is the essential requirement, which is related to the inductance variation and machine load conditions. In order to evaluate the machine saliency level, a virtual synchronous reference frame which has a $\Delta\theta$ phase angle difference from the actual synchronous reference frame is described as shown in Fig. 3.9. Using the transformation matrix $T(\Delta\theta)$ which is

$$T(\Delta\theta)=\begin{bmatrix}\cos(\Delta\theta) & -\sin(\Delta\theta)\\ \sin(\Delta\theta) & \cos(\Delta\theta)\end{bmatrix} \tag{3.19}$$

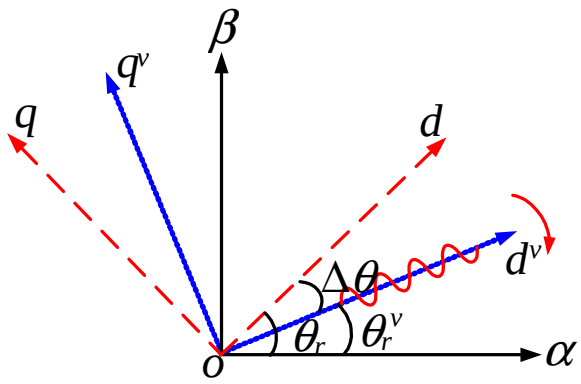


Fig. 3.9. Actual and virtual synchronous reference frame.

The high-frequency voltage model in the synchronous reference frame can easily be presented as

$$\begin{bmatrix}v_{dh}\\ v_{qh}\end{bmatrix}=\begin{bmatrix}L_{dh} & L_{dqh}\\ L_{qdh} & L_{qh}\end{bmatrix}p\begin{bmatrix}i_{dh}\\ i_{qh}\end{bmatrix} \tag{3.20}$$

where $p$ is the differential operator, $L_{dqh}$ and $L_{qdh}$ are the high frequency mutual inductances, and $L_{dh}$ and $L_{qh}$ are the high frequency incremental $d$- and $q$-axis self-inductances. Then, with the aid of (3.19) and (3.20), the HF voltage model of Test Machine-I in the virtual synchronous reference frame can be represented as

$$\begin{bmatrix} v_{dh}^{v} \\ v_{qh}^{v} \end{bmatrix} = T(\Delta\theta)\begin{bmatrix} L_{dh} & L_{dqh} \\ L_{dqh} & L_{qh} \end{bmatrix} T^{-1}(\Delta\theta)\cdot p\begin{bmatrix} i_{dh}^{v} \\ i_{qh}^{v} \end{bmatrix} \tag{3.21}$$

The differential of the HF carrier response current in the virtual synchronous reference frame is derived as

$$p\begin{bmatrix} i_{dh}^{v} \\ i_{qh}^{v} \end{bmatrix} = \begin{bmatrix} \frac{1}{L_p} + \frac{1}{L_n}\cos(2\Delta\theta + \theta_m) & \frac{1}{L_n}\sin(2\Delta\theta + \theta_m) \\ \frac{1}{L_n}\sin(2\Delta\theta + \theta_m) & \frac{1}{L_p} - \frac{1}{L_n}\cos(2\Delta\theta + \theta_m) \end{bmatrix} \cdot \begin{bmatrix} v_{dh}^{v} \\ v_{qh}^{v} \end{bmatrix} \tag{3.23}$$

A high frequency pulsating carrier voltage vector (3.13) is injected into the virtual synchronous reference frame; the high frequency carrier current response can be rewritten as

$$\begin{bmatrix} i_{dh}^{v} \\ i_{qh}^{v} \end{bmatrix} = \begin{bmatrix} I_p + I_n\cos(2\Delta\theta + \theta_m) \\ I_n\sin(2\Delta\theta + \theta_m) \end{bmatrix} \cdot \sin\alpha \tag{3.24}$$

Then, by applying the synchronous detection method and a low-pass filter (LPF), the amplitude of carrier current response is obtained as shown in Fig. 3.11 (a) by

$$\begin{bmatrix} \left|i_{dh}^{v}\right| \\ \left|i_{qh}^{v}\right| \end{bmatrix} = LPF\left(\begin{bmatrix} i_{dh}^{v} \\ i_{qh}^{v} \end{bmatrix} \cdot 2\sin\alpha\right) = \begin{bmatrix} I_p + I_n\cos\left(2\Delta\theta + \theta_m\right) \\ I_n\sin\left(2\Delta\theta + \theta_m\right) \end{bmatrix} \tag{3.25}$$

### 3.3.1 Experimental Evaluation of Machine Saliency Level

To investigate the machine magnetic saturation-induced rotor saliency in the Test Machine-II, a simple experimental method as shown in Fig. 3.10, is employed to investigate the existence of machine saliency level. A high-frequency carrier voltage signal with a magnitude of 10V, and frequency of 330Hz, are selected in this chapter, and is injected into the virtual reference frame.

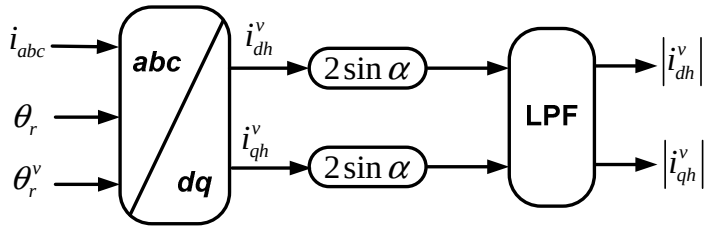


Fig. 3.10. Basic principle for the machine saliency investigation.

When the rotor, i.e. actual synchronous reference frame, is locked at a fixed zero position ($\theta_r = 0^o$) and the virtual synchronous reference frame rotates at a constant angular speed in the negative direction. Hence, the phase angle of high frequency *d*- and *q*-axis current responses will be the same, and the response current amplitude is modulated by the position difference $\Delta\theta$ between actual and virtual synchronous reference frames as illustrated in Fig. 3.11.

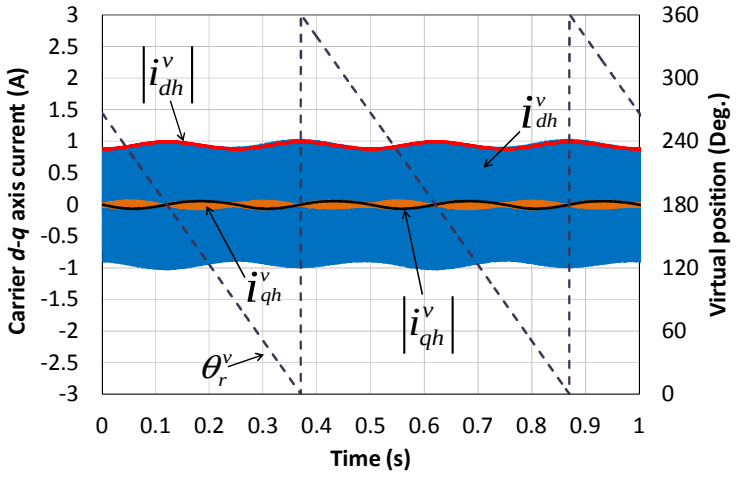


(a) Measured response currents with virtual position

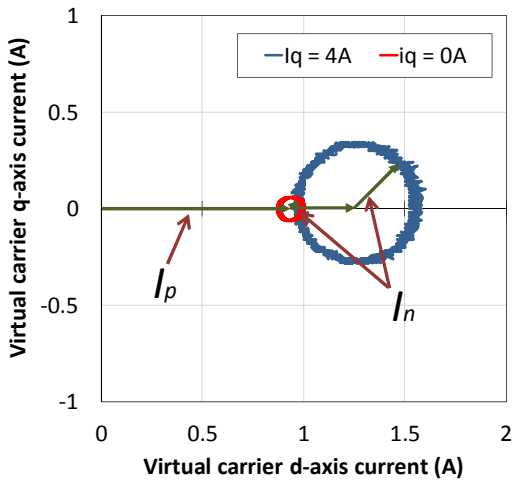


(b) Locus of carrier current circle by machine saliency

Fig. 3.11. Measured HF current response in virtual *d*-*q* reference frame.

Furthermore, with the aid of the machine operates with a sensor, it can be clearly seen in Fig. 3.11 (a) that the position difference is $0^o$ or $180^o$, the amplitude of *d*-axis carrier current response achieves the maximum value while the *q*-axis is almost zero degree in which the

cross-saturation angle $\theta_m$ is negligible without applying the fundamental excitation. In addition, the carrier current response is modulated as two cycles per single cycle of electrical position, as described in Fig. 3.11 (a). The amplitude locus of $d^v$-$q^v$ carrier current variations without and with full load are depicted in Fig. 3.11 (b), where the center location of the machine saliency circle is determined by $I_p$ and the radius of saliency circle is dependent on $I_n$ which indicates the machine saliency level. If the radius of saliency circle is longer and clearly identified, then the machine is suitable for high-frequency injection-based sensorless control scheme. In addition, the radius of the locus, $I_n$, at different load condition has a significant change due to the variation of inductances versus fundamental excitation while the offset, $I_p$, is also affected by the inductance variation.

From the foregoing theoretical analysis of machine rotor saliency, a fundamental excitation can be applied to the machine in order to obtain the machine saliency information. According to this analysis, it can be concluded that the radius of current circle, $I_n$, due to machine saliency shown in Fig. 3.12 can still be clearly identifiable under different load conditions even though the carrier current circle by the machine saliency is small. Hence, the HF carrier voltage signal injection-based sensorless control strategies are applicable to the prototype SPM machine.

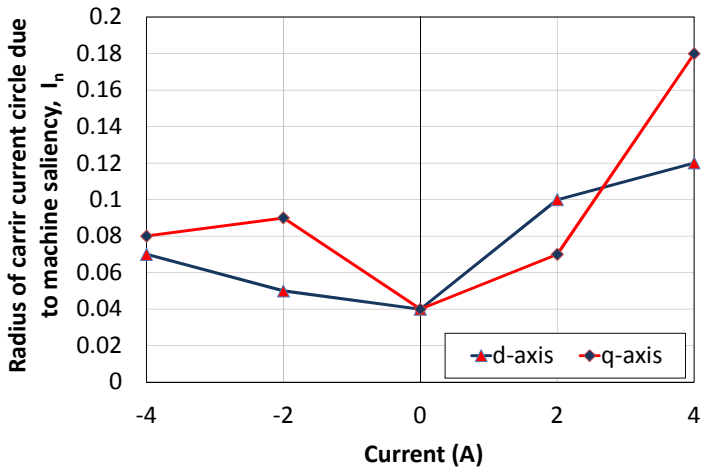


Fig. 3.12. Radius of carrier current circle by machine saliency, $I_n$, against the fundamental $d$- and $q$- axis.

### 3.3.2 Influence of Cross-Saturation

Due to the magnetic saturation by the variation of load, the influence of cross-saturation is usually a cause for the error in the rotor position estimation. Without the fundamental excitation current, the cross-saturation angle is usually close to $0^0$ in which the cross-saturation can be ignored. Nevertheless, by applying the fundamental *q*-axis excitation currents, the cross-saturation angle of $\theta_m$ is measured and becomes clearly identified as shown in Fig. 3.13. It can be concluded that the cross-saturation effect strongly depends on load currents but this issue can be easily compensated following the straightforward method which proposed in [ZHU11] [KOC09] [ZHU07].

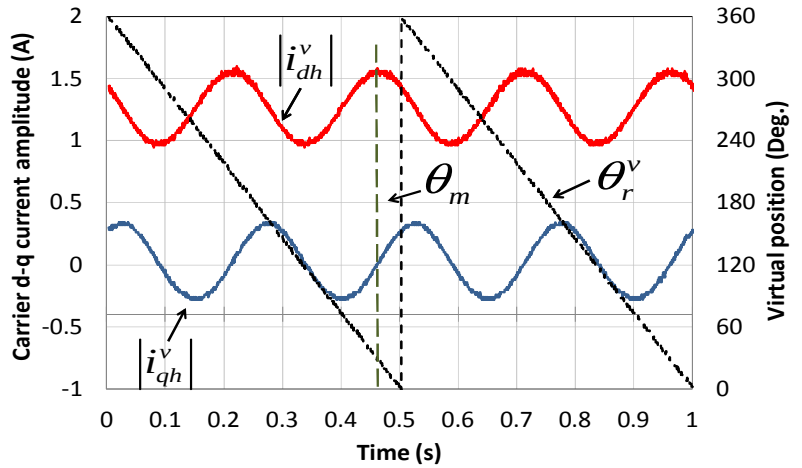


(a) $i_d$ = 0A, $i_q$ = 4A

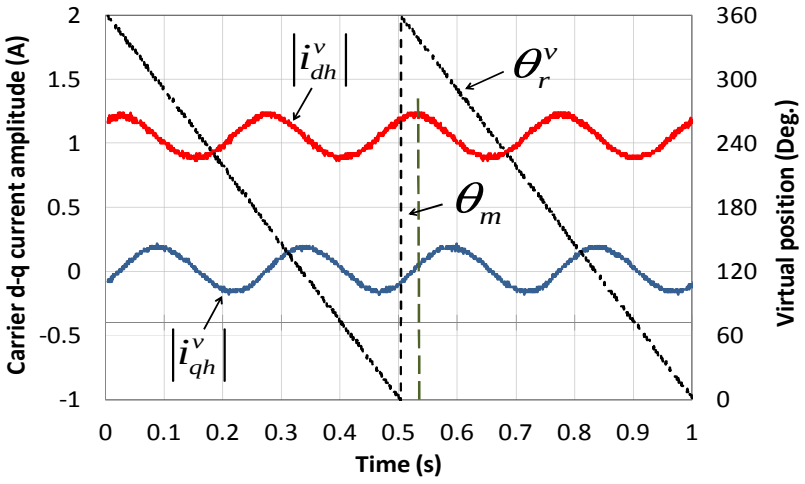


(a) $i_d$ = 0A, $i_q$ = -4A

Fig. 3.13. Measured *d-q* axis carrier current amplitude with virtual position and cross-saturation angle of $\vartheta_m$ under load conditions.

With the aid of sensored operation ($\Delta\theta$=0), the load-dependent cross-saturation angle $\theta_m$ is measured as described in Fig. 3.14. It can be seen that the large positive and negative $q$-axis currents lead to increased cross-saturation angle.

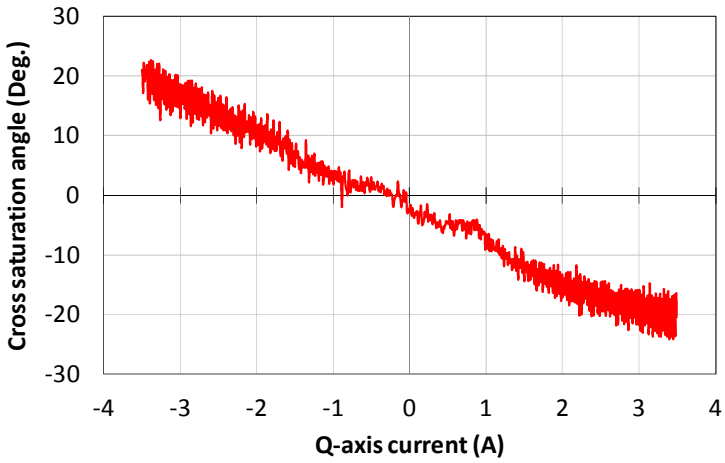


Fig. 3.14. Measured cross-saturation angle in sensored operation.

## 3.4 High-Frequency Loss Reflected-Resistance Induced Rotor Saliency

### 3.4.1 High-Frequency Machine Model Considering Resistance Variation

The HF eddy-current loss can be reflected as the rotor resistance [YAN12a]. According to [YAN12a], the stator resistance and HF eddy-current loss reflected-resistance in the actual and estimated rotor reference frames can be expressed as follows

$$R_{dq} = \sum R \begin{bmatrix} 1 & 0 \\ 0 & 1 \end{bmatrix} + \Delta R \begin{bmatrix} 1 & 0 \\ 0 & 1 \end{bmatrix} [\Omega] \tag{3.26}$$

$$R^{e}_{h\_dq} = \sum R \begin{bmatrix} 1 & 0 \\ 0 & 1 \end{bmatrix} + \Delta R \begin{bmatrix} \cos(2\Delta\theta^r) & -\sin(2\Delta\theta^r) \\ -\sin(2\Delta\theta^r) & -\cos(2\Delta\theta^r) \end{bmatrix} [\Omega] \tag{3.27}$$

where $\Sigma R$ and $\Delta R$ are referred to the average and differential values of the HF eddy current loss reflected-resistance, respectively, and $\Delta\theta^r$ is the position error between the estimated and actual synchronous reference frames.

For the rotor position estimation, a high-frequency pulsating carrier voltage signal (3.13) is injected in the estimated d-axis synchronous reference frame. The resistance-based carrier

response current is magnitude modulated by the rotor position information, which can be used for the sensorless rotor position estimation. Then, considering both resistive and inductive saliencies [YAN12a][ YAN12b], the overall carrier current response can be written as

$$\begin{bmatrix} i_{dh}^r \\ i_{qh}^r \end{bmatrix} = \left( \begin{bmatrix} \Delta R\cos(2\Delta\theta^r) \\ \Delta R\sin(2\Delta\theta^r) \end{bmatrix} \cdot \cos\alpha \right) - \left( \begin{bmatrix} \Delta L\cos(2\Delta\theta^r) \\ \Delta L\sin(2\Delta\theta^r) \end{bmatrix} \cdot \sin\alpha \right) \tag{3.28}$$

The carrier currents consist of two forms of current components, which are proportional to $\Delta R$ and $\Delta L$, respectively. Also, there is a phase difference of $90^0$ between resistance-based carrier current and inductance-based carrier current. For the resistance-based sensorless control, the carrier currents are multiplied by cos$\alpha$ and then the amplitudes of carrier current responses can be obtained with the aid of LPF, which can be represented as

$$\begin{bmatrix} \left|i_{dh}^r\right| \\ \left|i_{qh}^r\right| \end{bmatrix} = LPF\left( \begin{bmatrix} i_{dh}^r \\ i_{qh}^r \end{bmatrix} \cdot 2\cos\alpha \right) = \begin{bmatrix} \Delta R\cos(2\Delta\theta^r) \\ \Delta R\sin(2\Delta\theta^r) \end{bmatrix} \tag{3.29}$$

Consequently, the position estimation error can be derived for resistance-based sensorless control.

### 3.4.2 Analysis of the HF Eddy-Current Loss

This section analyzes the influences of high-frequency eddy-current loss-reflected resistance effect on the prototype 3-slot 2-pole SPM machine [ZHU97].

Firstly, the SPM machine considering the eddy-current loss is investigated by FE analysis [YAN12a][ YAN12b]. For the injection signal, a fixed injected voltage with carrier frequencies of 330Hz and 2500Hz, are selected and the machine is controlled at zero speed at different rotor positions to calculate the loss components as illustrated in Fig. 3.15. According to the results, it can be found that the machine eddy-current losses have the highest value for the loss at $\theta=0^0$ and the lowest value for the loss at ($\theta=90^0$ or $-90^0$). The total HF eddy-current loss is much smaller than the machine tested in [YAN12a][ YAN12b] due to large equivalent air-gap length (1.5mm). Therefore, since the HF eddy-current loss is

relatively small, the iron losses reflected-resistance based induced-saliency can be negligible in the prototype machine for simplified analysis.

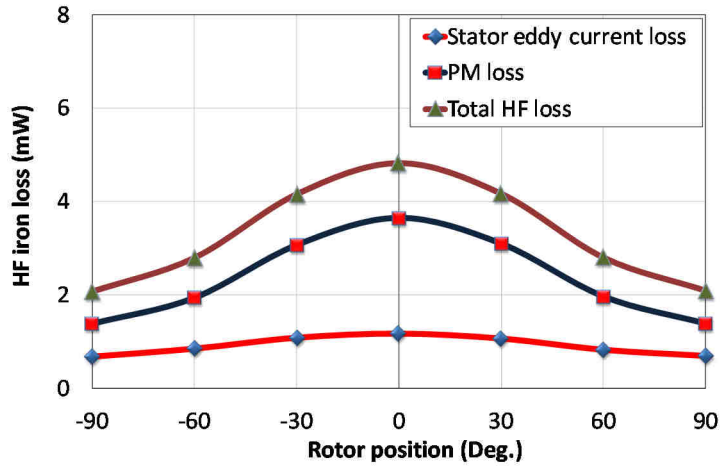


(a) 330Hz, no load

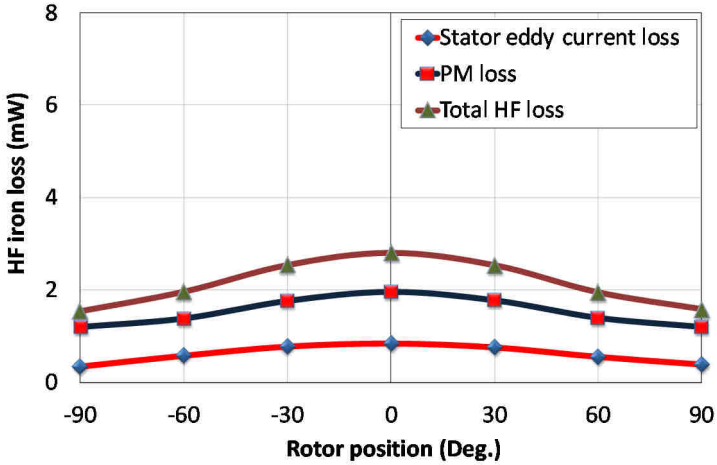


(b) 2500Hz, no load

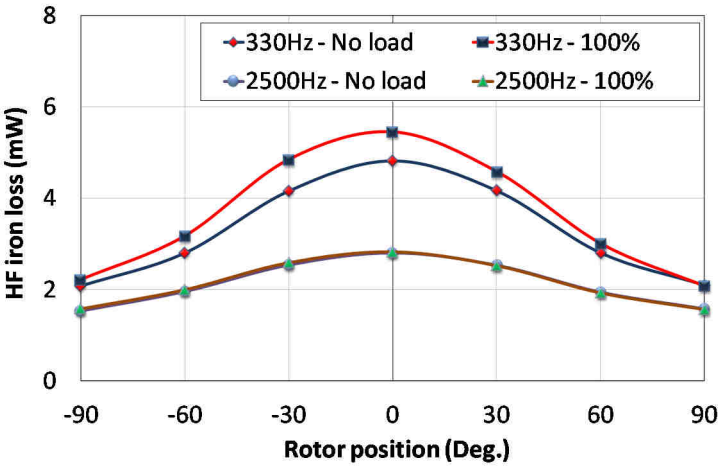


(c) Total HF loss at different load and frequency conditions

Fig. 3.15. High-frequency iron loss versus rotor position based on different injection frequencies.

## 3.5 Detection of Magnetic Polarity and Rotor Position Tracking Observer

### 3.5.1 Magnetic Polarity Detection

In order to avoid a phase shift angle of $180^0$, several methods for the magnetic polarity detection have been published, such as short pulses injection [AIH99] [HOL08], secondary harmonic [JEO05] and high-frequency carrier current response [GON13] against different fundamental excitation current.

More importantly, the magnetic polarity identification is an essential procedure before the machine start-up when applying the HF injection-based sensorless control technique. To obtain the magnetic polarity information for the initial rotor position detection, a simple method is applied as shown in Fig. 3.16, which is integrated into the HF pulsating carrier voltage signal injection based sensorless control method, and is also applicable for the HF rotating injection technique.

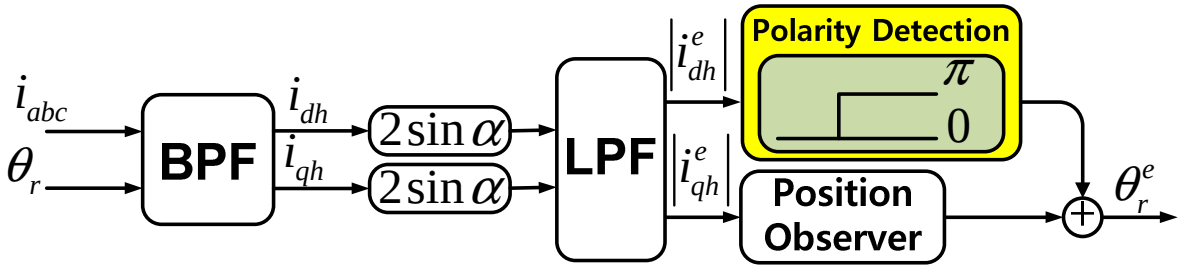


Fig. 3.16. Principle of initial rotor position detection.

Based on (3.4) and (3.5), the equation can be derived from (3.15), as shown below

$$\begin{aligned} \left|i^e_{dh}\right| &= I_p + I_n \cos(2\Delta\theta + \theta_m) \approx I_p + I_n \cos\theta_m \\ &\approx \frac{V_c}{\omega_c} \cdot \frac{L_{qh}}{L_{dh}L_{qh} - L^2_{dqh}} \end{aligned} \tag{3.30}$$

The mutual inductance can be ignored since it is usually small, $L^2_{dqh} << L_{dh}L_{qh}$. Thus, (3.31) can be simplified as

$$\left|i_{dh}^{e}\right| \approx \frac{V_c}{\omega_c} \cdot \frac{1}{L_{dh}} \tag{3.31}$$

Using the accurate rotor position information from an encoder, the *d*-axis current responses can be measured by applying different fundamental currents as shown in Fig. 3.17. It can be seen that the amplitude of the *d*-axis fundamental current response is changed at different current levels and the positive *d*-axis current is slightly higher. According to this result, the magnetic polarity can be relied on the comparison of carrier current responses at different *d*-axis fundamental current levels due to the magnetic-saturation effect. It should be noted that $i_d$ = -1A is not utilized in this method, and only to compare the peak to peak value between these different applied current.

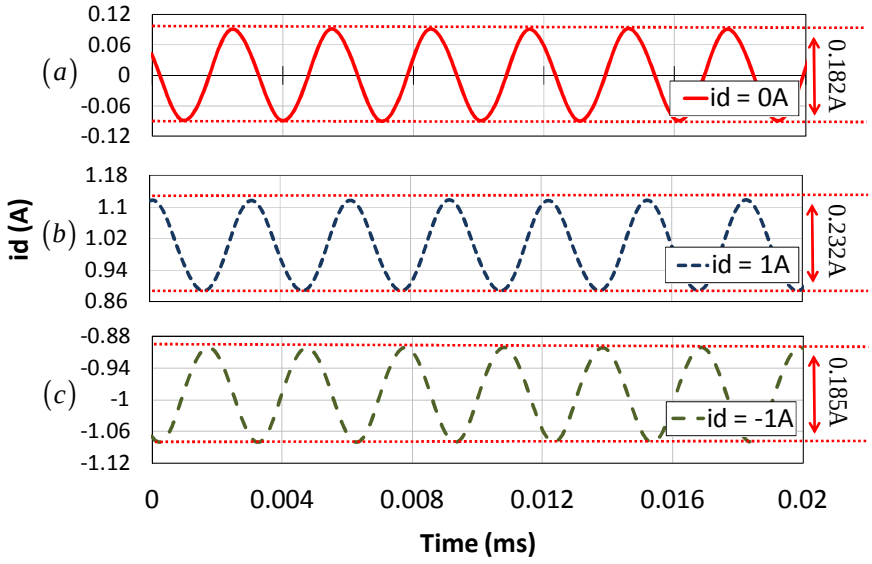


Fig. 3.17. Measured *d*-axis carrier current response at different current levels.

The procedure of magnetic polarity detection is simple and easy to implement. First of all, by applying the HF injection based techniques without fundamental excitation ($i_{df}$=0A, $i_{qf}$=0A), the rotor position information is therefore obtained and then the estimated rotor position direction is either the correct position or shifted by $\pi$ ($180^0$). Secondly, the selected reference fundamental excitation currents ($i_{df}$=1A, $i_{qf}$=0A) is applied to the prototype machine. Meanwhile, the average amplitude of *d*-axis carrier current is recorded at this load

condition. Finally, the reference fundamental excitation current has to be reset to ($i_{df}$=*0A*, $i_{qf}$=*0A*). During the whole process, the *d*-axis carrier current amplitude at different current levels are all recorded and compared. The amplitude increase of the *d*-axis carrier current suggests the estimated rotor position direction is at the correct rotor direction, otherwise, the phase shift of $\pi$ ($180^0$) has to be added.

The experimental results shown in Fig. 3.18 validate the effectiveness of the magnetic polarity detection with the aid of estimated rotor position. By applying the fundamental *d*-axis current 1A, the amplitude of *d*-axis carrier current response will reflect the magnetic polarity. In comparison, the decrease in $|i_{dh}|$ suggests that the estimated rotor position is correct without the phase shifted, as shown in Fig. 318 (a). On the other hand, the period of amplitude increase in $|i_{dh}|$ shown in Fig. 3.18 (b) detects that the phase shifted $180^0$ of the estimated rotor position need to be added the value of $\pi$ due to the magnetic saturation effect of *d*-axis fundamental excitation. The judgment of $|i_{dh}|$ for the magnetic polarity detection is described in Fig. 3.18 (c) which explains whether the polarity estimation is correct or wrong.

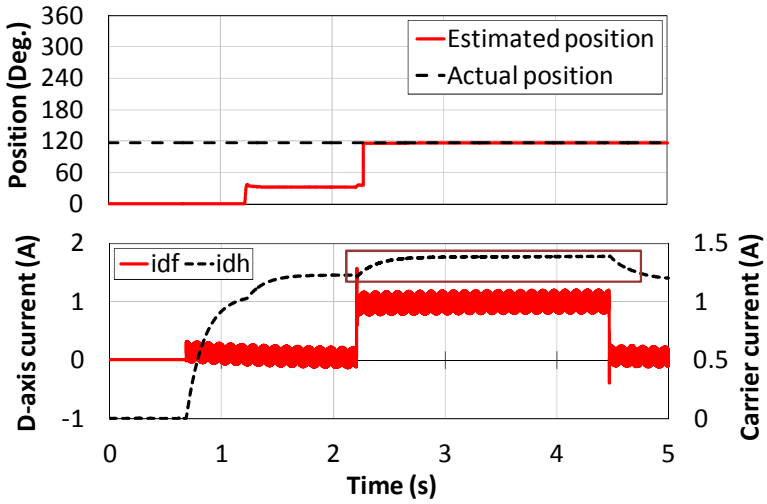


(a) With adding π, ($180^0$)

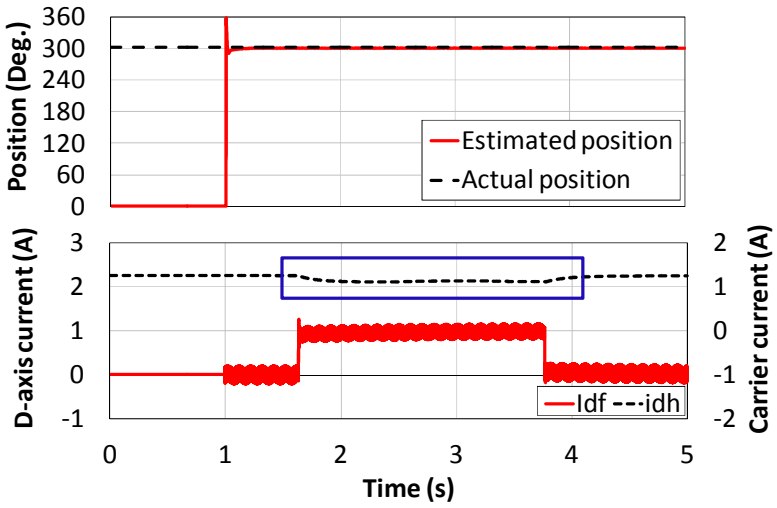


(b) Without adding π, ($180^0$)

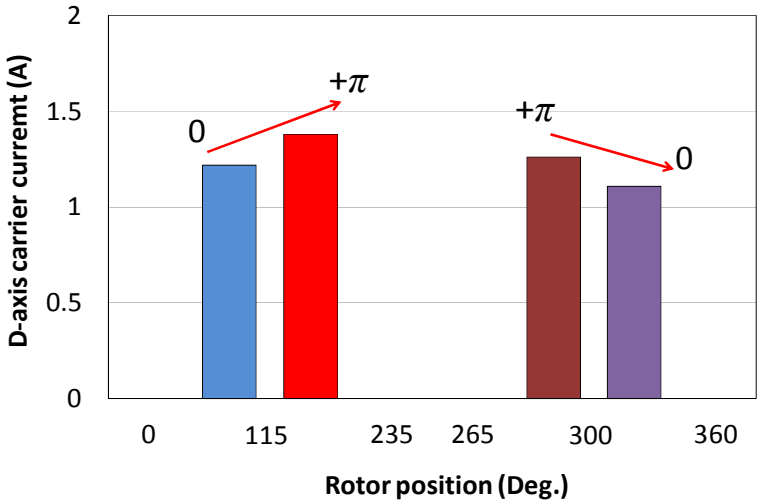


(c) Judgment of detection by $i_{dh}$

Fig. 3.18. Magnetic polarity detection, standstill.

### 3.5.2 Rotor Position Tracking Observer for Sensorless Control

For the HF carrier signal injection based sensorless control techniques, arc-tangent function ($\tan^{-1}$) [TES03] can be used to obtain the rotor position information. However, since the noise on signal input is the problem to the estimated position, the position tracking observer is better in sensorless position estimation due to its immunity to harmonics while implementing the dynamic position tracking operation. Although a nonlinear controller has proposed [JAN04] to improve the dynamic performance, it has a drawback in steady-state response. Hence, the linear controller is employed in sensorless position observer in this chapter

[HAR00] [CUP10].

Using the signal $f(\Delta\theta)$ as the input to the position observer for the rotating and pulsating voltage signal injections, the basic principle of position observer using the PI controller is described in Fig. 3.19.

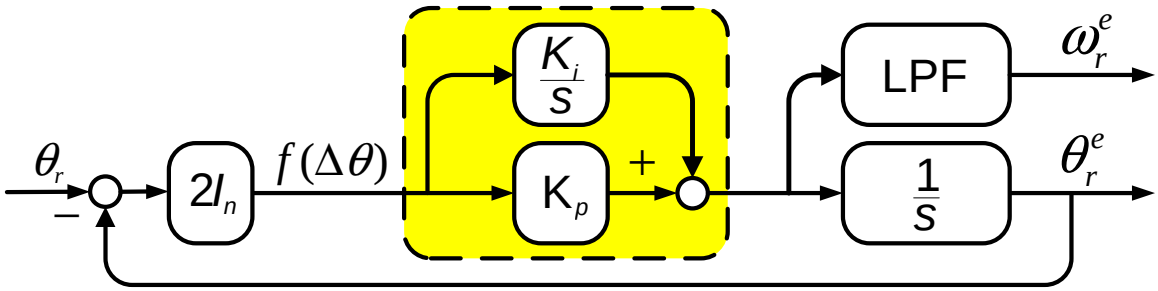


Fig. 3.19. Rotor position tracking observer.

In terms of the rotor position estimation, the rotor position tracking observer considering the cross-saturation compensation is therefore employed and its basic principle is described in Fig. 3.19. Taking the amplitude of $q$-axis carrier current response as the input to the position observer for both the rotating and pulsating voltage signal injections which can be expressed as

$$f\left(\Delta\theta\right)=\left|i_{qh}^{e}\right|=I_n\sin\left(2\Delta\theta+\theta_m\right) \tag{3.32}$$

As mentioned earlier, when the cross-saturation effect is negligible, $\theta_m$ is almost close to zero, and then the rotor position can be estimated accurately in which the load-dependent estimated error ($-\theta_m/2$) is compensated [ZHU11][LI09].

To obtained the estimated rotor position, the transfer function between the actual and the estimated rotor position information according to Fig. 3.19, can be derived as

$$\frac{\theta_r^e}{\theta_r}=\frac{2I_nk_p\cdot s+2I_nk_i}{s^2+2I_nk_p\cdot s+2I_nk_i} \tag{3.33}$$

Since $I_n$ is load-dependent, the values of $k_p$ and $k_i$ of PI controller need to be on-line

adjusted with $I_n$ in order to maintain the constant bandwidth. Also, $k_p$ and $k_i$ could be selected based on the value of $I_n$ on no load condition.

## 3.6 Experimental Validation of Sensorless Operation Capability

To evaluate the sensorless control capability, several experiments are carried out on a dSPACE platform. The Test Machine-I is the prototype SPM machine as introduced in Chapter 2, and the parameters are listed in Table 2.2. The load machine is a brushed DC machine, and an encoder with resolution of 2048PPR is equipped on the test rig to provide the actual rotor position to dSPACE. Both the A/D current-sampling and inverter pulse-width-modulation switching frequencies are 10 kHz, which is the same as the current sampling frequency and The DC bus voltage is 50V.

With the aid of theoretical analysis and experimental measurements in the investigation of machine saliency, it clearly explains that the machine saturation-induced saliency is not too large, but still suitable for implementing the high-frequency carrier voltage signal injection-based sensorless control methods. Hence, the overall control strategy of high-frequency carrier signal injection methods such as pulsating or rotating carrier signal injection is applied to the SPM machine as shown in Fig. 3.20 in order to validate the sensorless control capability. A high-frequency carrier voltage signal with a magnitude of 10V, and frequency of 330Hz, is selected for the prototype machine used in this chapter, and is injected into the stationary reference frame or estimated synchronous reference frame. It is then utilized to obtain the saliency-dependent carrier response current, the estimated rotor position information is therefore obtained.

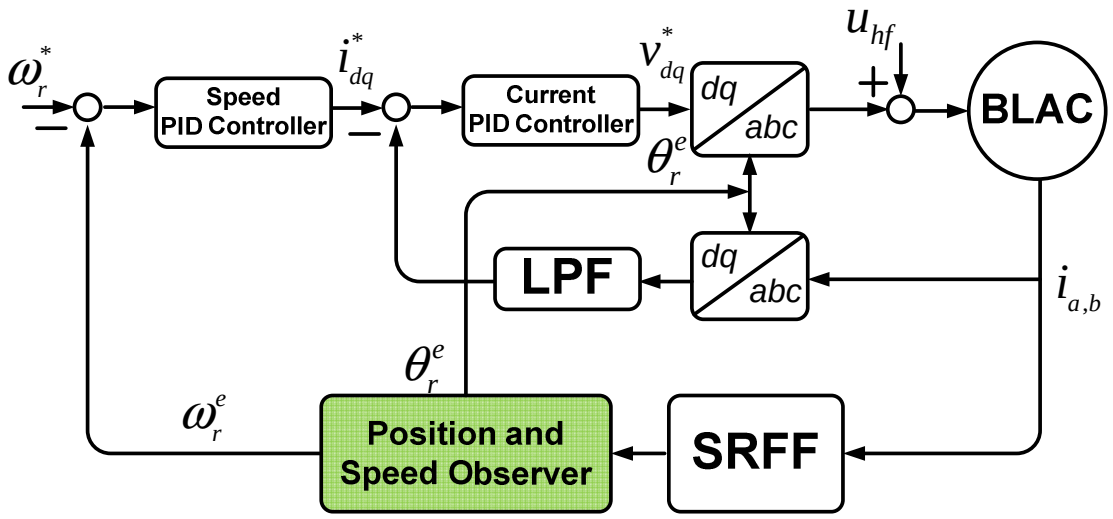


Fig. 3.20. Overall control scheme based on high-frequency carrier voltage signal injection techniques.

### 3.6.1 Rotor Position Estimations in Steady and Dynamic States

In order to validate the effectiveness of sensorless operation, the high-frequency carrier signal injection techniques are applied to the prototype machine. The negative rotor saliency is utilized to detect the rotor position for rotating carrier signal injection, which is rotor position dependent. Similarly, the pulsating carrier signal injection is based on both saliency components for positive and negative carrier signals in the estimated rotor frame.

According to the experimental results in Fig. 3.21, the estimated rotor position shows a good position tracking performance considering the cross-saturation compensation for both rotating and pulsating carrier injections at constant speed, 50 r/min. As it can be clearly seen in Figs. 3.21 (a) and (b), the magnitude of the estimated rotor position oscillation error in steady state from the rotating carrier voltage signal injection is bigger than that obtained by the high-frequency pulsating carrier voltage signal injection method.

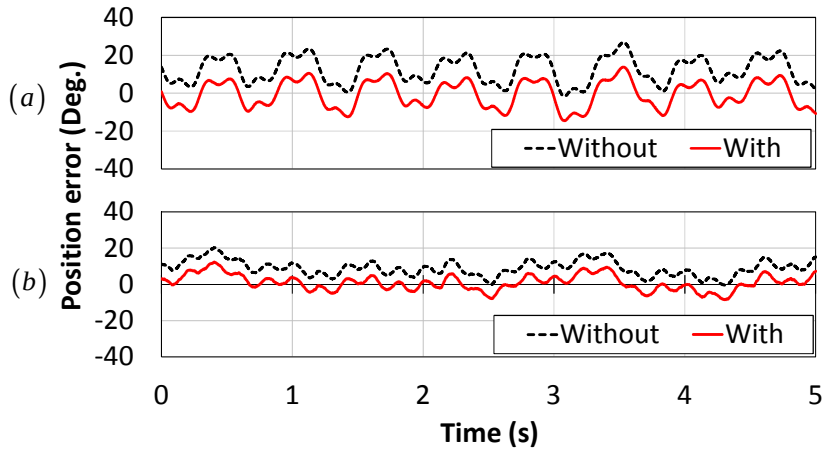


Fig. 3.21. Rotor position estimation with cross-saturation compensation, 50r/min. (a) Rotating carrier voltage signal injection. (b) Pulsating carrier voltage signal injection.

Although the estimated rotor position error is larger by applying the high-frequency rotating carrier voltage signal injection method, the distortion of the estimated rotor position error occurs under the same load condition as that of pulsating carrier voltage signal injection method. The average saliency ratio is suitable to enable the rotor position estimation to be less sensitive to rotor information detection.

The experimental tests on dynamic performance are carried out when the speed command changes from the rotor initial speed 0 r/min and step-change in rotor speed to 25 r/min and then 50 r/min, as demonstrated in Figs. 3.22 (a) and (c). The estimated and actual rotor positions, as well as the position estimation error, are obtained by applying the high-frequency rotating and pulsating carrier voltage signal injection methods as shown in Figs. 3.22 (b) and (d). Although the estimated position error reaches up to $\pm 60^0$ during the dynamic transient process, the estimation position error can still be limited to $\pm 20^0$ in steady state on no-load as presented in Fig. 3.22 (b). Furthermore, the dynamic performance of pulsating carrier signal injection technique is better than the rotating carrier signal injection strategy in terms of the accuracy of rotor position estimation, as compared in Figs. 3.22 since its estimated position error is significantly small in both steady ($\pm 5^0$) and dynamic transient

($\pm 10^0$) states which is clearly presented in Fig. 3.22 (d).

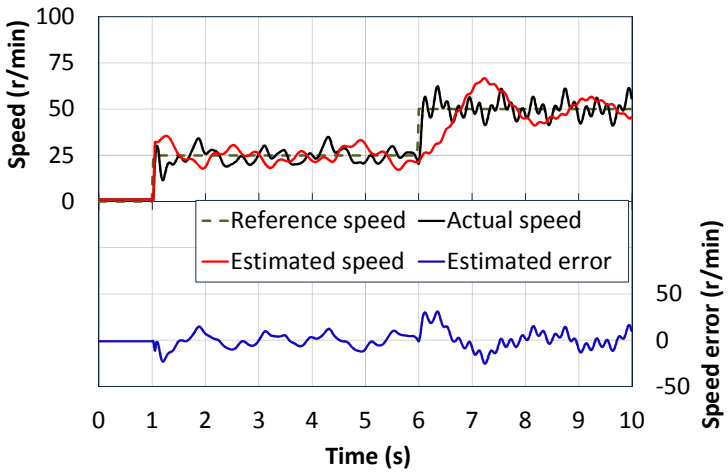


(a) Rotating injection-speed

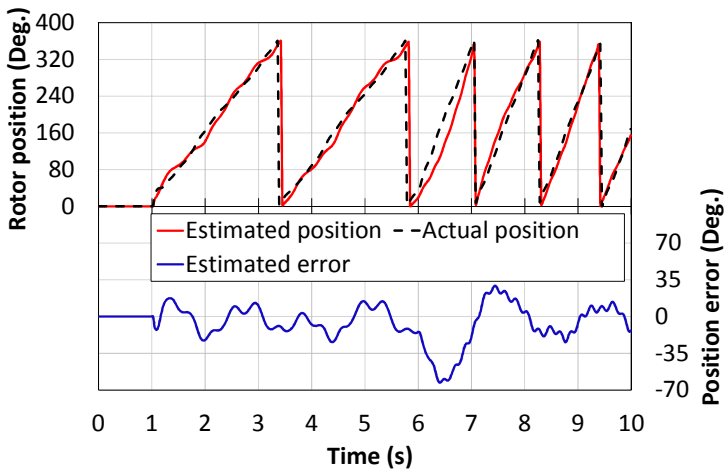


(b) Rotating injection-position

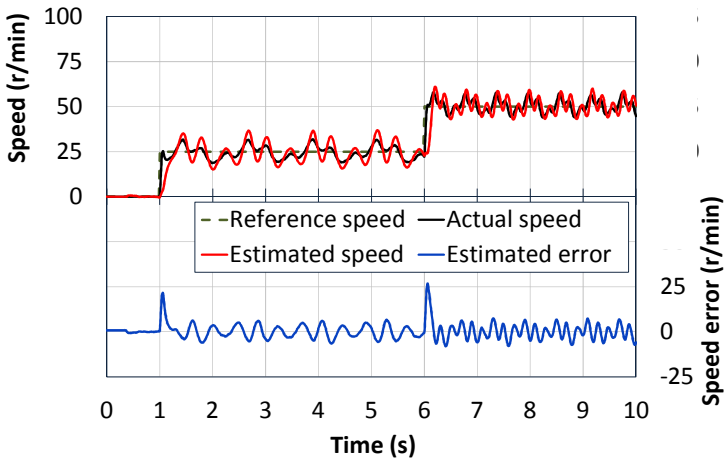


(c) Pulsating injection-speed

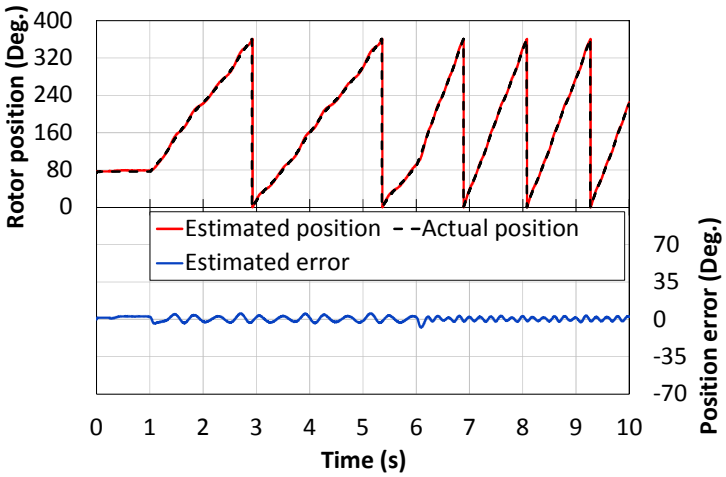


(d) Pulsating injection-position

Fig. 3.22. Rotor position and speed estimation in dynamic state, 0-25-50 r/min.

In Fig. 3.23, the dynamic performance under the step-load change condition is applied to the prototype machine where the *q*-axis current is step changed from, 0.2A to 4A, and then back 0.2A for both HF injection techniques, 100 r/min, under full load condition. The experimental results prove that the sensorless capability of prototype SPM machine is applicable for the high frequency inductance-based methods.

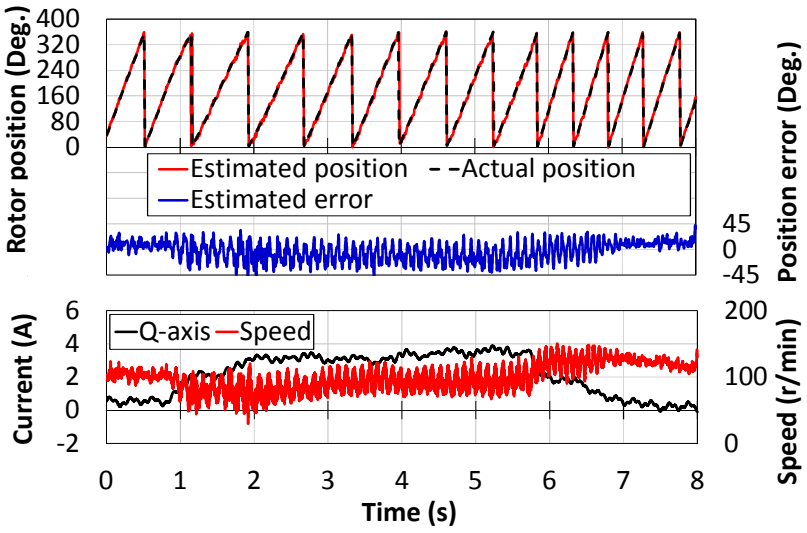


(a) Rotating carrier voltage signal injection

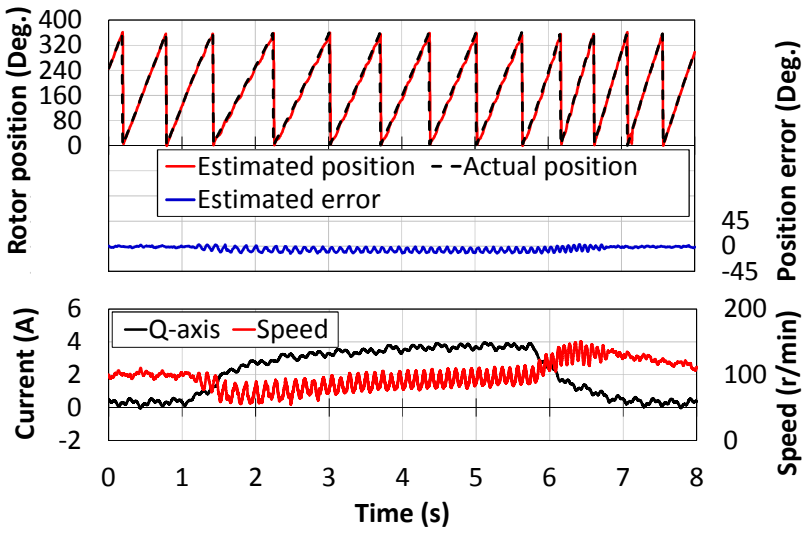


(b) Pulsating carrier voltage signal injection

Fig. 3.23. Rotor position and speed estimation in dynamic step-load change state, 100 r/min.

### 3.6.2 Different Injection Frequency and Load Effects

Fig. 3.24 compares the saliency-induced carrier current responses with different injected carrier frequencies and fixed injection voltage ($V_c$=10V) at fixed position ($\theta$=$0^0$). It is demonstrated that the amplitude of $q$-axis carrier current is reduced as the carrier frequency increases due to the increase of impedance [JAN04].

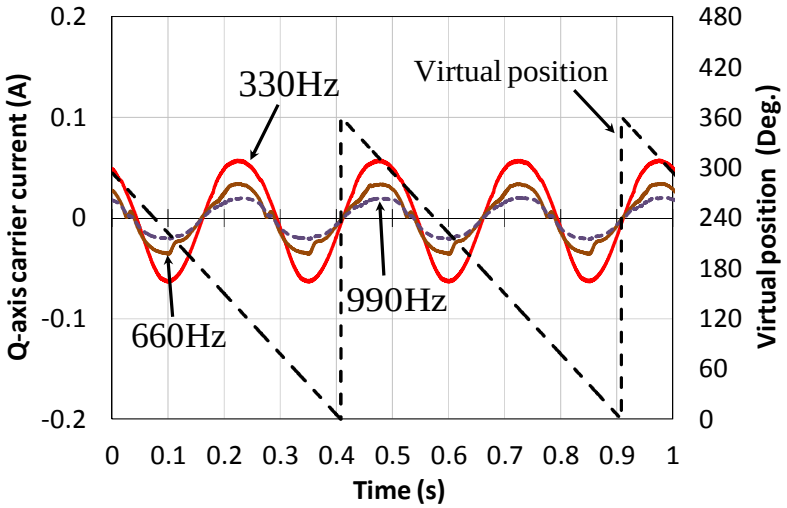


Fig. 3.24. Comparison of saliency-induced carrier current based on different injection frequencies with virtual position (zero speed, $V_c$ = 10V).

Furthermore, the comparison of rotor position estimation errors between rotating and pulsating carrier voltage signal injections based on different injection frequency and load conditions are shown in Fig. 3.25. It is shown that how different levels of injected carrier frequency and fundamental excitations cause the errors in the rotor position estimation. In Fig. 3.25 (a), it can be concluded that the higher the injection frequency, the higher the rotor position estimation error due to the digital sampling delay [KOC09] [GHA13]. In Fig. 3.25 (b), the estimation errors due to saturation-induced saliency occur under different levels of fundamental excitations. The estimation error increases with fundamental current level because of the multiple saliency effect [OVR04] [FRE05] [DEG98].

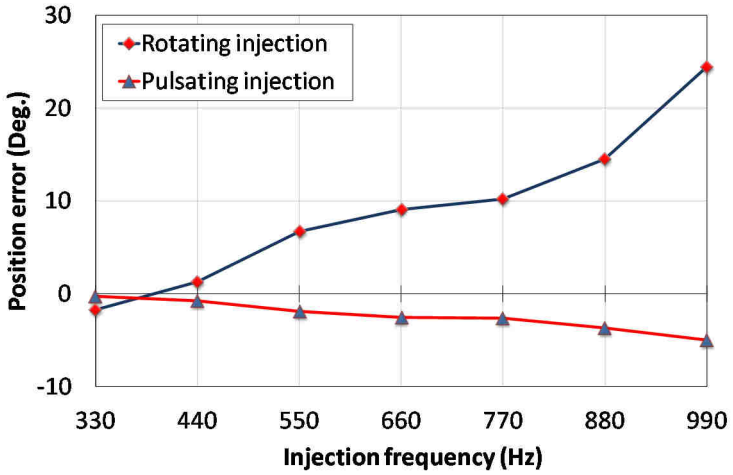


(a) Different frequency conditions on no load

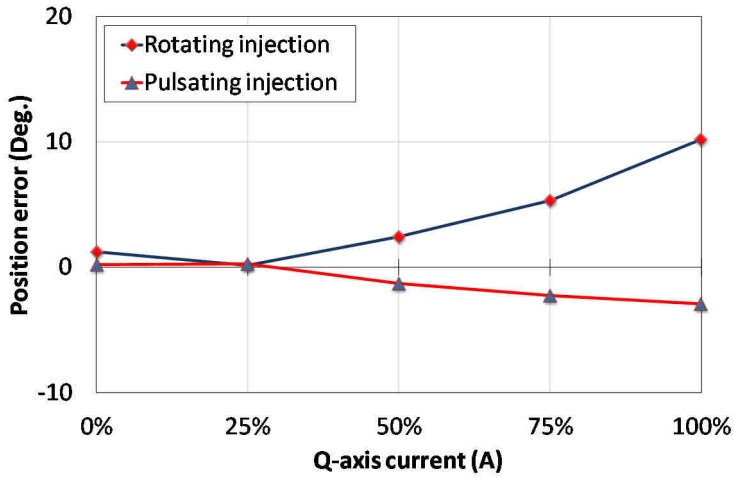


(b) Different load conditions

Fig. 3.25. Comparison of electrical rotor position estimation errors.

## 3.7 Conclusion

In this chapter, the potential operation of capability of a SPM machine to be used with sensorless control at zero and low speed has been systematically investigated. The prototype SPM machine is tested by the saturation-induced saliency method and the resistance-based saliency method is also considered, in terms of the sensorless position estimation.

The variation of machine saliency level against load is experimentally measured, and indicates that the saliency level is suitable for the HF techniques. Additionally, by analyzing the influence of HF eddy-current loss reflected-resistance, the total HF iron losses are much smaller than the machine tested in [YAN12a] [YAN12b] due to large equivalent air-gap length, and can be negligible.

Furthermore, the effectiveness of the sensorless capability is validated under different operating conditions, i.e. steady and dynamic states considering the cross-saturation compensation with and without load.

## References


[AIH99] T. Aihara, A. Toba, T. Yanase, A. Mashimo, and K. Endo, “Sensorless torque control of salient-pole synchronous motor at zero-speed operation,” *IEEE Trans. Power Electron.*, vol. 14, no. 1, pp.202-208, January 1999.

[CUP10] F. Cupertino, P. Giangrande, L. Salvatore and G. Pellegrino, “Model based design of a sensorless control scheme for permanent magnet motors using signal injection,” *IEEE Energy Conversion Congress and Exposition* (ECCE), 2010, pp. 3139-3146.

[DEG98] M. Degner and R. Lorenz, “Using multiple saliencies for the estimation of flux, position, and velocity in ac machines,” *IEEE Trans. Ind. Appl.*, vol. 34, no. 5, pp. 1097–1104, Sep./Oct. 1998.

[FRE05] T. Frenzke, “Impacts of cross-saturation on sensorless control of surface

permanent magnet synchronous motors," in *Proc. Eur. Conf. Power Electron. Appl.*, 2005, pp. 1–10.

[GON11] L.M. Gong and Z.Q. Zhu, "A novel method for compensating inverter nonlinearity effects in carrier signal injection-based sensorless control from positive-sequence carrier current distortion," *IEEE Trans. Ind. Appl.*, vol. 47, no. 3, pp. 1283-1292, 2011.

[GON13] L. Gong, and Z.Q. Zhu, "Robust initial rotor position estimation of permanent magnet brushless AC machines with carrier signal injection-based sensorless control" *IEEE Trans. Ind. Appl.*, vol. 49, no. 6, pp. 2602-2609, Nov./Dec., 2013.

[HAR00] L. Harnefors and H.P. Nee, "A general algorithm for speed and position estimation of AC motors," *IEEE Trans. Ind. Electron.*, vol. 47, no. 1, pp. 77-83, 2000.

[HOL08] J. Holtz, "Acquisition of position error and magnet polarity for sensorless control of PM synchronous machines," *IEEE Trans. Ind. Appl.*, vol. 44, no. 4, pp. 1172–1180, 2008.

[JAN04] J.H. Jang, J.I. Ha, M. Ohto, K. Ide, and S.K. Sul,, "Analysis of permanent-magnet machine for sensorless control based on high-frequency signal injection," *IEEE Trans. Ind. Appl.*, vol. 40, pp. 1595-1604, Nov./Dec., 2004.

[JAN04] J.H. Jang, J.I. Ha, M. Ohto, K. Ide, and S.K. Sul,, "Analysis of permanent-magnet machine for sensorless control based on high-frequency signal injection," *IEEE Trans. Ind. Appl.*, vol. 40, pp. 1595-1604, Nov./Dec., 2004.

[JEO05] Y.S. Jeong, R.D. Lorenz, T.M. Jahns, and S.K. Sul, "Initial rotor position estimation of an interior permanent-magnet synchronous machine using carrier-frequency injection methods," *IEEE Trans. Ind. Appl.*, vol. 41, no.1, pp. 38 – 45, 2005.

[KIM04] H. Kim and R.D. Lorenz, "Carrier signal injection based sensorless control methods for IPM synchronous machine drives," *Proc. of IEEE-IAS Annual Meeting*, Vol. 2, pp.977 – 984, Oct. 2004.

[KOC09] W.H. De Kock, M.J. Kamper, R.M. Kennel, "Anisotropy comparison of reluctance and PM synchronous machines for position sensorless control using HF carrier injection," *IEEE Trans. Power Electron.*, vol.24, no.8, pp.1905-1913, 2009.

[LEI11] R. Leidhold, "Position sensorless control of PM synchronous motors based on zero-sequence carrier injection," *IEEE Trans. Ind. Electron.*, vol. 58, no. 12, pp. 5371–5379, Dec. 2011.

[LI09] Y. Li, Z.Q. Zhu, D. Howe, C.M. Bingham, and D. Stone, “Improved rotor position estimation by signal injection in brushless AC motors, accounting for cross-coupling magnetic saturation,” *IEEE Trans. Ind. Appl.*, vol.45, no.5, pp.1843-1849, 2009.

[OVR04] S. Ovrebo, “Control of Permanent Magnet Synchronous Machines”, Ph.D. dissertation, Dept. of Electrical Power Engineering, Norwegian University of Science and Technology (NTNU), Trondheim, 2004.

[RAC08] D. Raca, P. Garcia, D.D. Reigosa, F. Briz and R.D. Lorenz, “A comparative analysis of pulsating vs. rotating vector carrier signal injection-based sensorless control,” *IEEE Applied Power Electronic Conference and Exposition* (APEC) 2008, pp.879 – 885, Feb. 2008.

[YAN12a] S.-C. Yang, and R. D. Lorenz, “Surface permanent magnet synchronous machine self-sensing position estimation at low speed using eddy current reflected asymmetric resistance,” *IEEE Trans. Power Electron.*, vol. 27, no. 5, pp. 2595–2604, May 2012.

[YAN12b] S.-C. Yang and R. D. Lorenz, “Comparison of resistance-based and inductance-based self-sensing controls for surface permanent-magnet machines using high-frequency signal injection,” *IEEE Trans. Ind. Appl.*, vol.48, no.3, pp.977-986, May-June 2012.

[ZHU07] Z.Q. Zhu, Y. Li, D. Howe, and C.M. Bingham, “Compensation for rotor position estimation error due to cross-coupling magnetic saturation in signal injection based sensorless control of PM brushless AC motors,” *Electric Machines & Drives Conference, 2007. IEMDC '07. IEEE International,* vol. 1, 2007, pp. 208 – 213

[ZHU11] Z.Q. Zhu and L.M. Gong, “Investigation of effectiveness of sensorless operation in carrier signal injection based sensorless control Methods,” *IEEE Trans. Ind. Electron.*, vol. 58, no. 8, pp. 3431-3439, Aug., 2011.

[ZHU97] Z.Q. Zhu, K. Ng, and D. Howe, “Design and analysis of high-speed brushless permanent magnet motors,” *Electrical Machines and Drives, 1997 Eighth International Conference* on (Conf. Publ. No. 444), pp.381-385, 1-3 Sep 1997.

[GHA13] M.A Ghazi Moghadam, and F. Tahami, “Sensorless control of PMSMs with tolerance for delays and stator resistance uncertainties,” *IEEE Trans. Power Electron.*, vol.28, no.3, pp.1391-1399, March 2013.

# CHAPTER 4

# INVESTIGATION OF MACHINE SALIENCY IN SWITCHED-FLUX PERMANENT MAGNET MACHINE USING HIGH-FREQUENCY SIGNAL INJECTION

## 4.1 Introduction

In order to facilitate the selection of a machine as to whether it is suitable for high-frequency signal injection-based sensorless control or not. This chapter describes a complete experimental investigation method for the analysis and validation of machine saliency level, including primary saliency which is essential for high-frequency injection-based sensorless control and the secondary saliency which will deteriorate the rotor position estimation.

Therefore, a model of high-frequency carrier voltage signal injection is applied to the prototype SFPM machine (Test Machine-II) based on practical implementation to show the importance of the machine saliency to the HF injection-based sensorless control. In order to investigate the machine saliency level of SFPM machine with unknown machine parameters, a simple experimental investigation method is proposed to measure the spatial saliency level and multiple saliencies information in this chapter. Firstly, a pulsating vector voltage carrier signal is injected into the virtual synchronous reference frame which rotates at a fixed angular speed when the rotor is locked at zero position, and then, according to the current response, the machine saliency circles which indicate the full information of the machine saliency at no load or different load conditions, can be easily obtained. Meanwhile, a secondary spatial saliency is measured with the aid of actual rotor position information from an encoder to investigate its influence on the estimation of rotor position for sensorless control operation.

Thus, the influence of the primary and secondary saliencies of the prototype SFPM machine on the HF injection-based sensorless control performance can be fully investigated without the need of any information of parameter values for the first time.

The effectiveness of the proposed experimental method and investigation will be proved by the several experiments on a dSPACE platform with a laboratory SFPM machine. In addition, the sensorless current and speed control based on HF pulsating voltage signal injection will be implemented to verify the results of the saliency investigation.

## 4.2 Investigation of Primary Machine Saliencies

### 4.2.1 Saliency Information of Permanent Magnet Machine

In general, when the carrier frequency is significantly higher than the fundamental excitation frequency, a PM machine behaves as a pure inductive load. Then, the high-frequency voltage model for a PM BLAC machine in the synchronous reference frame can be simplified as (3.20). The definition of these HF inductances are given as

$$\begin{cases} L_{dh} = \left[ \psi_d^r \left( i_d^r + \Delta i_d^r, i_q^r \right) - \psi_d^r \left( i_d^r, i_q^r \right) \right] / \Delta i_d^r \\ L_{qh} = \left[ \psi_q^r \left( i_d^r, i_q^r + \Delta i_q^r \right) - \psi_q^r \left( i_d^r, i_q^r \right) \right] / \Delta i_q^r \\ L_{dqh} = \left[ \psi_d^r \left( i_d^r, i_q^r + \Delta i_q^r \right) - \psi_d^r \left( i_d^r, i_q^r \right) \right] / \Delta i_q^r \\ L_{qdh} = \left[ \psi_q^r \left( i_d^r + \Delta i_d^r, i_q^r \right) - \psi_q^r \left( i_d^r, i_q^r \right) \right] / \Delta i_d^r \end{cases} \tag{4.1}$$

Normally, $L_{dqh}$ and $L_{qdh}$ are different from each other and related with the cross-saturation effect. However, in most practical applications, $L_{dqh}$=$L_{qdh}$ is considered for simplifying the analysis. Meanwhile, $L_{dh}$ and $L_{qh}$ are also different due to the rotor geometric and magnetic saturation, and the difference between them which is $L_{qh}$-$L_{dh}$ indicates the saliency level of the machine. Since all HF signal injection-based sensorless control depends on the saliency-dependent corresponding, if the information of $L_{qh}$-$L_{dh}$ is constant and large enough at a given load condition, and independent on the rotor position, then the machine would be

suitable for HF injection-based sensorless control. Even though $L_{dh}$ and $L_{qh}$ can be measured by injecting HF voltage signal in advance, due to the variation at different mechanical rotor position and different fundamental excitation currents, it is too complicated to operate. Therefore, to analyze the saliency of the prototype SFPM machine, a simple experimental investigation is proposed as follows.

### 4.2.2 Analysis of Primary Saliency

To investigate the machine saliency, a virtual synchronous reference frame which has a $\Delta\theta$ phase angle difference from the actual synchronous reference frame as shown in Fig. 3.9, is developed. Then, with the aid of transformation matrix $T(\Delta\theta)$ which is (3.19). The high frequency voltage model of SFPM machine in virtual synchronous reference frame can be derived from the model in actual synchronous reference frame which is shown in (3.20), i.e. [CUP11] into (3.21). Solving equation (3.21), the differential of the high frequency carrier current response in virtual synchronous reference frame will be (3.23).

Then inject a HF pulsating carrier voltage vector (4.2) into the virtual synchronous reference frame,

$$\begin{bmatrix} v_{dh}^{vr} \\ v_{qh}^{vr} \end{bmatrix} = V_c \begin{bmatrix} \cos\alpha \\ 0 \end{bmatrix}, \alpha = \omega_c t + \varphi \tag{4.2}$$

where $V_c$, $\omega_c$ and $\varphi$ are the amplitude, angular speed and initial phase angle of the injected carrier voltage, respectively. Then, the HF response current in virtual synchronous reference frame is derived as (3.24).

Based on (3.5), (3.6), and (3.16), and assuming $L_{dqh}$ is small enough, $I_n$ could be rewritten as

$$I_n = \frac{V_c}{\omega_c \dfrac{L_{dh}L_{qh} - L_{dqh}^2}{\sqrt{L_{sd}^2 + L_{dqh}^2}}} \approx \frac{V_c}{\omega_c} \frac{L_{sd}}{L_{dh}L_{qh}} \tag{4.3}$$

Hence, due to pre-defined and constant injected voltage ratio of $U_c/\omega_c$, $I_n$ will be proportional to $L_{sd}$ which is the difference of $q$- and $d$-axis incremental inductances, and can directly reflect the machine saliency level.

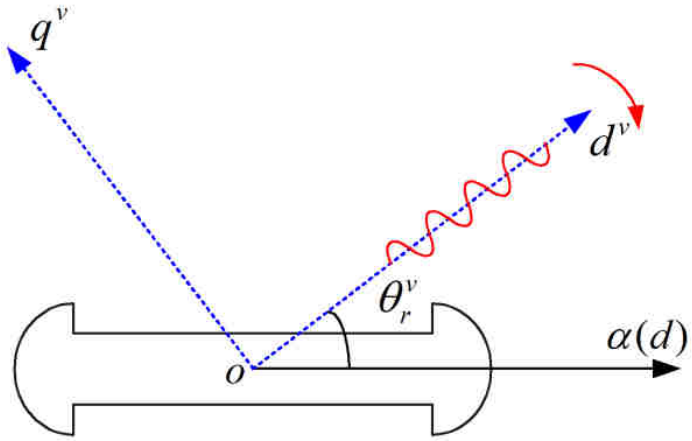


Fig. 4.1. Experimental method for Machine saliency investigation.

The block diagram to investigate the saliency level as shown in Fig. 3.10 is implemented. When the rotor of the SFPM machine i.e. actual synchronous reference frame is locked at a fixed rotor position and the virtual synchronous reference frame is rotating at a constant angular speed, Fig. 4.1, then the high frequency $d$- and $q$-axis current responses will have the same phase angle, and the amplitude of response current is modulated by the position difference $\Delta\theta$ between virtual and actual synchronous reference frames as illustrated in Fig. 4.2 (a).

Then, applying the synchronous detection technique, the amplitude of HF response current which is position difference dependent, is obtained as shown in Fig. 4.2 (b) by (3.25). Moreover, the locus of the amplitude is depicted in Fig. 4.2 (c) where the radius of the current locus which is $I_n$ indicates the saliency level. If the radius is constant and clearly identified, then the SFPM machine is suitable for HF injection-based sensorless control.

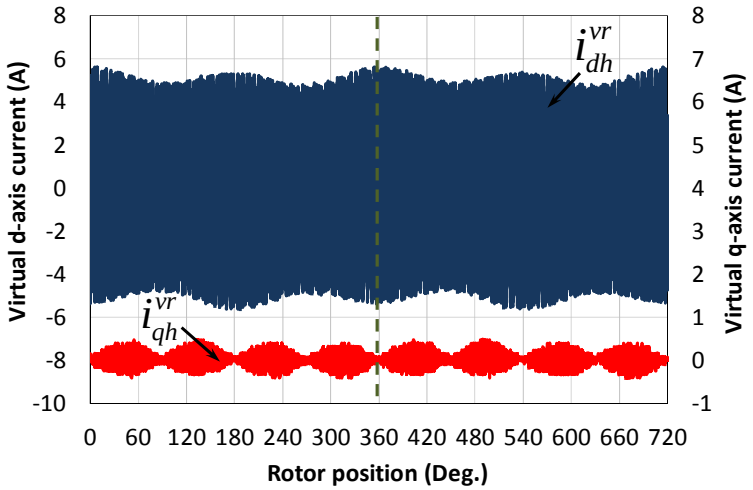


(a) Measured response current

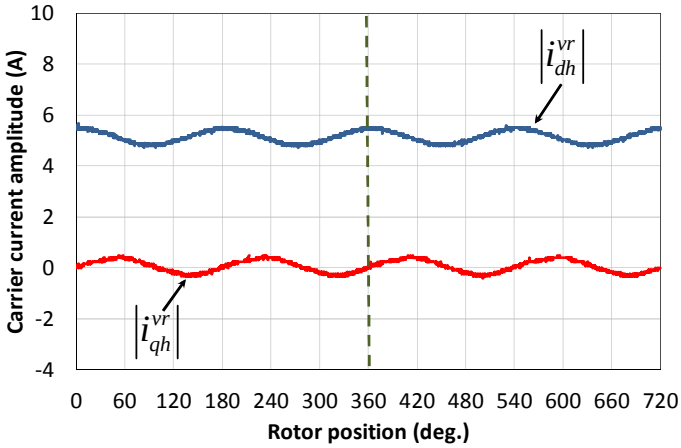


(b) Variation of HF response current amplitude

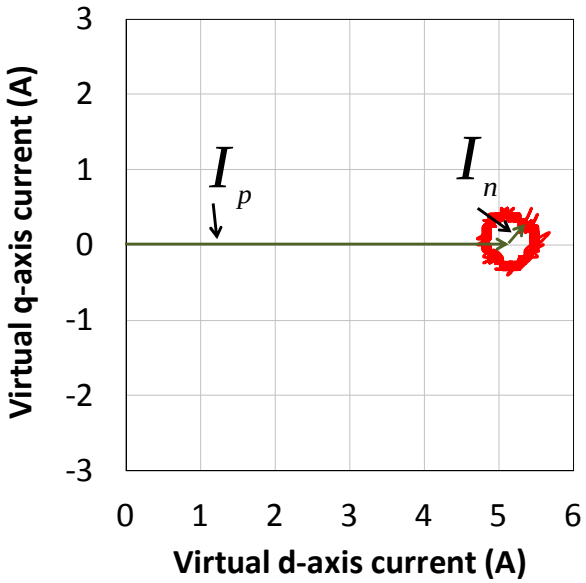


(c) Locus of carrier current circle by machine saliency

Fig. 4.2. Measured HF current response in virtual *d-q* reference frame.

### A. Experimental Evaluation of Primary Machine Saliency

From the foregoing theoretical analysis of primary saliency, the rotor is locked at zero position ($\theta_r$ = 0 deg.), thus the phase angle of the virtual synchronous reference frame is the phase angle difference $\Delta\theta$. Then, a pulsating voltage sinusoidal signal (4.6) with amplitude of 8V and frequency of 550Hz is injected into the virtual synchronous reference frame ($d^{vr}$-$q^{vr}$), which rotates at a constant speed of 2Hz in the negative direction, as shown in Fig. 4.1, without applying fundamental excitation. Further, the measured amplitude of carrier current using synchronous detection technique (3.25) is shown in Fig. 4.3. From Fig. 4.3 (a) that when the position difference is $0^o$ or $180^o$, the *d*-axis current amplitude reaches the maximum value, while the amplitude of *q*-axis current is close to zero, which indicates that the cross-saturation angle $\theta_m$ is close to zero and the cross-saturation effect is negligible at unloaded condition.

Furthermore, the carrier current amplitude is modulated as two cycles per single electrical cycle of position which defines the angle of $180^o$ in sensorless rotor position estimation, as shown in Fig. 4.3 (a). The locus of $d^{vr}$-$q^{vr}$ carrier current amplitude variations is depicted in Fig. 4.3 (b), where the value of $I_p$ is used to determine the center location of the carrier current circle and the radius of carrier current circle is dependent on $I_n$. Based on the previous analysis, the radius of the locus cycle $I_n$ is proportional to $L_{sd}$ which is the difference of *q*- and *d*-axis incremental inductances, and contains the full machine saliency information. Hence, the scale of the carrier current circle can be explained as the machine saliency level.

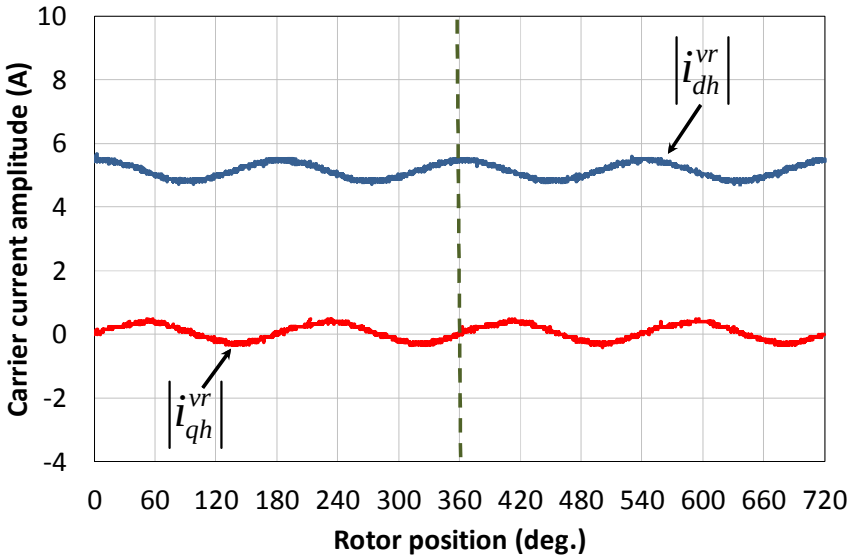


(a) Variation of HF carrier current amplitude

8

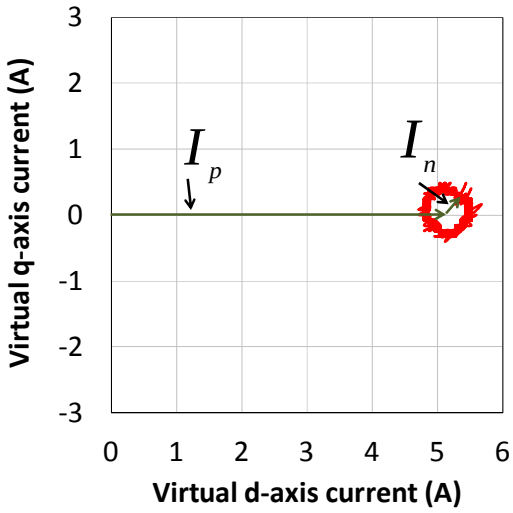


(b) Locus of carrier current circle by machine saliency

Fig. 4.3. Measured carrier current amplitude variation with position difference at no-load (without fundamental excitation, $i_d$=0A, $i_q$=0A).

The machine saliency information at different load conditions have been investigated by applying fundamental excitation current to the prototype Test-Machine II, as drawn in Fig. 4.4. The measured experimental results shown the saliency level is different at each fundamental excitation current level. Meanwhile, the positive *q*-axis current leads to the higher saliency level, which gives more benefits for saliency-based sensorless control

methods.

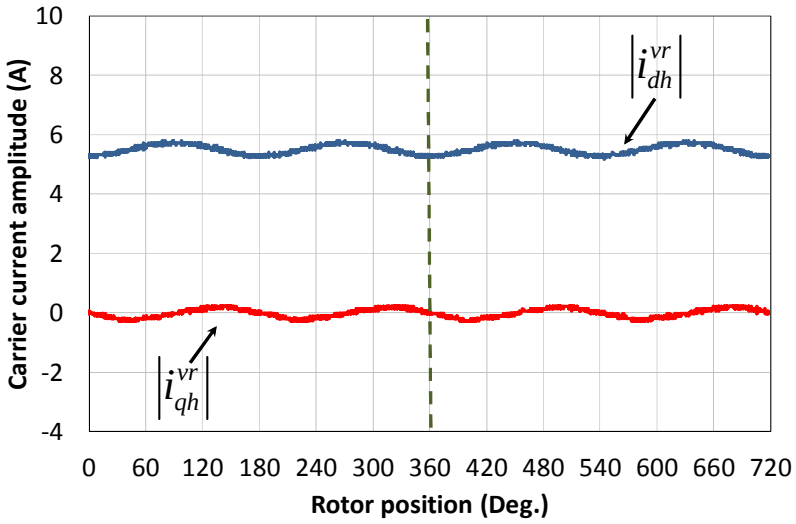


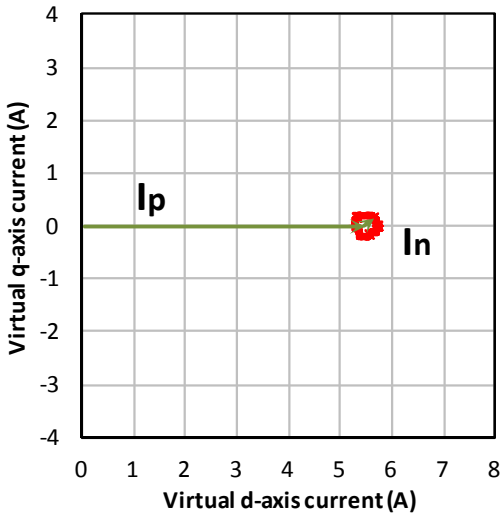


(a) $i_d$ = 3A, $i_q$ = 0A

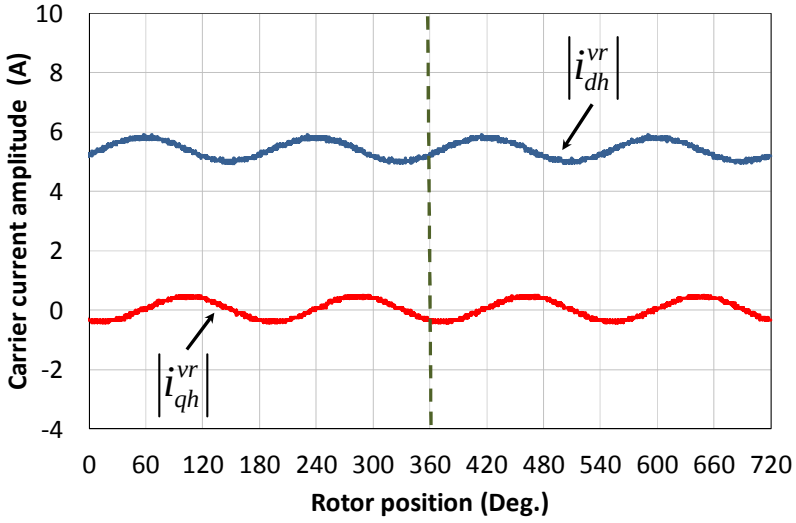

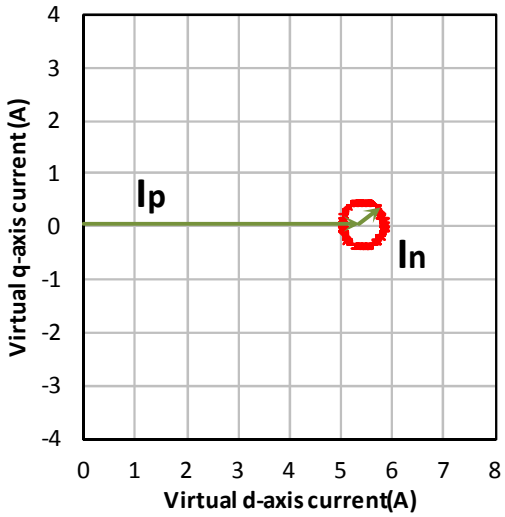


(b) $i_d$ = 6A, $i_q$ = 0A

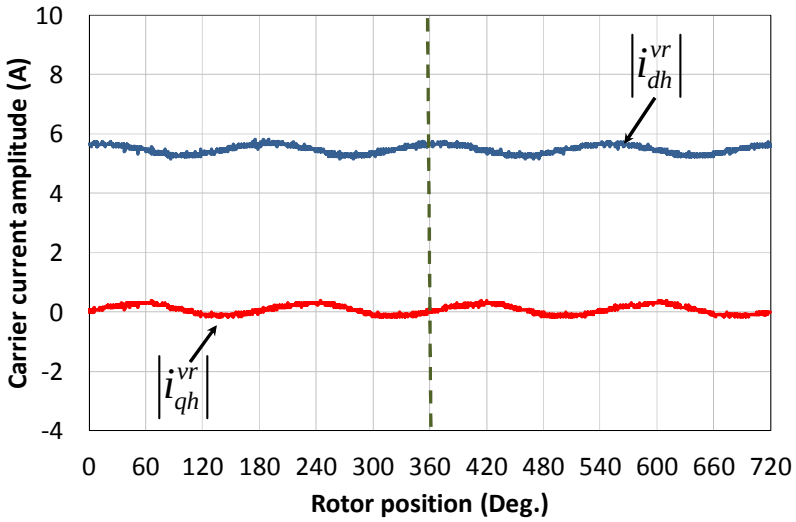


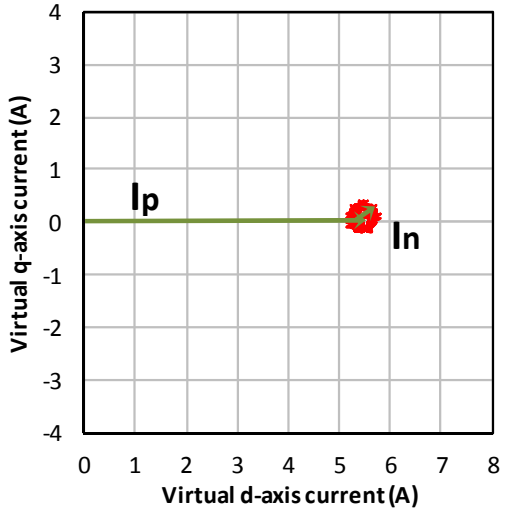


(c) $i_d$ = 0A, $i_q$ = 3A

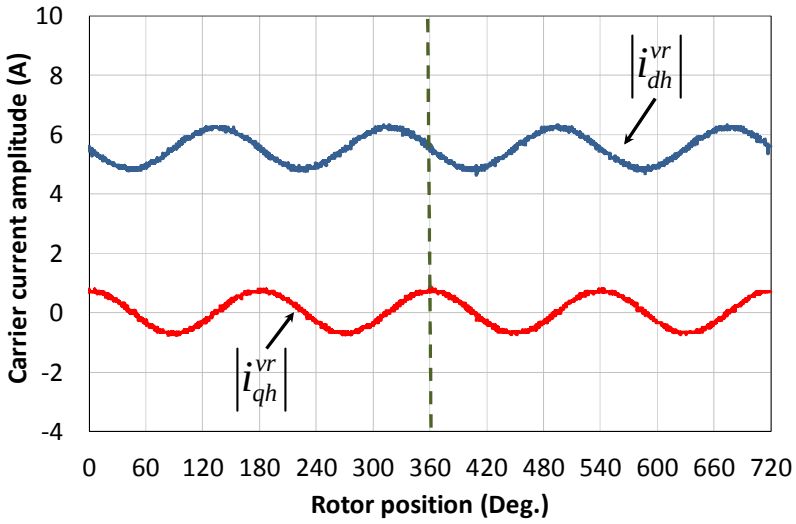


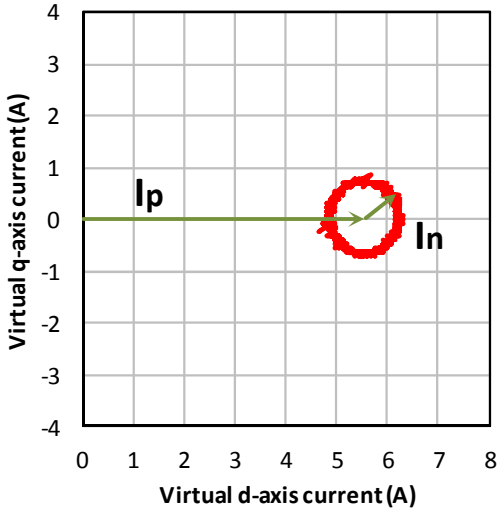


(c) $i_d$ = 0A, $i_q$ = 6A

Fig. 4.4. Measured HF carrier current responses under different load conditions.

### 4.2.3 Analysis of Secondary Saliency (Multiple Saliencies Effect)

The machine primary saliency investigation discussed in the previous section only relates to the existence of a single spatial machine saliency, which is described as primary saliency and essential for the sensorless rotor position estimation. Due to some problems of practical design to PM machine, such as slotting and magnetic saturation etc… [HOL98] [KIM04], however, there may introduce other harmonic components which can be referred as secondary saliency [DEG98] and adding the primary and secondary saliency together that is

represented as the multiple saliencies effect. Hence, when the high-frequency voltage signal is injected into the machine, the additional carrier current components would occur corresponding to the secondary saliency. Unlike the cross-saturation effect, which produces a constant error in the estimated position information at a given load condition, the estimation error caused by multiple saliencies varies with rotor position, which inevitably affects, the accuracy of estimated position information, the bandwidth of the position observer, the sensorless operation stability and the operating efficiency.

Based on the previous discussion, the primary machine saliency undergoes two cycles per electrical period. However, the secondary saliency behaves different from the primary saliency and there will exist more cycles in one electrical period.

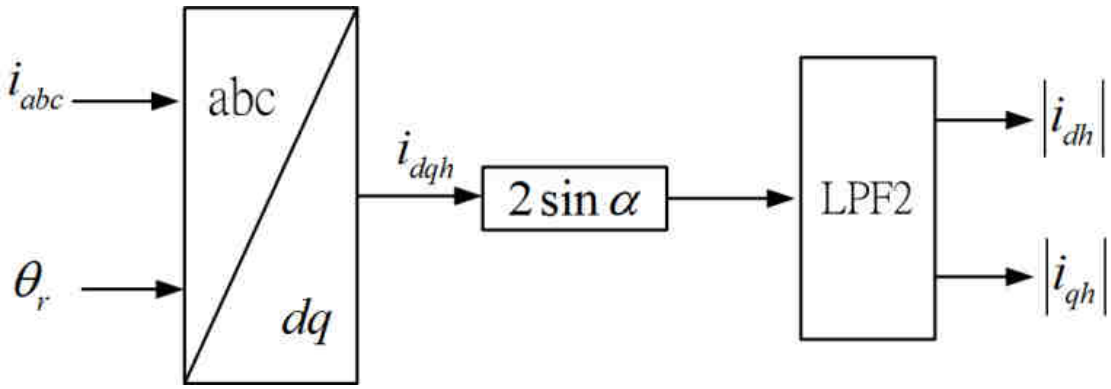


Fig. 4.5. Basic principle for the secondary saliency & multiple saliencies investigation.

The block diagram for the investigation of the secondary saliency is shown in Fig. 4.5. Pre-define the average and difference of the secondary *d*- and *q*-axis inductances and the average multiple inductance [RAC10] [KIM04] as

$$L_{sa\_hm} = \frac{L_{q\_hm} + L_{d\_hm}}{2},\ L_{sd\_hm} = \frac{L_{q\_hm} - L_{d\_hm}}{2},$$
$$\sum L = \frac{L_{qh} + L_{dh} + \sum L_{q\_hm} + \sum L_{d\_hm}}{4} \tag{4.4}$$

A HF pulsating carrier voltage as shown in (4.2) is injected on the actual synchronous reference frame. Then, the HF carrier current response in the actual synchronous reference

frame is represented as

$$\begin{bmatrix} i_{dh} \\ i_{qh} \end{bmatrix} = \frac{1}{2}\begin{bmatrix} I_p + I_n \cos(2\theta_r) + \sum I_{n\_hm} \cos((2-hm)\theta_r - \Delta\varphi) \\ I_n \sin(2\theta_r) + \sum I_{n\_hm} \sin((2-hm)\theta_r - \Delta\varphi) \end{bmatrix} \cdot \sin\alpha \tag{4.5}$$

Where

$$I_p = \frac{V_c}{\omega_c} \frac{\sum L}{\sum L^2 - L_{sa}^2 - \sum L_{sa\_hm}^2 - 2\sum L_{sd} L_{sd\_hm} \cos((2-hm)\theta_r - \Delta\varphi)} \tag{4.5a}$$

$$I_n = \frac{V_c}{\omega_c} \frac{L_{sd}}{\sum L^2 - L_{sa}^2 - \sum L_{sa\_hm}^2 - 2\sum L_{sd} L_{sd\_hm} \cos((2-hm)\theta_r - \Delta\varphi)} \tag{4.5b}$$

$$I_{n\_hm} = \frac{V_c}{\omega_c} \frac{L_{sd\_hm}}{\sum L^2 - L_{sa}^2 - \sum L_{sa\_hm}^2 - 2\sum L_{sd} L_{sd\_hm} \cos((2-hm)\theta_r - \Delta\varphi)} \tag{4.5c}$$

In (4.5), $I_{n\_hm}$ is the disturbance depending on the rotor position due to secondary saliency, where *hm* indicates the harmonic component the order of primary or secondary saliency and *hm*=4,6,8 …. $\Delta\varphi$describes the initial phase difference between primary and secondary saliency. Then, applying the synchronous detection technique, the HF carrier current amplitude considering the secondary saliency can be expressed as

$$\begin{bmatrix} |i_{dh}| \\ |i_{qh}| \end{bmatrix} = LPF\left(\begin{bmatrix} i_{dh} \\ i_{qh} \end{bmatrix} \cdot 2\sin\alpha\right) = \frac{1}{2}\begin{bmatrix} I_p + I_n \cos(2\theta_r) + \sum I_{n\_hm} \cos((2-hm)\theta_r - \Delta\varphi) \\ I_n \sin(2\theta_r) + \sum I_{n\_hm} \sin((2-hm)\theta_r - \Delta\varphi) \end{bmatrix} \tag{4.6}$$

Ideally, if there is no secondary saliency in the machine, the measured carrier current magnitude $|i_{dh}|$ and $|i_{qh}|$ should be constant and independent of the rotor position according to (3.25). From the view of the multiple saliencies, the estimated saliency angle is assumed the same as the actual rotor position, however, the inconstant carrier current $|i_{dh}|$ and $|i_{qh}|$ is depended on the rotor position $\theta_r$ as discussed in (4.6). It can be predicted that the unwanted ripple component would be generated by the multiple saliencies effect.

With aid of the actual rotor position from the encoder, the HF pulsating voltage signal (3.13) is ($V_c$ = 8V, $f_c$ = 550Hz) injected on the actual synchronous reference frame, while the test PM machine is slowly spun manually or by the torque DC machine. Then, the amplitude of the

*dq*-axis carrier response currents can be derived.

Experimental results of the prototype SFPM BLAC machine is presented in Fig. 4.6, and can be seen that the small current ripples are observed and clearly reveal the existence of multiple saliencies and indicated that the SFPM machine is rotor-position-dependent and this ripple term is six times to fundamental frequency. The experimental result at no-load is shown in Fig. 4.6 (a), and with-load condition is in Figs. 4.6 (b) and (c), respectively. From Fig. 4.6, different ripple amplitude can be observed at different load conditions, which indicates that the effect of multiple saliencies is also load-dependent.

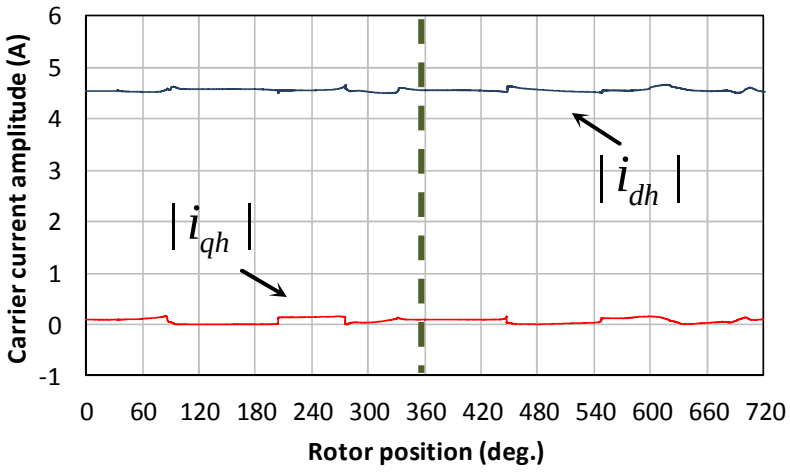


(a) $i_d$ = 0A, $i_q$ = 0A

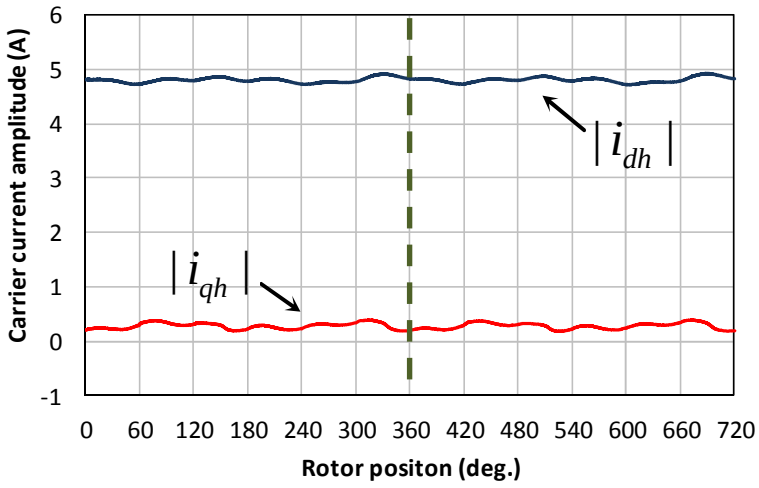


(b) $i_d$ = 0A, $i_q$ = 2A

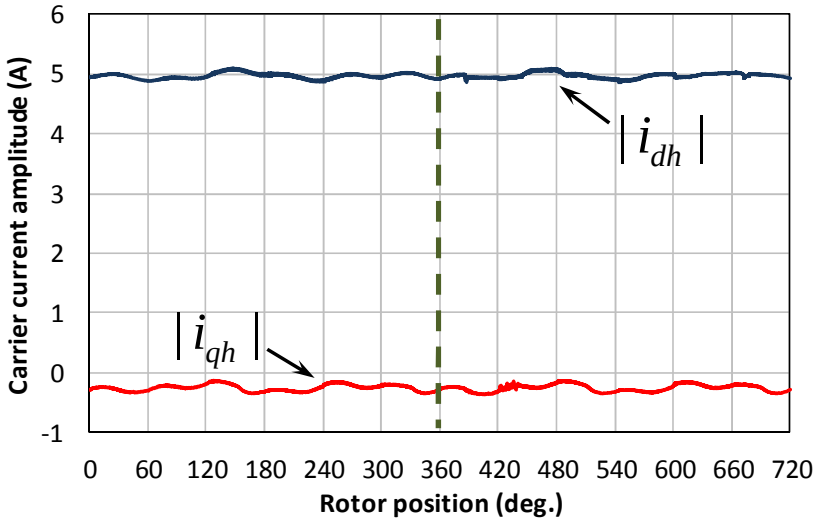


(c) $i_d$ = 0A, $i_q$ = -2A

Fig. 4.6. Rotor-position-dependence of SFPM saliency at no-load and under different-load conditions.

Clearly, the multiple saliencies inevitably affect the bandwidth of the position observer and the accuracy of position information estimation. However, since the effect is limited, it can be neglected and not needed to be compensated in the HF injected-based sensorless control for the prototype SFPM machine.

## 4.3 Influence of Cross-Saturation

In term of the cross-saturation effect, the cross-saturation angle usually exists. When $i_q$ current is zero amp, $\theta_m$ is almost close to zero, which can be equivalent as the cross-saturation effect is negligible. However, with the fundamental excitation current, the measured cross-saturation angle $\theta_m$ becomes identified as drawn in Fig. 4.7, which proves that the cross-saturation effect depends on both *d*- and *q*-axis current.

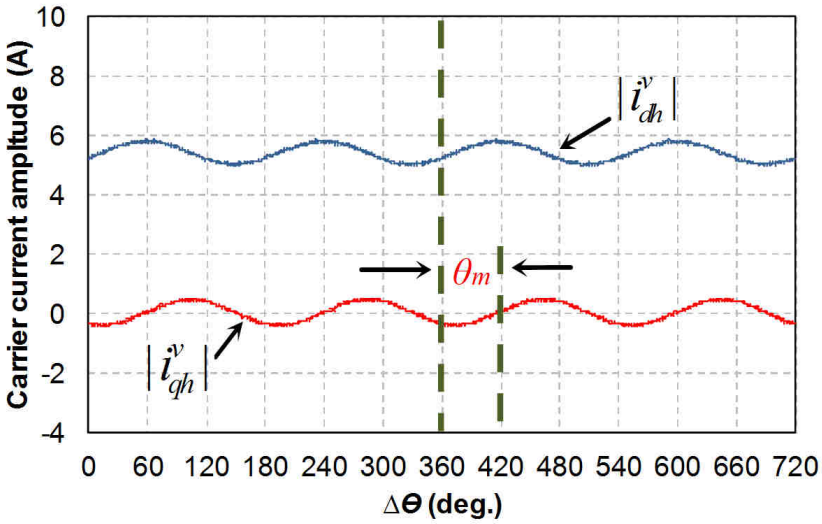


(a) $i_d$ = 6A, $iq$ = 0A

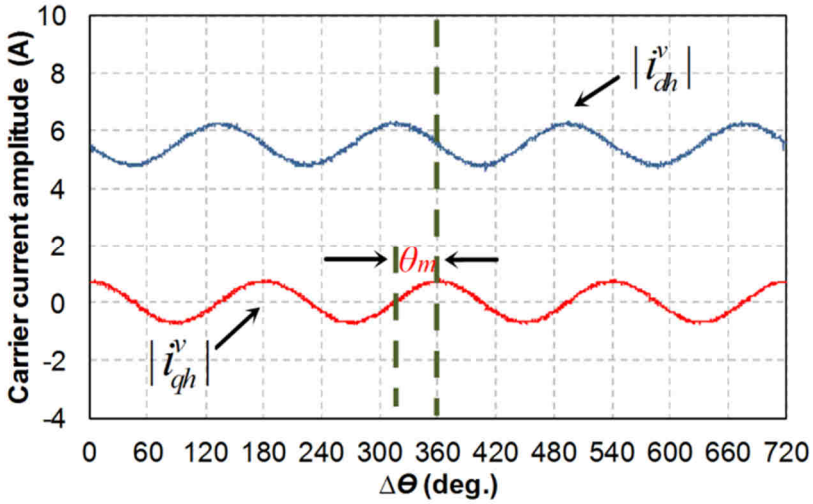


(b) $i_d$ = 0A, $i_q$ = 6A

Fig. 4.7. Measured carrier current amplitude variation with position difference and offset angle of cross-saturation, $\vartheta_m$ under different-load conditions.

## 4.4 Experimental Validation of Sensorless Control Operation

Based on the theoretical analysis and experimental results, it clearly shows that although the machine saliency is not too large and varies with load current, it is still identical and suitable for implementing the HF injection-based sensorless control, but need to be validated by experiments. Hence, the HF pulsating carrier voltage signal injection-based technique

considering cross-saturation effect is applied to the prototype SFPM machine to estimate the accurate rotor position, which is based on the current and speed close-loop sensorless control, as shown in Fig. 4.8.

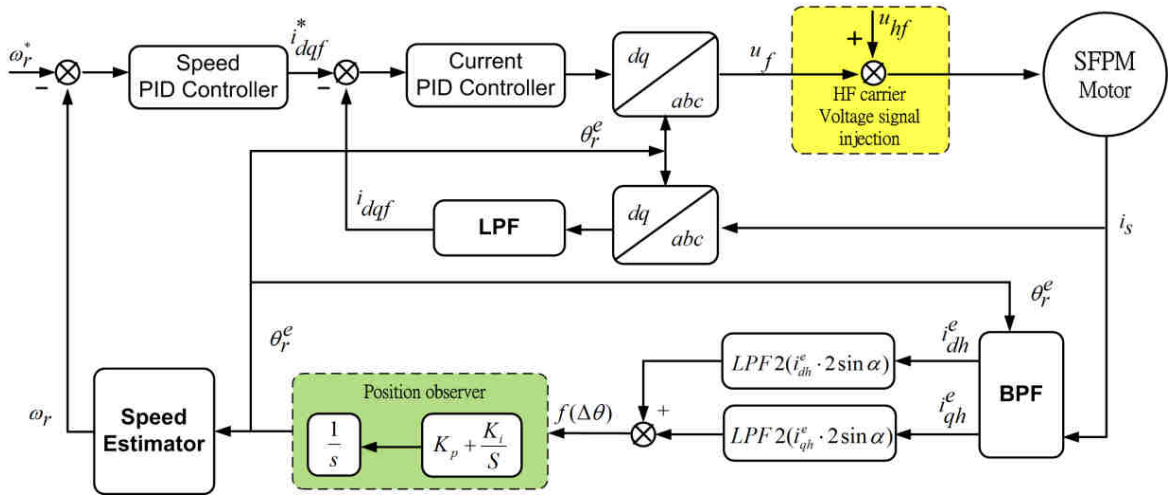


Fig. 4.8. Basic structure for Sensorless control operation of SFPM machine using HF pulsating voltage signal injection scheme.

A HF pulsating voltage signal ($V_c$ = 8V, $f_c$ = 550Hz) is injected into the estimated synchronous reference frame of Test Machine-II, and the rotor position is estimated from the saliency-dependent response currents.

### 4.4.1 Sensorless Current Control at Steady and Dynamic States

The saliency level and cross-saturation effect are both affected by the fundamental current due to the variation of HF inductances. Hence, the effect of fundamental current for sensorless control is of great importance for the prototype machine and the cross-saturation is compensated by the method introduced in [HAR00]. The current-closed loop control under the step-transient in current, from $i_q$ = 1.5A to $i_q$ = -1.5A (speed 20 r/min to -20 r/min), is applied to investigate the influence of fundamental current, and the experimental results considering the cross-saturation effect are shown in Fig. 4.9.

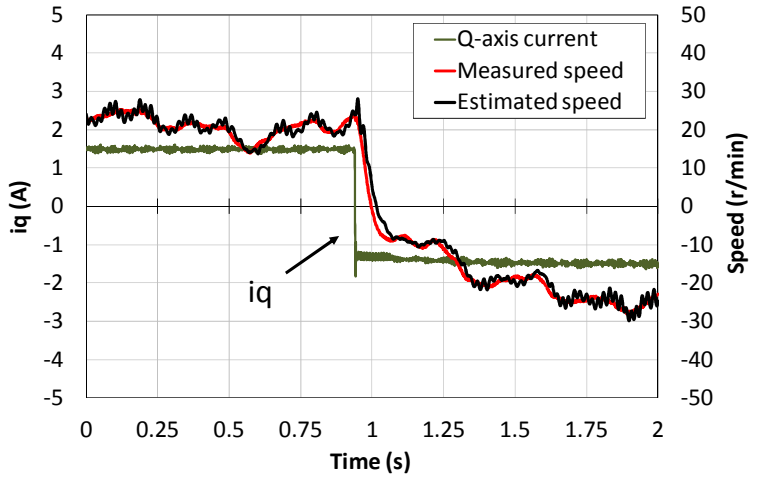


(a) *q*-axis current and open-loop speed responses

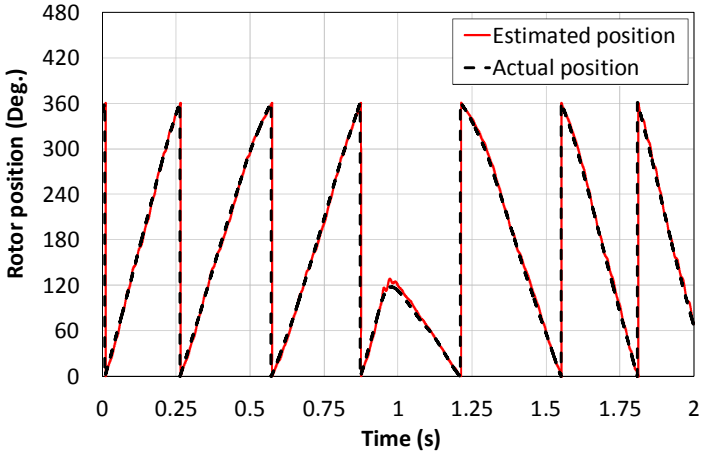


(b) Actual and estimated rotor positions

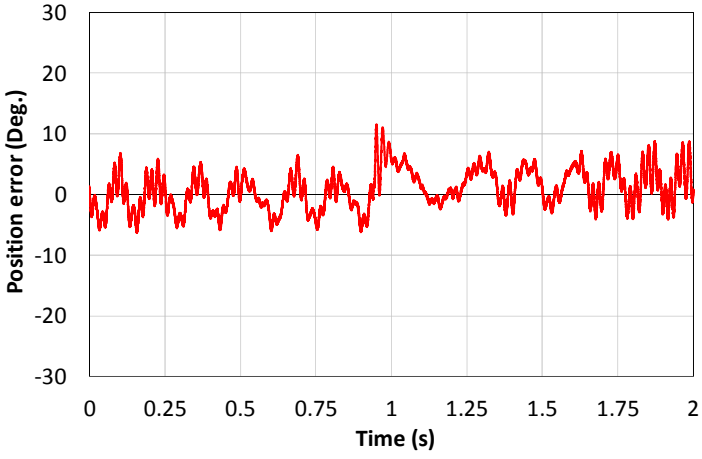


(c) Estimated rotor position error

Fig. 4.9. Measured step-current transient response for sensorless current control operation, i*q* = 1.5A to i*q* = -1.5A (20 r/min to -20 r/min).

From the results, it clearly shows that during the current step transient, $i_q$ current and open-loop speed responses are performed well as depicted in Fig. 4.9 (a) and estimated rotor position and estimation error are shown in Figs. 4.9 (b) and (c), respectively. Since the secondary saliency information is rotor position dependent and not very obvious in the SFPM machine, there exists minor rotor position estimation error oscillation which is not easy to be compensated. Fig. 4.10 shows the sensorless speed control in steady-state using a pulsating voltage signal injection-based sensorless control scheme.

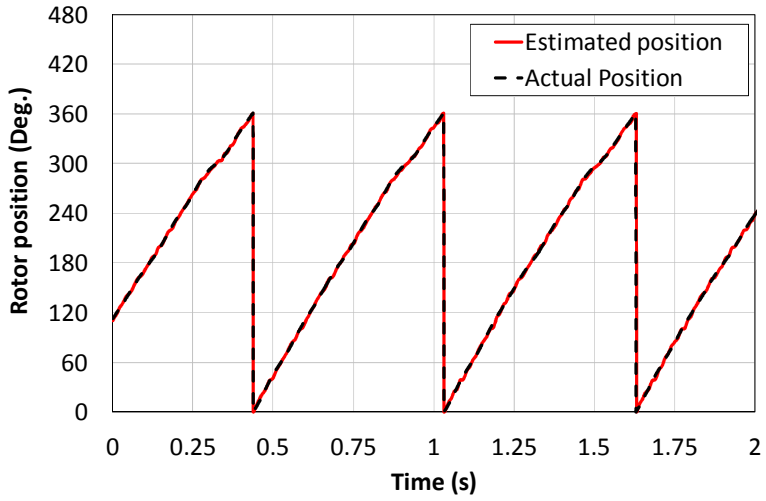


(a) Actual and estimated rotor position

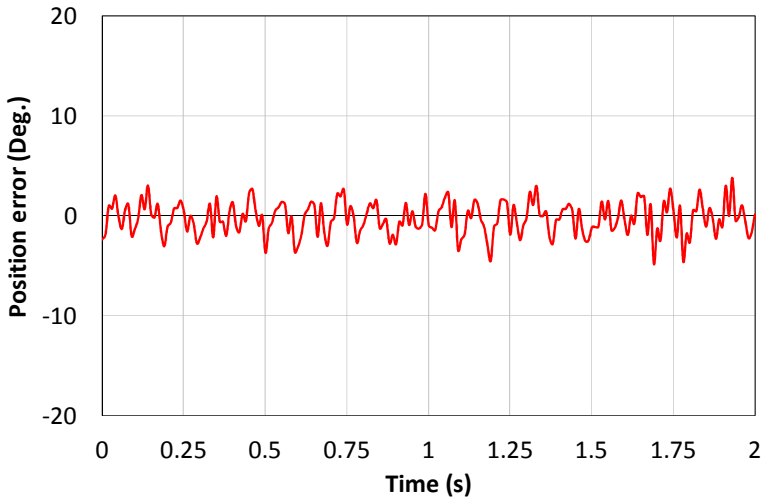


(b) Estimated rotor position error

Fig. 4.10. Rotor position estimation for sensorless-speed-control in steady-state, 10rpm.

### 4.4.2 Sensorless Speed Control at Steady and Dynamic States

The experimental result shows good performance of the tracking position at constant speed, 10 r/min. The results for the dynamic performance of step-change in rotor speed under no-load, from 0 r/min - 10 r/min - 20 r/min - 10 r/min – 0 r/min, are presented in Fig. 4.11. Hence, the good sensorless control performance is obtained under both steady and dynamic transient states. Although the estimated position error reaches up to ±20 deg. during the transient process, the estimation position error can still be limited to ±5 deg. under steady state with no-load.

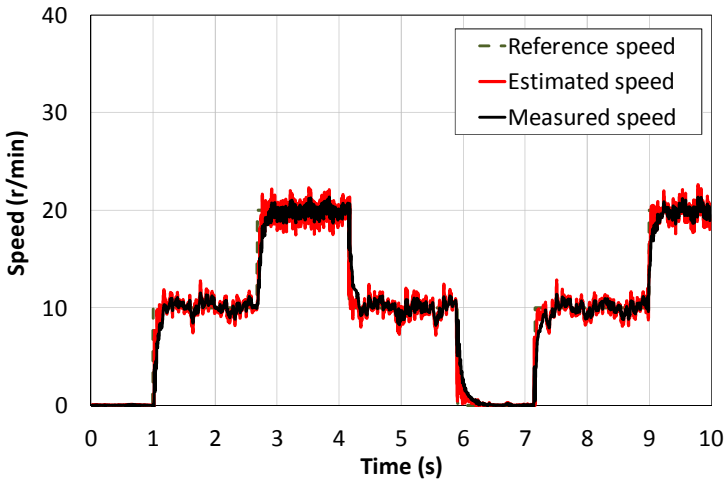


(a) Speed responses

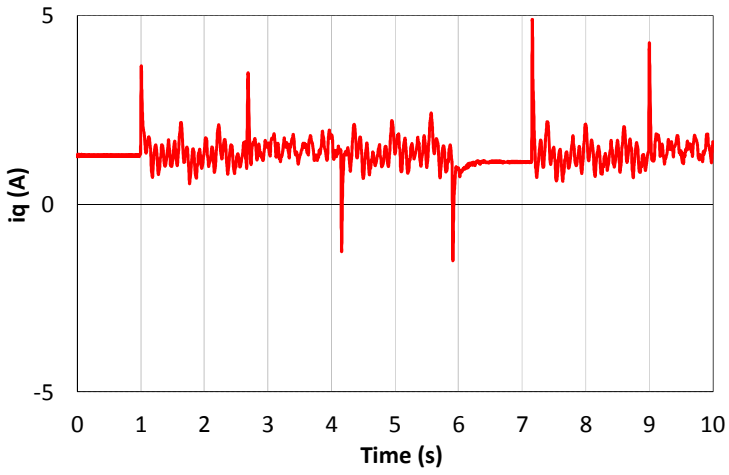


(b) *q-axis* current response

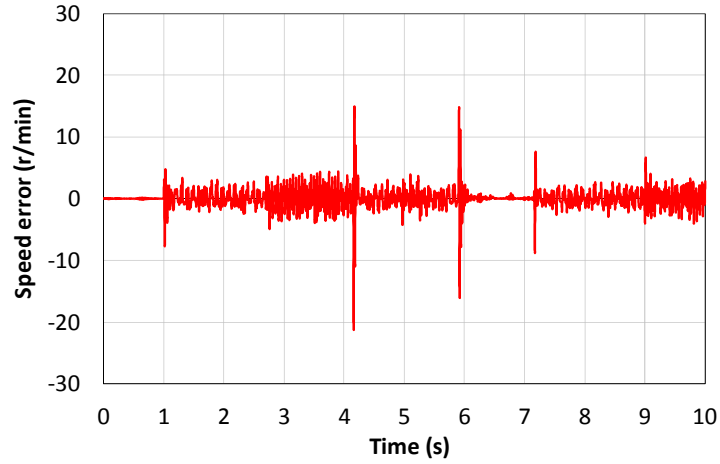


(c) Estimated speed error

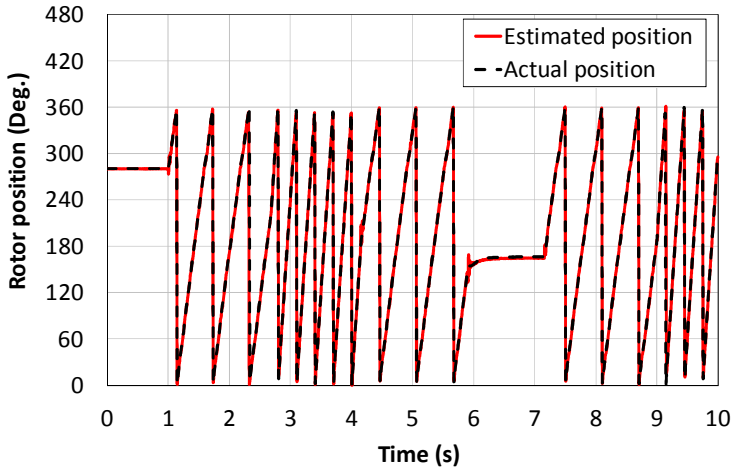


(d) Actual and estimated rotor positions

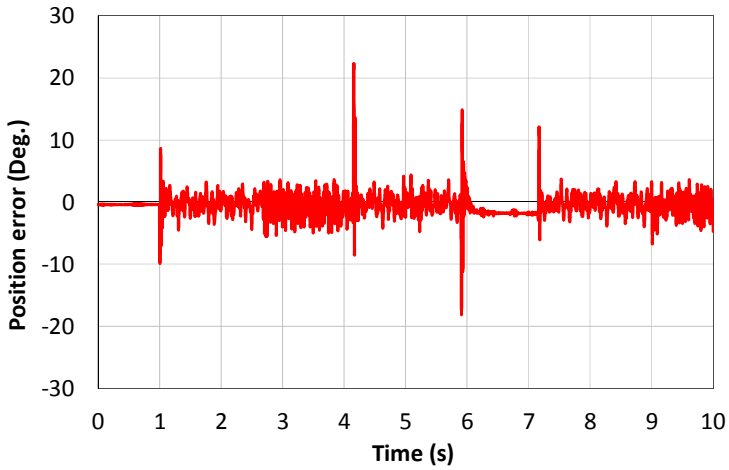


(e) Estimated rotor position error

Fig. 4.11. Measured step-speed response for sensorless-speed-control in dynamic-state under no-load.

Furthermore, another rotor speed step-transient, from 0 r/min to 20 r/min under full-load condition is depicted in Fig. 4.12, it can clearly be seen that the estimated rotor position error is increased (±12 deg, Fig 4.12 (e)) under full-load operation for the pulsating carrier voltage injection due to the fundamental excitation current induced magnetic saturation.

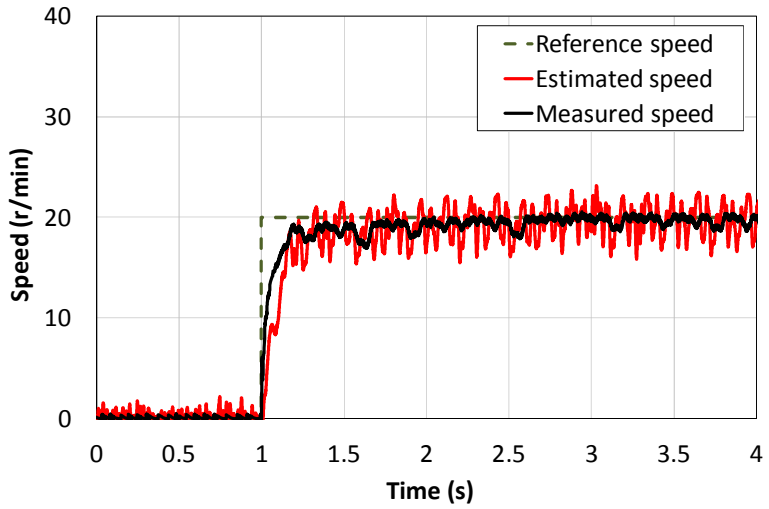


(a) Speed responses

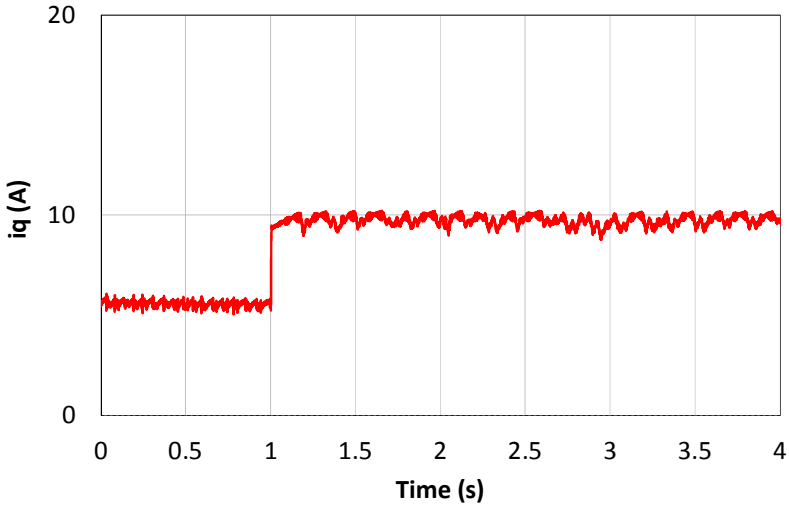


(b) *q-axis* current response

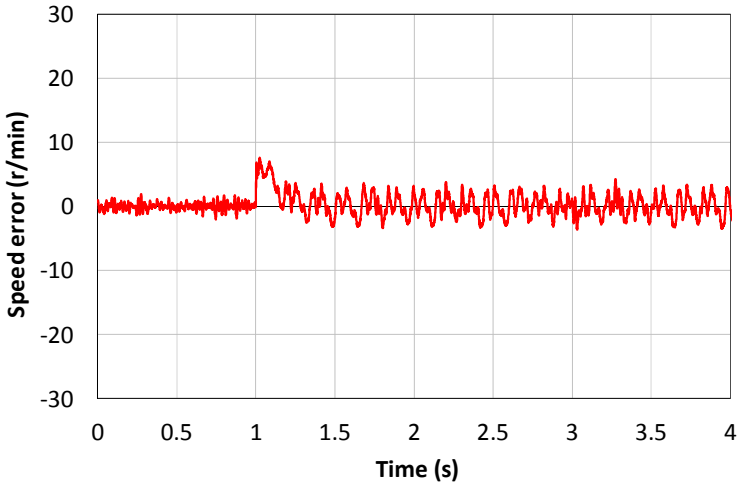


(c) Estimated speed error

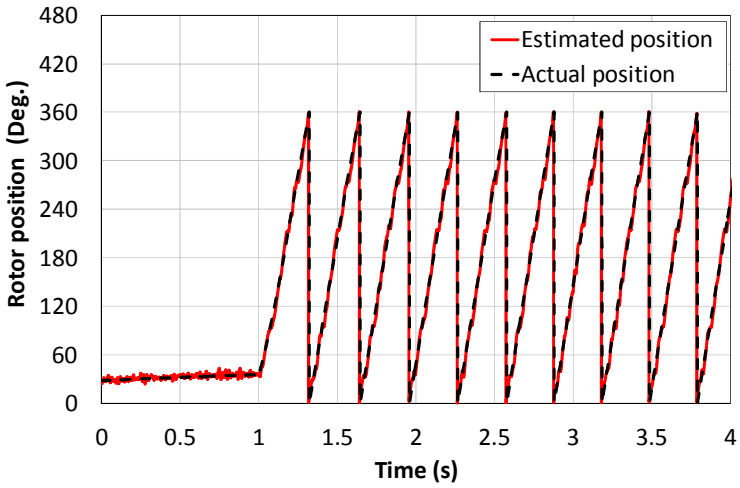


(d) Actual and estimated rotor positions

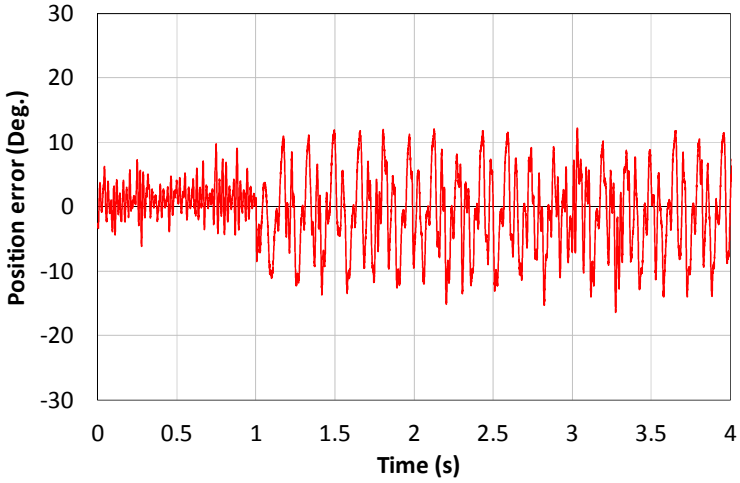


(e) Estimated rotor position error

Fig. 4.12. Measured step-speed response for sensorless-speed-control in dynamic-state under full load, 0 r/min to 20 r/min.

Meanwhile, the speed-tracking behavior is compared in Fig. 4.13, showing that from forward rotating to backward rotating the estimated speed response in sensorless control mode is shown a good agreement with the measured speed response in sensored mode.

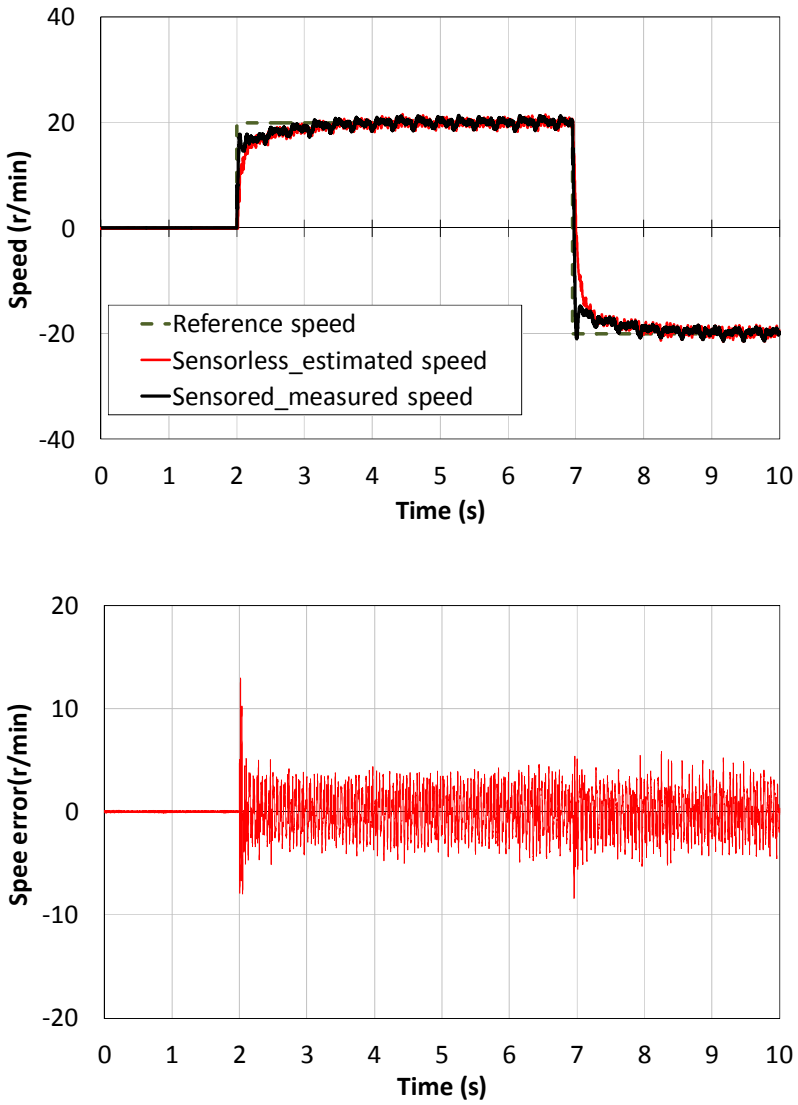


Fig. 4.13. Comparison of measured step-speed responses for sensored and sensorless speed-control operations under no-load condition.

## 4.5 Conclusion

In this chapter, a complete experimental investigation method has been proposed in order to analyze and verify the saliency level without the need of any information of parameter values

for the first time using high-frequency pulsating signal injection and implemented on a new type of SFPM machine.

The experimental results validate that the primary saliency of prototype SFPM machine is large enough and suitable for high-frequency signal injection-based sensorless control and the limited secondary saliency will not deteriorate the performance in the rotor position estimation and the bandwidth of position observer much. Furthermore, the conclusion is also verified by the experiments based on the high-frequency pulsating signal injection-based sensorless control in both steady and dynamic states at zero and low speeds.

## References


[CUP11] F. Cupertino, P. Giangrande, G. Pellegrino and L. Salvatore, "End effects in linear tubular motors and compensated position sensorless control based on pulsating voltage injection," *IEEE Trans. Ind. Electron.*, vol. 58, no.2, pp.494-502, Feb. 2011.

[DEG98] M. Degner and R. Lorenz, "Using multiple saliencies for the estimation of flux, position, and velocity in ac machines," *IEEE Trans. Ind. Appl*., vol. 34, no. 5, pp. 1097–1104, Sep./Oct. 1998.

[HAR00] L. Harnefors and H.P. Nee, "A general algorithm for speed and position estimation of AC motors," *IEEE Trans. Ind. Electron.*, vol. 47, no. 1, pp. 77-83, 2000.

[KIM04] H. Kim and R.D. Lorenz, "Carrier signal injection based sensorless control methods for IPM synchronous machine drives," *Proc. of IEEE-IAS Annual Meeting*, Vol. 2, pp.977 – 984, Oct. 2004.

[RAC10] D. Raca, P. Garcia, D.D. Reigosa, F. Briz, R.D. Lorenz, "Carrier-signal selection for sensorless control of PM synchronous machines at zero and very low speeds," *IEEE Trans. Ind. Appl*., vol. 46, no.1, pp.167-178, 2010.

# CHAPTER 5

# IMPROVEMENT OF SENSORLESS CONTROLLED PERMANENT MAGNET SYNCHRONOUS MACHINES HAVINE ASYMMETRIC BACK-EMF

## 5.1 Introduction

The sensorless control techniques become more and more popular in PMSM drive systems, which can successfully obtain the rotor position information from machine voltages and currents. Among those sensorless control schemes, it is reported that the HF signal injection based techniques can accurately estimate the rotor position at zero and low speeds [LIN14][LIU14][YOO14][CHE14], as introduced in Chapters 3, 4 and 6, whereas the back electromotive force (EMF) based sensorless control scheme has superior performance for medium and higher speed applications [CHE03][ZHA11][KIM03].

Recently, a new class of brushless machines having PMs located in the stator, for example, the switched-flux PM (SFPM) and doubly salient PM (DSPM), have been reported due to its high efficiency, high power density and robust rotor [ZHU05] [CHE11]. It is identified that the SFPM machine has a better torque performance than the DSPM machine [ZHU10]. In [OWE10], a newly developed SFPM machine with an alternate poles wound, being with good performances, such as fault tolerance, high power density, was investigated. However, the back-EMF of this machine is asymmetric and non-sinusoidal, which can also be found in a lot of other types of PMSM machines including DSPM machines, and hence a higher torque ripple may be caused by the back-EMF harmonic components.

In this chapter, the performances of sensorless control of SFPM with two different winding configurations being depicted in Fig. 5.1(a) and (b) are investigated, whose back-EMFs

exhibit different waveform characteristics, such as sinusoidal, asymmetric and non-sinusoidal waves. The single-layer machine is found to exhibit asymmetric back-EMFs, due to which the performance of conventional flux-observer based sensorless control will deteriorate. In order to overcome this issue, a modified flux-linkage observer is developed and acts in synergy with a harmonic elimination technique, by which a higher accuracy of rotor position estimation is achieved. The performance of proposed sensorless control strategy is experimentally validated on a prototype SFPM machine, and the effectiveness of the proposed rotor position estimation will be demonstrated by comparing with that of a conventional flux-linkage observer based sensorless control under both steady and dynamic states.

## 5.2 Topologies of PM Machines and Analysis of Back-EMFs

In this section, the various machine topologies based on Test Machine-II will be firstly introduced and the analysis of asymmetric and non-sinusoidal back-EMF waveforms will be given in order to highlight its potential influence on the rotor flux-linkage based sensorless control techniques.

### 5.2.1 Topologies of PM Machines

Test Machine-II with different stator topologies as shown in Fig. 5.1, i.e. all poles wound (Fig. 5.1(a)) and alternate poles wound (Fig. 5.1(b)), are under investigation and exhibit the different back-EMF features. Both topologies have the same machine structure, i.e. very simple and robust rotor, and “U-shaped” laminated iron segments around magnetized PMs in the stator [ZHU05][HOA97].

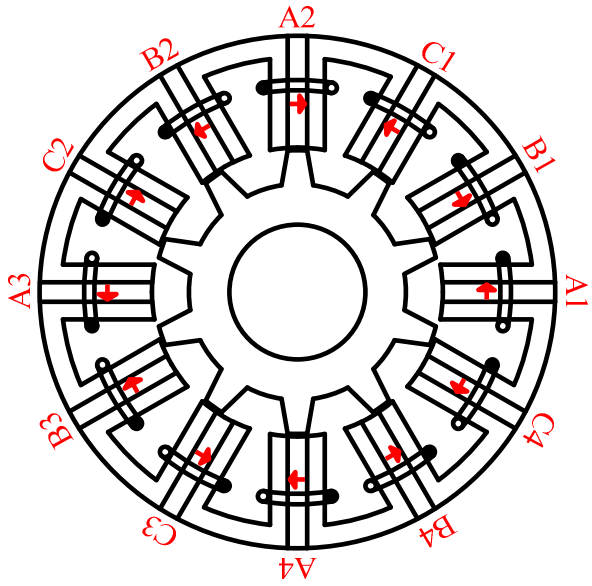


(a) Double-layer winding - all poles wound

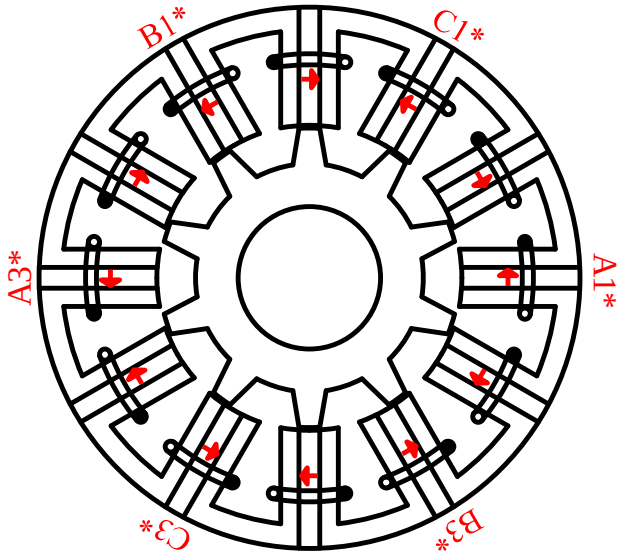


(b) Single-layer winding - alternate poles wound

Fig. 5.1. Topologies of a SFPM machines.

The differences between these two machine topologies can be identified and compared in Fig. 5.1. Fig. 5.1 (a) shows the conventional machine structure with all poles wound around stator poles as explained in [ZHU05][HOA97], i.e. double-layer winding, and four series-connected coils as one phase. Additionally, each stator slot contains two coils of two

phases. Unlike the conventional machine structure, the second machine topology is designed to have single-layer windings, in which each stator slot contains coils of one phase only and alternate poles are wound. However, the slot area is still the same as the double-layer winding machine, and each phase just utilizes two series-connected coils rather than four, Fig. 5.1(b). Since the winding configurations are not the same, the measured back-EMF waveforms are different.

### 5.2.2 Back-EMFs Analysis

In order to investigate the back-EMF characteristics, and assuming the winding inductances of the Test Machine-II are constant, the three-phase back-EMFs can be represented as

$$\begin{cases} u_{an} = R_s i_a + (L - M)\, p i_a + e_a \\ u_{bn} = R_s i_b + (L - M)\, p i_b + e_b \\ u_{cn} = R_s i_c + (L - M)\, p i_b + e_c \end{cases} \tag{5.1}$$

$$i_a + i_b + i_c = 0 \tag{5.2}$$

Therefore, no matter which mode of operation, i.e. either BLDC or BLAC, the voltage equation can be derived as

$$u_{an} + u_{bn} + u_{cn} = e_a + e_b + e_c \tag{5.3}$$

Hence, the three-phase back-EMFs can be represented as

$$\begin{cases} e_a = \sum_{i=1}^{N} e_{ai} = -E_{mgi} \sin\theta_r - \cdots \\ e_b = \sum_{i=1}^{N} e_{bi} = -E_{mgi} \sin(\theta_r - 2\pi/3) - \cdots \\ e_c = \sum_{i=1}^{N} e_{ci} = -E_{mgi} \sin(\theta_r + 2\pi/3) - \cdots \end{cases} \tag{5.4}$$

where $e_{ai}$, $e_{bi}$ and $e_{ci}$ are the $i$th-order harmonics of the three-phase harmonic back-EMFs. $E_{mgi}$ presents the magnitude of the $i$th-order harmonics of the phase back-EMF.

Moreover, in order to investigate the influence of harmonics in different stator topologies, the original winding configuration (Fig. 5.1 (a)) is separated into two series-connected coils

for each set which transforms the double-layer winding machine into a single-layer winding machine as the alternate poles wound machine (Fig 5.1 (b)), i.e. (coils A1$^*$ and A3$^*$) is described as $e_{A1^*+A3^*}$, and then the back EMF of phase A is given as

$$e_a^* = e_{A1^*+A3^*} = e_{A1^*} + e_{A3^*} \tag{5.5}$$

where $e_a^*$ is the phase A back-EMF of alternate poles wound machine. $e_{A1^*}$ and $e_{A3^*}$ are the back-EMFs of coils A1$^*$ and A3$^*$, respectively. Thus, the expression of back-EMF waveform of alternate poles wound machine can be re-written as

$$\begin{cases} e_{A1^*} = \sum_{i=1}^{N} e_{Ami^*} \left[ \cos\left( i \cdot \omega t + \varphi_{Ami^*} \right) \right] \\ e_{A3^*} = \sum_{i=1}^{N} e_{Ami^*} \left[ \cos\left( i \cdot \omega t + \varphi_{Ami^*} \right) \right] \end{cases} \tag{5.6}$$

where $e_{Ami*}$, and $\varphi_{Ami*}$ are the magnitudes and phase angles of $i$th-order back-EMF harmonic and $i$ is the order number of harmonic component for coils A1$^*$ and A3$^*$, respectively. The frequency of the fundamental component is $\omega$.

In order to verify the foregoing analysis, the measured phase back-EMF waveforms of alternate poles wound (A1A3 or A2A4) and all poles wound machines at 400 r/min are shown in Fig. 5.2 (a). In addition, the Discrete Fourier Transform (DFT) for each winding configuration is also analyzed and shown in Fig. 5.2 (b). Clearly, the vertical pair of coil combination i.e. A1A3 and A2A4, their back-EMF waveforms are identical but not symmetrical and non-sinusoidal in alternate poles wound SFPM machines, whereas it is very sinusoidal in all poles wound SFPM machine. It is obvious that the back-EMF waveform of alternate poles wound SFPM machine includes some even harmonics as shown in Fig. 5.2 (b), because the positive and negative half cycles of back-EMFs of each pair of series-connected A1A3 or A2A4 are not symmetrical. Furthermore, in Fig. 5.2 (c), the phase angle of the second, fourth and sixth harmonics for both coil combinations, A1A3 and A2A4, are positive and negative, which can make the resultant back EMF waveform essentially sinusoidal. This

is due to the series-connection of two winding sets of the all poles wound SFPM machine, which will result in a coil compensation effect [HUA08] because its phase angle difference is $180^0$ and $-180^0$ as shown in Fig. 5.2 (d).

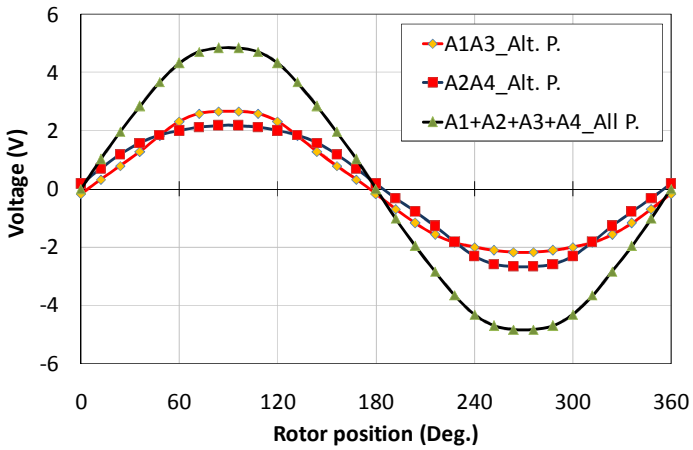


(a) Phase A Back-EMFs

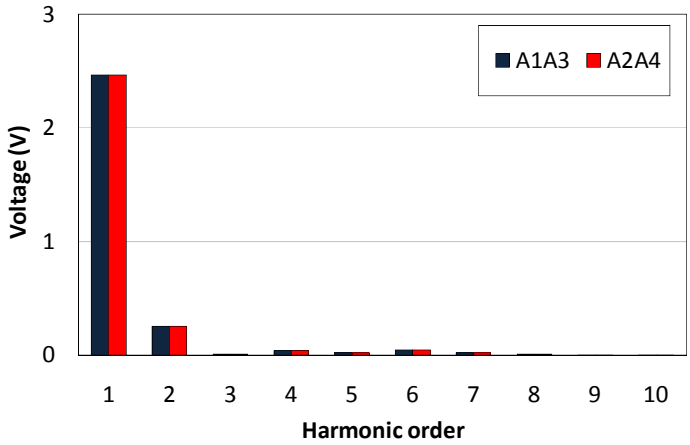


(b) Harmonic analysis

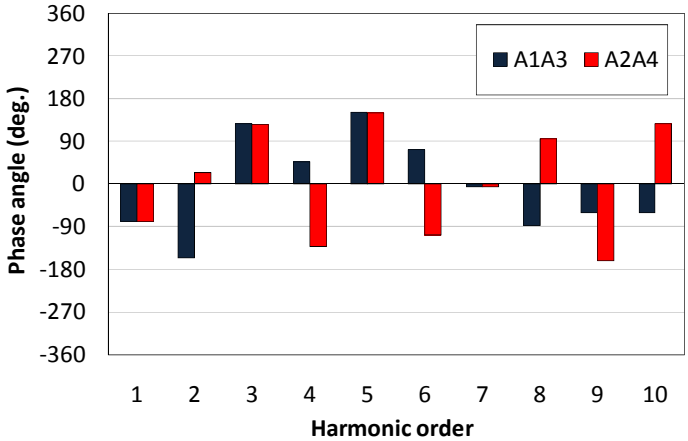


(c) Phase angles

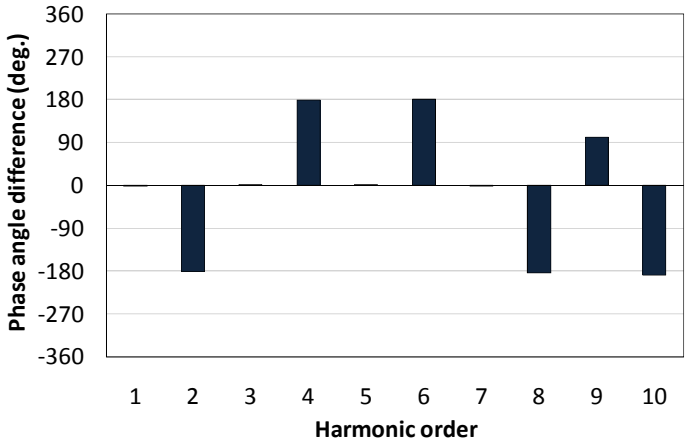


(d) Phase angle difference

Fig. 5.2. Analysis of measured back-EMFs and FFT analysis.

## 5.3 Conventional Flux-Linkage Observer Based Rotor Position Estimation

### 5.3.1 Flux-Linkage Observation

Generally, the rotor flux-linkage can be estimated by the flux-linkage observer, which is produced by the permanent magnet and also can be used for the rotor position estimation [MAR97]. In a conventional flux-linkage observer, the PM excitation flux-linkage is usually calculated by the integration of terminal voltage [WU91]. A simplified representation of the flux-linkage observer is based on the phasor diagram of a PMSM shown in Fig. 5.3, where the current vector $I_s$ and the voltage vector $U_s$ are derived from the measured current and terminal voltage, and the reference frame transformation from the *a-b-c* reference frame to the stationary $\alpha$-$\beta$ reference frame. The $\alpha$- and $\beta$-axis voltages which are obtained from the command voltages of the space vector pulse width modulation (SVPWM) and the measured $\alpha$- and $\beta$-axis currents are shown in Fig. 5.4.

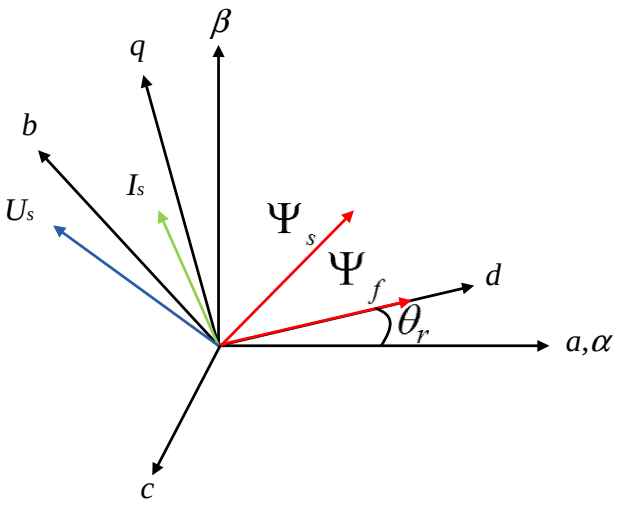


Fig. 5.3. Phasor diagram of different reference frame of PM machine.

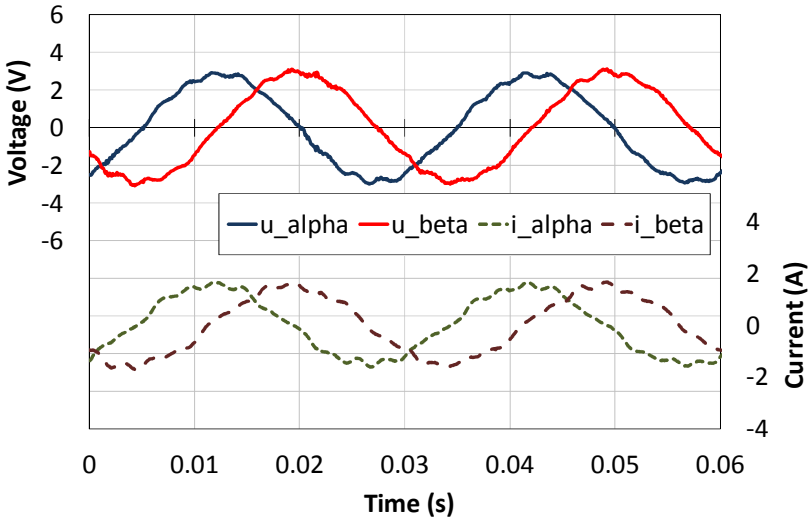


Fig. 5.4. Measured $\alpha$- and $\beta$-axis voltages and currents.

The stator voltage equations can be expressed as

$$U_s = \frac{d\Psi_s}{dt} + R_s \cdot I_s \tag{5.7}$$

where $U_s$ and $I_s$ are the stator voltage and current vectors, respectively. $R_s$ presents the stator phase resistance, and $\Psi_s$ is referred to as the stator winding flux-linkage. The stator flux-linkages in the stationary reference frame can be derived from the $\alpha$- and $\beta$- voltages and

currents shown in Fig. 5.4 which are mathematically expressed as

$$\begin{cases} \Psi_{s\alpha} = \int_0^t \left(U_s - R_s \cdot I_s\right) dt \\ \Psi_{s\beta} = \int_0^t \left(U_s - R_s \cdot I_s\right) dt \end{cases} \tag{5.8}$$

Based on [SHE02], the rotor flux-linkage can be calculated by

$$\Psi_f = \Psi_s - L_s I_s \tag{5.9}$$

Hence, the PM excitation flux-linkage in the stationary reference frame can be expressed as [SHE02][LEE11][LUU03][IDR02][HIN03][PEL11]

$$\begin{cases} \Psi_{f\alpha} = \int_0^t \left(U_{s\alpha} - R_s \cdot I_{s\alpha}\right) dt - L_s I_{s\alpha} \\ \Psi_{f\beta} = \int_0^t \left(U_{s\beta} - R_s \cdot I_{s\beta}\right) dt - L_s I_{s\beta} \end{cases} \tag{5.10}$$

where $L_s$ is the winding inductance. Then, the rotor position can be estimated from PM excitation flux-linkage shown in Fig. 5.5 which is given by

$$\theta_r = \text{atan}^2\left(\frac{\Psi_{f\beta}}{\Psi_{f\alpha}}\right) \tag{5.11}$$

Afterwards, the rotor speed can be derived by

$$\omega_r = \frac{d\theta_r}{dt} \tag{5.12}$$

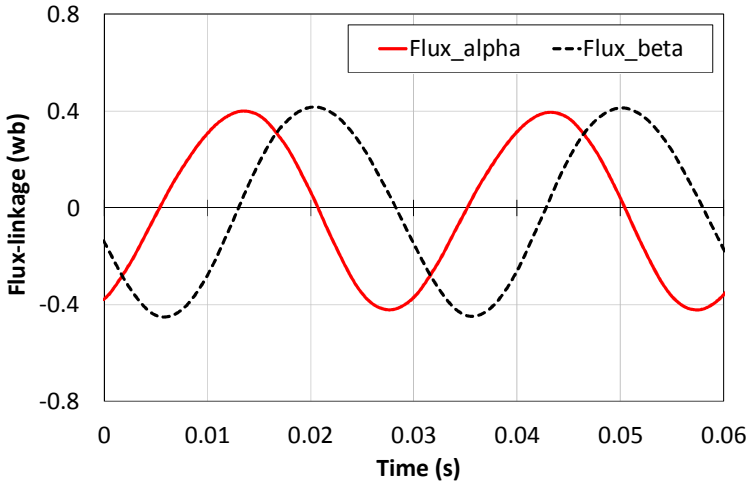


(a) $\alpha$- and $\beta$-axis flux-linkages

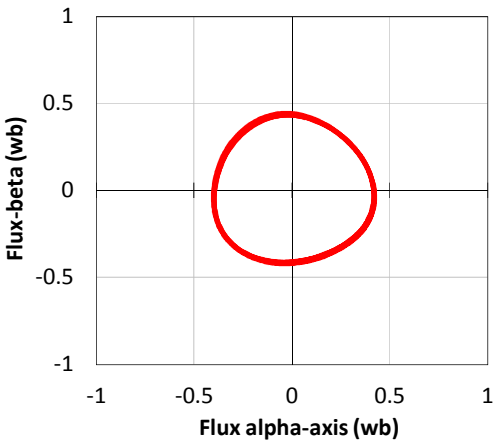


(b) Locus of flux-linkage circle

Fig. 5.5. Measured $\alpha$- and $\beta$-axis flux-linkages.

It should be noted that for a PM machine, its stator flux-linkage is usually dominated by the PM flux, whose magnitude is almost constant during the operation. Besides, the other part of the stator flux is contributed by the stator winding current and is relatively small. In [WU91], the angle of stator flux vector is directly used to estimate the rotor position while the influence of stator winding current produced flux linkage is neglected. In addition, this control strategy is not too sensitive to the inductance variation. Nevertheless, in general, since this sensorless control technique relies on the stator flux-linkage, the stator winding resistance should be accurately obtained and an integration of voltage is needed.

More importantly, there is a drift problem caused by the integrator due to the offset error components in both the measured voltages and currents. This offset is usually of a small dc value and varies slowly, but can still drive the output of integrator into saturation and result in an incorrect value. Thus, it needs to be compensated in order to improve the accuracy of estimated flux-linkage. Additionally, the accuracy of the rotor position estimation will also be affected by the asymmetric and non-sinusoidal back-EMF. Hence, in order to overcome the above issues, an improved rotor flux-linkage based rotor position estimation with the aid of back-EMF harmonic elimination is proposed for the enhancement of the accuracy of sensorless operation and will be discussed in the next subsection.

### 5.3.2 Sensorless Control Performance at Steady-State

Fig. 5.6 shows the rotor position estimations and position errors of the all poles wound and the alternate poles wound machines at the steady-state of constant speed (200 r/min). According to the experimental results in both Figs. 5.6 (a) and (b), the significant position estimation error occurs due to the inaccurate machine parameters and machine controller. By comparison, the oscillation error caused by the machine based on the alternate poles wound topology (Fig. 5.6 (b)) is more obvious than that of the machine based on all poles wound topology (Fig. 5.6 (a)) due to asymmetric back-EMF effect.

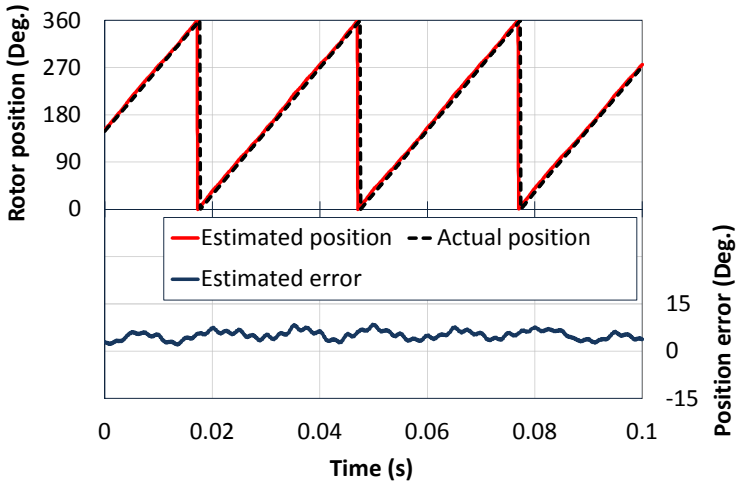


(a) All poles wound machine

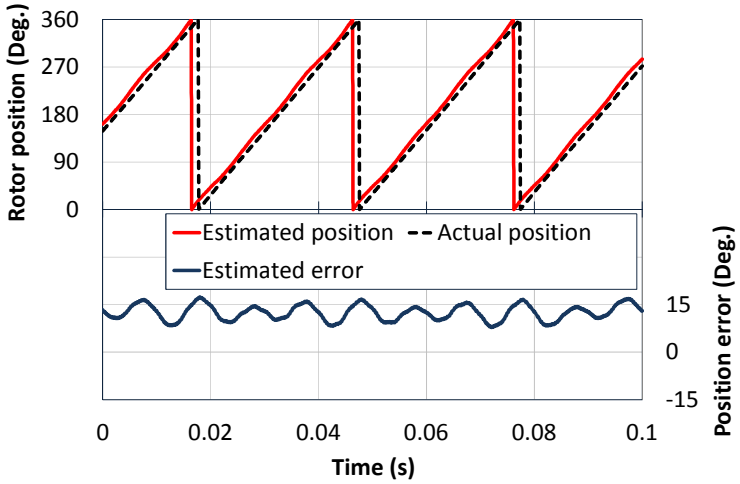


(b) Alternate poles wound machine

Fig. 5.6. Sensorless rotor position estimation at steady-state by conventional flux-linkage observer without compensation, 200 r/min.

### 5.3.3 Sensorless Control Performance at Dynamic-state

The experiments of sensorlesss control performance are carried out at the dynamic state of a step-change in rotor speed, changing from 100 r/min to 200 rmin, based on the all poles wound and the alterate poles wound machine topologies, as shown in Figs. 5.7 and 5.8, respectively. Similarly, the experimental results obtained form the steady-state, the alterate poles wound machine still performs worse than that of the all poles wound machine, in terms of the sensorless rotor position estimation error, which needs a futher improvement, as will be described in the next section.

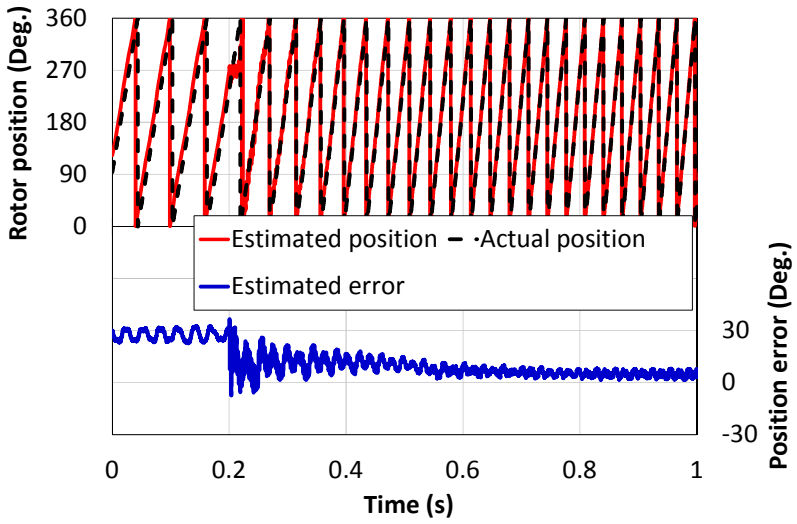


(a) Rotor position and error

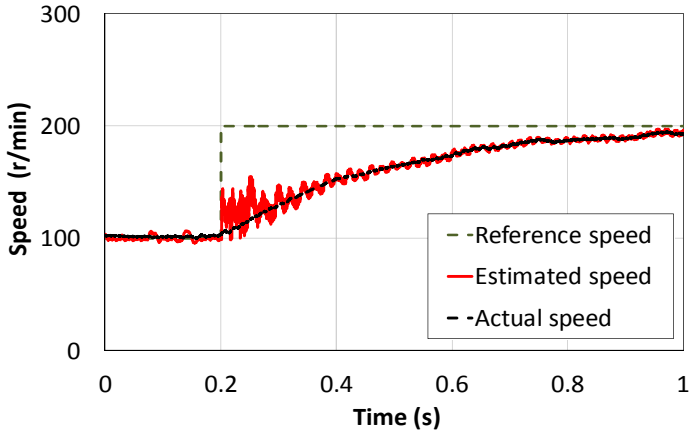


(b) Speed response

Fig. 5.7. Rotor position estimation at dynamic-state based on all poles wound machine topology, 100-200 r/min.

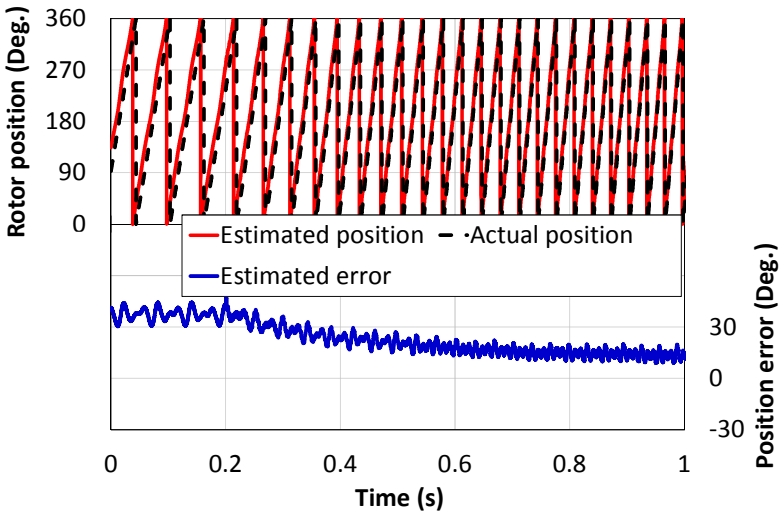


(a) Rotor position and error

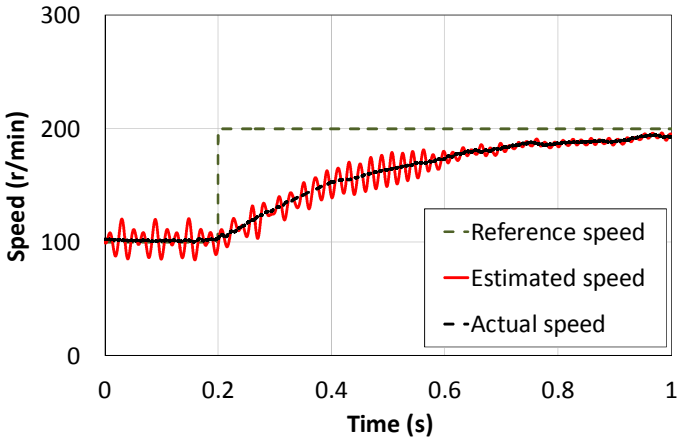


(b) Speed response

Fig. 5.8. Rotor position estimation at dynamic-state based on alternate poles wound machine topology, 100-200 r/min.

## 5.4 Proposed Rotor Position Estimation Based on Flux-Linkage Observer

A 12-slot 10-pole prototype SFPM brushless machine as introduced in Chapter 2 is used for the validation of proposed control strategies. The proposed rotor position error compensation based on asymmetric back-EMF with the aid of back-EMF harmonics elimination method is described in Fig. 5.9. The parameters of testing machine are listed in Table 2.3. The load machine is a 500W brushed DC machine, and an encoder with resolution of 2048PPR is

equipped on the test-rig to provide the actual rotor position to the whole control system.

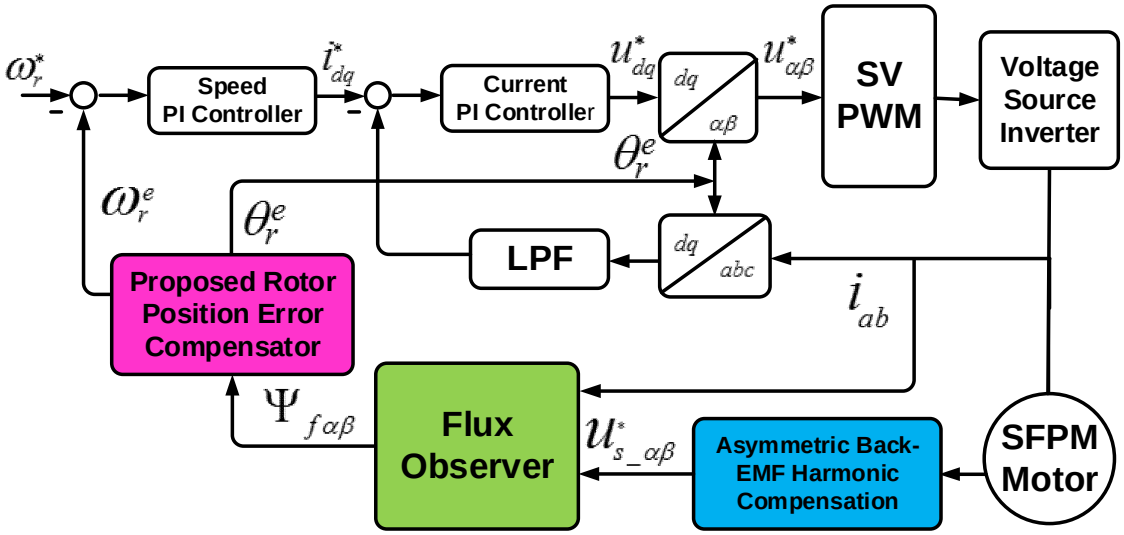


Fig. 5.9. Basic structure of overall sensorless control scheme.

The Test Machine-II has a winding configuration which can be separated into two series-connected windings, the influence of different machine topologies, i.e. all pole wound and alternate pole wound machines, are investigated in order to highlight the effectiveness of proposed rotor position estimator and compare with that of the conventional rotor position tracking observer.

It is should be noted that only one PM machine with double-layer windings/all poles wound is prototyped. It is used for the investigation of sensorless control performance of such a machine with either single-layer or double-layer windings. Thus, for single-layer winding machine, only one set of windings wound on alternate poles is employed. In practice, the full slot space will be utilized for the single layer windings and its torque or power density is the same (or even higher due to higher winding factor) as but harmonics would be usually higher than the PM machine with double-layer winding.

### 5.4.1 Compensation of Asymmetric Back-EMF Effect

As discussed in the previous section, the harmonics in the three phase back-EMFs due to

the asymmetric and non-sinusoidal effects may result in inaccurate rotor position estimation. Thus, those harmonics need to be eliminated before the developed compensation of position error. In order to minimize the influence of asymmetric back-EMF in advance, the harmonic elimination scheme shown in Fig. 5.10 is employed which is based on an adaptive closed-loop noise cancellation method, namely, adaptive notch filter (ANF) [WID75][JUN11][WAN14].

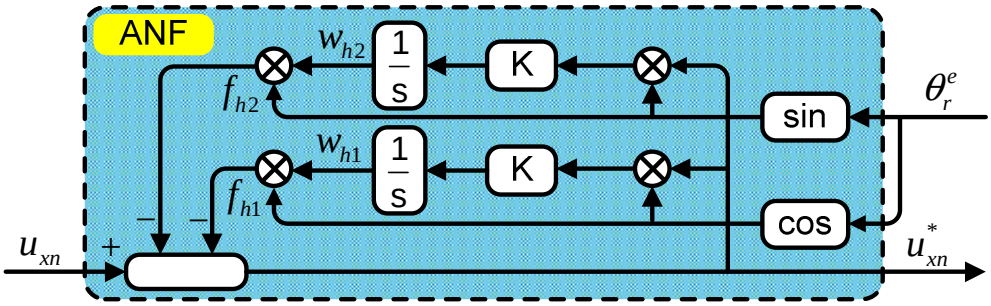


Fig. 5.10. Asymmetric back-EMF harmonic compensation method.

The measured back-EMF with harmonics can be utilized as the reference input signal to the ANF which requires the functions of sin and cosine corresponding to the feedback of estimated rotor position. Besides, since the even harmonics (2nd, 4th, 6th, …) in the phase back-EMFs are of non-negligible amplitudes, their influences will be mainly investigated in this application, whereas the odd harmonics (3rd, 5th, 7th, …) with small amplitudes are neglected. Hence, the three-phase back-EMFs according to (5.4) can be re-written as

$$\begin{cases} e_a^* = \sum_{i=1}^{N} e_{ai} = -E_{mgi}\sin\theta_r^e + E_{mgi}\sin\left(i\cdot\theta_r^e\right) + E_{mgi}\cos\left(i\cdot\theta_r^e\right) \\ e_b^* = \sum_{i=1}^{N} e_{bi} = -E_{mgi}\sin\left(\theta_r^e - 2\pi/3\right)\theta_r^e \\ \quad +E_{mgi}\sin\left[i\cdot\left(\theta_r^e - 2\pi/3\right)\right] + E_{mgi}\cos\left[i\cdot\left(\theta_r^e - 2\pi/3\right)\right] \\ e_c^* = \sum_{i=1}^{N} e_{ci} = -E_{mgi}\sin\left(\theta_r^e + 2\pi/3\right) \\ \quad +E_{mgi}\sin\left[i\cdot\left(\theta_r^e + 2\pi/3\right)\right] + E_{mgi}\cos\left[i\cdot\left(\theta_r^e + 2\pi/3\right)\right] \end{cases} \quad (5.13)$$

where $E_{mgi}$ and $i$ are the amplitudes of phase back-EMFs and the order number of harmonic components, respectively.

According to Fig. 5.9, the two closed-loops have the same structure and characteristics. By analyzing the cosine closed-loop as an example for the phase A, the weight $w_{h1}$ can be obtained by the integrator as [JUN11] as

$$w_{h1} = \int \left( k \cdot u_{an}^{*} \cdot \cos \omega_h t \right) dt \tag{5.14}$$

where $\omega_h$ is the frequency of harmonics and $k$ is referred to as the adaption value. The same working principle can also be extended to the sin closed-loop [JUN11]. The Laplace transform of (5.14) can be presented as

$$\begin{aligned} W_{h1}(s) &= L(w_{h1}) = L\left( \int k \cdot u_{an}^{*} \cdot \frac{e^{j\omega_h t} + e^{-j\omega_h t}}{2} \right) \\ &= \frac{k}{2s} \cdot \left[ u_{an}^{*}(s + j\omega_h) + u_{an}^{*}(s - j\omega_h) \right] \end{aligned} \tag{5.15}$$

where $L$ denotes that the Laplace transform of the expression within the parentheses is taken. Then, multiplying by the $\cos\omega_h t$, the Laplace transform of $f_{h1}$ can be obtained as

$$\begin{aligned} f_{h1}(s) &= \frac{1}{2} \cdot \left[ W_{h1}(s + j\omega_h) + W_{h1}(s - j\omega_h) \right] \\ &= \frac{k}{4(s + j\omega_h)} \cdot \left[ u_{an}^{*}(s) + u_{an}^{*}(s + 2j\omega_h) \right] + \frac{k}{4(s - j\omega_h)} \cdot \left[ u_{an}^{*}(s) + u_{an}^{*}(s - 2j\omega_h) \right] \end{aligned} \tag{5.16}$$

Similarly, the Laplace transform of $f_{h2}$ is given by

$$f_{h2}(s)=\frac{k}{4(s+j\omega_h)}\cdot\left[u_{an}^{*}(s)-u_{an}^{*}(s+2j\omega_h)\right]+\frac{k}{4(s-j\omega_h)}\cdot\left[u_{an}^{*}(s)-u_{an}^{*}(s-2j\omega_h)\right] \tag{5.17}$$

Since $u_{an}^{*}=u_{an}-f_{h1}-f_{h2}$, the Closed-loop transfer function of the ANF can be expressed as

$$Z(s)=\frac{u_{an}^{*}(s)}{u_{an}(s)}=\frac{s^2+\omega_h^2}{s^2+ks+\omega_h^2} \tag{5.18}$$

Based on the theoretical analysis, the harmonic compensation shown in Fig. 5.10 is of the similar principle as the second-order notch filter. The frequency $\omega_h$ is the main factor that the ANF can filter out the harmonic components. The value of $k$ is used to determine the settling time for the system response, e.g. the larger value of $k$, the system response will be faster.

The three-phase back-EMFs with/without the harmonic compensation scheme and the DFT analysis are given in Fig. 5.11. It can clearly be seen that the three-phase back-EMF waveforms have been significantly improved and become more sinusoidal, and the harmonics are effectively reduced by the ANF harmonic elimination method as shown in Fig. 5.11 (b), and the DTF analysis is shown in Fig. 5.11 (c).

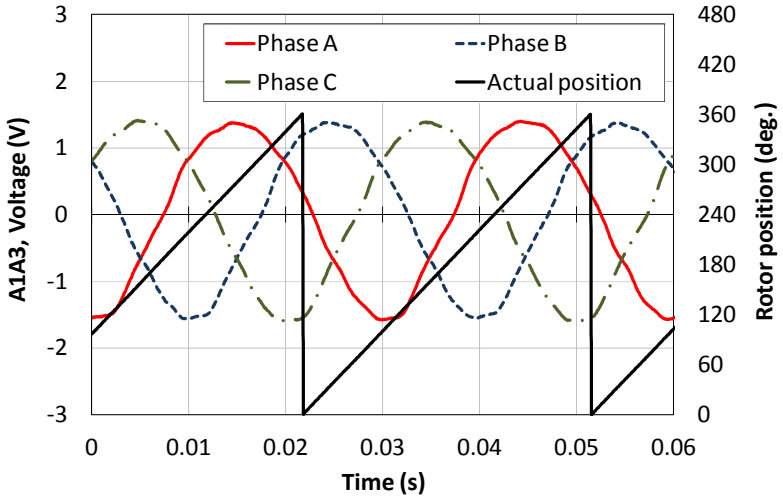


(a) Without harmonic compensation

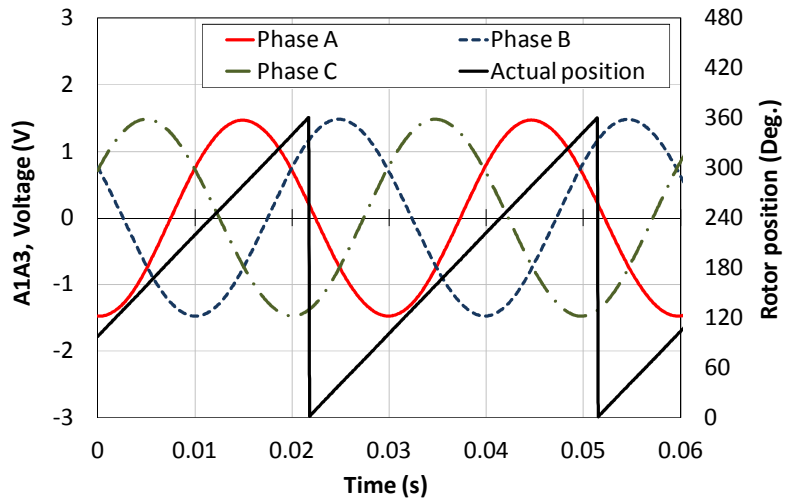


(b) With harmonic compensation

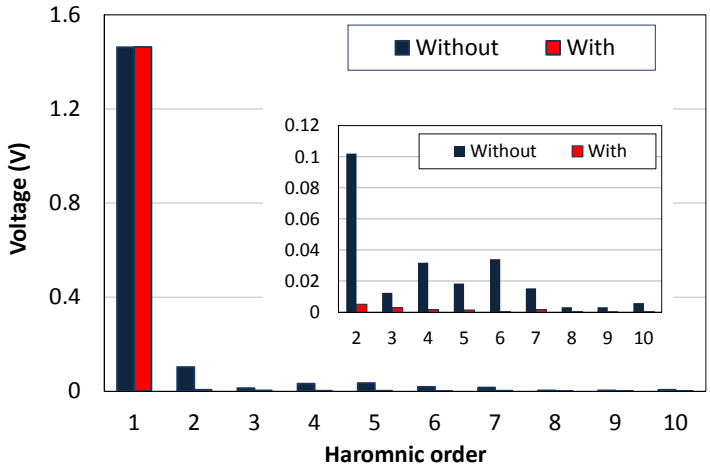


(c) Harmonic analysis – phase A

Fig. 5.11. Measured three-phase back-EMFs.

With the aid of back-EMF harmonic compensation method, the loci of the measured voltage and PM excitation flux-linkage, as can be seen in Figs. 5.12 and 5.13, respectively, the non-sinusoidal flux-linkage in Fig. 5.13 (a) is caused by the asymmetric back-EMFs shown in Fig. 5.12 (a). With the aid of proposed back-EMF harmonic compensation method, the loci of both voltages and flux-linkages have been significantly improved as can be seen in Figs. 5.12 (b) and 5.13 (b), respectively. Additionally, Figs. 5.12 (c) and 5.13 (c) show the DFT analysis for both the voltages and flux-linkages without/with the compensation. It can be clearly seen that those high order harmonics are eliminated.

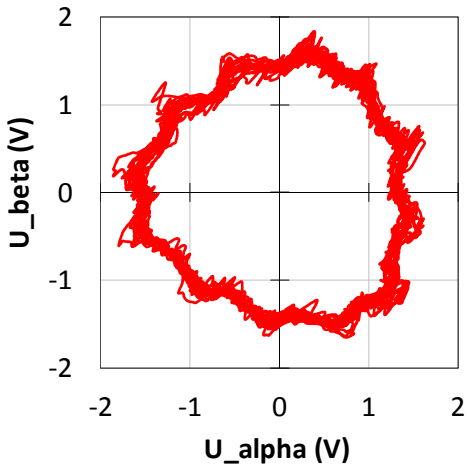


(a) Without harmonic compensation

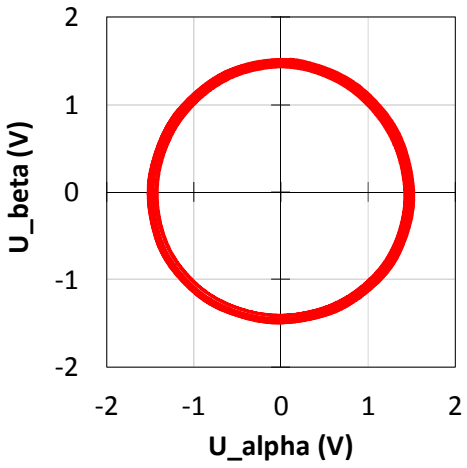


(b) With harmonic compensation

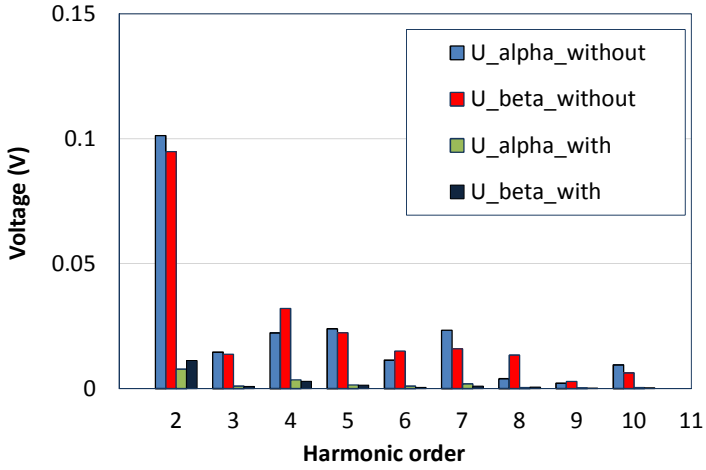


(c) Harmonics analysis

Fig. 5.12. Measured $\alpha$- and $\beta$-axis voltage loci - alternate poles wound.

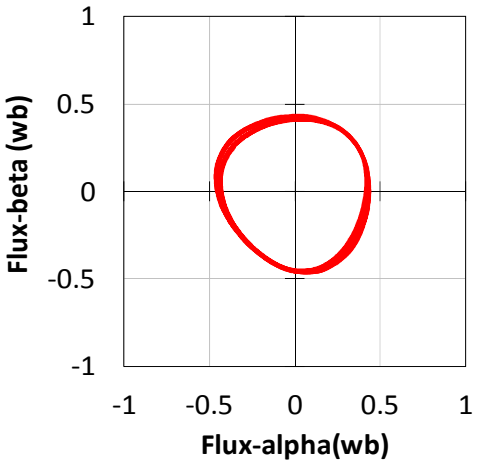


(a) Without harmonic compensation

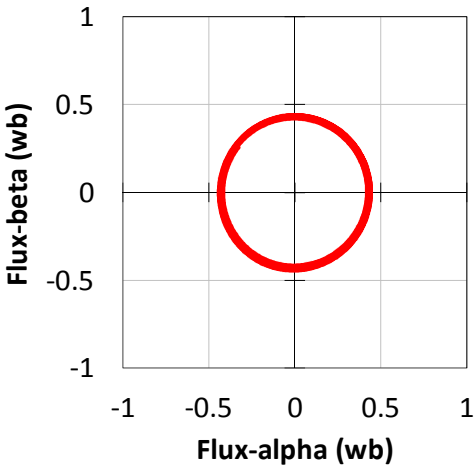


(b) With harmonic compensation

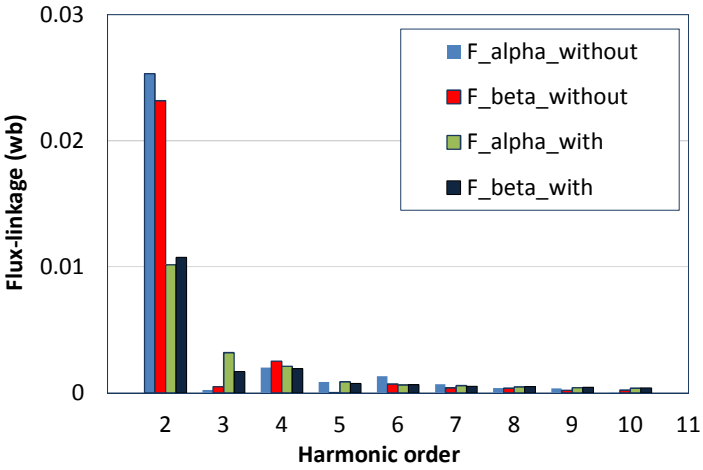


(c) Harmonics analysis

Fig. 5.13. Measured PM excitation flux-linkage loci - alternate poles wound. (a) Without harmonic compensation. (b) With harmonic compensation. (c) Harmonics analysis.

### 5.4.2 Proposed Rotor Position Observer and Positon Error Compensation

As mentioned earlier, there is an offset error in the conventional flux-linkage observer, which is caused by the integration operation of (5.10). Hence, the high-pass filter (HPF) which has a transfer function, $s/(s+\omega_0)$, is utilized as an integrator. Similarly, as the pure integrator is $1/s$, the combined transfer function becomes $1/(s+\omega_0)$, which is of the same principle as a LPF [SHE02][LUU03]. Then, based on (5.10), the estimated flux-linkage can be represented as

$$\begin{cases} \Psi_{f\alpha} = HPF\left[-\omega_0\Psi_s + \left(U_s - R_s \cdot I_s\right)\right] - I_s \cdot L_s \\ \Psi_{f\beta} = HPF\left[-\omega_0\Psi_s + \left(U_s - R_s \cdot I_s\right)\right] - I_s \cdot L_s \end{cases} \tag{5.19}$$

where $\omega_0$ is the cut-off frequency. According to (5.19), $\Psi_f$ is the total resultant PM excitation flux-linkage vector after low-pass filtering the stator flux-linkage. The LPF based flux-linkage observer can reduce the drift offset error, but still have some phase and amplitude errors in the total PM excitation flux-linkage. Moreover, it should be noted that all the machine parameters, i.e. $R_s$ and $L_s$, need to be accurate for ensuring the accuracy of rotor

position estimation. However, $R_s$ and $L_s$ usually vary when the operation and temperature conditions are different and difficult to obtain their actual values. All these issues may deteriorate the sensorless operation and result in inaccurate rotor position estimation.

In order to improve the accuracy of rotor position estimation, the rotor position error compensation based on the rotor flux-linkage is proposed and its procedure is described in Fig. 5.14.

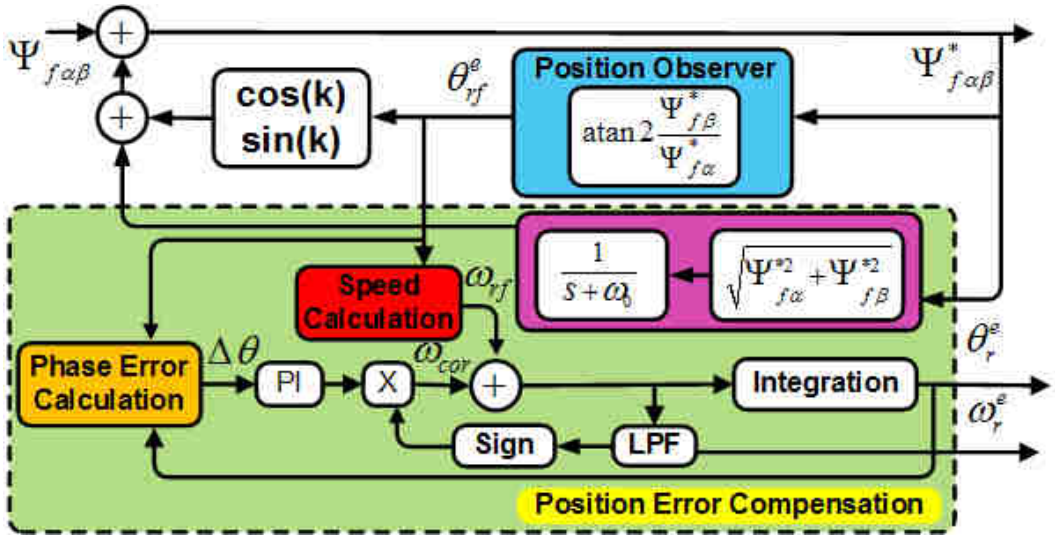


Fig. 5.14. Proposed rotor position error compensation scheme.

Basically, the PM flux-linkage is utilized as the two reference input signals, and the LPF ($1/s+\omega_0$) is also employed to make the proposed compensator more effective in the rotor position estimation. Hence, the compensating flux-linkage vector can be written as

$$\begin{cases} \Psi^{**}_{f\alpha} = \left( \dfrac{1}{s+\omega_0} \cdot \Psi^{*}_{f\alpha} \right) + \left( \cos \cdot k \left( \theta^{e}_{rf} \right) \right) \\ \Psi^{**}_{f\beta} = \left( \dfrac{1}{s+\omega_0} \cdot \Psi^{*}_{f\beta} \right) + \left( \sin \cdot k \left( \theta^{e}_{rf} \right) \right) \end{cases} \tag{5.20}$$

where $\omega_0$ presents the cut-off frequency, $\theta^{e}_{rf}$ is the estimated rotor position calculated from the compensating flux-linkage vector ($\Psi^{*}_{f\alpha}$ and $\Psi^{*}_{f\beta}$). $k$ is referred to as the adaption value.

Theoretically, the proposed rotor position compensation is low insensitive to the machine parameters. However, the position error compensation based on (5.20) can only exhibit a good performance at steady-state due to slow dynamic response. Since its dynamic response is not fast enough for the variable speed operation, a speed error based compensation is therefore proposed, as shown in Fig. 5.14.

Firstly, the phase difference needs to be calculated, which can be expressed as

$$\Delta\theta = \arcsin\left(\theta_{rf}^{e} - \theta_{r}^{e}\right) \tag{5.21}$$

where $\theta_{r}^{e}$ is the resultant rotor position with the aid of the proposed position error compensation. Thus, the phase difference $\Delta\theta$ is derived and can be utilized as the rotor position estimation error. In order to improve the dynamic operation, the rotor speed can be calculated from the steady-state compensator which is derived as

$$\omega_{rf} = \left[\theta_{rf}^{e}(k) - \theta_{rf}^{e}(k-1)\right] / \Delta t_{s} \tag{5.22}$$

where $k$ presents the sampling instant, and $\Delta t_s$ is referred to as the duration time.

Normally, $\Delta t_s$ can be the same as the PWM sampling time (2e-6s). Hence, the calculated speed can reflect the change of estimated rotor position. In principle, the estimated rotor speed $\omega_{rf}$ is calculated by the estimated rotor position of (5.20). Then, the speed correction $\omega_{cor}$ corresponding to the position estimation error can be obtained by the PI controller when the phase difference $\Delta\theta$ (5.21) exists, which can be presented as

$$\omega_{cor} = -\left(k_{p} + \frac{k_{i} \cdot T_{s}}{1 + s^{-1}}\right) \cdot \left[\Delta\theta \cdot sign\left(\omega_{r}^{e}\right)\right] \tag{5.23}$$

where $T_s$ is the sampling interval.

When the compensator is at steady state, the speed correction $\omega_{cor}$ will be converged to zero and the same to the phase difference $\Delta\theta$. Consequently, the average rotor speed with the speed error can also be compensated. Thus, a higher accuracy of rotor position estimation can be achieved by the integrator under both steady and dynamic states.

### 5.4.3 Sensorless Control in Steady-State Performance

According to the theoretical analysis and discussion in the previous section, the estimated rotor flux-linkage-based observer technique is implemented for the sensorless control operation in order to verify the robustness of proposed position error compensation together with the harmonic-EMF compensation scheme. The experimental validation will firstly be tested at steady-state and then followed by the dynamic-state operation.

Figs. 5.15 and 5.16 show the rotor position estimations and position errors of the all poles wound and the alternate poles wound machines at steady-state of constant speed (200 r/min). By applying the back-EMF harmonic compensation and the position estimation error enhancement schemes, the oscillation error and DC constant error in rotor position estimation based on all poles wound machine shown in Fig. 5.15 are reduced and become smoother. Hence, the high accurate rotor position estimation is achieved for the all poles wound machine.

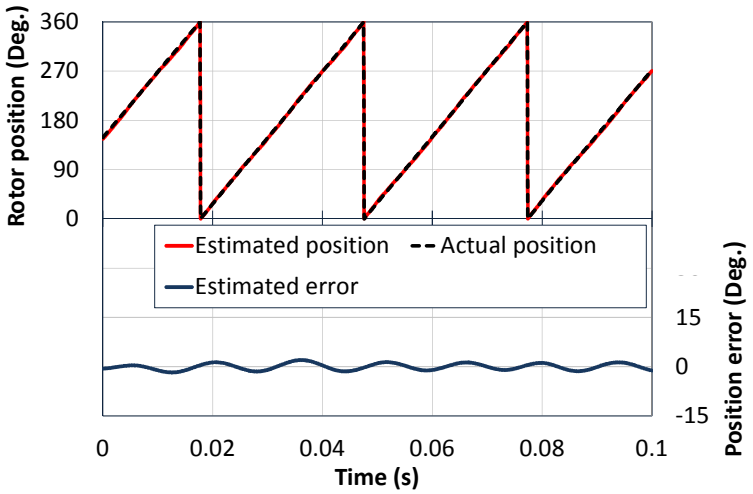


Fig. 5.15. Rotor position estimation at steady-state based on all poles wound machine with proposed harmonic and position estimation error compensation scheme, 200 r/min.

Furthermore, similar test is also conducted on the alterate poles wound machine. Firstly,

with the aid of adaptive harmonic compensation scheme, oscillation error caused by the asymmetric back-EMF can be reduced. However, the harmonic componsation scheme can only eliminate the error produced by the harmonics but the DC constant error still exists as shown in Fig. 5.16 (a). Hence, the accuracy of rotor position estimation is further improved by the proposed position error compensation method, Fig. 5.16 (b). It is obvious that the proposed position error compensator has significantly improved the accuracy of estimated rotor position.

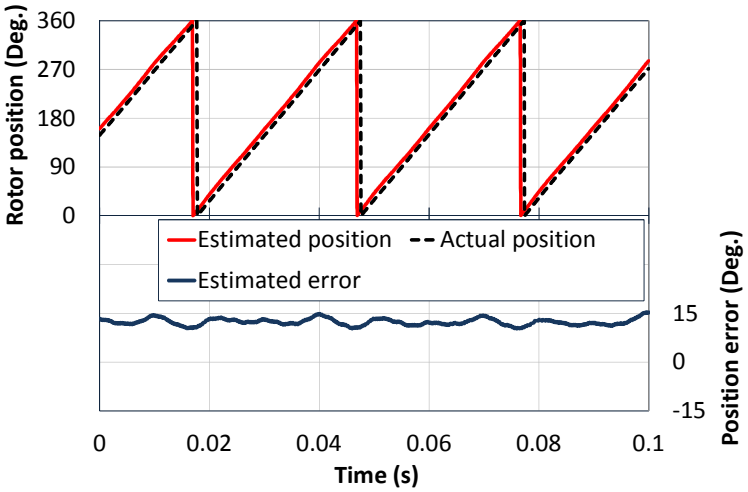


(a) With harmonic compensation

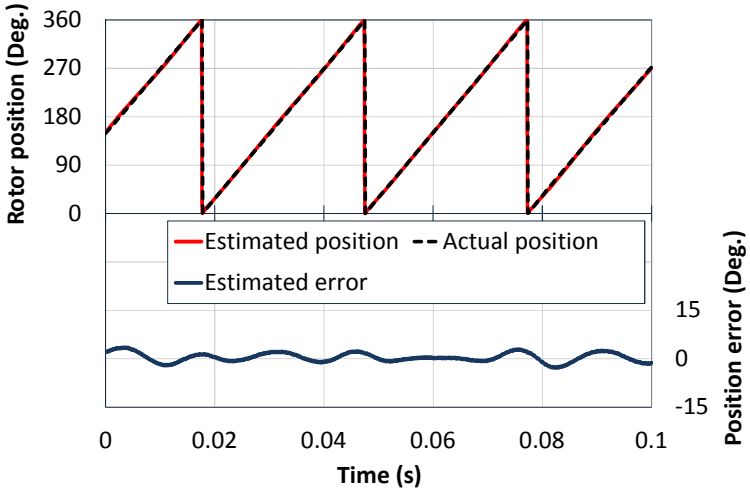


(b) With position error compensation

Fig. 5.16. Rotor position estimation at steady-state based on alternate poles wound machine topology, 200 r/min.

### 5.4.4 Sensorless Control in Dynamic-State Performance

The experimental dynamic performance for a step-change in rotor speed ranging from the 100 r/min to 200 r/min, is shown in Fig. 5.17. The rotor position and position error are estimated by the proposed position estimator based on the rotor flux-linkage with the aid of back-EMF harmonic compensation. Besides, the estimated rotor position error is significantly reduced and a better dynamic performance is also achieved by comparing with that of the conventional rotor position estimation shown in Figs. 5.7 and 5.8.

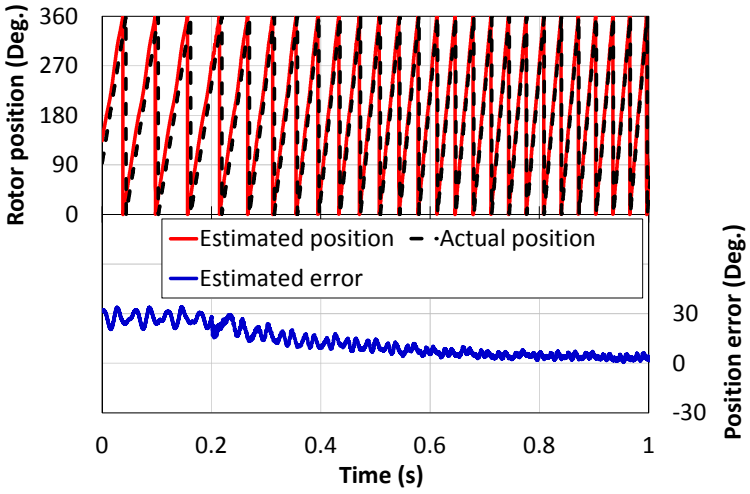


(a) Rotor position and error

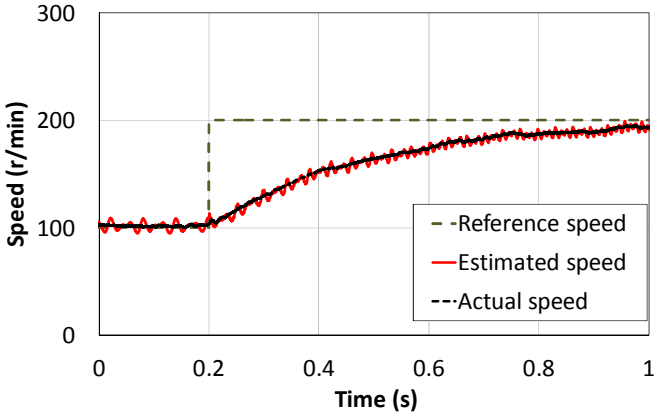


(b) Speed response

Fig. 5.17. Rotor position estimation with harmonics elimination and proposed position error compensation at dynamic-state based on alternate poles wound machine, 100-200 r/min.

### 5.4.5 Comparison of Sensorless Operations

The ability of position-tracking behavior is compared in Fig. 5.18. It shows that the proposed rotor position estimation exhibits lower position error and better performance than the conventional rotor position estimation without compensation, based on alternate poles wound machine topology, Fig. 5.18 (a). Moreover, by applying the proposed method to both the all poles wound and alternate poles wound machines, the similar performance can also be achieved as compared in Fig. 5.18 (b).

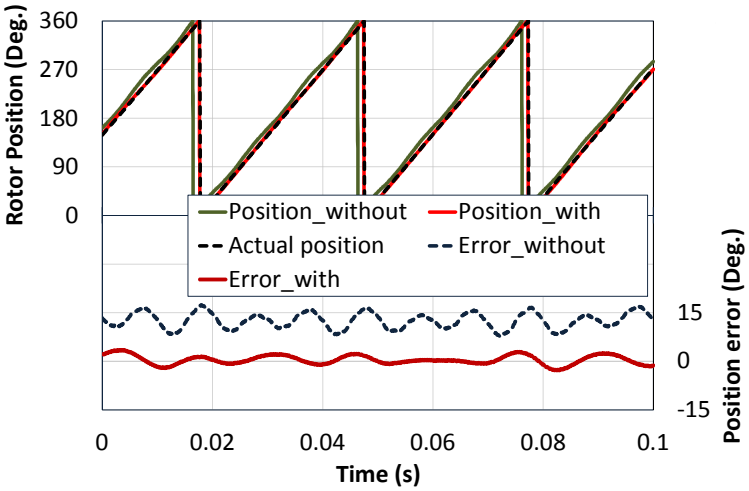


(a) Alternate poles wound machine with/without harmonic and position error compensation

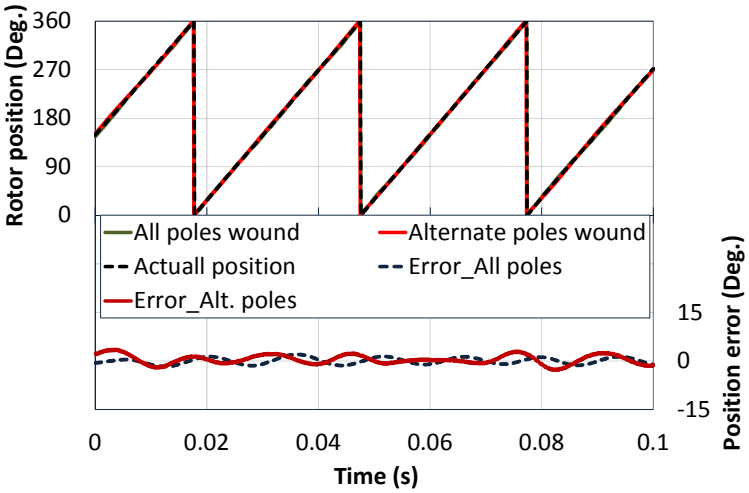


(b) Comparison between all poles wound and alternant poles wound machines.

Fig. 5.18. Comparison of rotor position estimations, 200 r/min.

Furthermore, the performance of proposed sensorless control under full-load condition is depicted in Fig. 5.19, from which it can be clearly seen that the position estimation error is increased for both machine topologies under full load operation due to the magnetic saturation induced by the increase of fundamental excitation current.

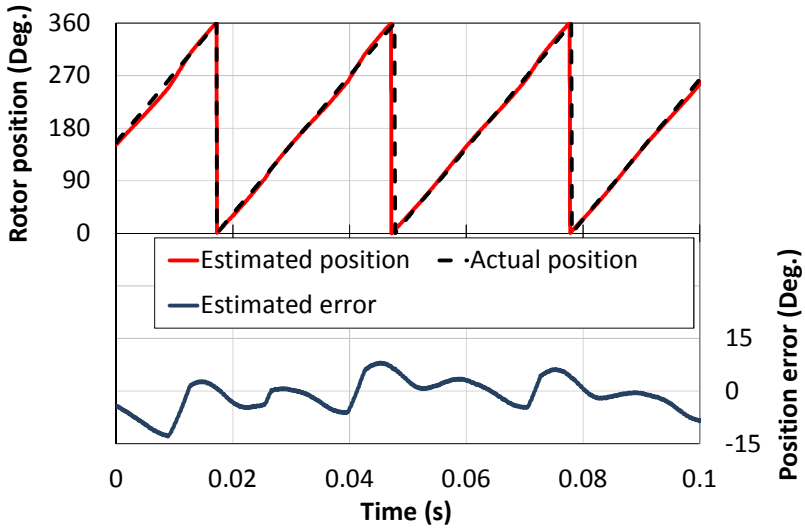


(a) Alternate poles wound machine

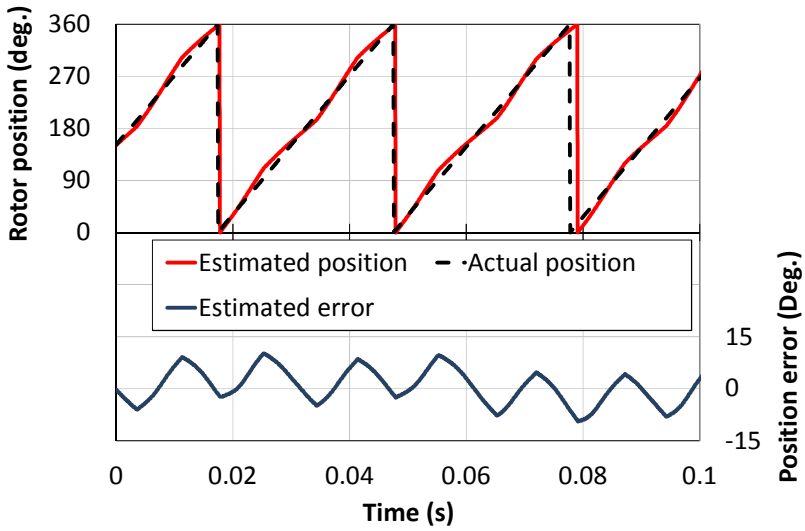


(b) All poles wound machine

Fig. 18. Rotor position estimation under full load condition, 200 r/min.

TABLE 5.1

COMPARSION OF CONVENTIONAL AND PROPOSED SENSORLESS CONTROL METHODS

| | Conventional method | Proposed method |
|---|---|---|
| Applicability | BLDC/BLAC | BLDC/BLAC |
| Standstill and low speed | NOT applicable | NOT applicable |
| Sensitivity of machine parameters | Sensitive | NOT sensitive |
| SNR | High | High |
| Steady-state operation | Medium | GOOD |
| Dynamic-state operation | Medium | GOOD |

## 5.5 Conclusion

This chapter has experimentally investigated the influence of asymmetric back-EMF on the sensorless control operation of the prototype SFPM machine under two different winding configurations, i.e. all poles wound and alternate poles wound. The all poles wound SFPM machine has a symmetrical back-EMF waveform, whilst the alternate poles wound SFPM machine exhibits an asymmetric back-EMF waveform.

The modified rotor flux-linkage observer with the aid of back-EMF harmonic elimination scheme can significantly reduce the oscillation error in the rotor position estimation and can achieve a higher accuracy in rotor position estimation. Additionally, the developed sensorless control strategy also has other advantages, i.e. easy implementation and less sensitive to the machine parameters.

Although the developed sensorless technique is applied to SFPM machines, it is equally

applicable to the DSPM machines and PMSMs with asymmetric and non-sinusoidal back-EMFs, e.g. caused by partial demagnetization of PMs and non-ideal magnet dimensions and properties etc.

## References


[CHE03] Z. Chen, M. Tomita, S. Doki, and S. Okuma, "An extended electromotive force model for sensorless control of interior permanent-magnet synchronous motors," *IEEE Trans. Ind. Electron.*, vol. 50, no. 2, pp. 288-295, 2003.

[CHE11] M. Cheng, W. Hua, J.Z. Zhang, and W.X. Zhao, "Overview of stator permanent magnet brushless machines," *IEEE Trans. Ind. Electron.*, vol. 58, no. 11, pp. 5087–510, 2011.

[CHE14] Z. Chen, J.B. Gao, F.X. Wang, Z.X. Ma, Z.B. Zhang and R. Kennel, "Sensorless control for SPMSM with concentrated windings using multi-signal injection method," *IEEE Trans. Ind. Electron*., vol.61, no.12, pp.6624-6634, Dec. 2014.

[HIN03] M. Hinkkanen, and J. Luomi, "Modified integrator for voltage model flux estimation of induction motors," *IEEE Trans. Ind. Electron.*, vol. 50, no. 4, Aug. 2003.

[HOQ97] E. Hoang, A.H. Ben-Ahmed, and J. Lucidarme, "Switching flux permanent magnet polyphased synchronous machines," *Proc. 7th Eur. Conf. Power Electronics and Applications*, vol. 3, pp. 903-908, 1997.

[HUA08] Wei Hua, Ming Cheng, Z.Q. Zhu, and D. Howe, "Analysis and optimization of back-EMF waveform of a flux-Switching permanent magnet motor," *IEEE Trans. Energy Conversion*, vol. 23, no. 3, pp. 727-733, Sep. 2008.

[IDR02] N. R. N. Idris, and A. H. M. Yatim, "An improved stator flux estimation in steady-state operation for direct torque control of induction machines," *IEEE Trans. Ind. Appl.*, vol. 38, no. 1, pp. 110–116, Jan./Feb. 2002

[JUN11] S. Y. Jung, and K. Nam, "PMSM control based on edge-field Hall sensor signals through ANF-PLL processing," *IEEE Trans. Ind. Electron.*, vol. 58, no. 11, pp. 5121–5129, Nov. 2011.

[Kim03] H. Kim, M.C. Harke, and R.D. Lorenz, "Sensorless control of interior permanent magnet machine drives with zero-phase lag position estimation," *IEEE Trans. Ind. Appl.*, vol. 39, no 6, pp. 1726- 1733, November/December

2003.

[LEE11] J.S. Lee, C.H. Choi, J.K. Seok, and R.D. Lorenz, “Deadbeat direct torque and flux control of interior permanent magnet machines with discrete time stator current and stator flux linkage observer,” *IEEE Trans. Ind. Appl.*, vol. 47, no. 4, July/Aug. 2011

[LIN14] T.C. Lin, L.M. Gong, J.M. Liu and Z.Q. Zhu "Investigation of saliency in switched-flux permanent magnet machine using high-frequency signal injection,” *IEEE Trans. Ind. Electron*., no.99, pp.5094-5104, 2014.

[LIU14] J.M. Liu and Z.Q. Zhu, “ Novel sensorless control strategy with injection of high-frequency pulsating carrier signal into stationary reference frame,” *IEEE Trans. Ind. Appl*., vol. 50, no. 4, pp. 2574-2583, July/Aug. 2014.

[LUU03] J. Luukko, M. Niemela, and J. Pyrhonen, “Estimation of the flux linkage in a direct-torque-controlled drive” *IEEE Trans. Ind. Electron.*, vol. 50, no. 2, pp. 283–287, Apr. 2003

[MAR97] M. Marchesoni, P. Segarich, and E. Soressi, “Simple approach to flux and speed observation in induction motor drives,” *IEEE Trans. Ind. Electron*., vol. 44, pp. 528-535, 1997.

[OWE10] R.L. Owen, Z.Q. Zhu, A.S. Thomas, G.W. Jewell and D. Howe, “Alternate poles wound flux-switching permanent-magnet brushless AC machines,” *IEEE Trans. Ind. Appl.*, vol. 46, no. 2, pp. 790–797, 2010.

[PEL11] G. Pellegrino, E. Armando, P. Guglielmi, “Direct flux vector control of IPM motor drives in the maximum torque per voltage speed range,” *IEEE Trans. Ind. Electron.*, vol. pp, no. 99, 2011.

[SHE02] J.X. Shen, Z.Q. Zhu, and D, Howe, “Improved Speed Estimation in Sensorless PM Brushless AC Drives, ” *IEEE Trans. Ind. Appl.*, vol. 38, no. 4, pp. 1072-1080 , 2002.

[WAN14] G. Wang, T. Li, G. Zhang, X. Gui, and D. Xu, “Position estimation error reduction using recursive-least-square adaptive filter for model-based sensorless interior permanent-magnet synchronous motor drives,” *IEEE Trans. Ind. Electron*., vol. 61, no. 9, pp. 5115–5125, Sep. 2014.

[WID75] B. Widrow, J. R. Glover, Jr., J. M. McCool, J. Kaunitz, C. S. Williams, R. H. Hearn, J. R. Zeidler, E. Dong, Jr., and R. C. Goodlin, “Adaptive noise cancelling: Principles and applications,” *Proc. IEEE*, vol. 63, no. 12, pp. 1692–1716, Dec. 1975.

[Y0014] Y.D. Yoon and S.K. Sul, “Sensorless control for induction machines based on square-wave voltage injection,” *IEEE Trans. Power Electron.*, vol.29, no.7, pp.3637-3645, July 2014.

[ZHA11] W. Zhao, M. Cheng, W. Hua, H. Jia, and R. Cao, “Back-EMF harmonic

analysis and fault-tolerant control of flux-switching permanent-magnet machine with redundancy," *IEEE Trans. Ind. Electron*., vol. 58, no. 5, pp. 1926–1935, May 2011.

[ZHU05] Z. Q. Zhu, Y. Pang, D. Howe, S. Iwasaki, R. Deodhar, and A. Pride, "Analysis of electromagnetic performance of flux-switching permanent magnet machines by nonlinear adaptive lumped parameter magnetic circuit model," *IEEE Trans. on Magn.*, vol. 41, no. 11, pp.4277-4287, Nov. 2005

[ZHU10] Z.Q. Zhu, J.T. Chen, "Advanced flux-switching permanent magnet brushless machines," *IEEE Trans. Magn.*, vol. 46, no. 6, pp. 1447–1453, 2010.

# CHAPTER 6

# IMPROVED SENSORLESS CONTROL BASED ON DIFFERENT WINDING CONFIGURATIONS USING HIGH-FREQUENCY SIGNAL INJECTION

## 6.1 Introduction

Newly developed switched-flux PM (SFPM) machine can be designed to have alternate poles wound structure, which provides fault tolerance and high power density, as reported and investigated in [OWE10]. However, due to the influence of asymmetric back-EMF in the alternate poles wound machine, higher torque ripples occur because of the back-EMF harmonics. [BAR10] analyzed the PM machine with two different rotor topologies and various winding configurations, e.g. dual three-phase windings, which can avoid the unbalanced radial forces and reduce the torque ripple under faulty operation. [BAR12] further investigated the sensorless position detection capability by the HF carrier signal injection at low speed and standstill in the PM machines controlled by dual inverters. In [LIN14], the authors validated the proposed method on a particular type of switched-flux PM machine having unknown parameters by investigating the primary saliency level and the influence of secondary saliency as well as the sensorless control performances. [XU13] proposed the square wave signal injection method to obtain the position information, which can simplify the signal process without using any low-pass filter (LPF).

Test Machine-II, the winding coil connections can be re-arranged into several types of machine winding configurations (MWC), such as all poles wound and alternate poles wound, single and dual three-phase topologies. Moreover, since Test Machine-II is usually based on an all poles wound topology, each phase comprising of four winding coils in series

connection, in which the winding coil connection (WCC) is changeable and have different machine saliency characteristics. This chapter investigates the influence of machine saliency on the sensorless control operation based on the different MWCs and WCCs. Firstly, by injecting a HF carrier signal, the machine saliency level can be evaluated experimentally. The influence of saliency on the HF signal injection-based sensorless operation for different MWCs and WCCs can then be investigated without any information of machine parameters. Further, by utilizing the mid-tapped winding wires, the machine saliency can be measured separately, in which the machine saliencies are similar to those as the machine based on the alternate poles wound machine.

However, a secondary saliency caused by the magnetic saturation or current harmonics may exist in the machine, due to which the sensorless control performance will deteriorate. Hence, the orthogonal signal based position tracking observer is proposed to improve the accuracy of rotor position estimation rather than utilizing existing position observer. Furthermore, the effectiveness of sensorless rotor position estimation based on different MWCs and WCCs will be demonstrated comparing those of the sensorless control performance without compensation, and the dual three-phase application. Finally, a simple position error compensation method will be proposed for improving the sensorless operation based on different winding coil connections.

## 6.2 Prototype Machine Topology and Difference Winding Configurations

### 6.2.1 Prototype Machine Topology

The 12/10 stator/rotor pole SFPM machine with the winding coil numbers shown in Fig. 6.1 has a simple machine structure and robust rotor. The conventional SFPM machine, Fig. 6.2 (a), is usually all poles wound (MWC-1) and each phase is comprised of four series-connected winding coils for each phase [ZHU05][HOA97], in which winding coils 1-4-7-10 are connected in series to form phase A, i.e. A1-A2-A3-A4 for phase A, and

similarly for phases B and C, as shown in Fig. 6.2 (a). Two winding coils of two phases are placed in each stator slot.

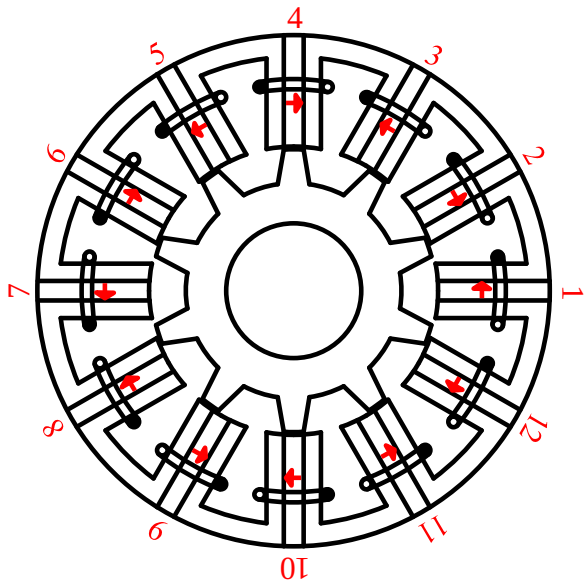


Fig. 6.1. Topologies of 12/10 stator/rotor with coils numbers.

### 6.2.1 Different Machine Winding Configurations

Unlike the conventional structure of MWC-1, Fig. 6.2 (a), the SFPM machine can also be alternate poles wound, MWC-2, Fig. 6.2 (b). In this case, coils 2, 4, 6, 8, 10, and 12 are removed and each phase only has two coils, e.g. coils 1 and 7 are connected in series for phase A, in which only one winding coil is contained in one stator slot. It is also possible to control Test Machine-II with dual 3-phase inverters, MWC-3, Fig. 6.2 (c), and MWC-4, Fig. 6.2 (d). In this case, there are two possible ways of winding connection. One is to form two three-phase windings by connecting coils 1 and 4 as A1 and A2, whilst coils 7 and 10 as A1* and A2*, Fig.1 (c). Another one is to form two three-phase windings by connecting coils 1 and 7 as A1 and A2, whilst coils 4 and 10 as A1* and A2*, Fig. 6.2 (d).

It should be noted that the relative positions between the stator poles and rotor poles are different in SFPM machines. By way of example, as can be seen from Fig. 6.1, the stator poles 1 and 7 are aligned with the rotor slots, whilst the stator poles 4 and 10 are aligned with the rotor poles. Consequently, in terms of the machine saliency, Test Machine-II having all

poles wound and alternate poles wound exhibit different machine saliency characteristics. Compared with the alternate poles wound machine (MWC-2), the saliency effect would be expected to be reduced due to a saliency cancelling effect in the all poles wound machine (MWC-1). Further, for dual 3-phase connections, the machine saliency of MWC-3 (Fig. 6.2 (c)) is expected to be identical to that of MWC-1 (Fig. 6.2 (a)), whilst the machine saliency of MWC-4 (Fig. 6.2 (d)) is expected to be identical to that of MWC-2 (Fig. 6.2 (b)).

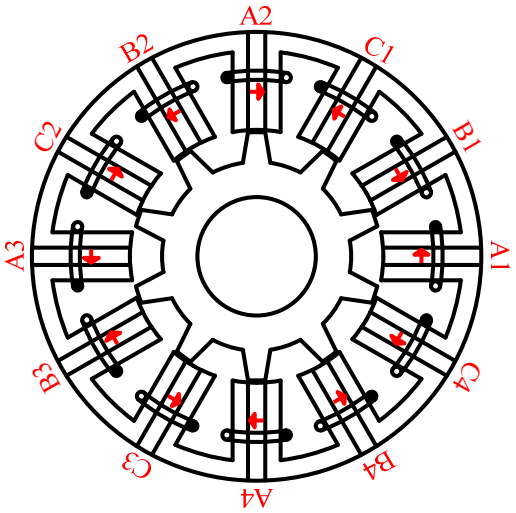


(a) MWC-1, All poles wound

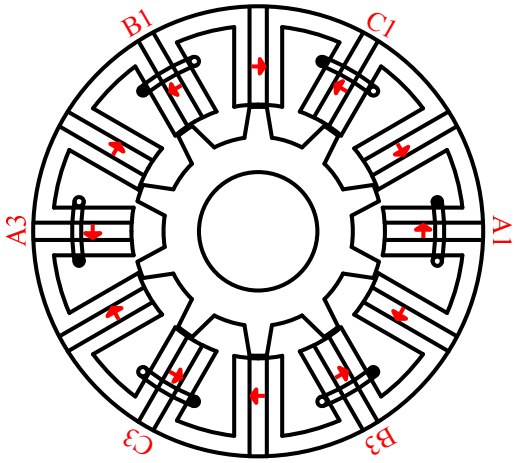


(b) MWC-2, Alternate poles wound

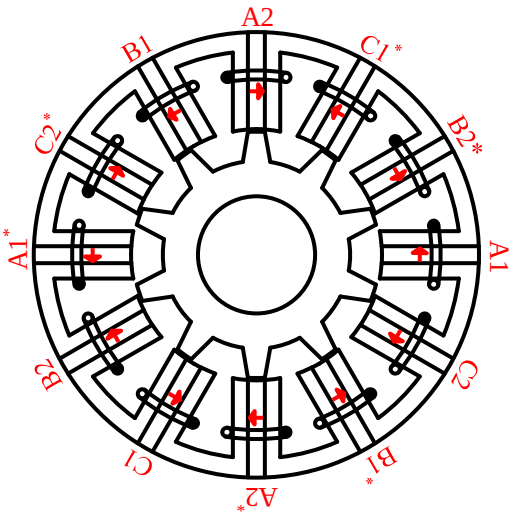


(c) MWC-3, dual three-phase connection 1

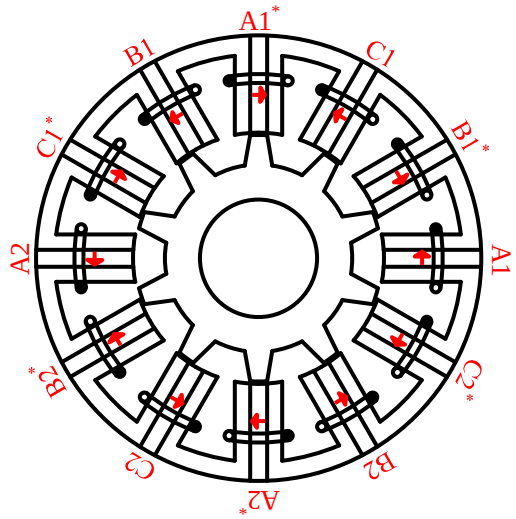


(d) MWC-4, dual three-phase connection 2

Fig. 6.2. Topologies of 12/10 stator/rotor SFPM machines based on winding coil arrangements.

Moreover, MWC-3 and MWC-4 can operate as two standard single three-phase machines with currents in phase, as shown in Fig. 6.3, rather than the $30^o$ phase shift as in the conventional dual three-phase PM machines. Hence, the currents will be the same for each set of single three-phase windings. These two MWCs have the benefit of a simple control algorithm, but exhibit complexity in the harmonic control algorithm.

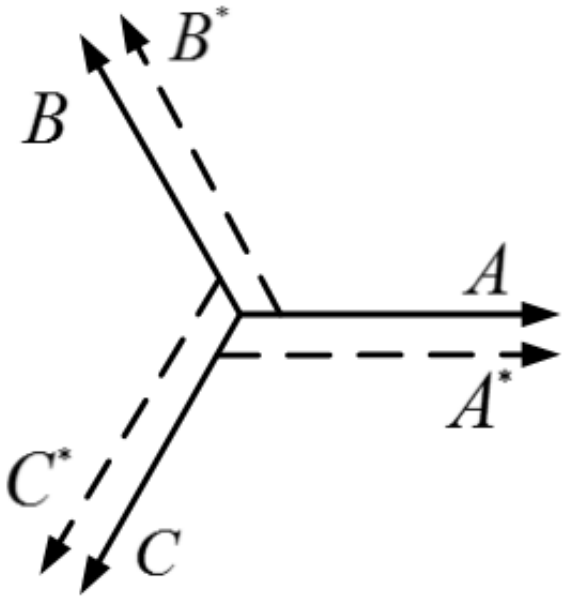


Fig. 6.3. Dual three-phase vector of winding arrangements.

## 6.3 Investigation of Machine Saliency Property

### 6.3.1 High-Frequency Permanent Magnet BLAC Machine Model

In terms of the evaluation of machine saliency, the saliency level will be investigated firstly based on different winding coil arrangements, which are shown in Fig. 6.1. Moreover, for illustration, the basic machine saliency investigation will be firstly based on MWC-1, which is the conventional structure of the prototype machine. For the PM machine with salient poles, the *d*-axis inductance is smaller than the *q*-axis inductance. Hence, it is possible to utilize the HF injection based method for the sensorless rotor position estimation. Then, the high-frequency voltage model for a PMSM in the synchronous *d*- and *q*- axis reference frame

can be expressed as (3.20). The definitions of these HF inductances are given by (4.1)

In general, $L_{dqh}$ and $L_{qdh}$ are different due to the influence of cross-saturation. However, $L_{dqh}$=$L_{qdh}$ is considered in many practical applications. Moreover, $L_{dh}$ and $L_{qh}$ are also different because of the rotor geometric and magnetic saturations. The difference between $L_{dh}$ and $L_{qh}$ which is $L_{qh}$-$L_{dh}$ indicates the saliency level of machine. Furthermore, if $L_{qh}$-$L_{dh}$ is constant and large enough, the machine would be suitable for the method of HF injection. Hence, the saliency level has to be investigated first in order to implement the sensorless operation. Therefore, to analyze the saliency of the prototype machine, a simple experimental investigation is proposed in the next section.

### 6.3.2 Primary Saliency Evaluation

To evaluate the machine saliency level, a simple measurement method for the primary saliency is employed as introduced in Chapters 3 and 4. The rotor position has to be locked stationary ($\theta_r = 0^o$), and the injection signal is $U_c$ = 8V, $f_c$ = 550Hz. Also, the speed rotational direction in the virtual synchronous reference frame is negative, Fig. 4.3. Then, the phase angle of HF *d*- and *q*-axis carrier current responses will be the same. Hence, the amplitude-modulated carrier current response can be obtained as illustrated in Fig. 6.4, which is based on MWC-1.

To obtain the amplitude of carrier current response from the carrier current response, the synchronous detection method [MAD95] and a low-pass filter (LPF) are applied. Therefore, the amplitude of position-dependent carrier current response can be obtained as shown in Fig. 6.4 (b) by (3.25). The carrier current circle by machine saliency is illustrated in Fig. 6.4 (c) where the radius of saliency circle $I_n$ indicates the saliency level, and the center location of saliency circle is determined by $I_p$. The higher value of $I_n$ indicates the higher saliency level. The machine saliency clearly exists. Therefore, the HF injection-based sensorless control can be applied to the prototype machine based on different MWCs.

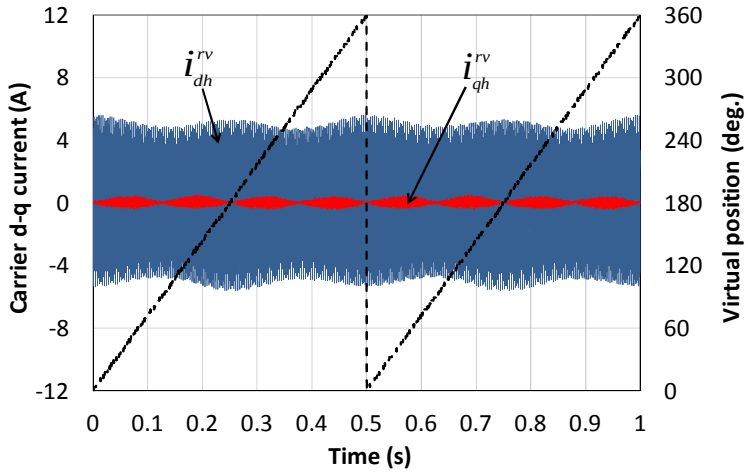


(a) Measured total carrier current responses

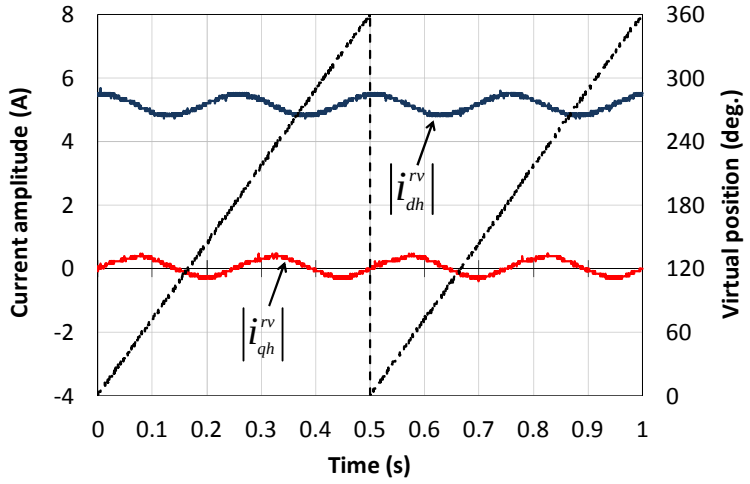


(b) Amplitude variation of carrier current response

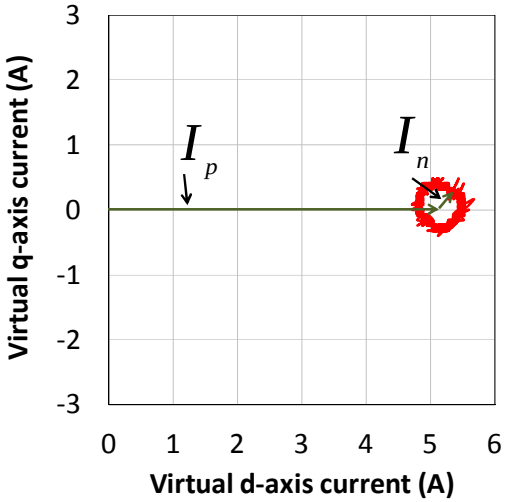


(c) Locus of carrier current circle by machine saliency

Fig. 6.4. Measured HF carrier currents in virtual *d-q* reference frame based on MWC-1, when $i_d$ = 0A, and $i_q$ = 0A.

### 6.3.3 Experimental Evaluation of Machine Saliency

From the foregoing theoretical analysis of primary saliency in the previous section, the machine saliency based on each MWCs needs investigate first in order to prove the influence of primary saliency or secondary saliency (multiple saliencies) [DEG98] [ROC10] [KIM04] on the sensorless control operations.

With an aid of accurate rotor position information from an encoder, a HF pulsating carrier sinusoidal voltage signal (6) ($U_c$ = 4V, $f_c$ = 550Hz) is injected into the virtual synchronous reference frame ($d^{vr}$-$q^{vr}$), while the machine in the speed close-loop control at low speed in the sensored mode, 25r/min, $i_q$ = 1.2A. The $d$- and $q$-axis carrier current responses and the carrier current circles due to machine saliency can be measured as shown in Figs. 6.5 and 6.6. The carrier current response is basically modulated as two cycle per single electrical rotor position. Also, as mentioned earlier, the higher amplitude indicates the higher saliency level. Thus, it can be found from the experimental results that the amplitude of carrier current of MWC-2 and MWC-4 shown in Figs. 6.5, 6.6 (b) and (d) are bigger than MWC-1 and MWC-3 as comparing in Figs. 6.5, 6.6 (a) and (c), due to the saliency cancellation in MWC-1 and MWC-3. Theoretically, MWC-1 should have identical saliency level as MWC-3, whilst MWC-2 should also have identical saliency level as MWC-4, the difference being the manufacturing tolerance.

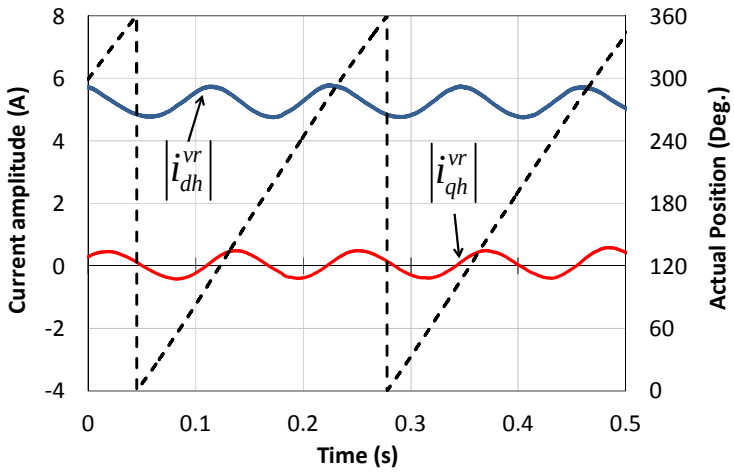

(a) MWC-1

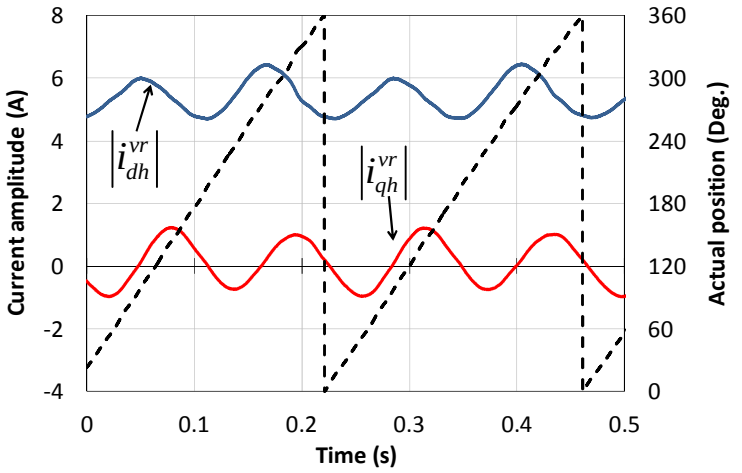


(b) MWC-2

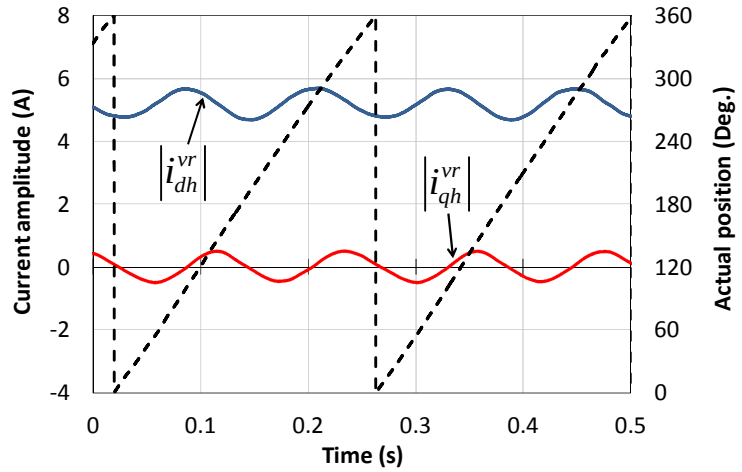


(c) MWC-3

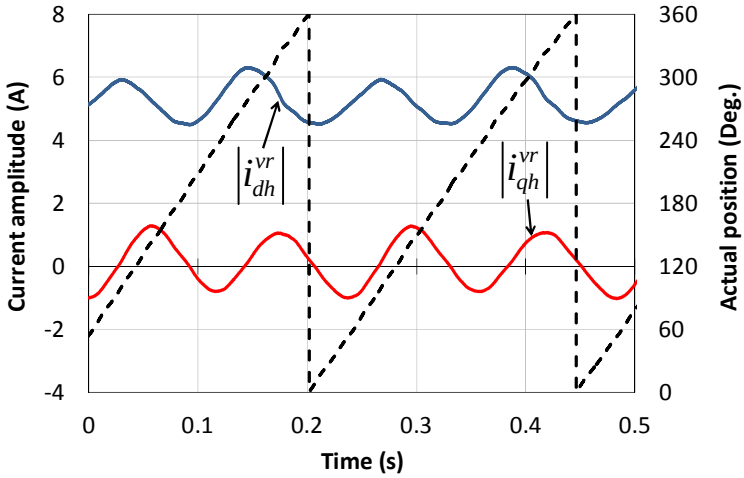


(d) MWC-4

Fig. 6.5. Amplitude variation of carrier current response various with actual rotor position based on four types of MWCs, 25 r/min.

Additionally, an interesting phenomenon can be found in MWC-2 and MWC-4 as shown in Figs. 6.5 (b) and (d), the amplitudes of measure *d*- and *q*-axis carrier current responses are non-constant, which is caused by the effect of multiple saliencies and will deteriorate the accuracy in sensorless rotor position estimation. On the other hand, when the winding coils 1, 4, 7 and 10 are all in series connection (MWC-1), the additional harmonics can be cancelled as shown in Figs. 6.6 (a), and similar situation is for winding coils 1 and 4 or 7 and 10 in series connection (MWC-3) as shown in Fig 6.6 (c) due to the coil compensation effect [HUA08].

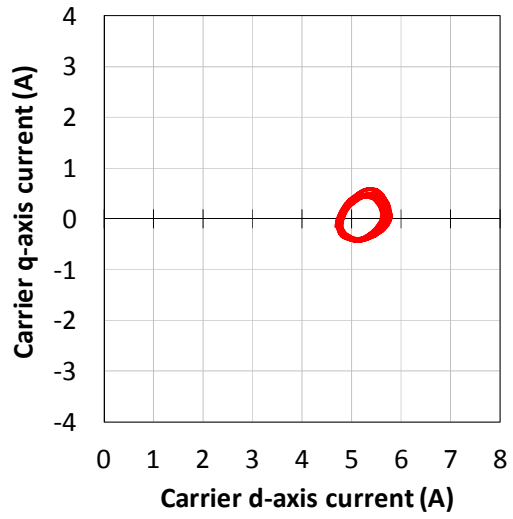


(a) MWC-1

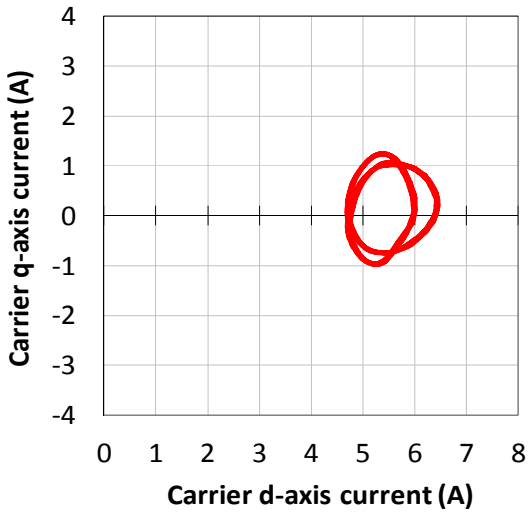


(b) MWC-2

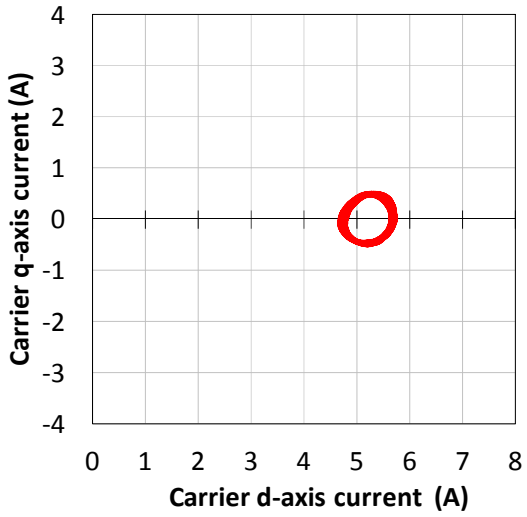


(c) MWC-3

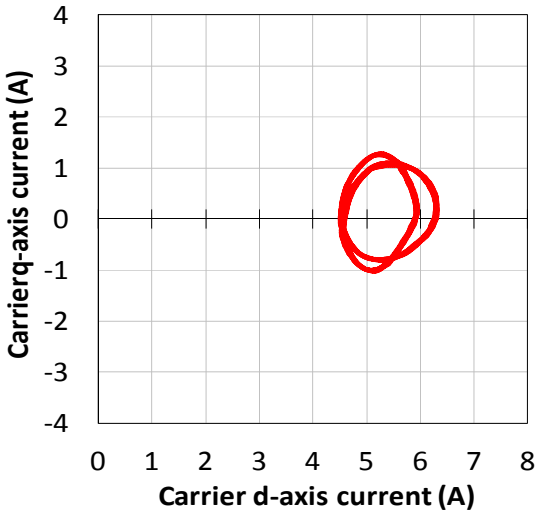


(d) MWC-4

Fig. 6.6. Machine carrier current circles due to machine saliency based on four types of MWCs, 25 r/min.

Considering the machine saliency information being determined by the radius of carrier current circle $I_n$, the measured radius of carrier current circle $I_n$ for the prototype machine under different winding configurations and load (current) conditions can be obtained, as shown in Fig. 6.7. Although the saliency level is not too large, it is still suitable for the HF carrier signal injection based sensorless control technique. As can be seen, MWC-1 has similar saliency level as MWC-3, whilst MWC-2 also has similar saliency level as MWC-4.

As mentioned earlier, the differences between MWC-1 and MWC-3, or MWC-2 and MWC-4 are due to the manufacturing tolerances, as well as the measurement errors. Also, different saliency characteristics are exhibited. The lower saliency for MWC-1 and MWC-3 are due to saliency cancelling effect, and the higher saliency for MWC-2 and MWC-4 are due to multiple saliencies effect caused by the magnetic saturation.

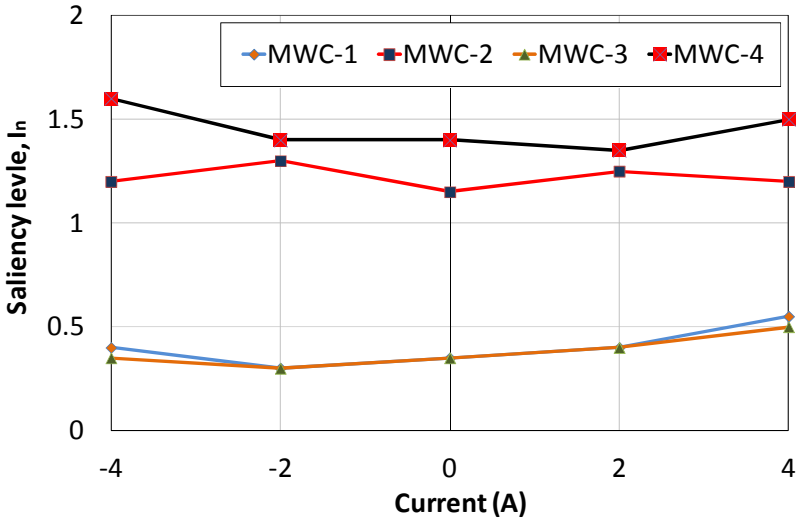


(a) *d*-axis

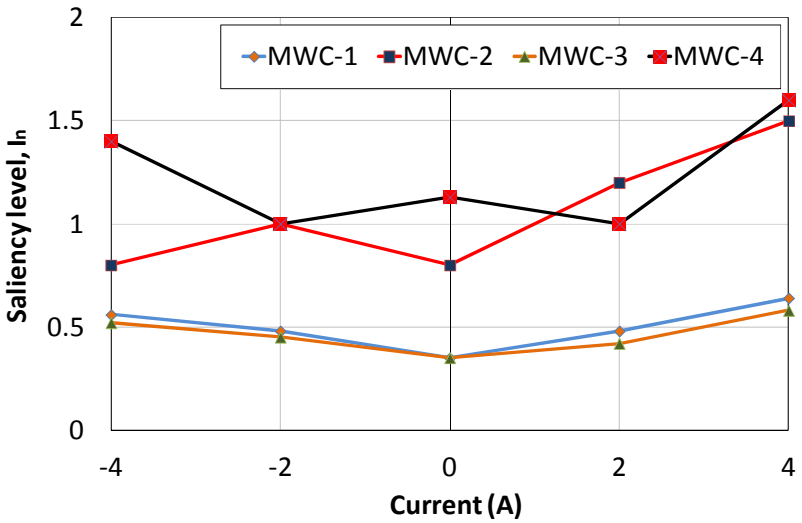


(b) *q*-axis

Fig. 6.7. Measured radius of carrier current circle by machine saliency, $I_n$, various with *d*- and *q*- axis.

## 6.4 Sensorless Rotor Positon Estimations

A dSPACE platform together with a 12/10 stator/rotor poles prototype SFPM machine shown in Fig. 2.11 are employed to evaluate the saliency level and sensorless control operations based on different MWCs. The overall sensorless control scheme based on the HF injection technique is described in Fig. 6.8. The testing machines are introduced in Section II, and the parameters are listed in Table 2.2. The load machine is a 500W brushed DC machine, and an encoder with high resolution of 2048PPR is equipped on the test-rig to provide the actual position information to the whole control system.

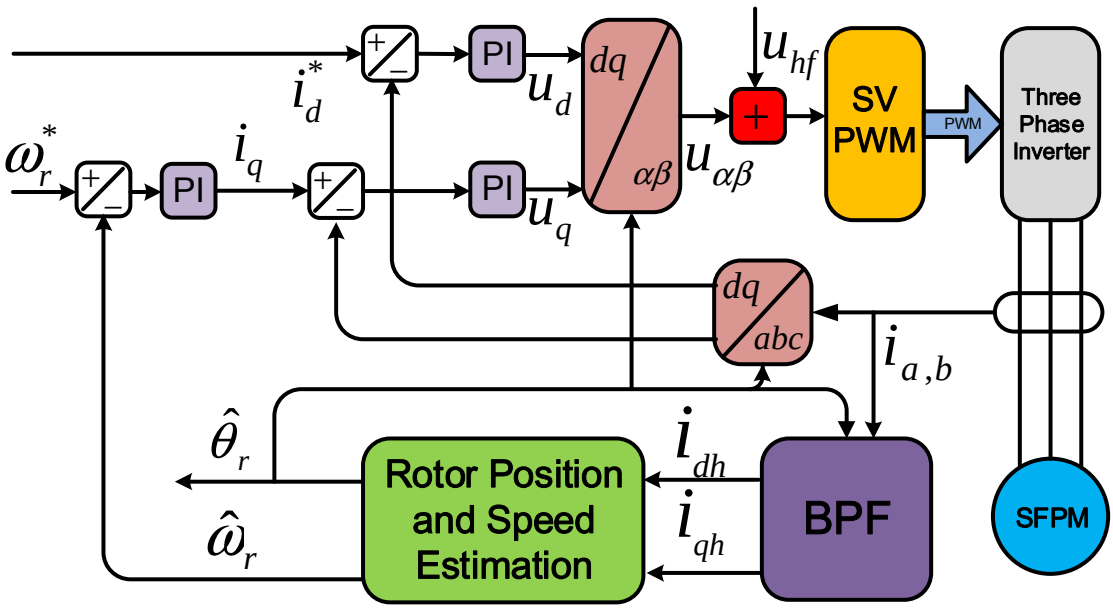


Fig. 6.8. Overall sensorless control scheme

In order to validate the effectiveness of sensorless control operations based on the four types of MWCs, the HF pulsating carrier voltage signal injection method is applied to the prototype SFPM machine. The testing conditions of injection voltage and frequency for MWC-1 are $U_c$ = 8V, $f_c$ = 550Hz, and MWC-2, MWC-3 and MWC-4 are $U_c$ = 4V, $f_c$ = 550Hz for each winding set, which is injected into the estimated synchronous reference frame,

and the rotor position information can be obtained from the carrier current response. Moreover, the winding coil connections based on MWC-1 and MWC-2 are controlled as a single three-phase machine, and coil arrangements based on MWC-3 and MWC-4 are operated as a dual three-phase machine

### 6.4.1 Existing Rotor Position Tracking Estimator

Before the rotor position estimation, the position dependent carrier current response should be extracted from the carrier current response by using the synchronous reference frame filter [DEG98]. However, since the noise on input signal has a great impact on the estimated rotor position, the position tracking observer is popular in the sensorless rotor position estimation. In addition, the PI controller is utilized in the sensorless rotor position tracking observer [HAR00] due to its fast response in the dynamic operation, but may slow down the response in steady state. The basic principle of position tracking observer is described in Fig. 6.9.

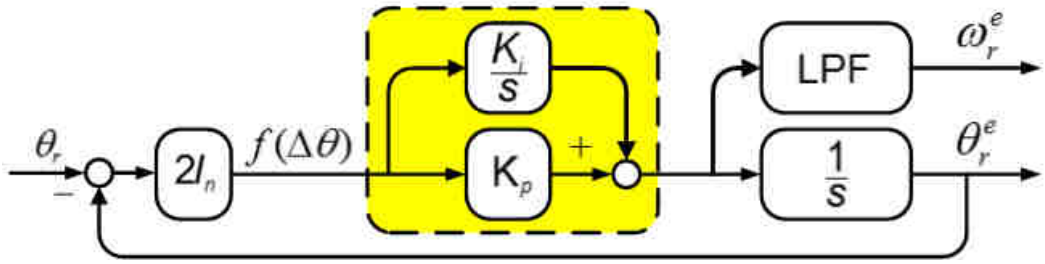


Fig. 6.9. Existing rotor position tracking observer.

Using the *q*-axis amplitude-modulated carrier current as the input signal to the position tracking observer, which can be expressed as

$$f\left(\Delta\theta\right)=\left|i_{qh}^{e}\right|=I_n\sin 2\left(\theta_r-\theta_r^e\right) \tag{6.1}$$

According to Fig. 6.9, when $I_n\sin 2\left(\theta_r-\theta_r^e\right)$ is small enough, the assumption that $I_n\sin 2\left(\theta_r-\theta_r^e\right)\approx 2I_n\left(\theta_r-\theta_r^e\right)$ is considered, and then the transfer function between the actual and estimated rotor positions, can be expressed as

$$\frac{\theta_r^e}{\theta_r} = \frac{2I_n k_p \cdot s + 2I_n k_i}{s^2 + 2I_n k_p \cdot s + 2I_n k_i} \tag{6.2}$$

where $I_n$ is load-dependent, and the values of $k_p$ and $k_i$ of PI controller can be on-line adjusted according to $I_n$ in order to maintain the bandwidth in the position tracking observer. To overcome the drawback of the observer, the improved position estimator will be discussed in the next section.

### 6.4.2 Improved Rotor Position Tracking Estimator

In order to enhance the accuracy of rotor position estimation, the orthogonal Phase-Locked Loop (PLL) observer shown in Fig. 6.10 can be utilized [JUN11]. The basic principle of PLL tracking observer is to synchronizes the input and output signals in phase, and use PI controller to force the generated sinusoidal waveform to follow the input signal. The advantage of PLL observer is that the harmonics occur in the carrier current response can be reduced and its phase angle contains the position information, which can be used for the position estimation error compensation.

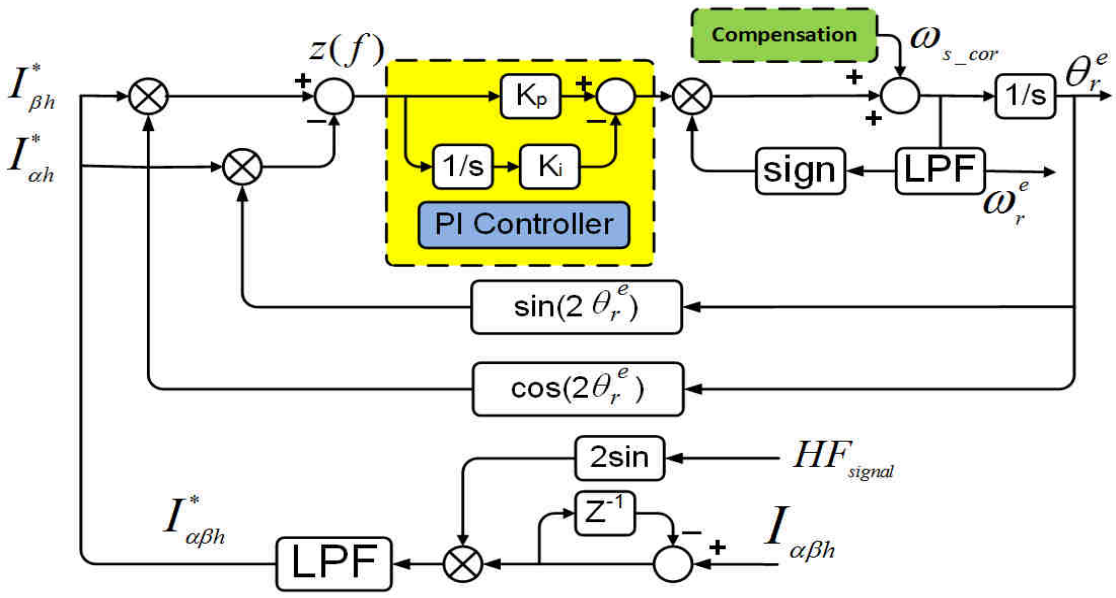


Fig. 6.10. Application of orthogonal PLL position tracking observer.

Generally, the frequency in the conventional PLL observer is fixed, but the fundamental

frequency is dependent on the speed of the machine. Hence, the orthogonal PLL tracking observer can be employed to avoid such an issue and to obtain a better performance than that of the conventional PLL observer. The high-frequency voltage equations can be presented as

$$\begin{bmatrix} u_{dh} \\ u_{qh} \end{bmatrix} = \begin{bmatrix} L_{dh} & 0 \\ 0 & L_{qh} \end{bmatrix} p \begin{bmatrix} i_{dh} \\ i_{qh} \end{bmatrix} \tag{6.3}$$

The transformation matrix can be given as

$$\begin{bmatrix} u_{dh} \\ u_{qh} \end{bmatrix} = \begin{bmatrix} \cos(\Delta\theta) & -\sin(\Delta\theta) \\ \sin(\Delta\theta) & \cos(\Delta\theta) \end{bmatrix} \begin{bmatrix} u_{\alpha h} \\ u_{\beta h} \end{bmatrix} \tag{6.4}$$

Meanwhile, the high-frequency carrier currents can be expressed as

$$\begin{bmatrix} i_{dh} \\ i_{qh} \end{bmatrix} = \begin{bmatrix} \cos(\Delta\theta) & \sin(\Delta\theta) \\ -\sin(\Delta\theta) & \cos(\Delta\theta) \end{bmatrix} \begin{bmatrix} i_{\alpha h} \\ i_{\beta h} \end{bmatrix} \tag{6.5}$$

From (6.3), and (6.5), (6.5) can be represented as

$$\omega_h \begin{bmatrix} L_{dh} & 0 \\ 0 & L_{qh} \end{bmatrix} \begin{bmatrix} \cos(\Delta\theta) & \sin(\Delta\theta) \\ -\sin(\Delta\theta) & \cos(\Delta\theta) \end{bmatrix} \begin{bmatrix} i_{\alpha h} \\ i_{\beta h} \end{bmatrix} \tag{6.6}$$

where $\omega_h$ is the angular frequency of high-frequency carrier current. Then, the high-frequency can be derived as

$$\begin{bmatrix} i_{\alpha h} \\ i_{\beta h} \end{bmatrix} = \frac{1}{\omega_h} \begin{bmatrix} \cos(\Delta\theta) & \sin(\Delta\theta) \\ -\sin(\Delta\theta) & \cos(\Delta\theta) \end{bmatrix}^{-1} \begin{bmatrix} L_{dh} & 0 \\ 0 & L_{qh} \end{bmatrix}^{-1} \times \begin{bmatrix} \cos(\Delta\theta) & -\sin(\Delta\theta) \\ \sin(\Delta\theta) & \cos(\Delta\theta) \end{bmatrix} \begin{bmatrix} u_{\alpha h} \\ u_{\beta h} \end{bmatrix} \tag{6.7}$$

After low-pass filtering, the carrier current $I^*_{\alpha h}$ and $I^*_{\beta h}$ are applied to the orthogonal PLL as input signals, which are filtered out from the carrier current response by low-pass filters. It should be noted that $z(f)$ is the phase detector output [HAR00][JUN11], and the second-order harmonic is ignored in the orthogonal PLL observer in which the value of PI gains can be easily determined. Hence, the two input signals can be presented as

$$\begin{aligned} I^*_{\alpha h}(s) &= A\sin 2\left(\omega_s t + \frac{\pi}{2}\right) = A\cos 2\omega_s t \\ I^*_{\beta h}(s) &= A\sin 2\omega_s t \end{aligned} \tag{6.8}$$

where $I^*_\alpha$(s) and $I^*_\beta$(s) are the quadrature input signals. $\omega_s$ is referred to the fundamental frequency of the input signal, and A is the amplitude of the fundamental. Then, $z(f)$ is equal to

$$z(f) = I^*_{\beta h}(s)\cos 2\omega^*_s t - I^*_{\alpha h}(s)\sin 2\omega^*_s t = A\sin 2\left(\left(\omega_s - \omega^*_s\right)t\right) \tag{6.9}$$

It should be noted that $z(f)$ is the phase detector output [HUA08][DEG98], and the second-order harmonic is ignored in the orthogonal PLL observer in which the value of PI gains can be easily determined. In order to compensate the position estimation error, the phase difference needs calculate first, which can be expressed as

$$\Delta\theta = \theta^e_r - \theta_r \tag{6.10}$$

where $\theta_r$ and $\theta^e_r$ are the actual and estimated rotor positions. Then, the speed error correction $\omega_{s\_cor}$ corresponding to the position estimation error can be obtained by the PI controller if the phase difference $\Delta\theta$ (6.10) exists, which can be presented as

$$\omega_{s\_cor} = -\left(k_p + \frac{k_i \cdot T_s}{1+s^{-1}}\right)\cdot\left[\Delta\theta \cdot sign\left(\omega^e_r\right)\right] \tag{6.11}$$

where $T_s$ is the sampling interval. After the stability of compensator at steady state, the speed correction $\omega_{s\_cor}$ will converge to zero and the same to the phase difference $\Delta\theta$. Consequently, the average rotor speed with the speed error can also be compensated, and the accuracy of rotor position estimation can be enhanced. The effectiveness of sensorless operations will be evaluated in the next section.

### 6.4.3 Validation of Sensorless Control Operations

Several experiments will be carried out to validate the effectiveness of sensorless control operations based on the four types of MWCs.

**A. Sensorless Control Performance at Steady-State**

Fig. 6.11 shows the sensorless rotor position estimations in steady-state by utilizing the existing rotor position tracking observer, which rotates at a constant speed, 25 r/min. The experimental results show good position tracking performances, but still exhibit the position estimation error such as significant oscillation error due to some additional current ripple

occurred in the carrier current response by the multiple saliencies (Fig. 6.11 (b) and (d)), and the DC error which may be caused by the cross-coupling effect or phase shifting in phase angle. By comparison, although MWC-2 and MWC-4 both have higher saliency level than that of machines based on MWC-1 and MWC-3, the accuracy of rotor positon estimation is still deteriorated by the influence of multiple saliencies which are already explained in Figs. 6.1 and 6.6. Hence, MWC-1 and MWC-3 are more accurate in the sensorless rotor position estimation.

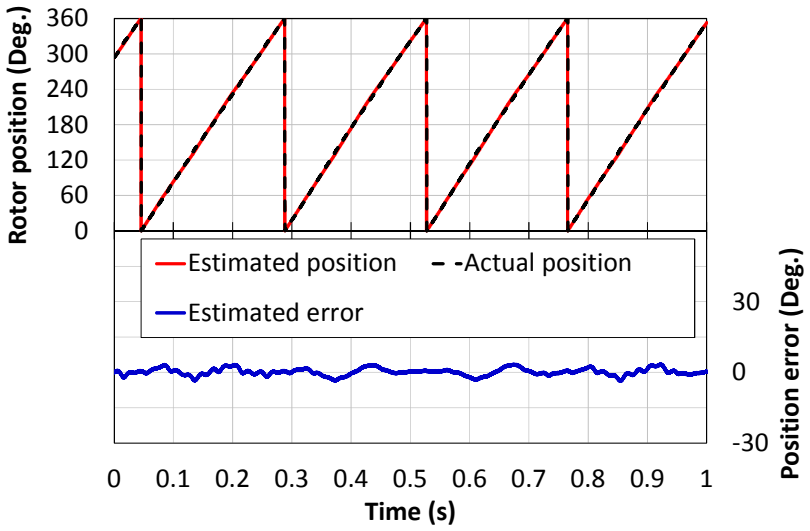


(a) MWC-1

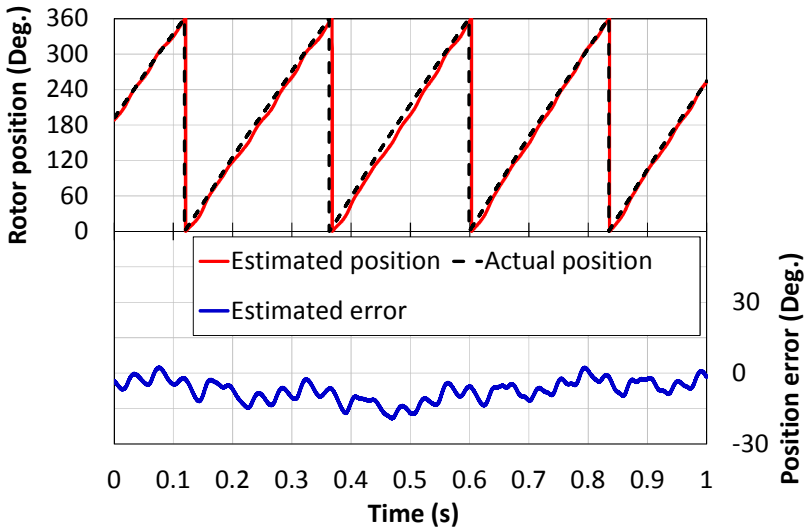


(b) MWC-2

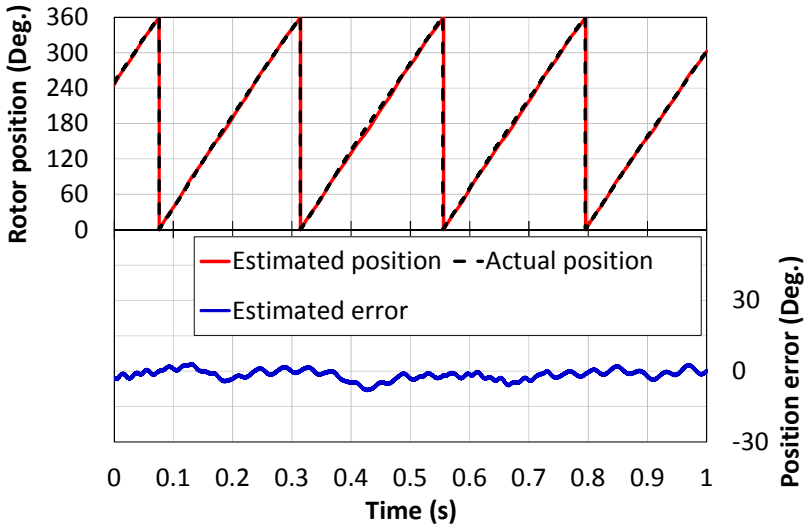


(c) MWC-3

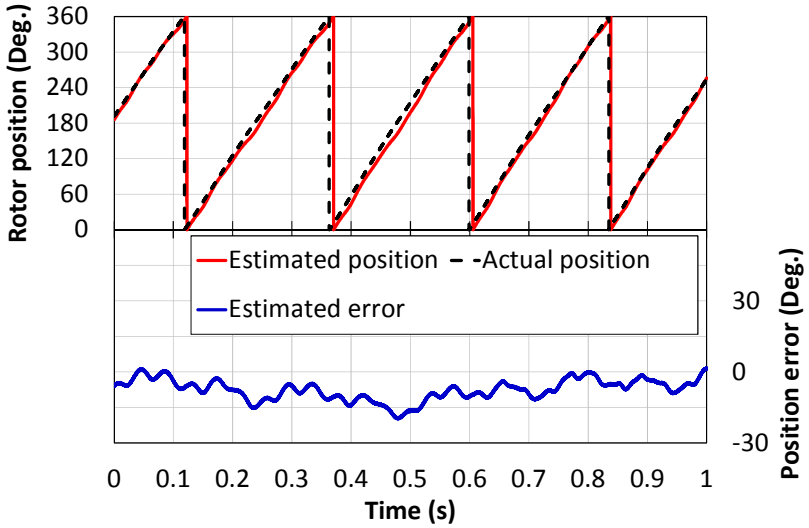


(d) MWC-4

Fig. 6.11. Sensorless rotor position estimation in steady-state based on existing position estimator, 25 r/min.

In Fig. 6.12, the accuracy of rotor position estimation is further improved by the proposed rotor position tracking observer. Obviously, the position estimation error in the sensorless rotor position estimation is slightly reduced (Figs. 6.12 (a) and (c)) and improved (Figs. 6.12 (b) and (d)). The proposed rotor position observer exhibits lower position estimation error and better performance than that of existing rotor position tracking observer. According to the experimental results based on the improved rotor position estimator, MWC-1 and MWC-3

are still better than MWC-2 and MWC-4 which exhibit multiple saliencies, in terms of sensorless rotor position estimation.

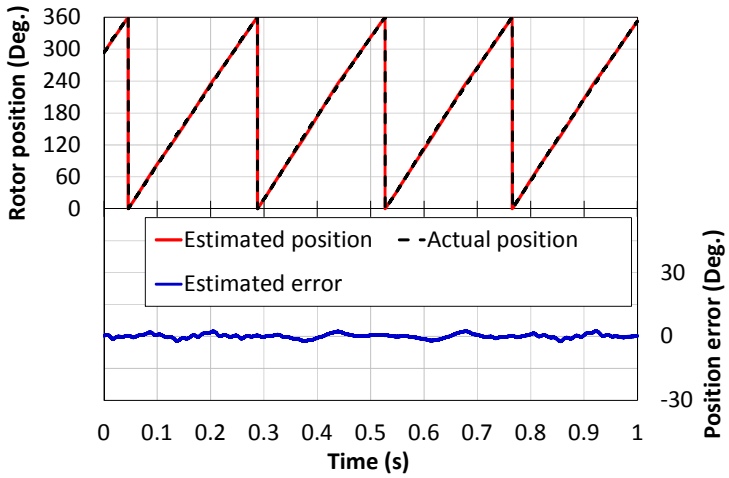


(a) MWC-1

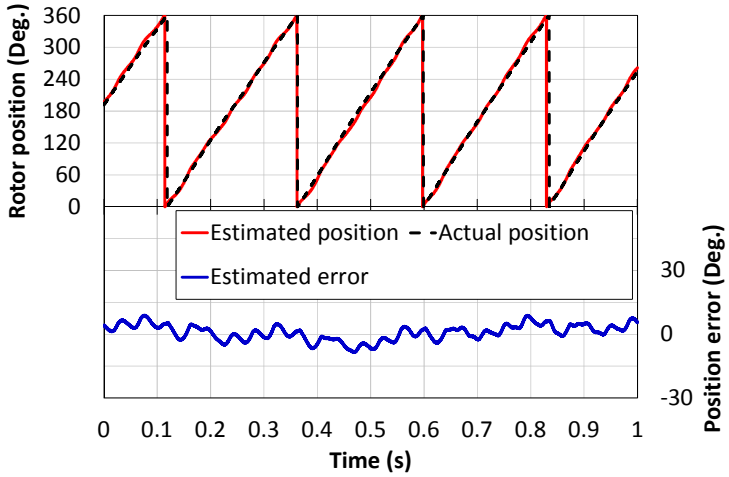


(b) MWC-2

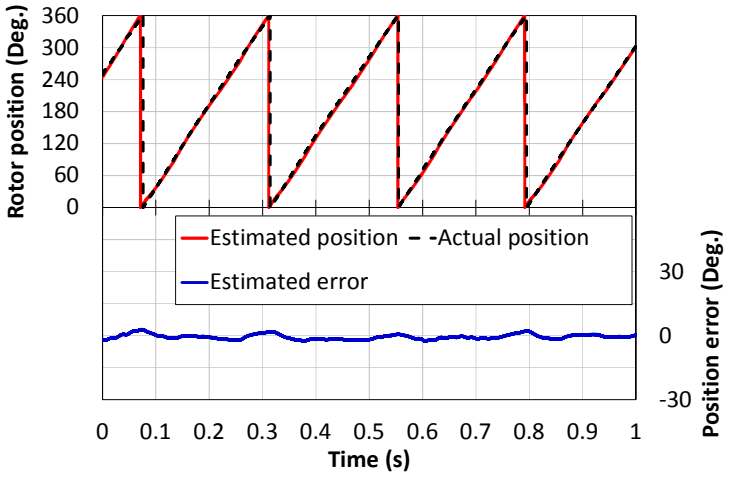


(c) MWC-3

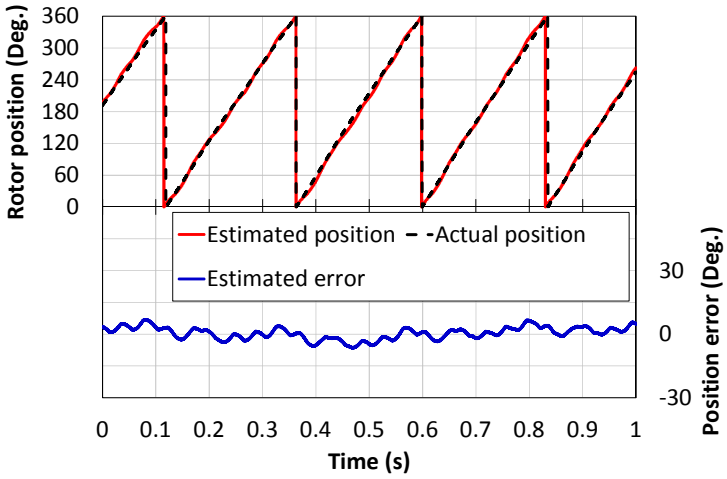


(d) MWC-4

Fig. 6.12. Sensorless rotor position estimation in steady-state based on improved position estimator, 25 r/min.

**B. Sensorless Control Performance at Dynamic-State**

Furthermore, the experimental dynamic performance of step-change in rotor speed based on the improved rotor position estimator, changing from standstill to 25 r/min, is presented in Fig. 6.13. During dynamic transient, the position tracking behavior and the speed responses are good for MWC-1 and MWC-3 but a bit slow to reflect the speed transient from standstill to 25r/min for MWC-2 and MWC-4. It shows that although the machine saliencies in MWC-2 and MWC-4 are higher, the influence of multiple saliency on the sensorless operation is more significant

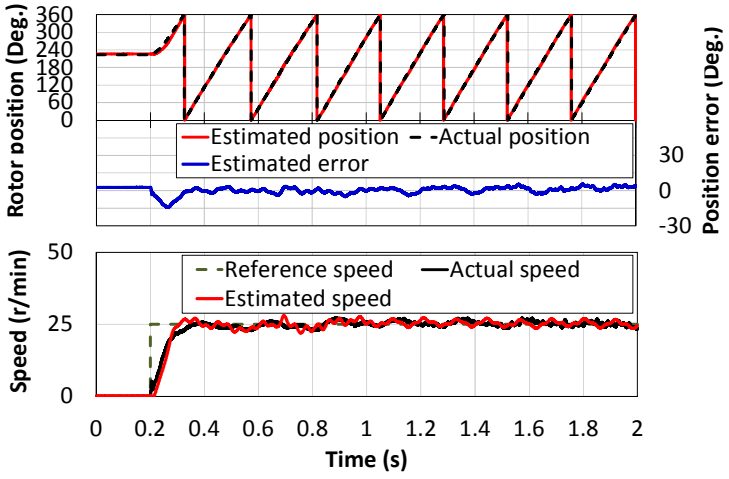


(a) MWC-1

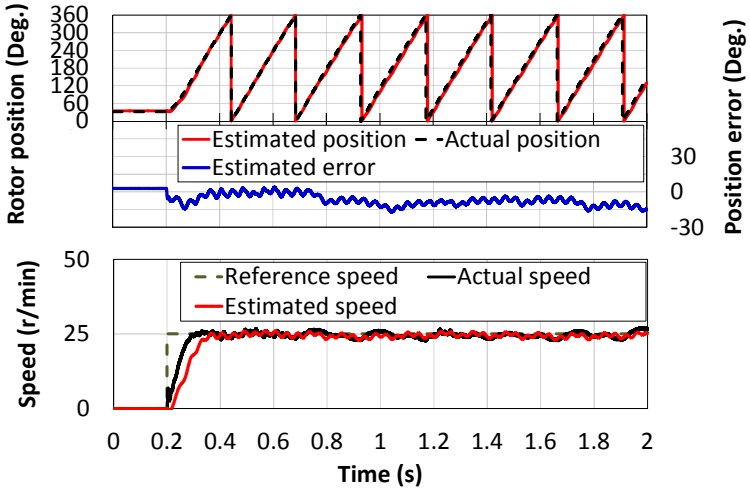


(b) MWC-2

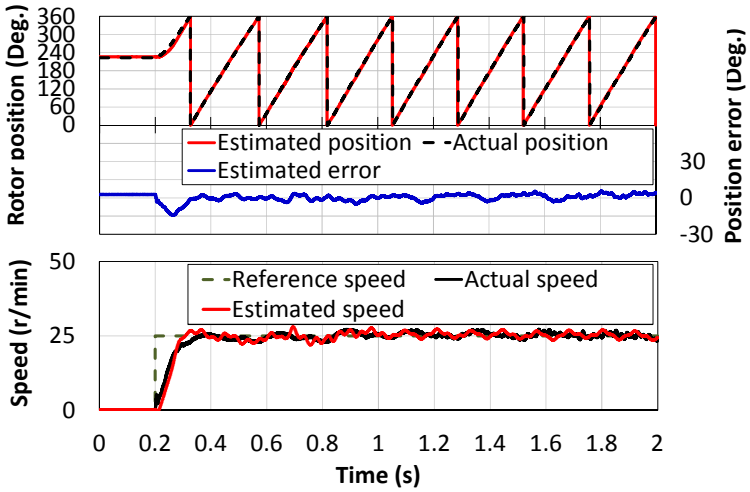


(c) MWC-3

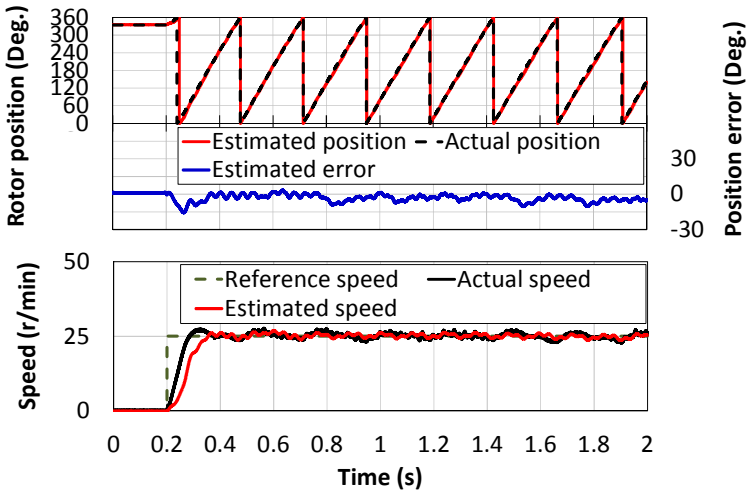


(d) MWC-4

Fig. 6.13. Sensorless rotor position estimation in dynamic-state based on improved position estimator, 0-25r/min.

**C. Comparison of Sensorless Control Operations Based on Different MWCs**

Although the machine saliency level based on MWC-2 and MWC-4 are significantly higher, the secondary saliency still exists due to the magnetic saturation. Hence, the sensorless control performances based on the four types of MWCs are summarized in Table 6.1.

TABLE 6.1

COMPARISON OF SENSORLESS CONTROL PERFORMANCES BASED ON DIFFERENT MACHINE WINDING CONFIGURATIONS

| | MWC-1 | MWC-2 | MWC-3 | MWC-4 |
|---|---|---|---|---|
| Saliency level | Medium | High | Medium | High |
| Multiple Saliencies effect | NO | YES | NO | YES |
| Position estimation error | Accurate | Inaccurate | Accurate | Inaccurate |
| DC constant position error | NO | YES | NO | YES |
| Oscillation error | NOT Obvious | Obvious | NOT Obvious | Obvious |
| Steady-state | Good | Medium | Good | Medium |
| Dynamic-state | Good | Medium | Good | Medium |

## 6.5 Improved High-Frequency Carrier Voltage Measurement

The conventional structure of SFPM machine, Fig. 6.1, is usually all poles wound as double layer machine, and each phase contains four winding coils in series connection [ZHU05][HOA97]. The first sequence type of WCCs is 1-4-7-10, which are in series connection to form one phase (Type-1), Fig. 6.15 (a), i.e. A1-A2-A3-A4 for phase A, and

similarly for phases B and C, as shown in Figs. 6.14 (a). Two winding coils of two phases are placed in each stator slot. Differing from the Type-1, the second sequence of WCC for SFPM machine can also be re-arranged as the winding coils 1-7-4-10 which are connected in series to operate as the phase A (Type-2), Fig. 6.15 (b), i.e. A1-A3-A2-A4 for phase A and similarly for phases B and C, as can be seen in Fig. 6.14 (a). In addition, it is also possible to control the prototype SFPM machines with dual three-phase inverters. In this case, the two three-phase windings by connecting winding coils 1 and 7 as A1 and A2 for set 1, whilst winding coils 4 and 10 as $A1^*$ and $A2^*$ for set 2, Fig. 6.14 (b). More importantly, it should be noted that there is a difference in relative position between the machine stator poles and rotor poles for set 1 and set 2. As can be seen from Fig. 6.1, the machine stator poles 1 and 7 are aligned with the rotor slots, whilst the machine stator poles 4 and 10 are faced the rotor poles. Due to different alignment between machine stator and rotor, the alternate coils in SFPM machine will exhibit different saliency features although the overall saliency in Type-1 and Type-2 WCCs is the same.

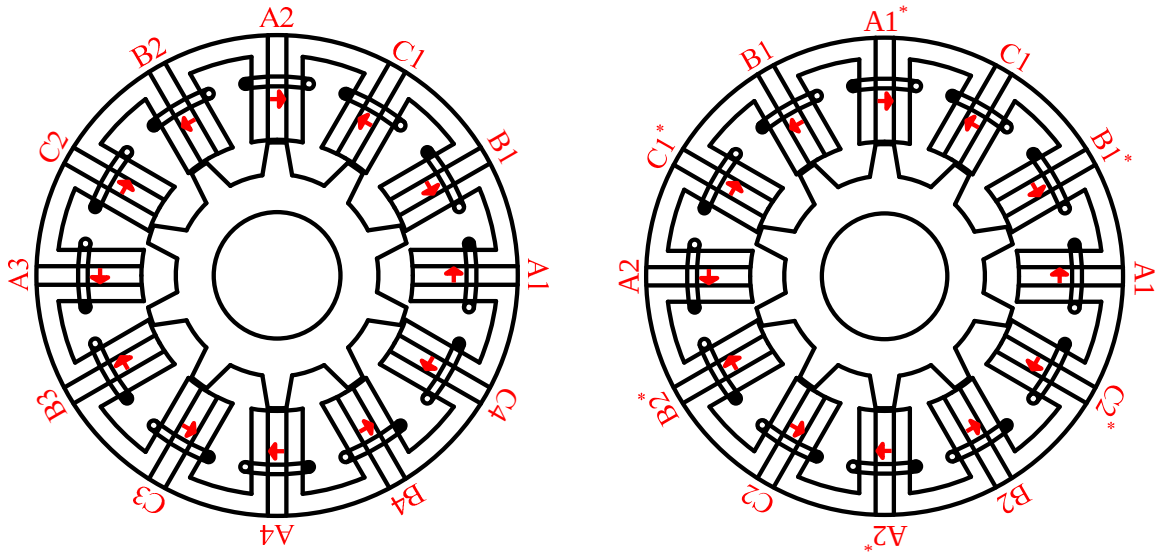


(a) All poles wound, single three-phase (b) All poles wound, dual three-phase

Fig. 6.14. Topologies of 12/10 stator/rotor SFPM machines.

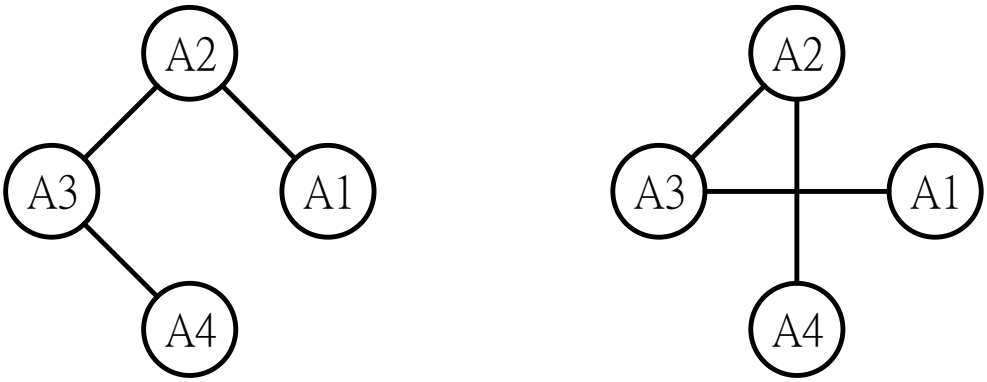


(a) Winding coil connection - Type-1 (d) Winding coil connection - Type-2

Fig. 6.15. Sequence of winding coil connections.

Additionally, with the aid of mid-tapped winding wires between winding coils A3 and A2 (Type-2), the machine saliency can be measured from the different part of the winding connections, i.e. winding coils A1 and A3 are referred to set A', and similarly winding coils A2 and A4 are presented as set A" as shown in Fig. 6.16. By connecting set A' and set A", the additional harmonics would be cancelled due to the coil compensation effect [HUA08] which can be referred to set A, Fig. 6.16. Compared with Type-2, the saliency effect in Type-1 would be expected to be reduced due to saliency cancelling effect and the multiple saliencies will not exist. According to Type-2, the machine saliency measured from set A' is expected to be identical to that of set A" (Fig. 6.16), but each may exhibit the secondary saliency, which will affect the sensorless control performance.

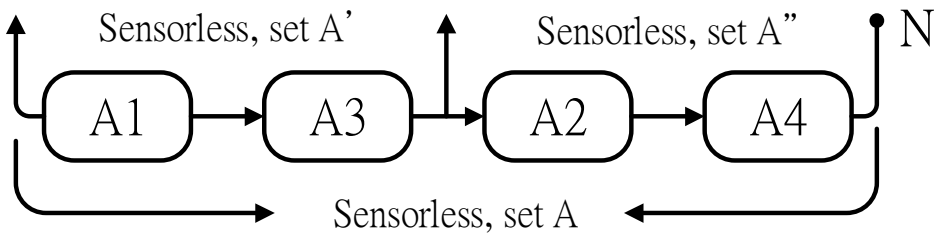


Fig. 6.16. Measurement of HF carrier voltage signals.

Injecting a HF pulsating carrier voltage signal (6.3) into the virtual synchronous reference

frame, the HF carrier voltages are derived as

$$\begin{bmatrix} u_{dh}^{vr} \\ u_{qh}^{vr} \end{bmatrix} = \begin{bmatrix} I_p + I_n \cos(2\Delta\theta + \theta_m) \\ I_n \sin(2\Delta\theta + \theta_m) \end{bmatrix} \cdot \sin\alpha \tag{6.12}$$

To evaluate the machine saliency information, a simple method for investigating the machine saliency is proposed as shown in Fig 6.17. With the aid of accurate rotor position information from an incremental encoder, a HF pulsating carrier sinusoidal voltage signal (6.3) ($U_c$ = 8V, $f_c$ = 550Hz) is injected into the virtual synchronous reference frame ($d^{vr}$-$q^{vr}$), while the machine operates at low speed in the sensored mode, 25r/min with current about 1.2A.

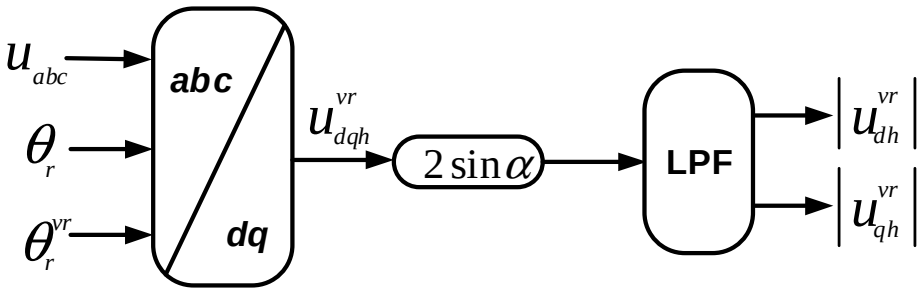


Fig. 6.17. Principle of machine saliency measurement.

By applying the synchronous detection method and low-pass filter (LPF), the amplitudes of positon-dependent carrier voltages can be obtained based on Type-1 and Type-2 as shown in Figs. 6.18 (a) and (c), and re-written as

$$\begin{bmatrix} |u_{dh}^{vr}| \\ |u_{qh}^{vr}| \end{bmatrix} = LPF\left(\begin{bmatrix} u_{dh}^{vr} \\ u_{qh}^{vr} \end{bmatrix} \cdot 2\sin\alpha\right) = \begin{bmatrix} I_p + I_n \cos\left(2\Delta\theta + \theta_m\right) \\ I_n \sin\left(2\Delta\theta + \theta_m\right) \end{bmatrix} \tag{6.13}$$

The machine saliency circles are illustrated in Figs. 6.18 (b) and (d) where the saliency circle indicates the full saliency information. If the circle is bigger, the saliency level is higher. As mentioned earlier, the overall saliency for set A in Type-I and Type-II are the same.

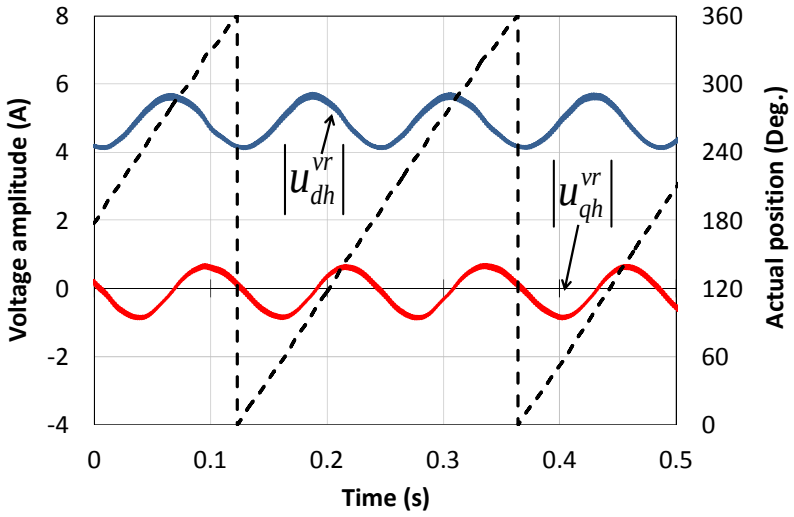


(a) Type-1, set A

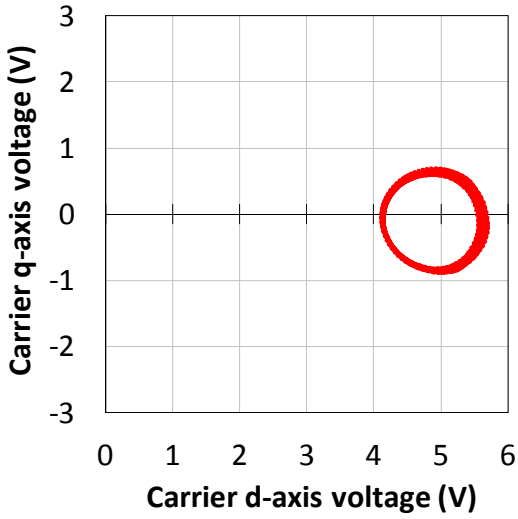


(b) Type-1 – carrier voltage circle by machine saliency, set A

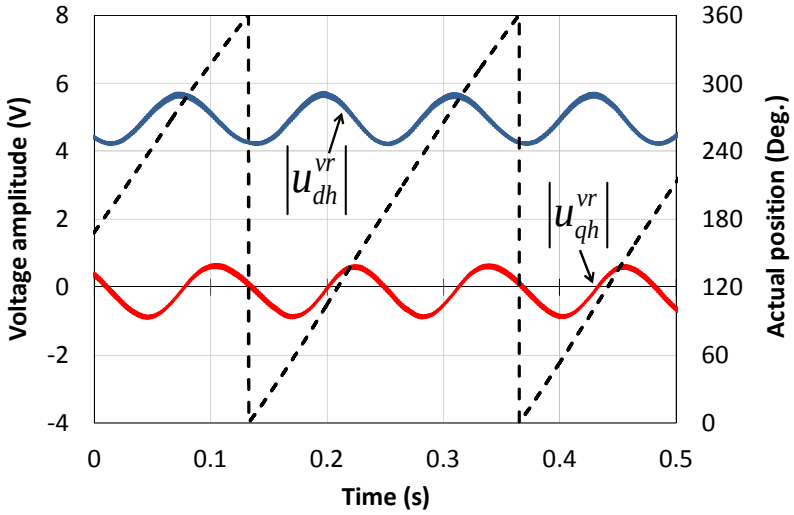


(c) Type-2, set A

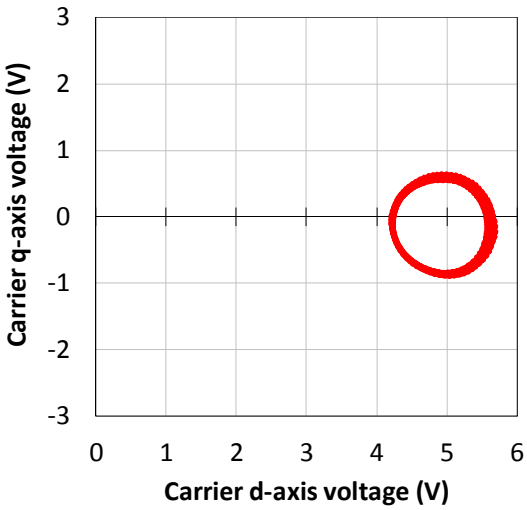


(d) Type-2 – carrier voltage circle by machine saliency, set A

Fig. 6.18. Measured HF carrier voltage responses based on different types of winding coil connections, 25 r/min.

### 6.5.1 Experimental Investigation of Machine Saliency

Based on the theoretical analysis of machine saliency in the previous section, the machine saliency based on different part of WCCs in Type-2 needs to be investigated in order to prove the influence of primary saliency or multiple saliencies on the sensorless rotor position estimation.

The same experimental conditions are also applied to the different WCCs based on Type-2. With the aid of mid-tapped winding wires, the *d*- and *q*-axis carrier voltage responses can be measured from the set A' and set A" at the same time as shown in Figs. 6.19. Clearly, similar to the principle of carrier current responses, the *d*- and *q*-axis carrier voltage responses are also modulated as two cycle per electrical position. Moreover, the higher amplitude of carrier voltage response indicates the higher machine saliency level. The experimental results show the saliency level in set A is significantly higher (Fig. 6.19 (a)) than that of the saliency measured from both set A' and set A" as shown in Figs. 6.19 (b) and (c) due to less winding coils and inductances. Theoretically, set A' have identical saliency level as set A" according the analysis in section II.

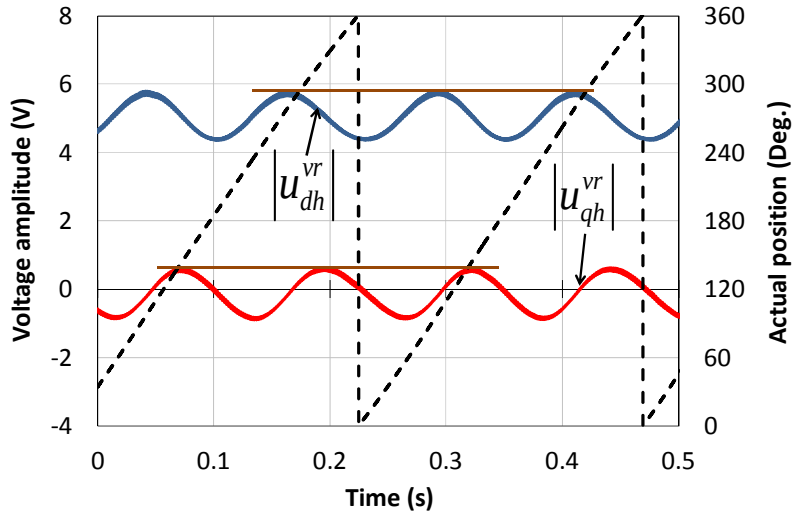


(a) Set A

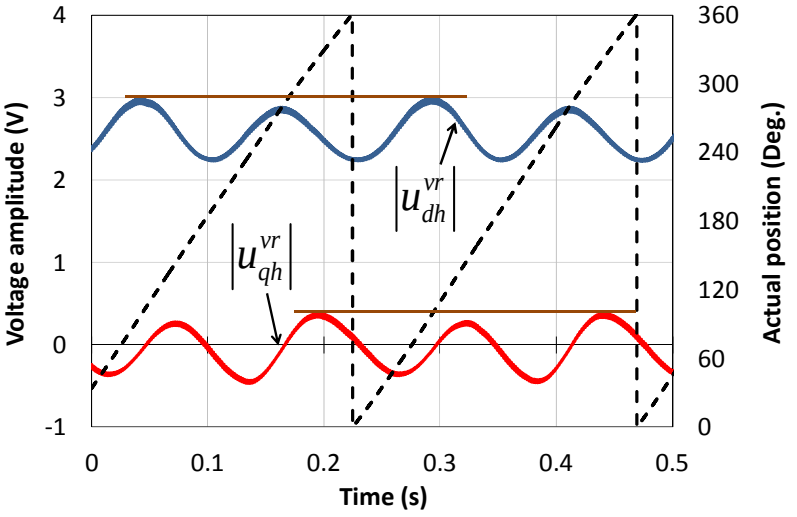


(b) Set A'

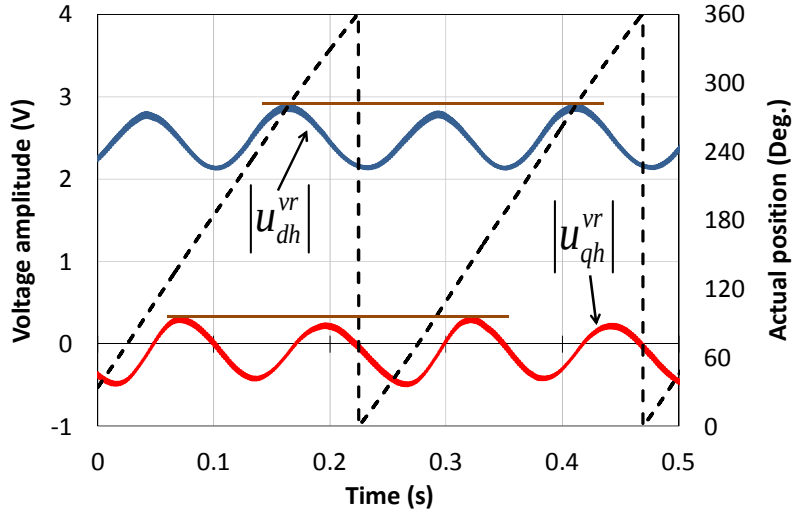


(c) Set A"

Fig. 6.19. Measured HF amplitude variations of carrier voltage responses based on types of winding coil connections in Type-2, 25 r/min.

Furthermore, the amplitudes of measure *d*- and *q*-axis carrier voltage responses in set A' and set A" in Type-2 are non-constant as shown in Figs. 6.19 (b) and (c), respectively. This non-constant issue is due to the secondary saliency (multiple saliencies effect). However, this issue can be avoided when the winding coils 1, 4, 7, 10 or 1, 7, 4, 10 are all connected in series (Type-1 and Type-2).

In Fig. 6.20, the locus of carrier voltage circle caused by machine saliency are measured by the mid-tapped winding wire based on the different sequence of WCCs in Type-2. As can be seen from Figs. 6.20 (b) and (c), set A' has similar saliency level as set A", and both sets are affected by the multiple saliencies, due to which the sensorless rotor position estimation will deteriorate. According to the FFT analyses Fig. 6.21, Type-1 and Type-2 are the same, and set A' and set A" are almost identical as discussed in the previous section.

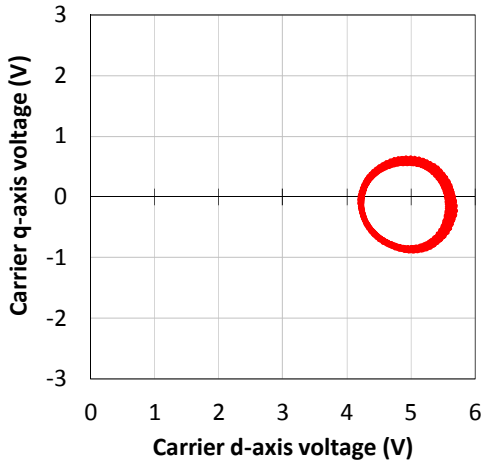


(a) Set A

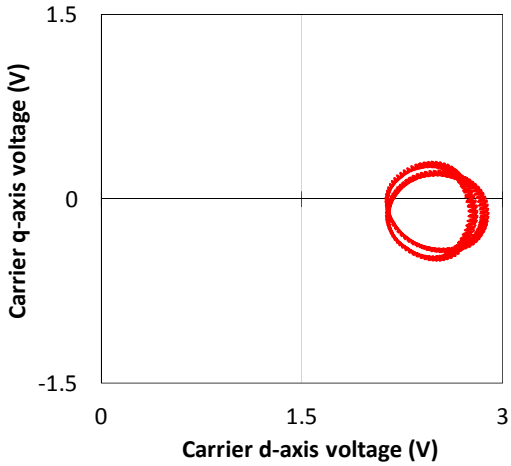


(b) Set A'

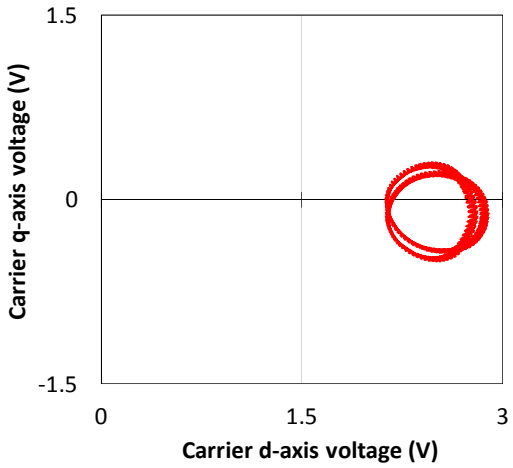


(c) Set A"

Fig. 6.20. Measured carrier voltage circles by machine saliency based on types of winding coil connections in Type-2, 25 r/min.

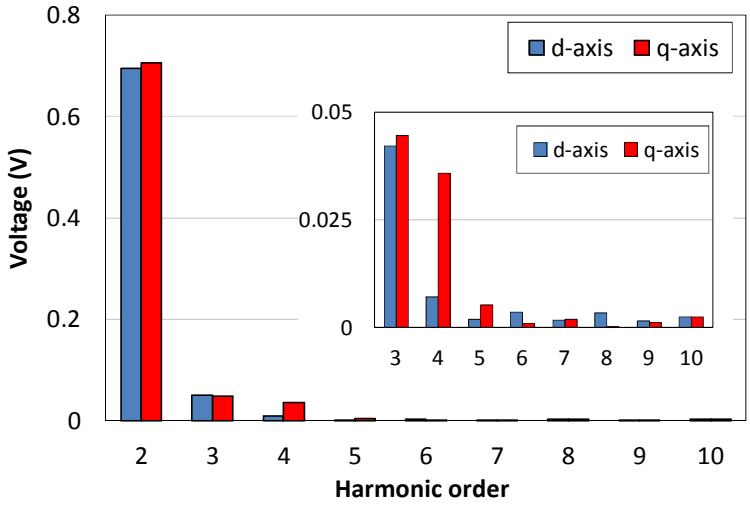


(a) Type-1, Set A

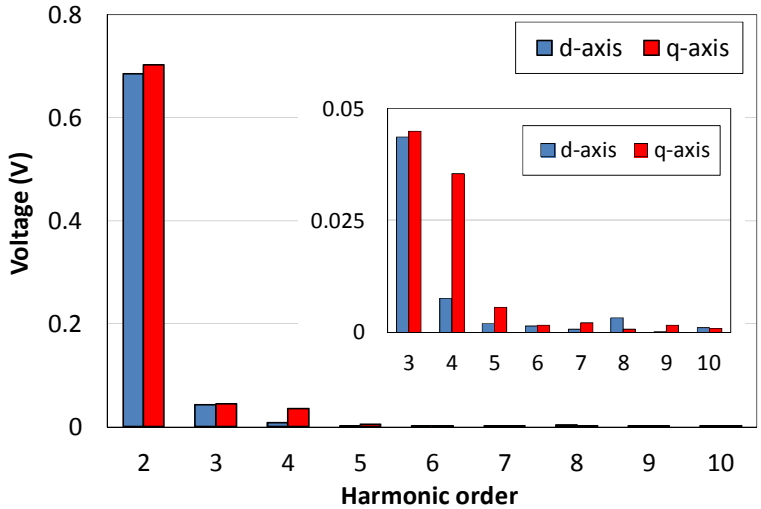


(a) Type-2, set A

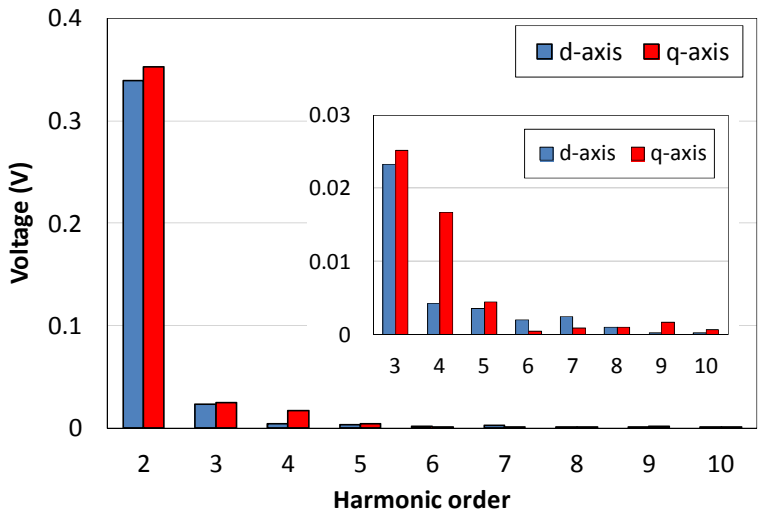


(b) Type-2, set A'

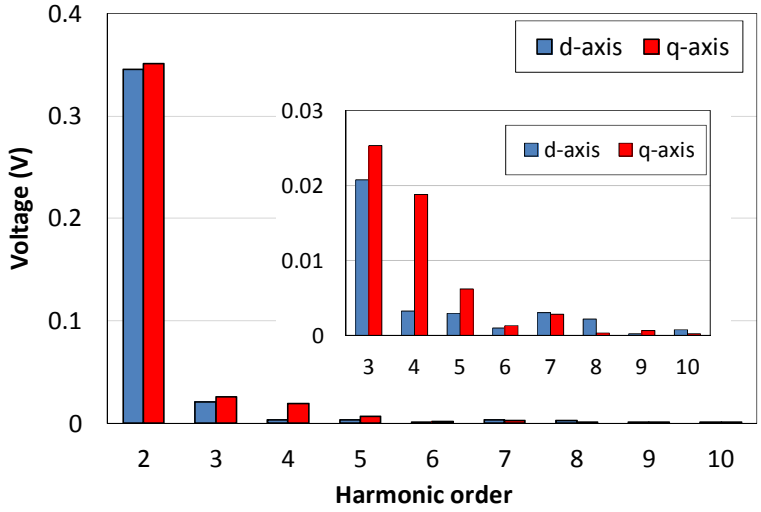


(c) Type-2, set A"

Fig. 6.21. FFT analysis based on types of winding coil connections in Type-2, 25 r/min.

### 6.5.2 Validation of Sensorless Rotor Positon Estimations

To validate the effectiveness of sensorless rotor position estimation based on the different sequence of WCCs, such as Type-1 and Type-2, as well as the mid-tapped winding wires based HF carrier voltage signal measurement, the HF pulsating carrier voltage injection technique is applied to the prototype SFPM machine. The experimental conditions of injection voltage and frequency for are $U_c$ = 8V, $f_c$ = 550Hz, which is injected into the estimated synchronous reference frame, and then the rotor position information can be obtained from the carrier voltage response.

### A. Single Three-Phase Operation

Fig. 6.22 shows the sensorless rotor position estimation at the steady state of constant speed 25 r/min with current, 2.2A, by utilizing the mid-tapped winding wires for extracting the HF carrier signals. The experimental results show good sensorless rotor position tracking performance based on the Type-1 and set A in Type-2, as shown in Figs. 6.22 (a) and (b), respectively. However, a significant oscillation error exists in the rotor position estimation based on set A' and set A" due to the additional harmonics in the carrier voltage response caused by the multiple saliencies effect, as shown in Figs. 6.22 (c) and (d), respectively. Additionally, the comparison between set A' and set A" in Type-2 is shown in Fig. 6.22 (e).

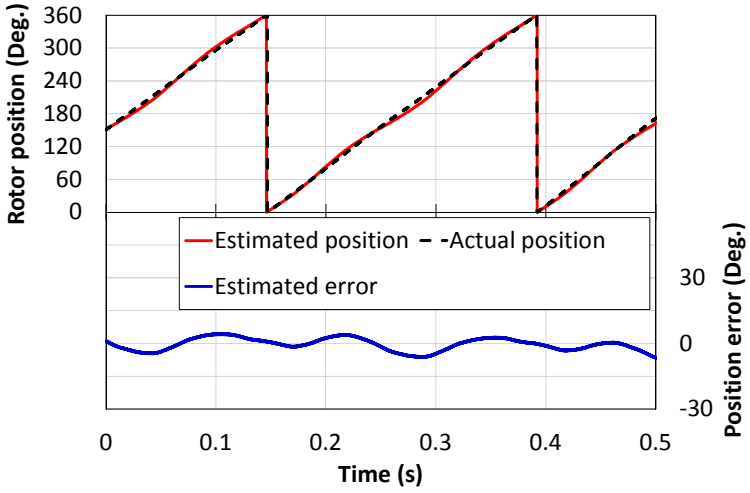


(a) Type-1, set A

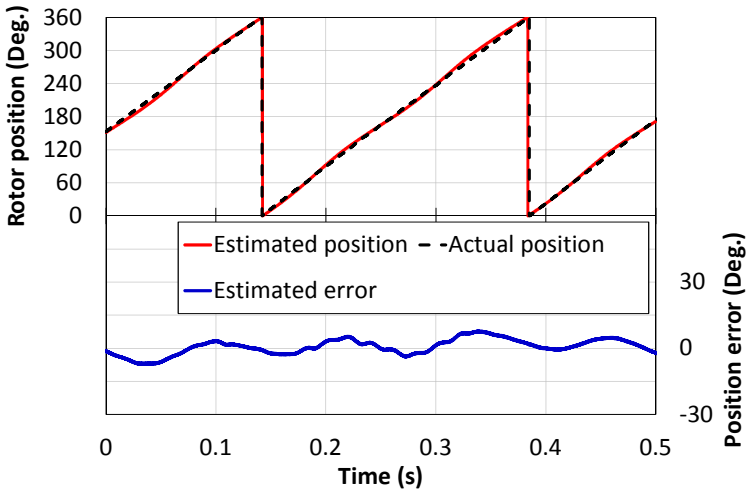


(b) Type-2, set A

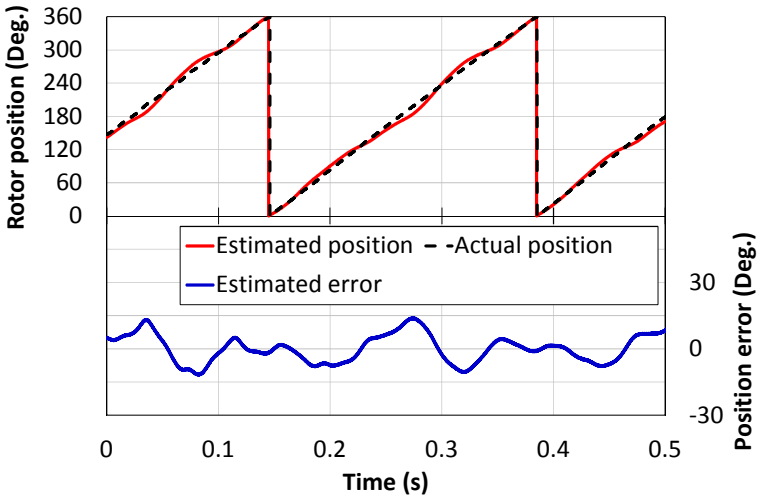


(c) Type-2, set A’

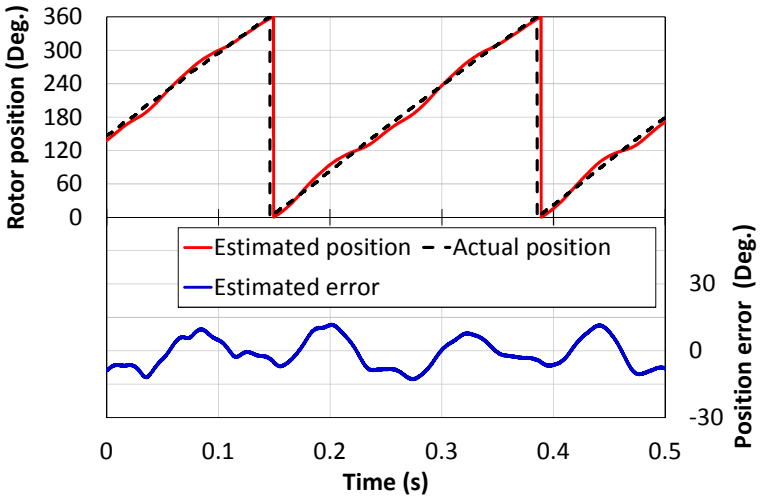


(d) Type-2, set A”

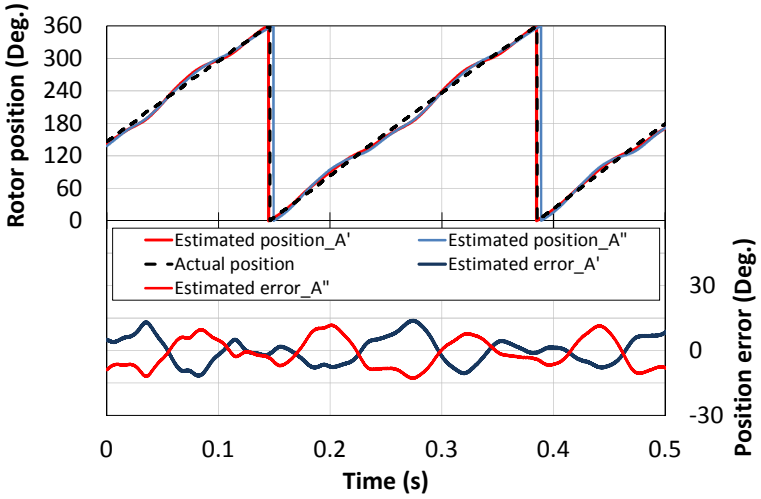


(e) Comparison

Fig. 6.22. Sensorless rotor position estimations at steady-state, 25 r/min.

As can be seen, the rotor position estimation based on set A' and set A" have similar performance but the peak error is in the opposite direction with each other, which can be a good feature for the rotor position compensation. According to the saliency analysis shown in Figs. 6.19 (b) and (c), comparing set A' with set A", there is a phase difference due to HF *d*- and *q*-axis carrier signals, which can be eliminated by the connection of two sets (A' + A") due to the saliency cancelling effect.

Similarly, using the same principle to reduce the error in the rotor position estimation, a very simple compensation method is proposed, Fig. 6.23. When the effect of multiple saliencies can be effectively cancelled, the oscillation error will significantly be reduced. By adding the rotor position estimation errors from both set A' and set A", the average rotor position estimation can be calculated, and then applied to the rotor positon tracking observer. Therefore, high accuracy of rotor positon can be achieved, whilst the oscillation error in the rotor positon estimation can be minimized, as shown in Fig. 6.24.

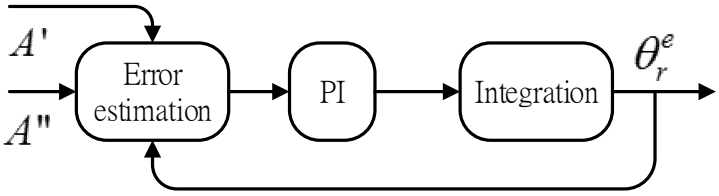


Fig. 6.23. Proposed rotor position estimation error compensation.

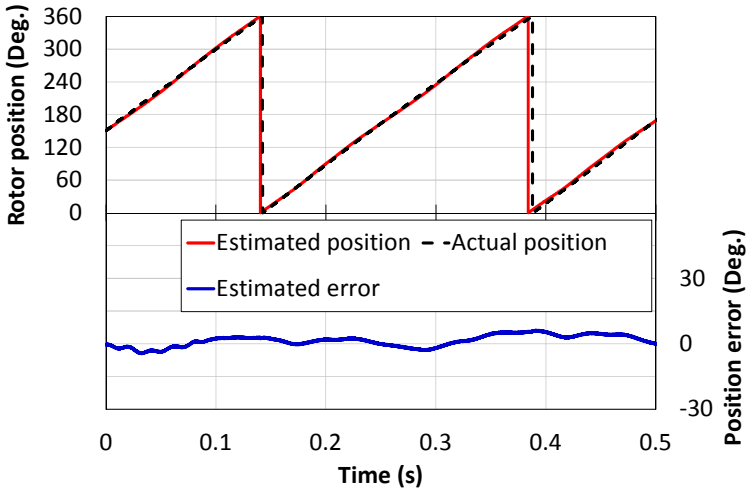


Fig. 6.24. Improved rotor positon estimation, 25 r/min.

**B. Dual Three-Phase Operation**

As mentioned in section II, the prototype machine can be operated as the dual three-phase machine, Fig. 6.25.

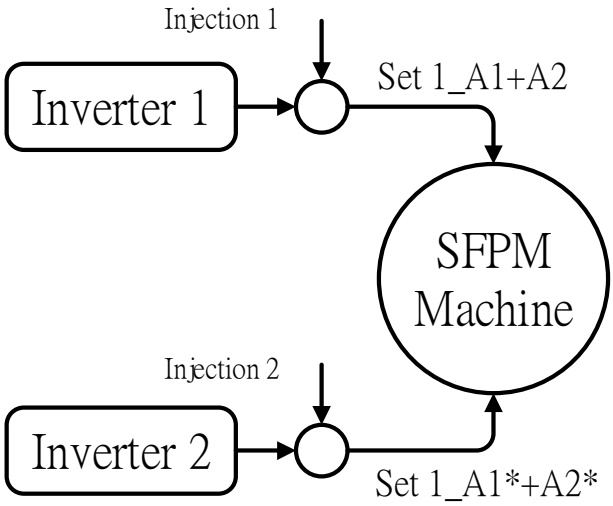


Fig. 6.25. Control of dual three-phase scheme.

Differing from the previous application, the mid-tapped winding wires are not required. Similarly, the same testing conditions are also applied ($U_c$ = 4V, $f_c$ = 550Hz for each set), the sensorless rotor position estimation at the steady state of constant speed 25 r/min with current, 2.2A, Fig. 6.26. However, a significant oscillation error is very obvious in the rotor position estimation based on set 1 and set 2 due to the multiple saliencies effect, as shown in Figs. 6.26 (a) and (b), respectively, which is the same as the position estimation based on set A' and set A". The comparison between set 1 and set 2 is shown in Fig. 6.26 (c). Clearly, the rotor position estimation based on set 1 and set 2 have similar performance as set A' and set A", and the peak errors are in the opposite direction with each other.

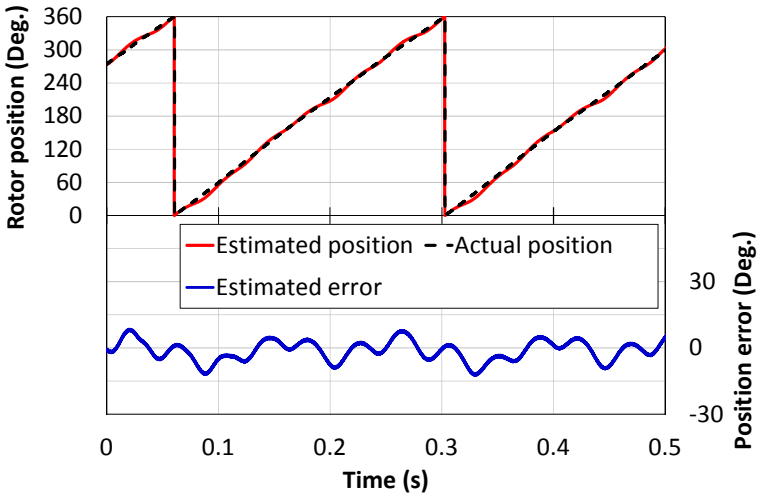


(a) A1 and A2, set 1

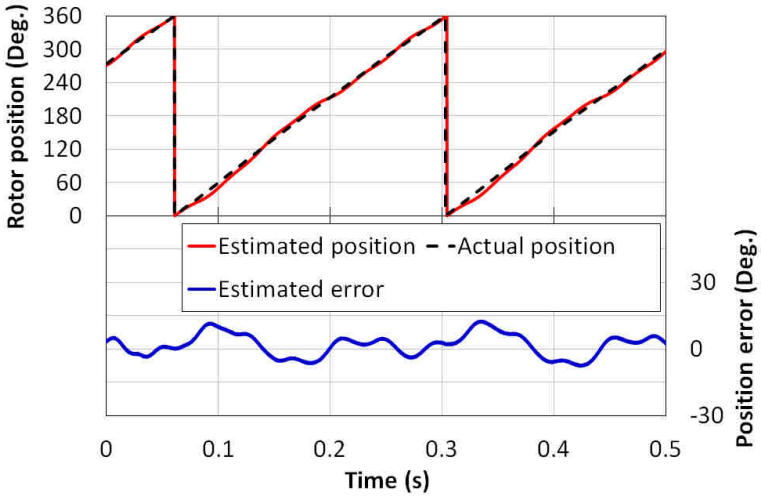


(b) A1* and A2*, set 2

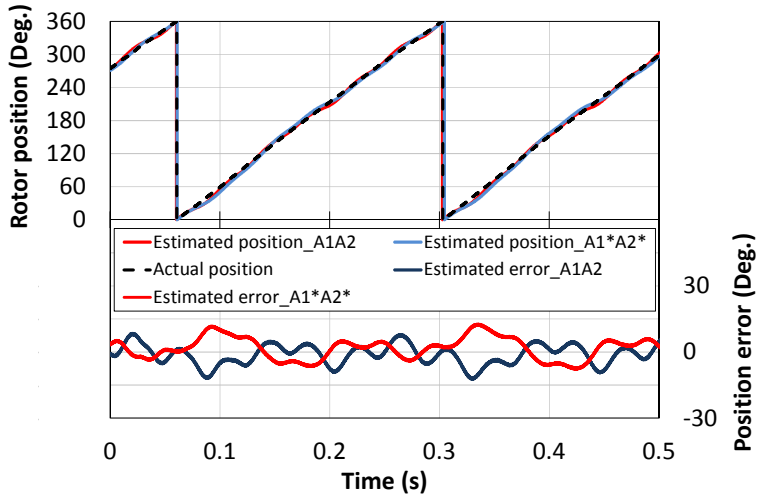


(c) Comparison

Fig. 6.26. Sensorless rotor position estimations at steady-state, 25 r/min.

Furthermore, by applying the same proposed rotor position estimation error compensation method, Fig. 6.23, the average rotor position estimation can be re-calculated, and then applied to the rotor positon tracking observer. Therefore, the good sensorless control performance with high accurate rotor position estimation is achieved, as shown in Fig. 6.27.

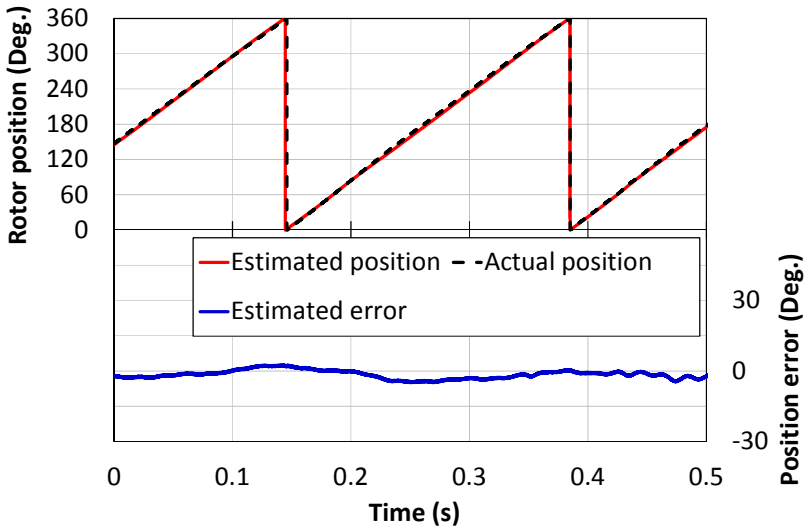


Fig. 6.27. Improved rotor positon estimation, 25 r/min.

It should be noted that the proposed rotor position estimation error compensation shown in Fig. 6.23 is based on the HF carrier voltage response, and it is also applicable to the rotor position estimation based on HF carrier current response based method.

### C. Comparison of Sensorless Control Operations Based on Different WCCs

The sensorless control performances based on the four types of WCCs are summarized in Table 6.2.

TABLE 6.2

COMPARISON OF SENSORLESS CONTROL PERFORMANCES BASED ON DIFFERENT WINDING COILS CONNECTIONS

| | WCC type-1 | WCC type-2 | WCC type-2_A’ | WCC type-2_A” |
|---|---|---|---|---|
| Saliency level | High | High | Medium | Medium |
| Multiple Saliencies effect | NO | NO | YES | YES |
| Estimation error cancellation | YES | YES | NO | NO |
| Multiple Saliencies error cancellation | YES | YES | NO | NO |
| Oscillation error | NOT Obvious | NOT Obvious | Obvious | Obvious |
| Steady-state | Good | Good | Good | Good |

## 6.6 Conclusion

This chapter has experimentally investigated the influence of machine saliency on the sensorless operations based on the different machine winding configurations and winding coil connections, by which the SFPM machine can operate in either single or dual three-phase mode.

The prototype SFPM machine exhibits the apparent saliency for applying the HF injection based method. By comparison, the saliency level based on MWC-2 and MWC-4 is obviously higher than MWC-1 and MWC-3. However, the secondary saliency also exists in MWC-2 and MWC-4 which will deteriorate the accuracy of the rotor position estimation.

In addition, the sensorless rotor position estimations based on the different sequence of WCCs (Type-1 and Type-2) have also experimentally investigated as well as the different WCCs in Type-2. Moreover, with the aid of mid-tapped winding wires, the machine saliency can be measured from set A' and set A" separately, of which the saliency level for set A' and set A" are similar but with phase shift, whilst the multiple saliencies are contained which will deteriorate the accuracy of the rotor position estimation.

Furthermore, the improved rotor position estimator can enhance the sensorless operation. The experimental results verify that the accuracy of rotor position estimation is improved, and the proposed position tracking observer is better than that of the existing position observer, in terms of multiple saliencies effect. Also, the proposed error cancellation method is applicable to dual three-phase SFPM machines, as confirmed by the experiments.

## References


[BAR10] M. Barcaro, N. Bianchi, and F. Magnussen, "Analysis and Tests of a Dual Three-Phase 12-Slot 10-Pole Permanent-Magnet Motor," *IEEE Trans. Ind. Appl.*, vol.46, no.6, pp.2355-2362, Nov.-Dec. 2010.

[BAR12] M. Barcaro, A. Faggion, N. Bianchi, and S. Bolognani, "Sensorless Rotor Position Detection Capability of a Dual Three-Phase Fractional-Slot IPM Machine," *IEEE Trans. Ind. Appl.*, vol.48, no.6, pp.2068-2078, Nov.-Dec. 2012.

[DEG98] M. Degner and R. Lorenz, "Using multiple saliencies for the estimation of flux, position, and velocity in ac machines," *IEEE Trans. Ind. Appl*., vol. 34, no. 5, pp. 1097–1104, Sep./Oct. 1998.

[HAR00] L. Harnefors and H.P. Nee, "A general algorithm for speed and position estimation of AC motors," *IEEE Trans. Ind. Electron.*, vol. 47, no. 1, pp. 77-83, 2000.

[HOA97] E. Hoang, A.H. Ben-Ahmed, and J. Lucidarme, "Switching flux permanent magnet poly phased synchronous machines," *Proc. 7th Eur. Conf. Power Electronics and Applications*, vol. 3, pp. 903-908, 1997.

[HUA08] Wei Hua, Ming Cheng, Z.Q. Zhu, and D. Howe, "Analysis and optimization of

back-EMF waveform of a flux-switching permanent magnet motor," *IEEE Trans. Energy Conversion*, vol. 23, no. 3, pp. 727-733, Sep. 2008.

[JUN11] S. Y. Jung, and K. Nam, "PMSM control based on edge-field Hall sensor signals through ANF-PLL processing," *IEEE Trans. Ind. Electron.*, vol. 58, no. 11, pp. 5121–5129, Nov. 2011.

[MAD95] A. Madani, J. P. Barbot, F. Colamartino, and C. Marchand, "Reduction of torque pulsations by inductance harmonics identification of a permanent-magnet synchronous machine," *Proc. 4th IEEE Conference on Control Applications*, 1995, pp. 787-792.

[OWE11] R.L. Owen, Z.Q. Zhu, A.S. Thomas, G.W. Jewell and D. Howe, "Alternate poles wound flux-switching permanent-magnet brushless AC machines," *IEEE Trans. Ind. Appl.*, vol. 46, no. 2, pp. 790–797, 2010.

[ZHU05] Z. Q. Zhu, Y. Pang, D. Howe, S. Iwasaki, R. Deodhar, and A. Pride, "Analysis of electromagnetic performance of flux-switching permanent magnet machines by nonlinear adaptive lumped parameter magnetic circuit model," *IEEE Trans. on Magn.*, vol. 41, no. 11, pp.4277-4287, Nov. 2005.

[LIN14] T.C. Lin, L.M. Gong, J.M. Lin and Z.Q. Zhu "Investigation of saliency in switched-flux permanent magnet machine using high-frequency signal injection," *IEEE Trans. Ind. Electron.*, vol. 61, no. 9, pp. 5094-5104, September. 2014.

[XU13] P.L. Xu, Z.Q. Deng, Y. Wang, and S. Xiong, "Sensorless Drive of 12/10 Flux-Switching Permanent Magnet Motor with High-Frequency Pulsating Sinusoidal Signal Injection," *Trans. of China Electrotechnical Society*, no. 28, pp. 307-313, 2013.

# CHAPTER 7

# SIXTH-HARMONIC BACK-EMF BASED SENSORLESS CONTROL FOR SWITCHED-FLUX PERMANENT MAGNET SYNCHRONOUS MACHINE

## 7.1 Introduction

Back-EMF is induced when there is a motion between the armature windings and the air-gap magnetic field generated by PMs. Thus, the back-EMF is related to the rotor position of electrical machine. Back-EMF based sensorless control techniques can be categorised as integration of back-EMF which is PM excitation flux-linkage [SHE02][PEL12][SAL10], zero-crossings of fundamental back-EMF [ROS03][VAI95], and harmonic back-EMF i.e. third order of harmonic components [SHE06a][SHE04][SHE06b][KRE94][MOR92][LIU14]. However, since the frequency and amplitude of back-EMF are both proportional to the rotor speed, the accuracy of rotor position estimation is limited at zero and low speed, but shows good performance above certain speed. Therefore, to overcome the limitation at standstill and low speed, the saliency-based sensorless control methods are usually employed [ZHU11][KIM03].

Some recent sensorless control techniques based on harmonic back-EMF have been reported. In [SHE06a][SHE04][SHE06b][LIU14], some practical issues in implementing the 3rd-harmonic back-EMF based sensorless control were reported for the rotor position detection. In [GEN10], a novel sensorless control algorithm based on the back-EMF without the use of voltage probes was presented. A simple robust method that can easily allow a speed transition and smooth torque for the sensorless vector control strategy under different load conditions was developed in [WAN12]. In [FAE09], a new software scheme using a

phase-locked loop (PLL) based on the 3rd-harmonic back-EMF detection was published and showed that the torque could be improved during the high speed operation. Moreover, the estimated flux-linkage harmonics result from the back-EMF can be utilized to compensate the influence of harmonic currents by adding the harmonic currents to the fundamental currents in order to reduce the torque harmonics in [DEG98].

In Test Machine-II, the 6th-harmonic back electromotive force (EMF) is dominant, whilst the 3rd-harmonic back-EMF is much smaller. Several new position estimation methods for the sensorless control based on the 6th-harmonic back-EMF will be introduced in this chapter. Firstly, by detecting the zero-crossings of the 6th-harmonic back-EMF with/without eliminating the influence of the 3rd-harmonic back EMF, the related rotor positions can be determined precisely at these zero-crossings. However, since the intermediate rotor positions need to be determined by linear interpretation between two zero-crossings, it only exhibits excellent performance under steady state but not at dynamic state. The continuous rotor position can be obtained from the proposed new observer by utilizing the combined 6th-harmonic back-EMF and flux-linkage, together with a synchronous reference frame filter (SRFF). Experimental validation show that (a) by eliminating the 3rd-harmonic back-EMF effect, the accuracy of the proposed 6th-harmonic back-EMF zero-crossings detection method can be improved, (b) SRFF is effective to minimize the influence of non-constant amplitudes of the 6th-harmonic back-EMF and flux-linkage, (c) the comparison between the fundamental, the 3rd-harmonic back-EMF and the proposed method are presented in order to highlight the effectiveness of proposed control strategy under different operating conditions.

## 7.2 Configuration of PM Machine and Back-EMF Analysis

### 7.2.1 Configuration of PM Machine

For the Test Machine-II which is 12/10 stator/rotor poles SFPM machine under investigation, it is comprised of four series-connected winding coils for each phase, i.e. coils

A1-A2-A3-A4 for phase A, and similarly for phase B and C, which is the conventional structure as shown in Fig. 7.1. The back-EMF waveforms induced in the different winding configurations are firstly analyzed in order to investigate the influence of harmonic components in the back-EMFs.

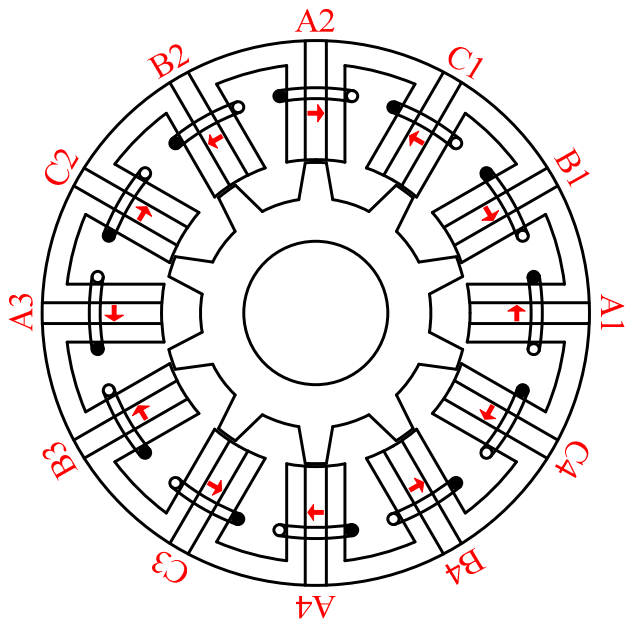


Fig. 7.1. Topology of SFPM machine.

### 7.2.2 Analysis of Back-EMFs

To investigate the harmonic components in the back-EMF, the back-EMF waveform can be analyzed under several types of back-EMF waveforms. The back-EMF waveforms for each of the two pairs of diametrically opposite coil combination, namely A1A3 and A2A4 are shown in Fig. 7.2 (a), together with the resultant back-EMF waveform when the two pairs of coil combination are connected in series. It can clearly be seen that the back-EMF waveforms for the two pairs of coil combination A1A3 and A2A4 are asymmetric and non-sinusoidal. It indicates that both back-EMF waveforms are rich of the harmonics, i.e. 2nd, 4th and 6th harmonics, which also includes odd harmonics with small amplitudes according to the Fast

Fourier Transform (FFT) analysis shown in Fig. 7.2 (b). However, when the two pairs of perpendicularly disposed coil combination A1A3 and A2A4 are connected in series, the harmonics in the back-EMF waveform can be cancelled. Therefore, the resultant phase back-EMF waveform is essentially sinusoidal, as can be seen in Fig. 7.2 (a).

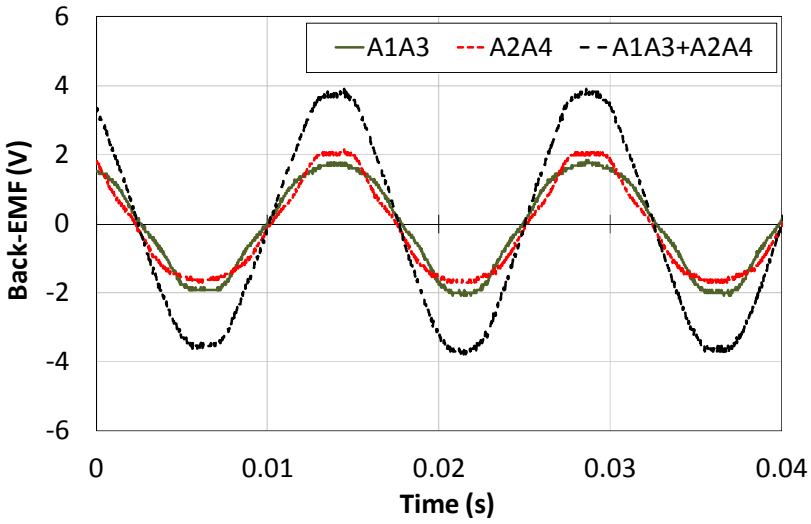


(a) Measured back-EMFs

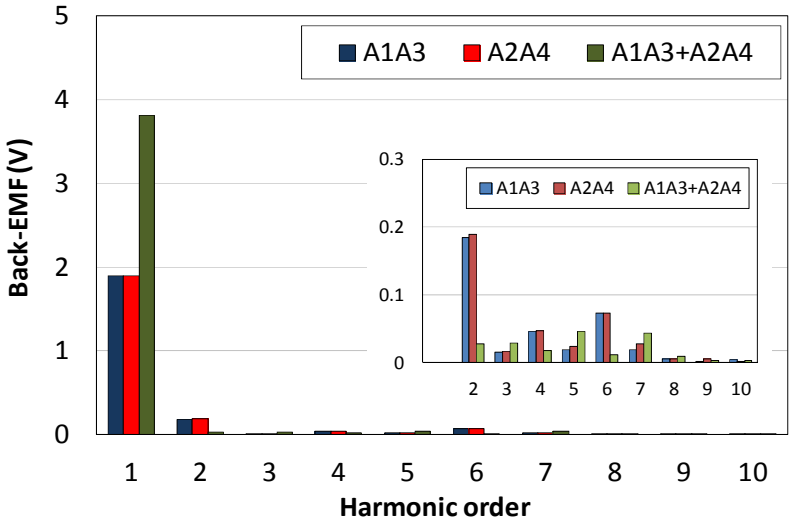


(b) FFT analysis

Fig. 7.2. Phase A back-EMFs based on different winding configurations.

## 7.3 Detection of Harmonic Back-EMFs and Third-Harmonic Cancellation

### 7.3.1 Detection of Harmonic Back-EMF

When the machine windings are Y-connected, the harmonic back EMF is included in the phase back EMF rather than line back EMF irrespective of the operational mode and synchronously rotates with the fundamental components. In order to detect the harmonic back-EMF, a very simple method is utilized in which Y-connected resistance network is required [SHE06b]. Hence, the neutral point "*n*" of Y-connected stator windings and the central point "*s*1" and "*s*2" of Y-connected resistance networks in Fig. 7.3 are employed for detecting the harmonic back-EMFs.

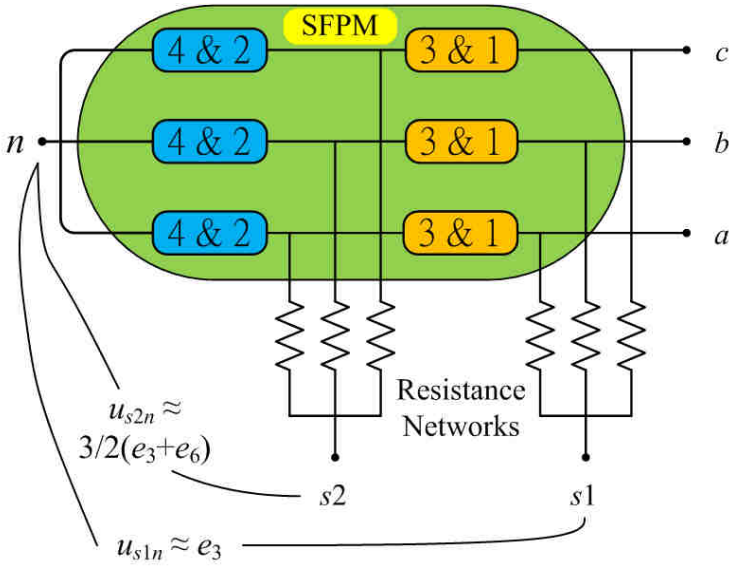


Fig. 7.3. Detection of harmonic back-EMFs.

Based on the Fourier analysis, the sum of three-phase voltage equation can be derived as

$$\begin{aligned} u_{an}+u_{bn}+u_{cn} &= e_{a\_1\&3+2\&4}+e_{b\_1\&3+2\&4}+e_{c\_1\&3+2\&4} \\ &= 3\times\left(e_{3\_1\&3+2\&4}+e_{6\_1\&3+2\&4}+e_{9\_1\&3+2\&4}+\cdots\right) \\ &\approx 3\times\left(e_{3\_1\&3+2\&4}\right) \end{aligned} \tag{7.1}$$

Then, the average of the sum of three phase back-EMFs can be expressed as

$$u_{s1n}=\left(u_{an}+u_{bn}+u_{cn}\right)/3 \tag{7.2}$$

According to (7.1) and (7.2), a triplen harmonics as described in (7.3) can be measured between the central point "*s*1" of the first resistance network and the machine neutral point "*n*", from which the harmonic back-EMF of $u_{s1n}$ can be obtained as

$$\begin{aligned} u_{s1n} &= \left(e_{3\_1\&3+2\&4} + e_{6\_1\&3+2\&4} + e_{9\_1\&3+2\&4} + \cdots\right) \\ &\approx e_{3\_1\&3+2\&4} \end{aligned} \tag{7.3}$$

Similarly, the harmonic back-EMF of $u_{s2n}$ is measured between the machine winding neutral point "*n*" and the central point "*s*2" of the second resistance network, which can be derived as

$$\begin{aligned} u_{s2n} &= \left(u_{an\_2\&4} + u_{bn\_2\&4} + u_{cn\_2\&4}\right)/3 \\ &= \left(e_{a\_2\&4} + e_{b\_2\&4} + e_{c\_2\&4}\right)/3 \\ &= e_{3\_2\&4} + e_{6\_2\&4} + e_{9\_2\&4} + \cdots \approx e_{3\_2\&4} + e_{6\_2\&4} \\ &\approx \frac{1}{2} \times \left(e_{3\_1\&3+2\&4} + e_{6\_1\&3+2\&4}\right) \end{aligned} \tag{7.4}$$

In Fig. 7.4, the harmonic back-EMF waveforms are measured by the method shown in Fig. 7.3. More specifically, on the condition of harmonic component in the back-EMF, the amplitude of $u_{s2n}$ is obviously bigger than that of $u_{s1n}$ as can be seen in Fig. 7.4, which shows the 6$^{th}$ harmonic component in $u_{s2n}$ is dominant and can be utilized for the sensorless rotor position estimation. However, it can also be found that $u_{s2n}$ contains a large 3$^{rd}$ harmonic component which may affect the effectiveness of sensorless control operations and needs to be further eliminated.

Additionally, Figs. 7.4 (a) and (b) show that the amplitudes of harmonic back-EMF of $u_{s1n}$ and $u_{s2n}$ are relatively small, which may easily fail the sensorless operation. Hence, the amplitudes of $u_{s1n}$ and $u_{s2n}$ can be amplified to a significant level as shown in Fig. 7.4 (c) and (d) by a Texas Instrument TL074 operational amplifier in order to increase the stability of sensorless control performances based on the 6th-harmonic back-EMF.

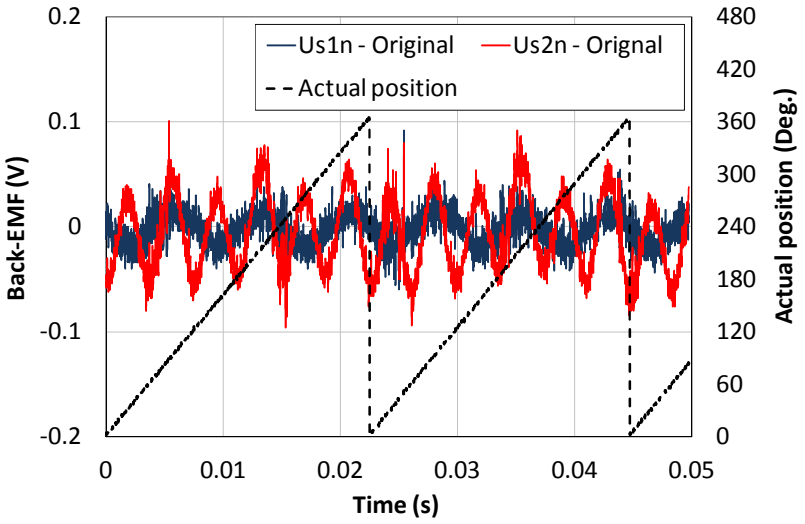


(a) Original Back-EMF waveforms with actual rotor position

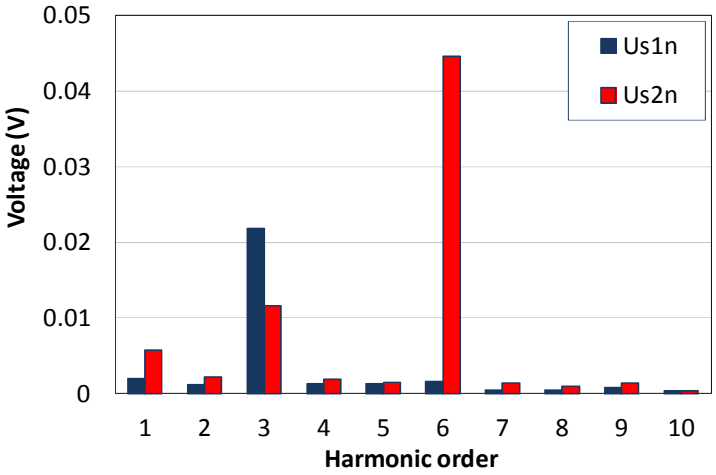


(b) FFT analysis - Original

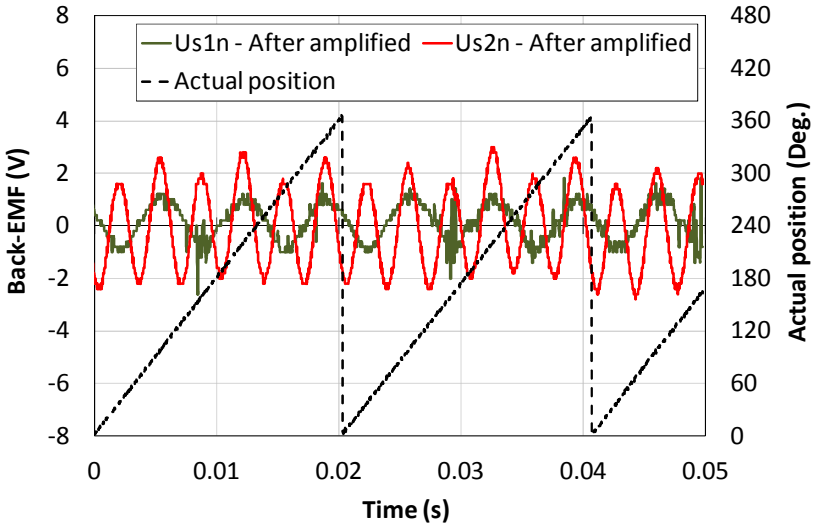


(c) Amplified Back-EMF waveforms with actual rotor position

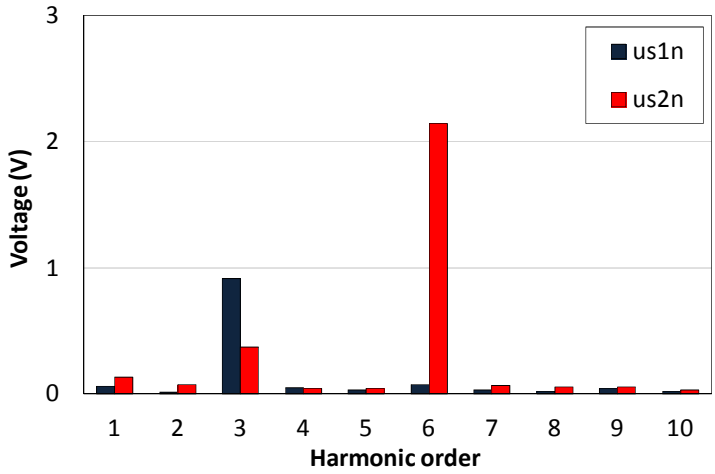


(d) FFT analysis - Amplified

Fig. 7.4. Measured harmonic back-EMFs and harmonic analysis.

### 7.3.2 Third Harmonic Effect and Cancellation

As mentioned earlier, $u_{s2n}$ has contained the large 3rd harmonic component, which will deteriorate the sensorless performances. Thus, the 3rd-harmonic component measured from $u_{s1n}$ can be utilized to reduce the influence of 3rd harmonic component on $u_{s2n}$ as its amplitude is twice, which can be derived as

$$u_{s1n} = e_{3\_1\&3} \approx 2 \times e_{3\_2\&4} \tag{7.5}$$

$$u_{s2n} = \frac{1}{2} \times \left( e_{3\_1\&3+2\&4} + e_{6\_1\&3+2\&4} \right) = e_{3\_2\&4} + e_{6\_2\&4} \tag{7.6}$$

To minimize the influence of 3rd harmonic component on $u_{s2n}$, a simple method is proposed, and can simply be re-expressed as

$$u_{s2n}^{*} = u_{s2n} - \left( u_{s1n} / 2 \right) \approx e_{6\_2\&4} \tag{7.7}$$

In Fig. 7.5, the 3rd harmonic component effect on $u_{s2n}$ is analyzed, and has significantly been reduced in $u_{s2n}$. Moreover, it can be anticipated that if the influence of the 3rd harmonic on $u_{s2n}$ can completely be eliminated by the proposed method; the more accurate rotor position estimation will be achieved.

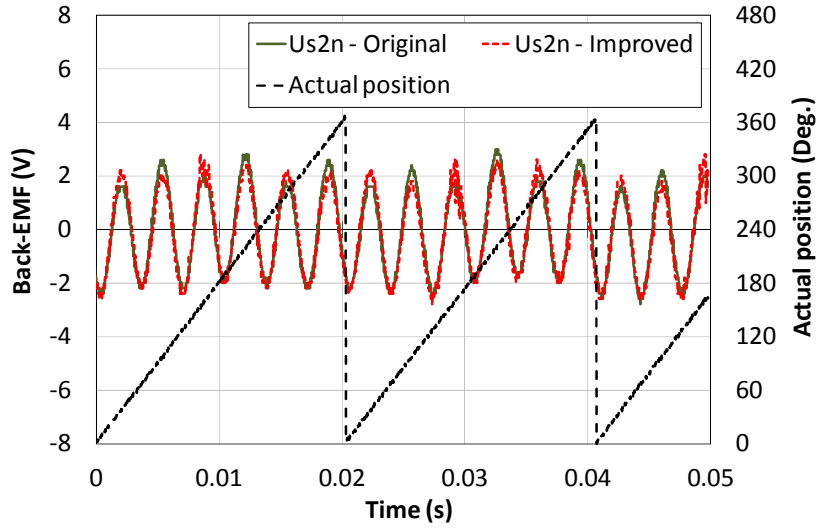


(a) Comparison of back-EMF waveforms

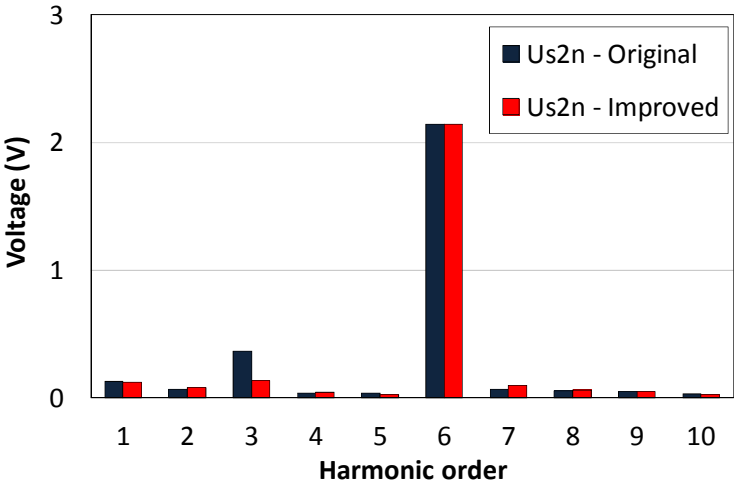


(b) FFT analysis

Fig. 7.5. Influence of third harmonic on back-EMF of $u_{s2n}$.

## 7.4 Existing Back-EMF Based Rotor Position Estimations

In this section, the conventional fundamental back-EMF and the existing harmonic back-EMF based sensorless rotor position estimations will briefly be described first and the improved rotor position estimation based on sixth-harmonic back-EMF will be introduced in the following section.

### 7.4.1 Rotor Position Estimation Based on Fundamental Back-EMF

The most commonly used method for sensorless control in medium and high speed ranges is the fundamental back-EMF based observer [SHE02][PEL12]. The algorithm of the fundamental back-EMF technique according to [WAN12], can be expressed as

$$u_\alpha = R_s i_\alpha + \frac{d}{dt}\left(L_s i_\alpha + \psi_{pm} \cdot \cos\theta_r\right) \tag{7.8}$$

$$u_\beta = R_s i_\beta + \frac{d}{dt}\left(L_s i_\beta + \psi_{pm} \cdot \sin\theta_r\right) \tag{7.9}$$

$$\psi_{s\_\alpha\beta} = \int \left(u_{\alpha\beta} + \psi_{pm} \times i_{\alpha\beta}\right) \cdot dt \tag{7.10}$$

$$\theta_r^e = \text{atan}2\frac{\psi_{s\_\beta}}{\psi_{s\_\alpha}} \tag{7.11}$$

where $\psi_{pm}$, $u$ and $i$ are the permanent magnet flux linkage, terminal voltage and measured current, respectively. $R_s$ is the stator resistance and $L_s$ is the winding inductance. $\theta_r$ is referred as the electrical rotor position. However, the problem for the fundamental method is the sensitivity of machine parameters which need to be accurate otherwise the accuracy of the rotor position estimation will be degraded.

#### A. Sensorless Control in Steady-state Performance

The steady-state performance for the fundamental back-EMF based sensorless control method is tested at the condition of 40V DC-link voltage, at a constant rotational speed 100 r/min with about 2A *q*-axis current is shown in Fig. 7.6. According to the experimental results, the DC position estimation error is occurred due to cross-coupling effect or inaccurate machine parameters.

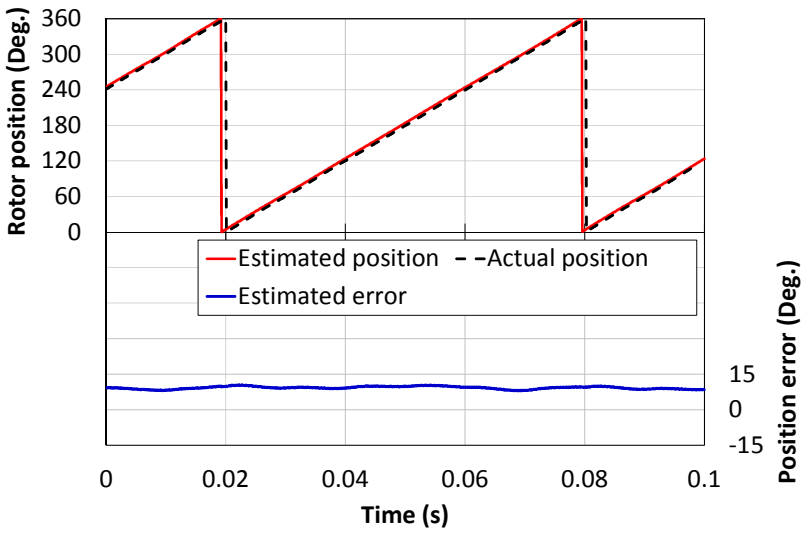


Fig. 7.6. Rotor position estimation at steady-state, 100 r/min.

### 7.4.2 Rotor Position Estimation Based on Third-Harmonic Back-EMF

Another back-EMF based method is to utilize the 3rd-harmonic back-EMF for the sensorless rotor position estimation which becomes more popular in the research study [SHE06b][KRE94][LIU14]. Since the 3rd-harmonic back-EMF has three cycles of frequency against the fundamental back-EMF, the zero-crossings in the 3rd-harmonic back-EMF are related to some particular positions [KRE94], i.e. 0, π/3, 2π/3, π, 4π/3, 5π/3, 2π, as illustrated in Fig. 7.7.

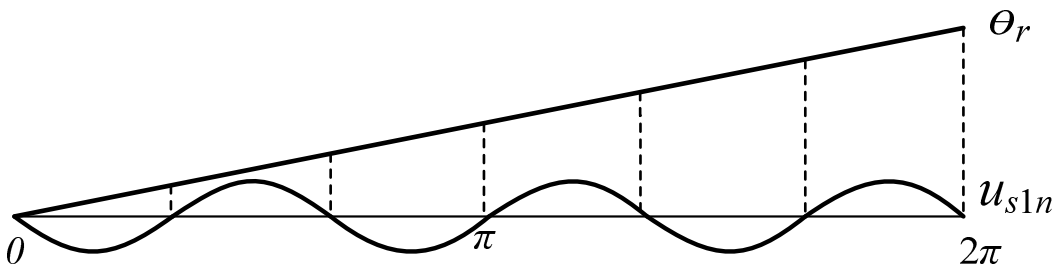


Fig. 7.7. Zero-crossings of the third-harmonic back-EMF.

According to [SHE06b][LIU14], the initial rotor position $\theta_0$ of each half-cycle between two

zero-crossings could be known. Then, the estimated rotor position can be calculated by a simple integration which can be derived as

$$\theta_r^e = \theta_0 + \int_0^t \omega_r^e dt = \theta_0 + \int_0^t \frac{\pi/3}{t_d} dt \tag{7.12}$$

where $\omega_r$ in (11) is actually the average machine speed which can be calculated from the time cycle of zero-crossings, whilst $\Delta tc$ is the time interval of position estimation. However, for the conventional 3rd-harmonic back-EMF based sensorless control, the estimated rotor position will only be accurate under steady-state and deteriorated during dynamic transient state due to the shape change of estimated rotor position.

**A. Sensorless Control in Steady-State Performance**

Similarly, the steady-state performance for the third-harmonic back-EMF based sensorless control method is operated at the condition of 40V DC-link voltage, at a constant rotational speed 100 r/min with about 2A *q*-axis current is shown in Fig. 7.8. It can be seen that the positon estimation error is larger and obvious due to the small amplitude of third-harmonic back-EMF in the Test Machine-II as explained in the previous section. Also, due to the inaccurate speed estimation, the position error will be accumulated since the estimated rotor position contains some error on each zero-crossing point.

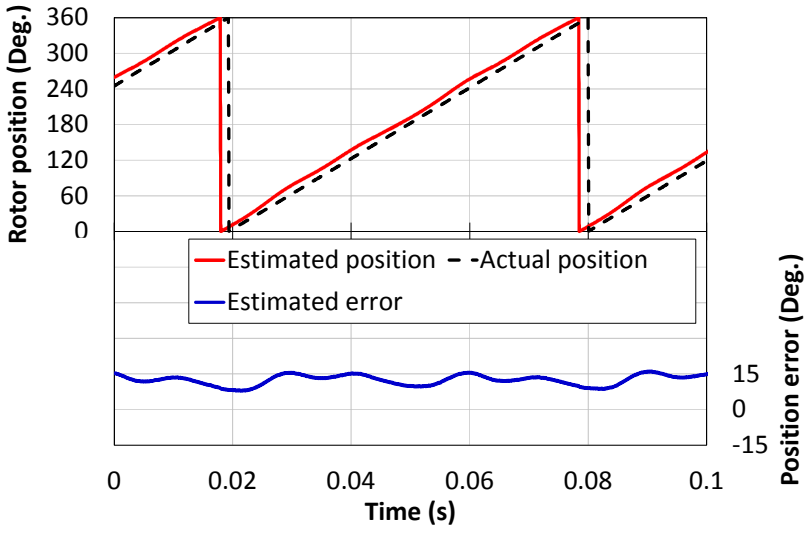


Fig. 7.8. Rotor position estimation at steady-state, 100 r/min.

## 7.5 Proposed Position Estimations Based on Sixth-Harmonic Back-EMF

Since the 6th-harmonic back-EMF in the Test Machine-II is dominant and can be used for the sensorless control operation, and has similar principle as the method based on the 3rd-harmonic back-EMF [SHE06b][LIU14]. The several new position estimation method for the sensorless control based on the 6th-harmonic back-EMF will be introduced in this section.

In order to demonstrate the effectiveness of the 6th-harmonic back-EMF based sensorless control operation, both steady and dynamic measurements have been carried out on the Test Machine-II, whose parameters are listed in Chapter 2, Table 2.3. Both the A/D current-sampling and inverter pulse-width-modulation switching frequencies were 10 kHz. In Fig. 7.9, the overall sensorless control scheme based on the 6th-harmonic back-EMF is implemented.

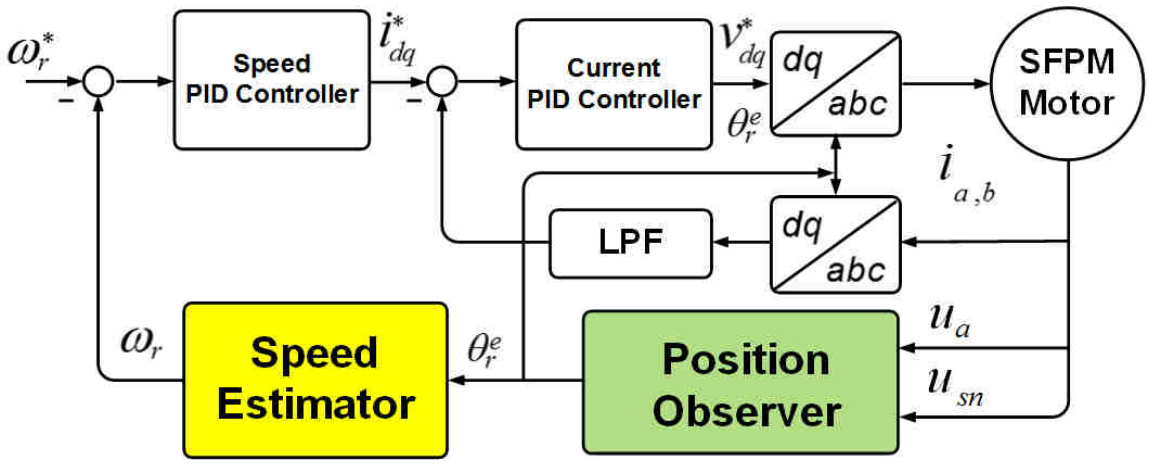


Fig. 7.9. Overall sensorless control scheme.

### 7.5.1 Rotor Position Estimation Based on Integration and Zero Crossings Detection

In this sub-section, the integration and zero-crossings detection of the 6th-harmonic back-EMF based rotor position estimations will be described in order to highlight its potential problems. In the next sub-section, a new continuous rotor position estimation method based on 6th-harmonic back-EMF will be proposed.

In Fig. 7.10, the initial rotor position $\theta_0$ is calculated from the integration of $u^*_{s2n}$ which is the 6th-harmonic flux-linkage of $\psi_{sn}$ comparing with the electrical rotor position $\theta_r$. It shows that one period of electrical rotor position over the six identical cycles of the 6th-harmonic back-EMF. Therefore, the terminal phase A voltage $u_a$ is required for detecting the first related rotor position of zero-crossings of $\psi_{sn}$ which is π/12. When the first related rotor position is obtained, the following discrete positions can also be located, which are π/4, 5π/12, 7π/12, 3π/4, 11π/12, 13π/12, 5π/4, 17π/12, 19π/12, 7π/4 and 23π/12 as shown in Fig. 7.10, in which the related can also be seen in Fig. 7.11. Then, to obtain the estimated rotor position, the rotor position estimator based on the integration and zero-crossing detection shown in 7.12 is implemented.

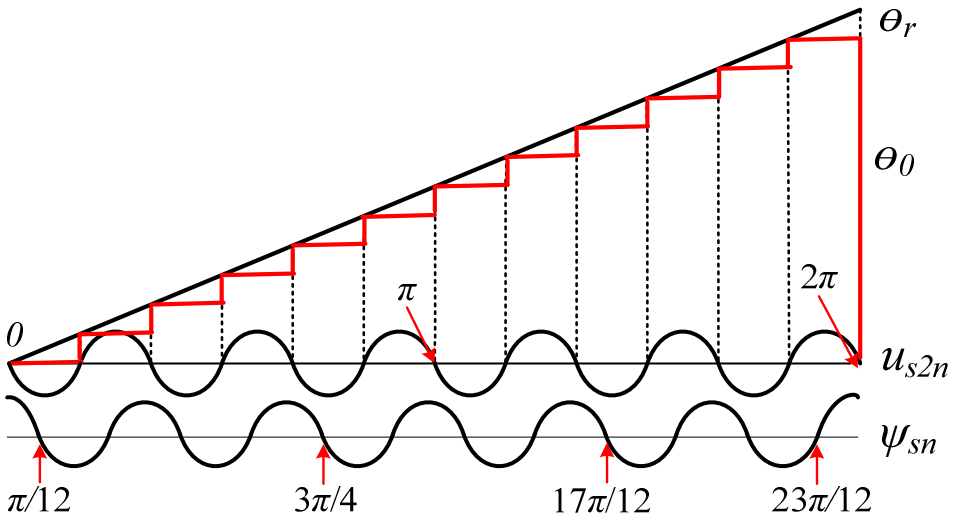


Fig. 7.10. Position detection from zero crossings.

Fig. 7.11 shows the relationship between the terminal phase-A voltage, the actual rotor position and related $\theta_0$ at each zero- crossing point of $\psi_{sn}$ at steady-state in constant speed of 100 r/min.

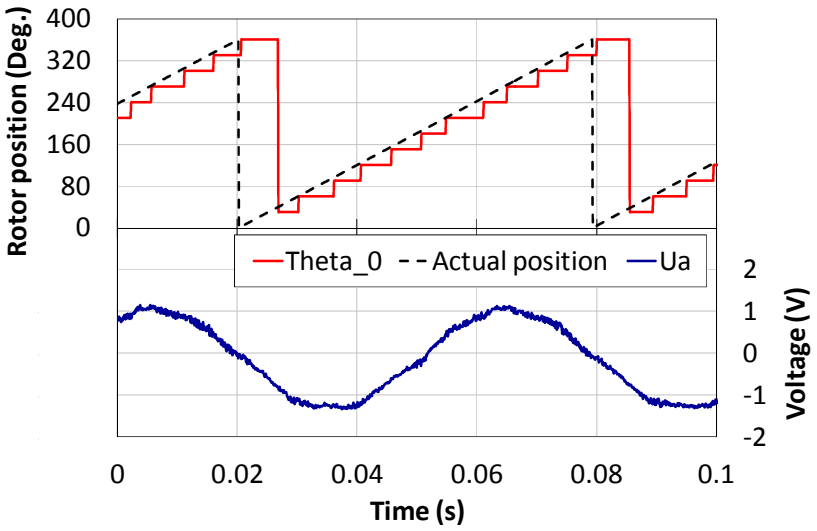


Fig. 6.11. Rotor positions with phase A terminal voltage, 100 r/min.

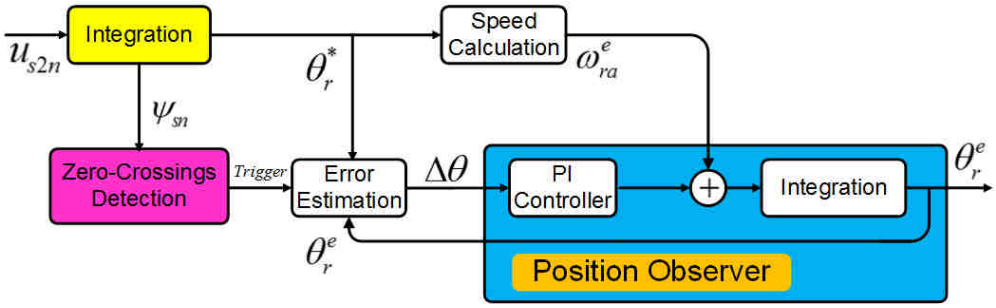


Fig. 7.12. Integration and zero-crossing detection based rotor position estimations.

### A. Integration based Rotor Position Estimation

Since the zero-crossings of the 6th-harmonic flux-linkage are related to the rotor positions, each cycle between two zero-crossings can be located in order to detect the initial rotor position $\theta_0$. Then, the estimated rotor position $\theta_r^e$ can be calculated by integration [SHE06b][LIU14] as

$$\theta_r^e = \theta_0 + \int_0^t \omega_r^e dt \tag{7.13}$$

where $\omega_r^e$ is the estimated speed that calculates from the time duration between the

zero-crossings of $\psi_{sn}$ and current, and usually the average speed between the last two zero-crossings of $\psi_{sn}$, i.e.

$$\omega_r^e = \frac{\pi / 6}{t_d} \tag{7.14}$$

where $t_d$ is referred as the time interval of the previous half cycle between two zero-crossings of $\psi_{sn}$.

Thus, the rotor position estimation at steady-state can exhibit accurate rotor position information since the speed is constant and does not change ideally. Fig. 7.13 shows the steady-state rotor position estimation based on integration, (7.13), at a constant speed, 100 r/min. Furthermore, the position estimation error may occur on each zero-crossing point due to the inaccurate speed estimation will be reset at each of zero-crossings and then the error is not increased.

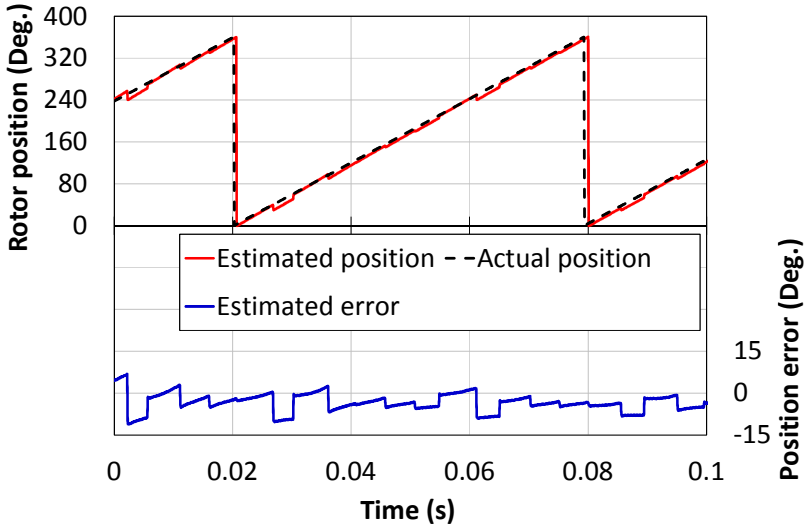


Fig. 7.13. Rotor position estimation based on integration, 100 r/min.

However, the variation of average speed $\omega_r^e$ is usually too slow to reflect the speed transient change. The dynamic operation of rotor speed step-change from 50 r/min to 100 r/min is demonstrated in Fig. 7.14. As it can be seen from the results, the large position estimation error is appeared during the speed transient change due to the sharp change of

estimated rotor position at each zero-crossing point which is shown in Fig. 7.14 (b).

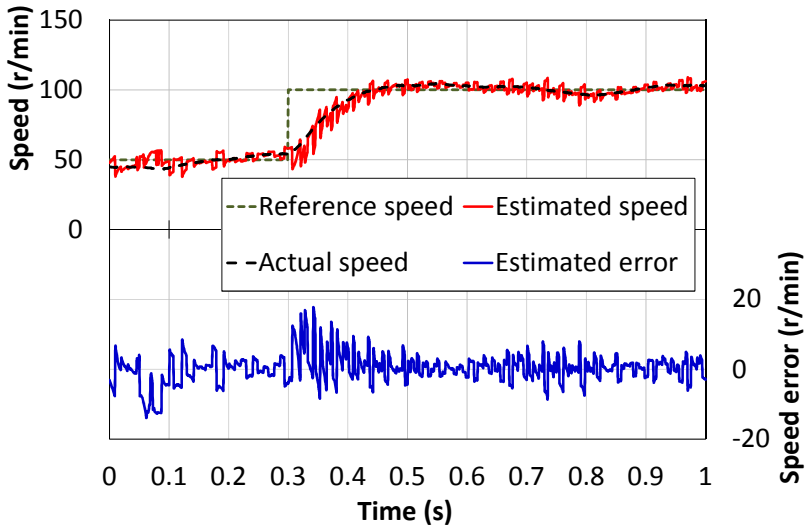


(a) Dynamic rotor speed estimation

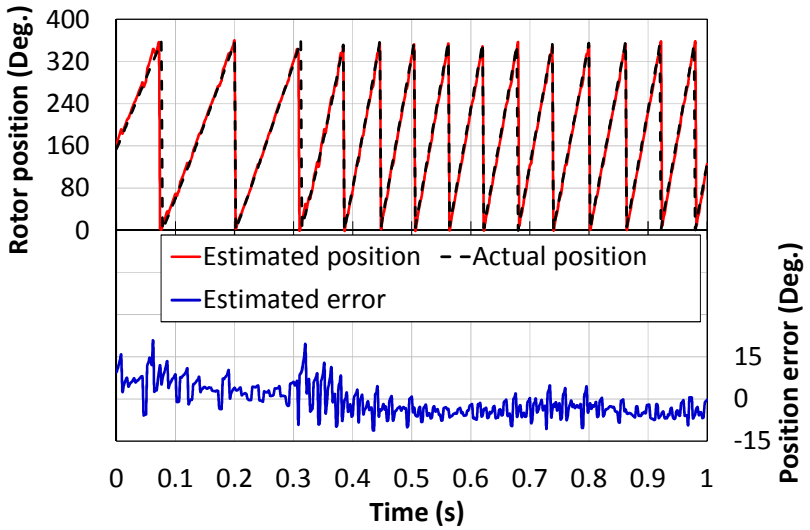


(b) Dynamic rotor position estimation

Fig. 7.14. Rotor speed and position estimations based on integration at dynamic-state, 50 - 100 r/min.

If the rotor speed is fast enough, the estimation error will not be accumulated, and then is automatically reset to zero when each zero-crossing point is detected. However, the sharp change of the estimated rotor position will also happen at low speed and deteriorate the

control performances, such as torque ripple and current distortion, due to inaccurate average speed estimation.

**B. Zero-Crossing Detection Based Rotor Position Estimation**

As mentioned in the previous section, the sharp change will happen to the estimated rotor position at each zero-crossing point during the dynamic transient or at low rotor speed, in which the operating performance will be degraded. Therefore, to avoid the sharp change of estimated rotor position, the conventional Phase-locked loop (PLL) based rotor position tracking observer can be utilized to improve the rotor and speed estimations. According to Fig. 6.9, the position difference between rotor position $\theta_0$ and estimated rotor position can be used as references to calculate the position estimation error, which has the same principle of position difference between actual rotor position and estimated rotor position. Then, the calculated estimation error can be applied to the PI controller. Hence, a speed correction can be expressed as

$$\omega_r^e = LPF \cdot \left( k_p + \frac{k_i \cdot \Delta t}{1 + z^{-1}} \right) \cdot \Delta\theta \tag{7.15}$$

where $k_p$ and $k_i$ are the proportional and integral gains of PI controller, respectively. $\Delta t$ is referred to the sampling interval.

The rotor position estimation based on zero-crossings detection at a constant speed at steady-state, 100 r/min, is shown in Fig. 7.15. The results show the similar performance as the rotor position estimation based on integration, but the sharp change of estimated rotor position is significantly improved. Moreover, the sensorless rotor and speed estimations based on zero-crossings detection at dynamic-state, 50 r/min to 100 r/min is shown in Fig. 7.16. The estimation error in both rotor position and speed estimations are reduced, but the DC error still exists which needs further improvement.

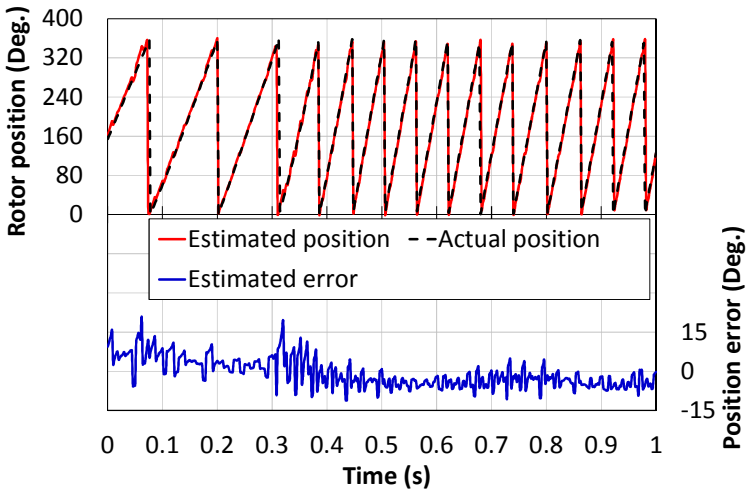


Fig. 7.15. Rotor position estimation based on zero-crossings detection, 100 r/min.

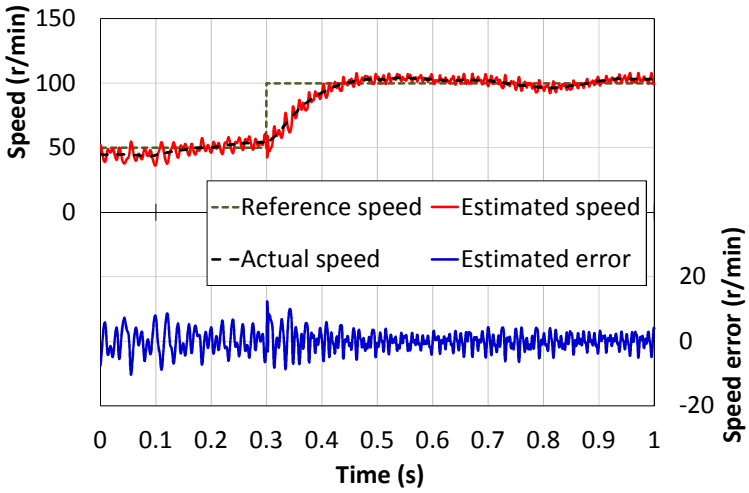


(a) Dynamic rotor speed estimation

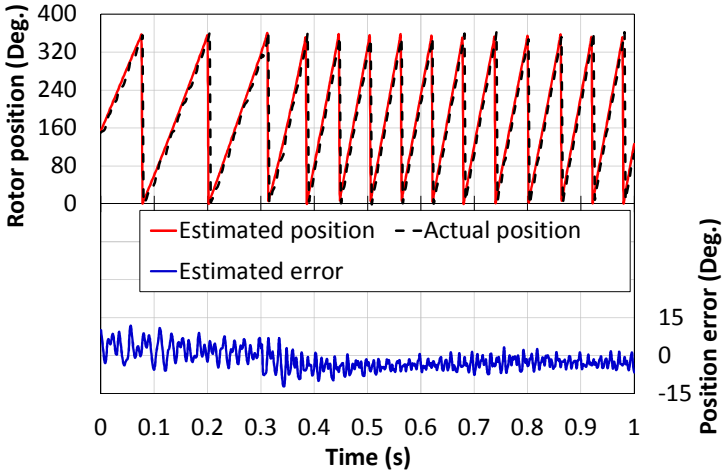


(b) Dynamic rotor positon estimation

Fig. 7.16. Rotor speed and position estimations based on zero-crossings detection at dynamic-state, 50 - 100 r/min.

It can be concluded that the rotor position and speed estimation still have large estimation errors, such as DC constant error or oscillation error, due to the unstable estimation of twelve accurate rotor positions. To further improve the accuracy of the rotor position estimation in the sensorless control performances, the Two-Phase type Phase-locked loop (TP-PLL) based rotor position tracking observer is employed, but the performance is still limited because of the non-constant amplitude of the 6th-harmonic back-EMF and its integration, the 6th-harmonic flux-linkage, which will be introduced in the next sub-section.

### 6.5.2 Improved Rotor Position Estimation Based on Sixth-Harmonic Back-EMF

To improve the accuracy of rotor position estimation, the TP-PLL observer with the aid of non-constant compensation based on $u^*_{s2n}$ and its integration $\psi_{sn}$ is proposed, Fig. 7.17.

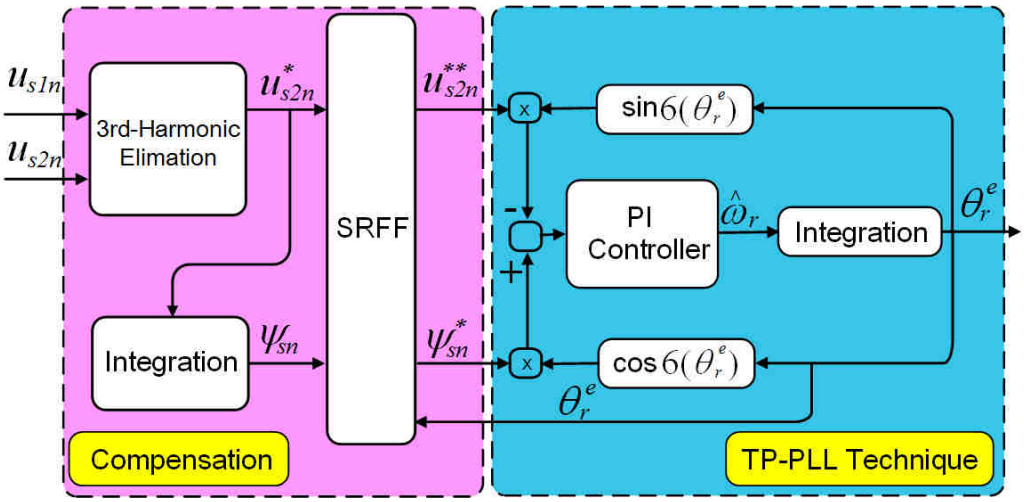


Fig. 7.17. Proposed rotor position estimation with non-constant compensation scheme.

As mentioned before, if the 3rd harmonic component in $u_{s2n}$ is completely cancelled, the calculated $u^*_{s2n}$ will mainly be the 6th-harmonic back-EMF. Hence, its integration, i.e. the 6th-harmonic flux-linkage $\psi_{sn}$ will be a continuous sinusoidal signal with constant amplitude which can be used as the reference input signal for the proposed rotor position tracking

observer. In fact, the amplitude of calculated $u_{s2n}^{*}$ is non-constant since the harmonics are not all eliminated. It will deteriorate the rotor position accuracy in the sensorless control operations. Therefore, a compensation scheme i.e. synchronous reference frame filter (SRFF) [REI13][DEG98] as shown in Fig. 7.18 and a novel rotor position estimation are proposed to reduce the error in the rotor position estimation.

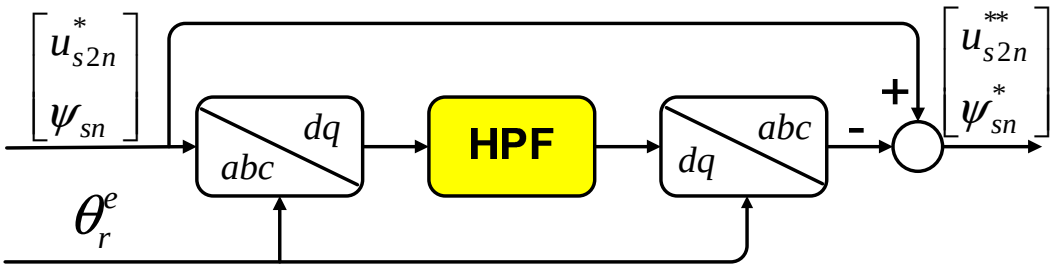


Fig. 7.18. Model of synchronous reference frame filter.

In this application, the high-pass filter (HPF) is chosen to eliminate all harmonics. SRFF is basically based on the two signals. One is (7.7) which can be rewritten as

$$u_{s2n}^{*} = K_{ap}\sin\left(\omega_r t+\varphi_u\right)+e_{6\_2\&4} = K_{ap}\sin\left(6\times\theta_r\right) \tag{7.16}$$

where $K_{ap}$, $\omega_r$ and $\varphi_n$ are the amplitude, angular speed and initial phase angle of the 6th-harmonic back-EMF, and its integration $\psi_{sn}$ which can be expressed as

$$\psi_{sn} = -A_{ap}\cos\left(6\times\theta_r\right) \tag{7.17}$$

where $A_{ap}$ is the amplitude of $\psi_{sn}$.

Basically, SRFF uses the reference frame transformation synchronizing system. When applying the frame transformation with the aid of estimated rotor position, the two input signals $u_{s2n}^{*}$ and $\psi_{sn}$ which are the spectral components of interest and will be centered at DC (0Hz). All the components including relevant fundamental and higher order harmonics will appear as harmonic ripples. Then with the aid of a HPF (5Hz cut-off frequency), the harmonic ripple components can be easily filtered out. Meanwhile, applying the reverse

frame transformation, the fundamental and high order harmonics which are contained in $u_{s2n}^{*}$ and $\psi_{sn}$ can be obtained. Then, subtracting from the original input signals, the spectral components of interest which are the 6th-order harmonic back-EMF and flux-linkage will be derived.

In Fig. 7.19, the effectiveness of the non-constant compensation scheme is validated. Clearly, the 6th-harmonic flux-linkage and the unified 6th-harmonic back-EMF with non-constant amplitude, Fig. 7.19 (a), have significantly been improved as shown in Figs. 7.19 (b) and (c).

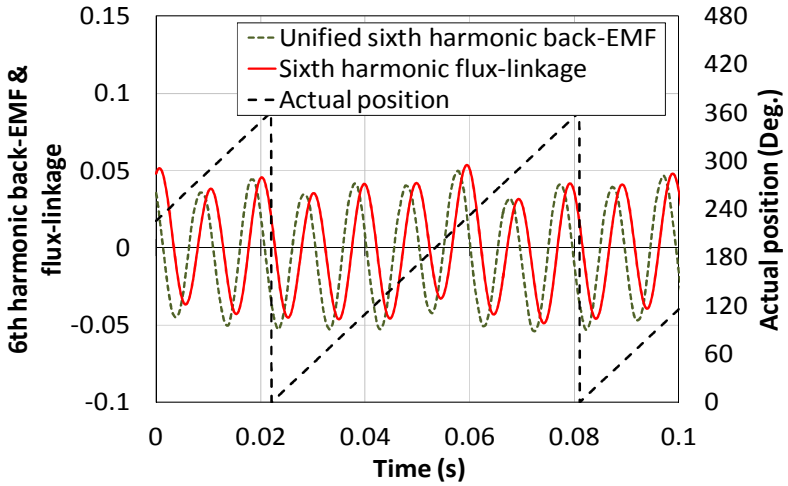


(a) Without

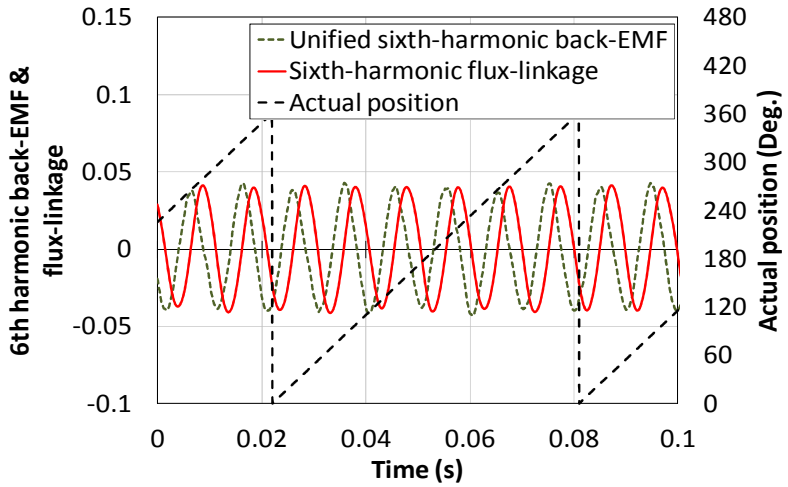


(b) With

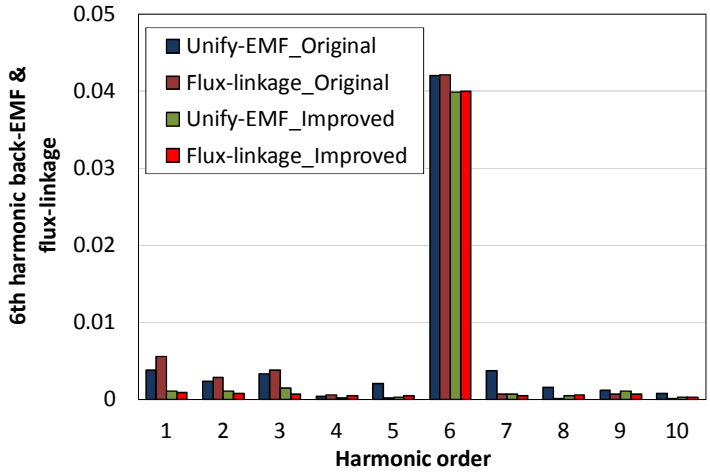


(c) FFT analysis

Fig. 7.19. Measured sixth-harmonic flux-linkage and unified sixth-harmonic back-EMF with proposed compensation scheme.

After compensating the non-constant issue, the 6th-harmonic flux-linkage will be a continuous signal with constant amplitude, which can be represented as

$$\psi_{sn}^{*} = -A_p \cos\left(6\times\theta_r\right) \tag{7.18}$$

where $A_p$ is the amplitude of $\psi_{sn}^{*}$. $A_p$ varies with different temperature of permanent magnet. So, it should be detected in every cycle in order to avoid the amplitude changing.

Moreover, the assistant signal of $u_{s2n}^{*}$, its amplitude is related to rotor position and varying with the rotor speed $\omega_r^e$, can be unified to $A_p$, which is rewritten as

$$u_{s2n}^{**} = \frac{K_p}{\omega_r^e} E_6 \sin\left(6\times\theta_r\right) = A_p \sin\left(6\times\theta_r\right) \tag{7.19}$$

where $\omega_r^e$ is the estimated speed response and $K_p$ is the unify-value of the 6th-harmonic back-EMF. In order to obtain the continuous rotor position from (7.18) and (7.19), the TP-PLL observer is employed which was first published in [EMU00], and its principle is simply explained in Fig. 7.20.

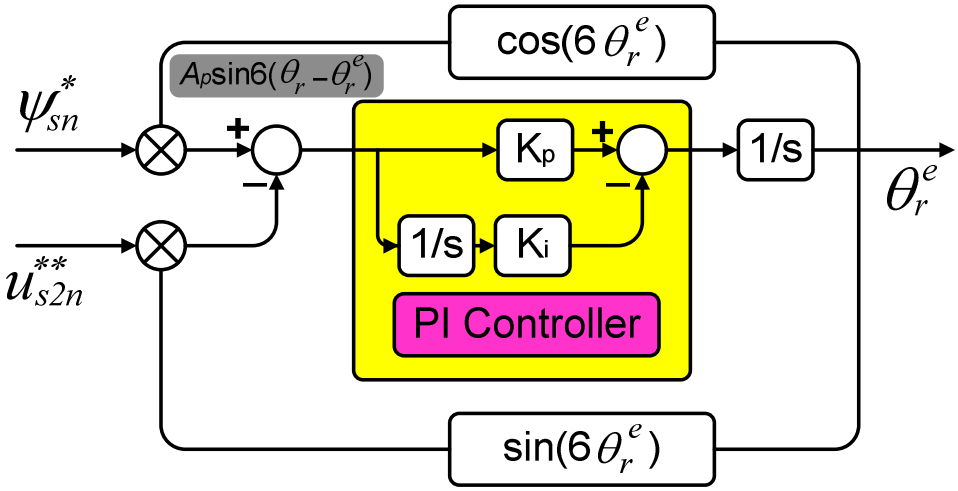


Fig. 7.20. Principle of two-phase type phase-locked loop observer.

According to the Fig. 7.20, the close-loop transfer function between the actual and estimated rotor position information can be expressed as

$$\frac{\theta_r^e}{\theta_r} = \frac{6A_p k_p \cdot s + 6A_p k_i}{s^2 + 6A_p k_p \cdot s + 6A_p k_i} \tag{7.20}$$

Equation (7.20) represents as a simple standard second-order control system. The values of $k_p$ and $k_i$ of PI controller can easily be determined and on-line adjusted.

By applying the TP-PLL observer, the sinusoidal signal can lock the input and output phase and then generate the phase angle in order to detect the phase error between the input and output signals. Furthermore, the frequency of the input signal can be obtained by the PI controller as a filter together with the integration to keep generating the estimated rotor position and also to avoid the sharp-change of the estimated rotor position. Therefore, with the aid of SRFF, a TP-PLL rotor position estimator can achieve high accuracy of continuous rotor position estimation at both steady and dynamic states.

**A. Sensorless Control in Steady and Dynamic Performances**

Several operating tests have been carried out to highlight the effectiveness of the proposed rotor position tracking observer. The estimated rotor position based on the proposed method,

at a constant speed of 100r/min, is shown in Fig. 7.21. Comparing the experimental result with integration and zero-crossing detection based rotor position estimations, the more accurate rotor position estimation is achieved, i.e. small oscillation error, and DC constant error caused by the cross-coulping effect is significantly improved. Meanwhile, the position-tracking behavior is compared in Fig. 7.22. It shows that the proposed new rotor position estimation exhibits lower position estimation error and better performance than that of the rotor position estimation without compensation.

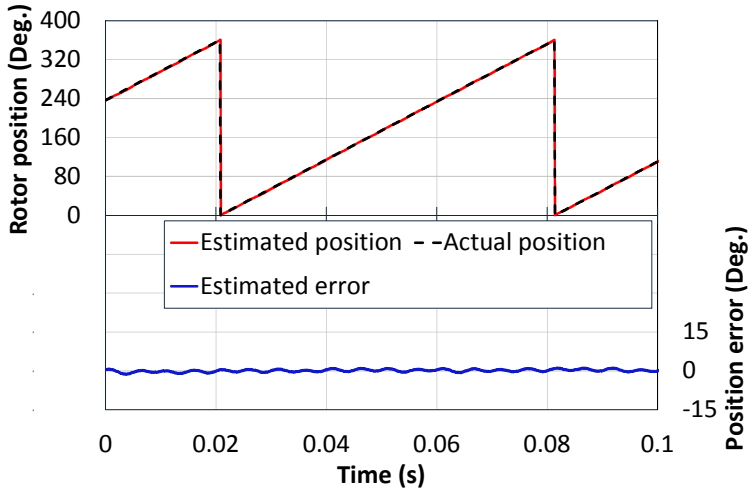


Fig. 7.21. Rotor position estimation based on proposed method at steady-state, 100 r/min.

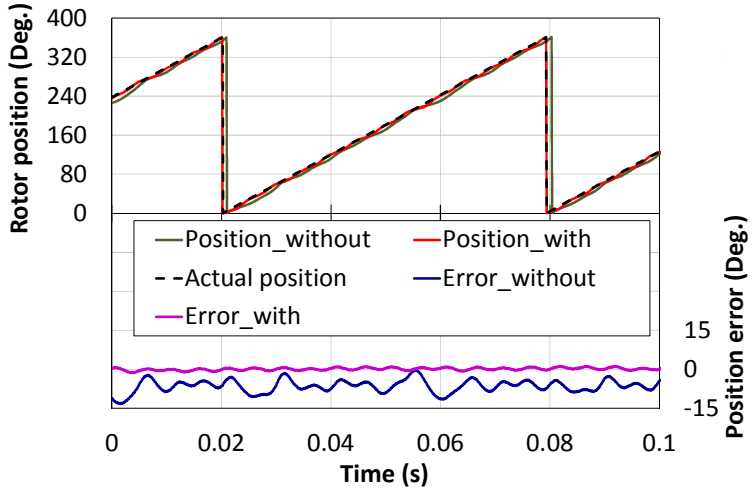


Fig. 7.22. Comparison of rotor position estimations for sensorless control, 100 r/min.

Furthermore, the same dynamic operating conditions are also applied to the Test Machine-II by the proposed method. In Fig. 7.23, the measured dynamic performance of

speed step-response from 50 r/min to 100 r/min is demonstrated. Clearly, the proposed method which is based on the continuous rotor position and a good speed response is obtained as shown in Fig. 7.23 (a). The position estimation error is significantly reduced, Fig. 7.23 (b). Hence, the better dynamic performance is achieved comparing with that of the positon estimation based on integration and zero-crossings detection. Moreover, although the estimated position error reaches up to ±10 deg. during the transient process, the estimation position error can still be limited to ±5 deg. at steady state.

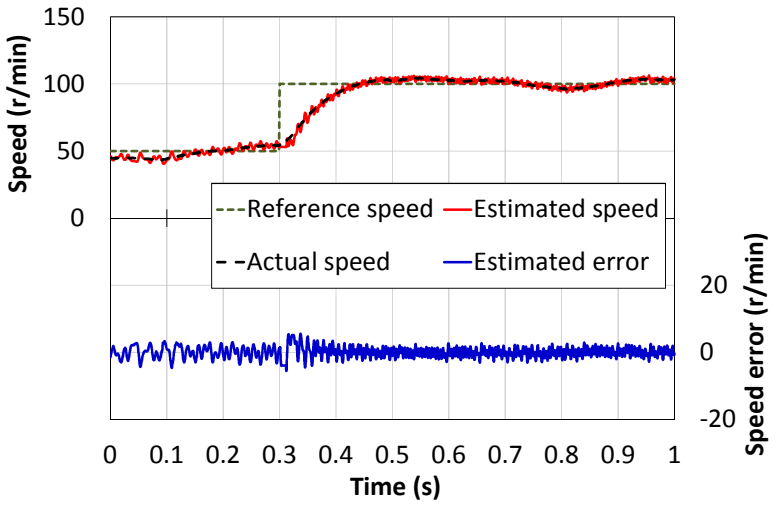


(a) Dynamic rotor speed estimation

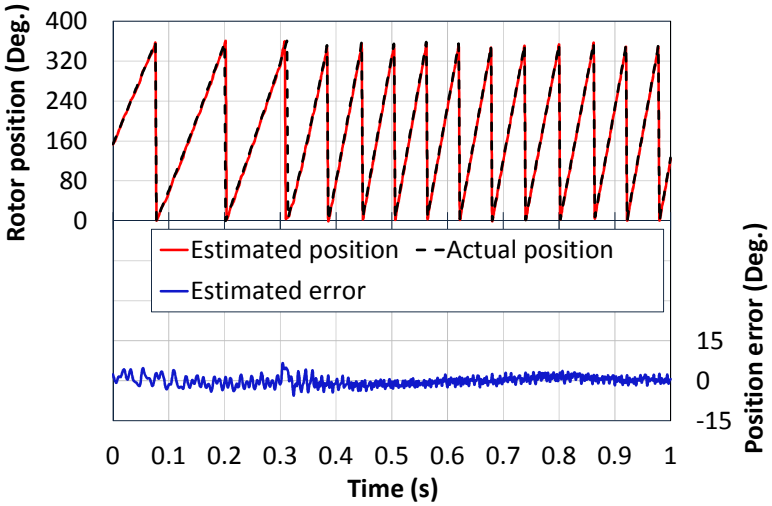


(b) Dynamic rotor position estimation

Fig. 7.23. Rotor speed and position estimations based on proposed method at dynamic-state, 50 - 100 r/min.

Additionally, the operating performance during the start up from standstill to 100 r/min is investigated in Fig. 7.24. The sensorless control stage is switched in at 0.37s. During the speed increasing period, the estimated position error is finally almost reduced to zero and the estimated speed also follows well to the desired speed, as shown in Figs. 7.23 (a) and (b). The switching from the low speed to sensorless control stage is smooth and achieved the high accuracy of rotor position estimation.

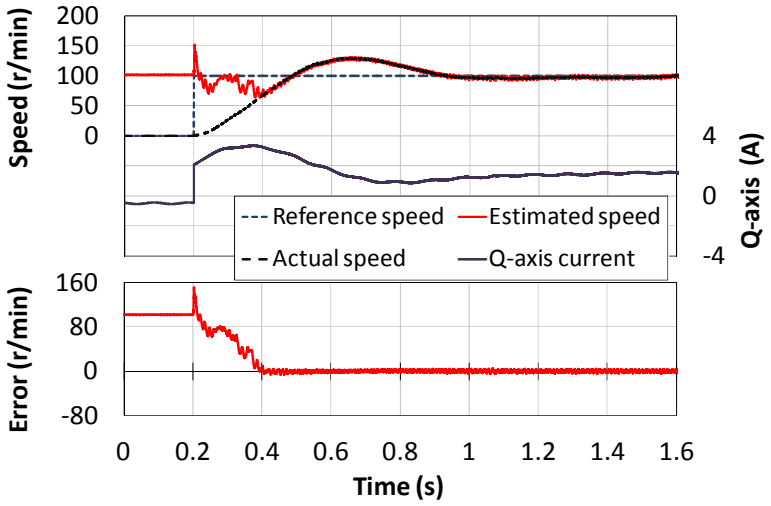


(a) Estimated speed and *q*-axis current response

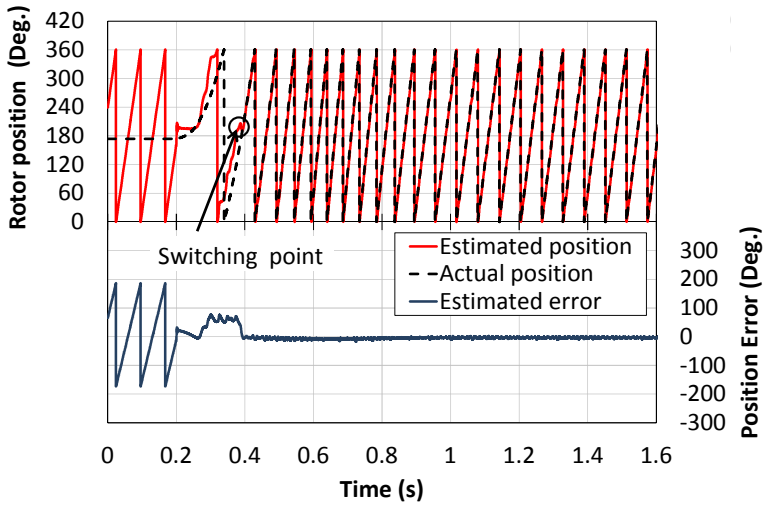


(b) Estimated position and error

Fig. 7.24. Measured speed-step responses, from 0 to 100 r/min, using proposed rotor position and speed estimation.

**B. Comparison of Back-EMFs Based Sensorless Operations**

The comparison of effectiveness of sensorless rotor position estimations based on the three back-EMF methods is shown in Fig. 7.25. By analyzing the estimated errors in the rotor position estimations under the same testing condition, the estimation accuracy in the fundamental back-EMF based and the 3rd-harmonic back-EMF based has not performed as good as the proposed method due to the influence of cross-coupling magnetic saturation [ZHU07].

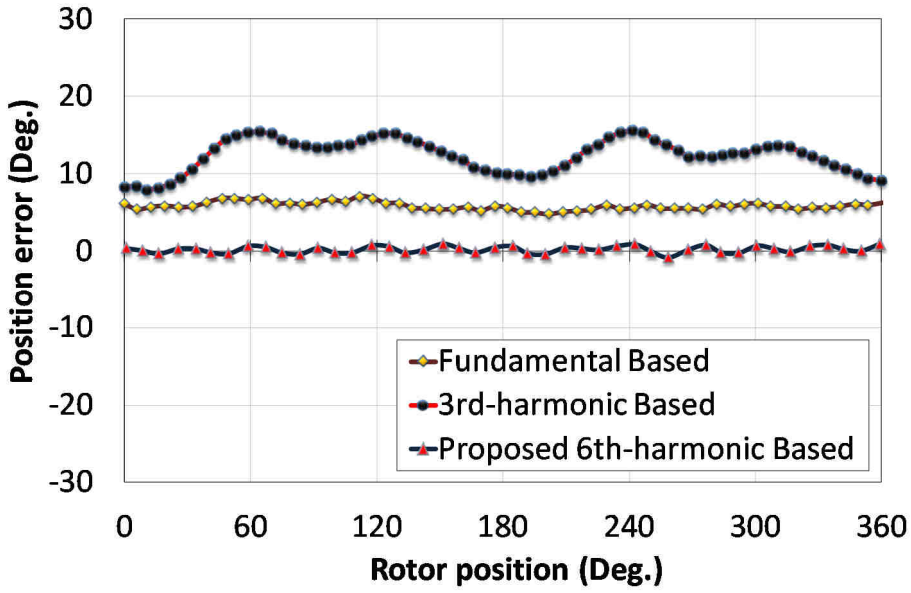


Fig. 7.25. Comparison of rotor position estimations based on different back-EMF methods, 100 r/min.

TABLE 7.1

PERFORMANCE COMPARSION OF BACK-EMF BASED SENSORLESS CONTROL

| | Fundamental back-EMF | 3rd-harmonic back-EMF | 6th-harmonic back-EMF |
|---|---|---|---|
| Standstill and low speed | NOT applicable | NOT applicable | NOT applicable |
| Sensitivity of machine parameters | Sensitive | NOT sensitive | NOT sensitive |
| Sensitivity of higher order harmonics | Less sensitive | Medium sensitive | Medium sensitive |
| Signal to noise ratio | High | Medium | Medium |
| Steady-state operation | Medium | Medium | High |
| Dynamic-state operation | Medium | Medium | High |

## 7.5 Conclusion

In this chapter, the 6th-harmonic back-EMF based sensorless control is proposed for the prototype Test Machine-II since its amplitude is bigger and dominant, whilst the 3rd-harmonic is relatively small which may easily fail in the rotor position estimation.

Considering the 3rd-harmonic and non-constant effects, the proposed new rotor position estimation together with the harmonic elimination and SRFF by utilizing the combined 6th-harmonic back-EMF and flux-linkage, the continuous rotor position is therefore obtained,

and more accurate rotor position estimation is achieved at both steady and dynamic states.

Furthermore, the comparison with the fundamental and the 3rd-harmonic back-EMF techniques shown that the proposed method has better response and performance due to less influence by the cross-coupling magnetic saturation, but it still has limit in the low speed region as any flux linkages or back-EMF based methods.

## References


[DEG98] M.W. Degner, and R.D Lorenz, "Using multiple saliencies for the estimation of flux, position, and velocity in AC machines," *IEEE Trans. Ind. Appl.*, vol. 34, no. 5, pp. 1097–1104, 1998.

[EMU00] T. Emura, L. Wang, M. Yamanaka, and H. Nakamura, "A high precision positioning servo controller based on phase/frequency detecting technique of two-phase-type PLL," *IEEE Trans. Ind. Appl.*, vol. 47, no. 6, pp. 1298–1306, Nov./Dec. 2000.

[FAE09] M. Faeq and D. Ishak, "A new scheme sensorless control of BLDC motor using software PLL and third harmonic back-EMF," *Industrial Electronics & Applications, 2009. ISIEA 2009. IEEE Symposium on*, vol. 2, 2009, pp. 861 - 865.

[GEN10] F. Genduso, R. Miceli, C. Rando, and G.R.Galluzzo, "Back-EMF sensorless-control algorithm for high-dynamic performance PMSM," *IEEE Trans. Ind. Electron.*, vol.57, no.6, pp.2092-2100, June 2010.

[KIM03] H. Kim, M. C. Harke, and R. D. Lorenz, "Sensorless control of interior permanent-magnet machine drives with zero-phase lag position estimation," *IEEE Trans. Ind. Appl.*, vol. 39, no. 6, pp. 1726–1733, Nov./Dec. 2003.

[KRE94] L. Kreindler, J.C. Moreira, A. Testa, and T. A. Lipo, "Direct field orientation controller using the stator phase voltage third harmonic," *IEEE Trans. Ind. Appl.*, vol. 30, no. 2, pp. 441-447, 1994.

[LIU14] J. Liu and Z. Zhu, "Improved sensorless control of permanent magnet synchronous machine based on third-harmonic back-EMF," *IEEE Trans. Ind.*

*Appl.*, vol.50, no.3, pp.1861-1870, May-June 2014.

[MOR92] J. Moreira, and T.A. Lipo, "Modeling saturated AC machines including air gap flux harmonic components," *IEEE Trans. Ind. Appl.*, vol. 28, no.2, pp. 343-349, 1992.

[PEL12] G. Pellegrino, E. Armando, and P. Guglielmi, "Direct flux vector control of IPM motor drives in the maximum torque per voltage speed range," *IEEE Trans. Ind. Electron.*, vol.59, no.10, pp.3780-3788, 2012.

[REI13] D. Reigosa, F. Briz, C. Blanco, A. Di Gioia, P. Garcia, and J.M. Guerrero, "Sensorless control of doubly fed induction generators based on rotor high-frequency signal injection," *IEEE Trans. Ind. Appl.*, vol. 49, no. 6, pp. 2593-2601, Nov.-Dec. 2013.

[ROS10] F. G. Rosario, C. Rando, and G. R. Galluzzo, "Back EMF sensorless- control algorithm for high-dynamic performance PMSM," *IEEE Trans. Ind. Electron.*, vol. 57, no. 6, pp. 2092–2100, Jun. 2010.

[SAL10] F.R. Salmasi, T.A. Najafabadi, P.J. Maralani, "An adaptive flux observer with online estimation of DC-link voltage and rotor resistance for VSI-based induction motors," *IEEE Trans. Power Electron.*, vol. 25,no. 5, pp. 1310 -- 1319, 2010.

[SHE02] J.X. Shen, Z.Q. Zhu, and D, Howe, "Improved speed estimation in sensorless PM brushless AC drives," *IEEE Trans. Ind. Appl.*, vol. 38, no. 4, pp. 1072-1080, 2002.

[SHE04] J.X. Shen, Z. Q. Zhu, and D. Howe, "Sensorless flux-weakening control of permanent-magnet brushless machines using third-harmonic back EMF," *IEEE Trans. Ind. Appl.*, vol. 40, no. 6, pp. 1629-1636, Nov./Dec. 2004.

[SHE06a] J.X. Shen, and S. Iwasaki, "Sensorless control of ultrahigh-speed PM brushless motor using PLL and third harmonic back EMF," *IEEE Trans. Indus. Electron.*, vol. 53 , no. 2, pp. 421 - 428, 2006.

[SHE06b] J.X. Shen, Z.Q. Zhu, and D. Howe, "Practical issues in sensorless control of PM brushless machines using third-harmonic back-EMF," *IEEE 5th International Power Electronics and Motion Control Conference, IPEMC2006*, 2006, pp. 1-5.

[VAI95] O. Vainio and S. J. Ovaska, "Noise reduction in zero crossing detection by predictive digital filtering," *IEEE Trans. Ind. Electron.*, vol. 42, pp. 58--62, Feb. 1995.

[WAN12] Z. Wang, K. Lu and F. Blaabjerg, "A simple startup strategy based on current regulation for back-EMF-based sensorless control of PMSM," *IEEE Trans. Power Electron.*, vol.27, no.8, pp.3817-3825, Aug. 2012.

[ZHU07] Z. Q. Zhu, Y. Li, D. Howe, C. M. Bingham, and D. Stone, "Influence of

machine topology and cross-coupling magnetic saturation on rotor position estimation accuracy in extended back-EMF based sensorless PM brushless AC drives," in *Proc. 42nd IAS Annu. Meet.*, 2007, pp. 2378–2385.

[ZHU11] Z.Q. Zhu and L.M. Gong, "Investigation of effectiveness of sensorless operation in carrier signal injection based sensorless control Methods," *IEEE Trans. Ind. Electron.*, vol. 58, no. 8, pp. 3431-3439, 2011.

# CHAPTER 8

# GENERAL DISCUSSIONS AND CONCLUSIONS

This thesis has mainly focused on the sensorless control of PMSMs, with particular reference to SFPM machines, based on the HF carrier signal injection method at standstill and in low speed region, and the fundamental and harmonic back-EMF techniques in medium and high speed regions, without the requirement of a position sensor.

## 8.1 Sensorless Control Techniques

### 8.1.1 Saliency Characteristics of Different Types of Permanent Magnet Machines

Machine saliency produced by the machine geometric anisotropy or magnetic saturation is an essential requirement for saliency based sensorless control techniques, such as HF carrier signal injection based techniques which are well developed in many industrial applications due to their effectiveness of sensorless control performances at zero and low speed range. Based on the practical application, this thesis presents a simplified experimental method for measuring the machine saliency information.

Besides, in reality, the lower magnitude of HF injected voltage the higher error may occur in the rotor position estimation and it is acceptable that 30% of total available DC bus voltage can be used for signal injection in terms of the selection of high-frequency injected voltage and the selection of injection frequency is between 1/50 ~ 1/10 PWM frequency.

Furthermore, based on the different types of PM machines, i.e. IPM, SPM, and SFPM machines, each type of PM machine exhibits different saliency characteristics which are summarized in Table 8.1. In addition, the different saliency features for the machine based on the different machine winding configurations are compared in Table 8.2.

TABLE 8.1

COMPARISON OF SALIENCY BASED ON THREE TYPES OF PM MACHINES

| | IPM machine | SPM machine | SFPM machine |
|---|---|---|---|
| Injection type | Pulsating voltage signal injection | | |
| Reference frame | Virtual/Estimated | | |
| Saliency detection | Detectable | | |
| Carrier current | Amplitude-modulated | | |
| Primary saliency | High | Medium | Low |
| Secondary saliency | Low | Low | Medium |
| Load effect | Sensitive | Sensitive | Sensitive |
| Signal to noise ratio | High | Low | Medium |

TABLE 8.2

COMPARISON OF SALIENCY BASED ON DIFFERENT WINDING CONFIGURATIONS

| | All poles wound | Alternate poles wound |
|---|---|---|
| Carrier signal injection | Pulsating voltage signal injection | |
| Saliency detection | Detectable | |
| Carrier current | Amplitude-modulated | |
| Primary saliency | Medium | High |
| Secondary saliency | Low | High |
| Load effect | Sensitive | Sensitive |
| Signal to noise ratio | Medium | High |

### 8.1.2 High-Frequency Carrier Signal Injection Based Sensorless Control

According to the detailed discussions on the conventional HF carrier signal injection based sensorless techniques in Chapter 3, the sensorless operation capability of SPM machine (Test Machine-I) has experimentally investigated. Since the main challenge of SPM machine is difficult to identify the rotor position due to its low ratio of spatial rotor saliency, the HF eddy-current loss reflected resistance-based saliency may be used for the sensorless rotor position estimation. However, the inductance based machine saliency level of Test Machine-I has met the requirements for implementing the HF carrier signal injection based sensorless control methods such as magnetic polarity detection, compensation for the influence of cross-saturation and the good performances at steady and dynamic states. Hence, the HF eddy-current loss reflected-based saliency can be negligible due to flux-density magnitude, and the influence of saturation will not be obvious with higher injection frequency.

Following the Test Machine-II which is SFPM machine, similar testing conditions are also applied in order to investigate its potential machine saliency level whether it is suitable for the HF pulsating carrier signal injection method based sensorless control, in which the sensorless operations are well performed under several experimental conditions such as sensorless current and speed close-loop control performances at steady and dynamic states under no load and full load conditions.

Since the Test Machine-II can be re-arranged into several machine winding configurations such as all poles wound topology and alternative poles wound topology, single and dual three-phase operations, the machine saliency level for each machine winding configurations have been experimentally measured. The prototype SFPM machine exhibits the apparent saliency, but the secondary saliency exists in the alternative poles wound machine which will affect the overall efficiency of sensorless control operations, and the improved rotor position tracking observer is utilized to enhance the accuracy of rotor position estimation.

### 8.1.3 Fundamental and Harmonic Back-EMFs Based Sensorless Control

Since the saliency based sensorless control method can only operate at standstill and low speed, the back-EMF based techniques are usually employed to overcome this issue such as fundamental and harmonic back-EMFs, flux-linkage observer and other observer based methods.

The comparison between these fundamental and harmonic back-EMF based methods is summarized in Table 8.3.

TABLE 8.3

COMPARISON BETWEEN FUNDAMENTAL AND HARONIC BACK-EMF BASED SENSORLESS CONTROL

| | Fundamental back-EMF | Third-harmonic back-EMF | Sixth-harmonic back-EMF | Asymmetric Back-EMF |
|---|---|---|---|---|
| Machine type | BLDC and BLAC | BLDC and BLAC | BLAC | BLAC |
| Neutral point | Not required | Required | Required | Not required |
| Machine parameters | Sensitive | NOT sensitive | NOT sensitive | Sensitive |
| Other-order harmonic components | NOT sensitive | Sensitive | Sensitive | NOT sensitive |
| Signal to noise ratio | High | Medium | Medium | High |
| Steady-state | Good | Good | Good | Good |
| Dynamic-state | Medium | Medium | Good | Medium |

The fundamental back-EMF based sensorless control method is applied to the Test Machine-II under different machine topologies, i.e. all poles wound and alternate poles wound machines, in which the alternate poles wound machine exhibit the asymmetric back-EMF.

However, the conventional control strategy based on flux-linkage observer is very sensitive to machine parameters, which will cause the inaccurate sensorless rotor position estimation. Additionally, for the alternate poles wound machine, the position estimation error is also affected by the asymmetric and non-sinusoidal back-EMF effect. Hence, to minimize the error in the rotor position estimation and improve the overall control performances, the position error compensation scheme with the aid of adaptive harmonic compensation method is proposed for the rotor flux-linkage based rotor position tracking observer. The issue of sensitivity of machine parameters can be avoided and the more accurate rotor position estimation is achieved. Meanwhile, the robustness of sensorless rotor position estimation is also enhanced.

Furthermore, a novel sensorless control method is introduced, which is based on the sixth-harmonic back-EMF. The new sensorless control based rotor position estimations have the similar principle as the method based on the third-harmonic back-EMF method. Several key features can be summarized as follows:

(1) The harmonic component must exist in the air-gap field.

(2) The natural point of Y-connected machine structure is accessible.

(3) The Y-connected resistance network is required

Without the aid of the resistance network and the natural point of Y-connected machine, the novel sensorless control technique based on the sixth-harmonic back-EMF cannot be used. In this thesis, the proposed rotor position estimator combining with the best feature of harmonic compensation, the high accuracy of sensorless rotor position estimation at steady and dynamic-states are achieved.

## 8.2 Future Work: Hybrid Sensorless Control for Wide Speed Operation

Since this thesis is focused on two different types of sensorless control strategy, each method exhibiting different working feature, the possible future work is to combine these two methods to achieve a good sensorless performance for wide speed range operation.

At standstill and in low speed region, the high-frequency carrier signal injection based methods can successfully estimate the rotor position information. However, carrier signal injection methods also have some disadvantages, such as extra losses, torque ripple, current harmonics and transient disturbances, in which the sensorless rotor position estimation may be failed in the higher speed range. Therefore, it is reasonable to combine with the back-EMF based sensorless control methods in order to achieve a sensorless control performance in the whole speed range operation since the back-EMF based methods can effectively performed in the medium and high speed ranges. Nevertheless, the back-EMF based sensorless control strategies, i.e. fundamental back-EMF based, flux-linkage based, and other observer based, are very sensitive to the machine parameters. Hence, the further sensorless control method needs to be developed in order to avoid this issue.

# APPENDICES

## Appendix I Specification of Prototype Machines

**Test Machine-I [ZHU97]**

| | |
|---|---|
| Air-gap length | 0.5 mm |
| Coils per phase | 2 connected in parallel |
| Inner diameter | 37.0 mm |
| Lamination axial length | 26.0 mm |
| Magnet axial length | 26.0 mm |
| Magnet height | 11.0 mm |
| Magnet out diameter | 12.0 mm |
| Magnet outer diameter | 34.0 mm |
| Magnetic recoil permeability | 1.05 |
| Magnets | SPM |
| Max. phase current amplitude | 6.0 A |
| Mutual-inductance | -1.31 mH |
| Number of poles | 2 |
| Number of slots | 3 |
| Outer diameter | 100.0 mm |
| Outer diameter of retaining sleeve | 36.0 mm |
| Output power | 1.0 KW |
| Phase resistance: | 0.466 ohm |
| Pole-arc/pole-pitch | 1.0 |
| Rated DC voltage | 70 V |
| Rated phase current amplitude | 2.2 A |
| Rated speed | 3000 rpm |
| Rated torque | 0.3 Nm |
| Retaining sleeve thickness | 1.0 mm |
| Self-inductance | 3.19 mH |
| Slot opening | 3.0 mm |
| Tooth body width | 22.0 mm |
| Tooth tip angle | 113.8 deg. |
| Turns per coil | 62 |

**Test Machine-II [CHE10]**

| | |
|---|---|
| Air-gap length | 0.5 mm |
| Coils per phase | 2 connected in parallel |
| Copper wire diameter | 1.03 mm |
| Inner diameter | 37.0 mm |
| Lamination axial length | 26.0 mm |
| Magnet axial length | 26.0 mm |
| Magnet height | 11.0 mm |
| Magnet out diameter | 12.0 mm |
| Magnet outer diameter | 34.0 mm |
| Magnetic recoil permeability | 1.05 |
| Magnets | SPM |
| Max. phase current amplitude | 6.0 A |
| Mutual-inductance | -1.31 mH |
| Number of poles | 2 |
| Number of slots | 3 |
| Outer diameter | 100.0 mm |
| Outer diameter of retaining sleeve | 36.0 mm |
| Output power | 1.0 KW |
| Phase resistance: | 0.466 ohm |
| Pole-arc/pole-pitch | 1.0 |
| Rated DC voltage | 70 V |
| Rated phase current amplitude | 2.2 A |
| Rated speed | 3000 rpm |
| Rated torque | 0.3 Nm |
| Remanence | 1.2 T |
| Retaining sleeve thickness | 1.0 mm |
| Self-inductance | 3.19 mH |
| Slot opening | 3.0 mm |
| Stator skewing | None |
| Supply voltage | 200.0 V |
| Tooth body width | 22.0 mm |
| Tooth tip angle | 113.8 deg. |

# Appendix II Sensorless Rotor Position Signal Faults in Sensorless Control Based on Harmonic Back-EMFs

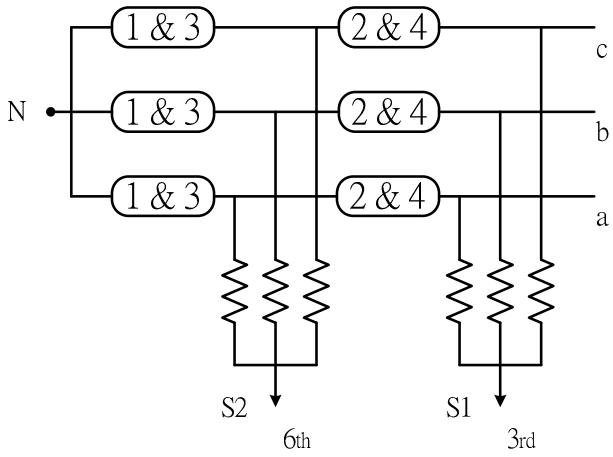


Fig. A1. Measurement of third and sixth harmonic back-EMF.

## Back-EMF Measurement and FFT Analysis

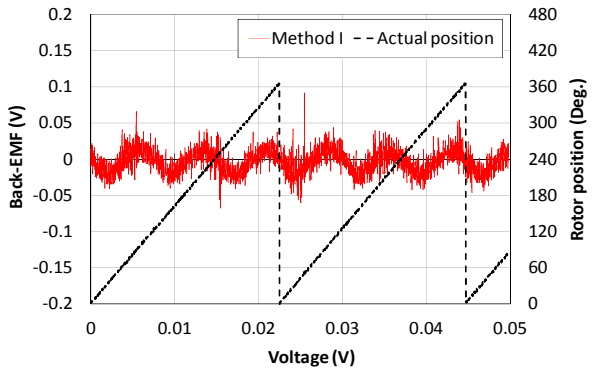


(a) Harmonic back-EMF waveforms

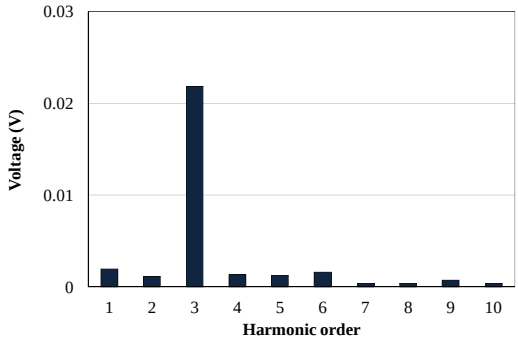


(b) FFT analysis of harmonics

Fig. A2. Method-I.

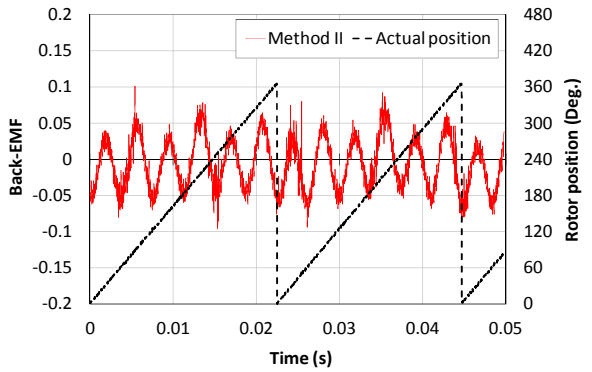


(a) Harmonic back-EMF waveforms

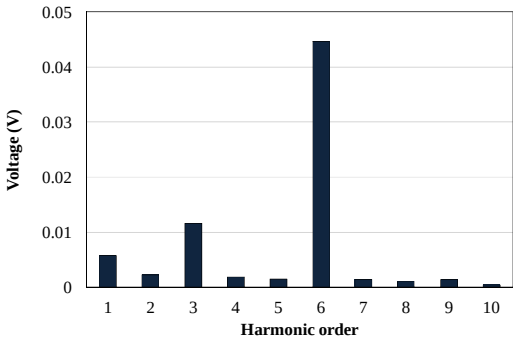


(b) FFT analysis of harmonics

Fig. A3. Method-II.

## Initial Rotor Position Detection

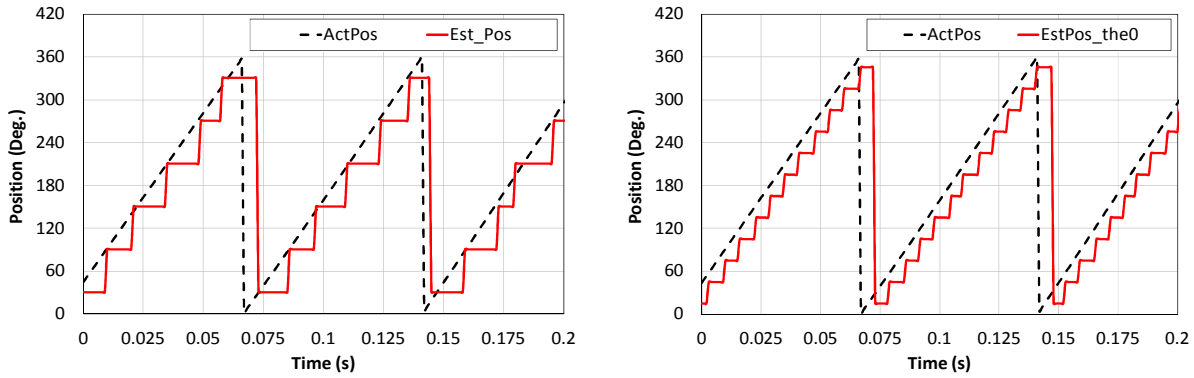


(a) Method-I (b) Method-II

Fig. A4. Rotor initial positions, 100 r/min.

## Rotor Position Estimation Based on TP-PLL

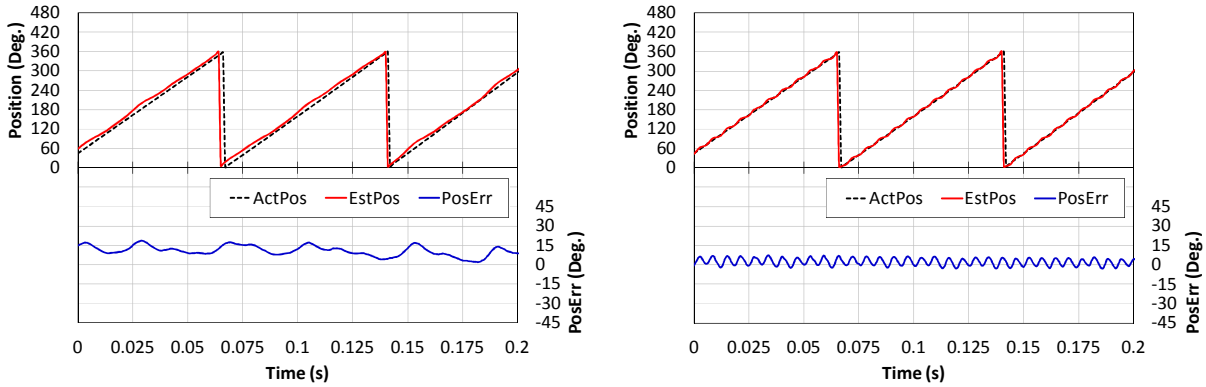


(a) Method-I (a) Method-II

Fig. A5. Rotor position estimations based on TP-PLL, 100 r/min.

## Faulty Monitoring

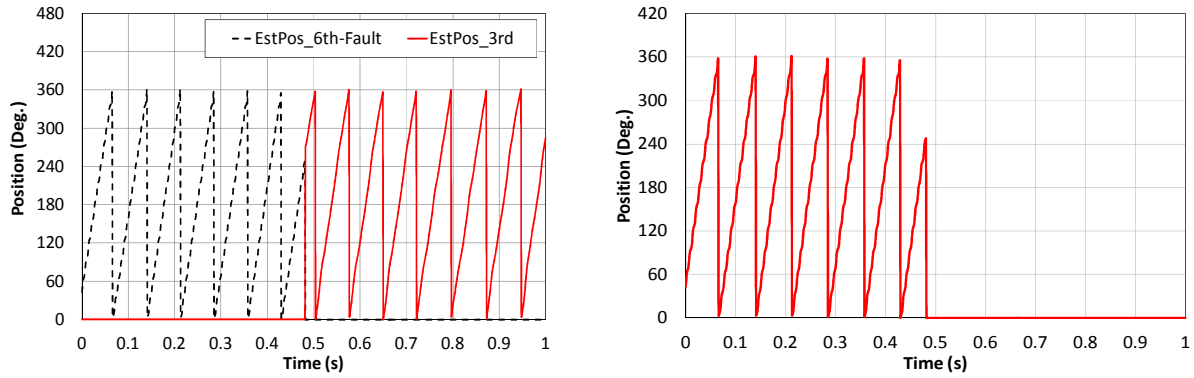


(a) Position fault (b) Position detection fault, sixth harmonic

Fig. A6. Faulty detection, 100 r/min.

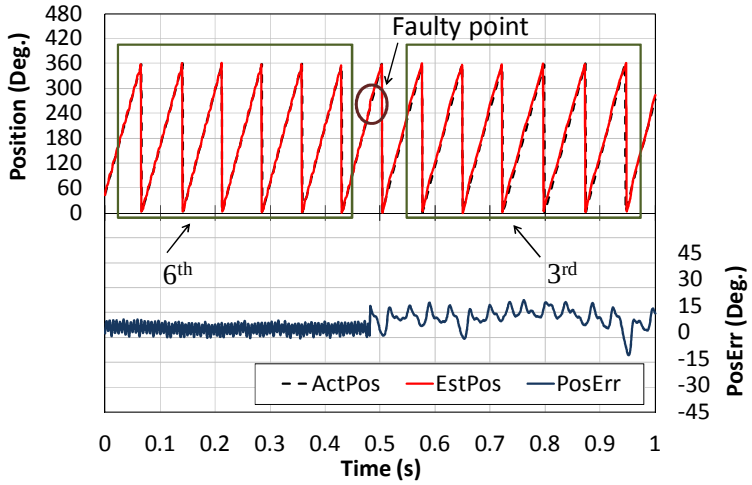


Fig. A7. Rotor position estimation based on sensorless fault tolerant control using third and sixth harmonics, 100 r/min.